

|

|

|



UNIVERSIDAD DE SEVILLA

DEPARTAMENTO DE QUÍMICA FÍSICA
Programa de Doctorado de Química Teórica y Computacional

Computational Chemistry of Actinoids in
Solution and Confined Media

Sergio Pérez Conesa
Sevilla, 2019

|

|

|



UNIVERSIDAD DE SEVILLA

DEPARTAMENTO DE QUÍMICA FÍSICA
Programa de Doctorado de Química Teórica y Computacional

Memoria presentada para optar al Grado de Doctor
en Química por la Universidad de Sevilla.

A handwritten signature in black ink that reads "Sergio".

Sergio Pérez Conesa

Vº Bº Directores de la Tesis

A handwritten signature in blue ink that reads "I. Sánchez M.".

Dr. Enrique Sánchez Marcos

A handwritten signature in blue ink that reads "José Manuel Martínez Fernández".

Dr. José Manuel Martínez Fernández

|

|

|

Me da vértigo el punto muerto
y la marcha atrás,
vivir en los atascos,
los frenos automáticos y el olor a gasoil.
Me angustia el cruce de miradas
la doble dirección de las palabras
y el obsceno guiñar de los semáforos.

Me arruinan las prisas y las faltas de estilo,
el paso obligatorio, las tardes de domingo
y hasta la línea recta.
Me enervan los que no tienen dudas
y aquellos que se aferran
a sus ideales sobre los de cualquiera.
Me cansa tanto tráfico
y tanto sinsentido,
parado frente al mar mientras que el mundo gira.

Francisco M. Ortega, (Fragmento en videoclip Standby
de Extremoduro)

|

|

|



Agradecimientos

Todos los químicos conocen el trabajo de Douglas Hartree, uno de los físicos padres de la química y la física cuántica molecular. Pocos en cambio conocen a su padre, William Hartree y a él todos los químicos deberíamos también estarle muy agradecido. Hartree padre, que era profesor de ingeniería jubilado, ayudó a su hijo a calcular numéricamente las soluciones a las ecuaciones de Hartree hijo, un trabajo muy arduo en esos tiempos. A parte de a su padre, Douglas Hartree debería estar muy agradecido a su madre, que era activista de los derechos de la mujer, por la educación en valores que seguramente le dio. Y probablemente le deba también mucho a su mujer que le alegraba cuando el trabajo le desanimaba o porque simplemente le hacía feliz.

Yo también quiero darle las gracias a todas las personas que en mayor o menor medida han contribuido a que presente esta tesis ayudándome directa o indirectamente:

- Al profesor Enrique Sánchez Marcos por hacer posible esta tesis y por todas las cosas que me ha enseñado sobre química física y la investigación.
- Al profesor José Manuel Martínez la persona de la que más he aprendido dinámica molecular y mecánica estadística y que ha hecho que sea mi parte favorita de la química teórica.
- Al profesor Rafael Rodríguez Pappalardo, el “señor Lobo” del grupo porque soluciona todos los problemas.

- Al Dr. Francisco Torrico que comenzó la aventura actínida del grupo y sin la cual esta tesis no habría sido posible.
- A mis antiguos compañeros de grupo Noelia y Dani por ayudarme al llegar al grupo y por enseñarme XAS.
- Al professor Michele Parrinello por acogerme en su laboratorio y enseñarme tantas cosas sobre metadinámica y más.
- Al Dr. Pablo Piaggi por hacer conmigo parte del trabajo de esta tesis y hacerme la estancia en Lugano mas alegre.
- Al resto del grupo del prof. Parrinello por hacer que mi estancia en Lugano fuera estupenda y por ayudarme desinteresadamente en mi proyecto.
- A Juanín por hablar tanto rato sobre las cosas de esta tesis tomando cervezas.
- A mi hermana por hacerme la portada y otros de los gráficos de la tesis.

- A mis padres y mi hermana de nuevo porque siempre habéis apoyado mi educación y porque quien soy es en gran medida gracias a vosotros.
- A la memoria de mis abuelos y a mis abuelas. Se que les hará mas ilusión aún que a mí.
- A mi novia Mari Ángeles porque eres la que me ha sufrido y apoyado durante estos cuatro años. Porque nunca olvidaremos lo bien que nos lo pasamos en Suiza. Porque estos años sin tí no habrían sido tan maravillosos. Porque en todo momento me haces muy feliz.



Contents

Contents	IX
List of Tables	XIII
List of Figures	XV
Abstract	XVII
Bibliography	XXI
1 Introduction	1
1.1. Nuclear Power	1
1.2. Nuclear Fuel, Nuclear Waste and Nuclear Cemeteries	3
1.3. High Level Radioactive Waste Permanent Storage	6
1.4. Hydrophobic Solvation	8
1.5. Systems Studied	11
1.6. Literature Review	13
1.7. Bibliography	16
2 Thesis Goals	21
3 Methods	25
3.1. Molecular Simulation	25
3.2. Metal Ion Force Fields	28

3.3.	The Hydrated Ion Model	32
3.4.	X-Ray Absorption Spectroscopy	36
3.4.1.	EXAFS Spectroscopy	39
3.5.	Entropy In Molecular Dynamics Simulations	43
3.6.	Metadynamics	45
3.7.	Bibliography	51
4	A hydrated ion model of $[UO_2]^{2+}$ in water: Structure, dynamics, and spectroscopy from classical molecular dynamics	59
4.1.	<i>J. Chem. Phys.</i> 2016 , <i>145</i> , 224502–224523	59
	Supplementary Material	72
5	A general study of actinyl hydration by molecular dynamics simulations using ab initio force fields	77
5.1.	<i>J. Chem. Phys.</i> 2019 , <i>150</i> , 104504–104514	77
	Supporting Information	89
6	Extracting the Americyl Hydration from an Americium Cationic Mixture in Solution: A Combined X-ray Absorption Spectroscopy and Molecular Dynamics Study	95
6.1.	<i>Inorg. Chem.</i> 2018 , <i>57</i> , 8089–8097	95
	Supplementary Material	107
7	Combining EXAFS and Computer Simulations to Refine the Structural Description of Actinyl in Water	119
7.1.	Pending on publication	119
	Supplementary Material	144
8	Hydration and Diffusion Mechanism of Uranyl in Montmorillonite Clay: MD Using an Ab Initio Potential	151
8.1.	<i>J. Phys. Chem. C</i> 2017 , <i>121</i> , 27437–27444	151
	Supporting Information	161
8.2.	<i>Erratum</i>	169
9	A local fingerprint for hydrophobicity and hydrophilicity: from methane to peptides	171
9.1.	<i>J. Chem. Phys.</i> 2019 , <i>150</i> , 204103–204108	171
	Supporting Information	181

9.2. Hydrophobicity fingerprint of actinyls	193
10 Results and Discussion	195
10.1. Force Fields Development	195
10.1.1. Actinyl Force Fields In Solution	195
10.1.2. Auxiliary Am ³⁺ force field	199
10.1.3. Hydrated Ion-Clay Interaction Potential	199
10.2. Physico-chemical properties of actinyls in solution	201
10.3. Modelling of actinyl EXAFS spectra	203
10.4. Modelling of americyl XAS spectra	204
10.5. Diffusion of uranyl in montmorillonite clay	206
10.6. Development of a local hydrophobicity/hydrophilicity fingerprint	207
10.6.1. Application to actinyl hydration	210
10.7. Bibliography	210
11 Conclusions	215

|

|

|



List of Tables

1.1. Composition of spent nuclear fuel	5
9.1. Fingerprint values for actinyls	193

|

|

|



List of Figures

1.	Cover Inorganic Chemistry	XIX
2.	Cover Journal Physical Chemistry C	XX
1.1.	Nuclear Fuel Cycle	4
1.2.	Montmorillonite clay minerals	7
1.3.	Hydrated montmorillonite clay containing uranyl cations	8
1.4.	Hydration of CH ₄	10
3.1.	Research Triangle	27
3.2.	Many body effects in the Po(VI) hydrate.	30
3.3.	Charge transfer in [Zn·(H ₂ O)] ²⁺	31
3.4.	Hydrated ion atom types	33
3.5.	X-Ray Absorption Spectrum	38
3.6.	Uranyl EXAFS spectrum	39
3.7.	EXAFS paths illustration	41
3.8.	Metadynamics algorithm	47
3.9.	Metadynamics free energy surface	48
8.1.	Correction to Electrostatic Potential Surface	169
10.1.	Components of the Hydrated Ion Model	196
10.2.	QM scans used to parametrize the HIC	200
10.3.	Snapshots of [NpO ₂ ·(H ₂ O) ₅] ²⁺ solvation	203

List of Figures

10.4. EXAFS spectra of Am	205
10.5. Strong interaction site for uranyl	206
10.6. Fingerprint values for the 20 aminoacids	209



Abstract

The nuclear power industry accounts for around 10% of the electricity production worldwide and up to 70% in some countries.¹ One of the problems of this otherwise clean energy source is the generation of high level radioactive waste which remains harmful for centuries.² Spent nuclear fuel is reprocessed to extract the actinoids that are still fissile (U and Pu) from highly radiotoxic minor actinoids (Np and Am).^{2–4} This is done typically through the PUREX process which is based on liquid-phase extraction of actinoids based on their physico-chemical properties. Some of the most important species in this process are the actinyl hydrated cations, $[AnO_2 \cdot (H_2O)_5]^{2+/+}$ (aq)] for An=U,Np,Pu,Am. The actinyls are linear oxo-cations formed by the oxidation states V and VI of the metal. High level radioactive waste resulting from the PUREX process are destined to be kept underground in permanent geological repositories for the centuries to come.² These repositories use clays as liner materials to prevent potential diffusion of radioelements to the environment.⁵ The main clay component is montmorillonite clay.⁵ In this thesis we will study the physico-chemical properties of actinyl cations in aqueous solution and in clays using computational chemistry.

In order to run molecular dynamics simulations (MD), *ab initio* force fields were developed for U(VI), Np(VI), Np(V), Pu(VI) and Am(VI) in water. One additional force field was developed for the interaction of uranyl with the montmorillonite clay aluminosilicate layers. The force fields are based on the hydrated ion model^{6–8} developed by the group in the mid 90's. This model

Abstract

accounts for many-body effects like polarization and charge transfer in a non-polarizable framework. Its main characteristic is to consider the hydrated ion and not the naked ion as the solute. In this way, first-shell water molecules and bulk water molecules are different species. This allows the assignment of different atom types, partial charges and interaction potentials to the first-shell than to bulk water molecules. It additionally parametrizes explicitly hydrated ion bulk-water molecule interactions.

Once the force fields were developed, MD simulations of the actinyls in water were run. The simulations reproduced satisfactorily a wide variety of physico-chemical properties of the system: hydration enthalpy, vibrational spectra, diffusion coefficients, XAS spectra, etc. This was a sign of the robustness of our force field development strategy. The first conclusion drawn from the simulations is that the solvation structure of the different actinoids is almost indistinguishable one from the other. Furthermore, despite the charge difference between $[NpO_2]^{2+}$ and $[NpO_2]^+$, their solvation resembled strongly. We observed that the equatorial solvation of the actinyls was equal to most conventional cations: the first-shell forms two hydrogen bonds with bulk water molecules. In contrast, the O_{yl} atom solvates hydrophobically: water molecules surround it forming hydrogen bonds with other solvent molecules but not with O_{yl} . We concluded that the actinyl cations are highly anisotropic amphiphilic cations that have a conventional hydration sphere capped at the poles by hydrophobic solvation regions.

The theoretical EXAFS spectra of the actinyls were calculated and compared to experiment. For uranyl, the theoretical-experimental agreement is good. For the rest of actinyls the reproduction is less satisfactory, particularly in the case of the triplet cation, $[NpO_2]^{2+}$. The force fields for these cations were developed at the DFT level of theory. With the aim of improving performance, the explicit treatment of static correlation was then taken into account. A NEVPT2^{9–11} force field was developed for the $[NpO_2]^{2+}$ -H₂O interaction. The effect of this increase in level of theory was studied, and the decomposition of the complex EXAFS signal was shown to be useful in the understanding of the main EXAFS spectrum features.

Due to its chemical instability, americyl ($[AmO_2]^{2+}$), has never been isolated in aqueous solution. As a result, the only EXAFS spectrum of $[AmO_2]^{2+}$ corresponds to a 70/30 mixture of americyl and Am³⁺.¹³ We simulated the EXAFS spectra of both species from their respective MD simulations and weighted them into a single spectrum to produce a simulated EXAFS of a

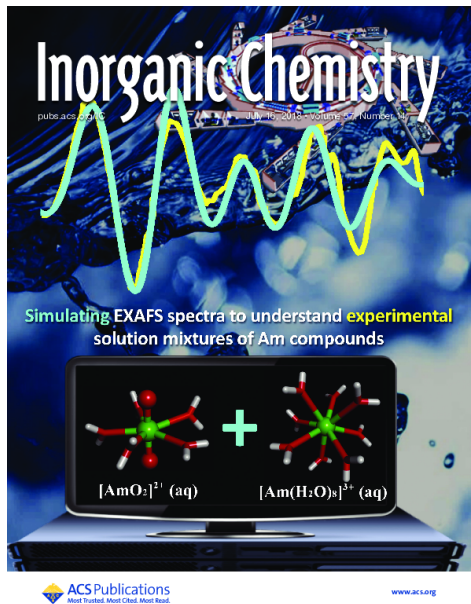


Figure 1 Cover of *Inorganic Chemistry* for the work “Extracting the Americyl Hydration from an Americium Cationic Mixture in Solution: A Combined X-ray Absorption Spectroscopy and Molecular Dynamics Study” presented in this thesis.¹²

mixture of species.¹² The good comparison of the simulated spectrum and experiment allowed us to predict theoretically the structural parameters and EXAFS spectrum of a pure americyl solution, a solution yet to be obtained experimentally.¹⁴ The same procedure was applied to the XANES spectrum. This work was featured in the cover of the issue 57 of *Inorganic Chemistry* of 2018, Figure 1.

The MD simulations of the uranyl hydrated ion in the aqueous interlayers of montmorillonite clays gave interesting microscopical details of the system hard to obtain experimentally.¹⁴ The simulations reproduced the few experimental microscopical information of the system: the uranyl hydrated ion interacts with the surface through the formation of an outer-shell complex¹⁵ and the uranyl axis is neither perpendicular nor parallel to the surface.¹⁶ We calculated for the first time from a MD simulation the constrictivity factor, δ_{int} , which was found to be near the right order of magnitude to experiment. Strong interaction sites for uranyl were found on the clay. These sites are groups of three magnesium substitutions around which uranyl cations are

Abstract

electrostatically attracted. As a consequence the diffusion of uranyl in the clay exhibits a hopping diffusion mechanism. Because of this, the diffusion of uranyl increases with increasing uranyl concentration due to cation-cation interactions and a larger coverage of surface sites. This work was featured in the cover of the issue 121 of the Journal of Physical Chemistry C of 2017, Figure 2. In addition it was chosen best article of a young member of the “Specialized Group of atomic and molecular physics” (GEFAM) of the Royal Spanish Society of Physics in 2017.

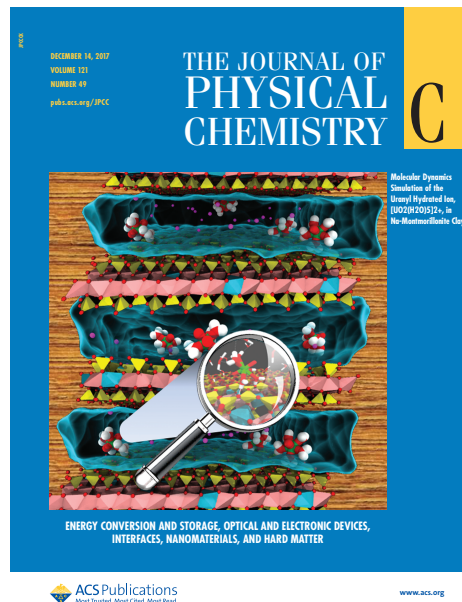


Figure 2 Cover of the *Journal of Physical Chemistry C* for the work “Hydration and Diffusion Mechanism of Uranyl in Montmorillonite Clay: Molecular Dynamics Using an Ab Initio Potential” presented in this thesis.¹⁴

Finally, a simple local fingerprint for hydrophobicity/hydrophilicity was developed. This fingerprint is inspired by the expansion of the entropy of a system as a sum of terms of increasing correlational order.^{17,18} The fingerprint, which refers to the translational component of the entropy, measures the hydrophobicity/hydrophilicity of individual atoms of a solute taking as input its radial distribution function with water. The fingerprint classifies satisfactorily, the atoms of the amino acids. Nevertheless, the fingerprint has mixed results in classifying the atoms of the actinyl pentahydrates. A future

improved fingerprint should probably make use of orientational pair entropy in addition to some techniques to consider the anisotropy of the solute in complex environments. Additionally, the fingerprint proved to be a useful solvation/desolvation collective variable for enhanced sampling simulations.

Bibliography

1. World Bank, Nuclear Energy Statistics World Bank. 2015; <https://data.worldbank.org/indicator/eg.elc.nucl.zs>.
2. Lozano Leyva, M. *Nucleares, ¿Por qué no?*; DEBOLSILLO: Barcelona, 2010.
3. Herbst, R. S.; Baron, P.; Nilsson, M. In *Adv. Sep. Tech. Nucl. Fuel Reprocess. Radioact. Waste Treat.*; Nash, K. L., Lumetta, G. J., Eds.; Woodhead Publishing Series in Energy; Woodhead Publishing: Cambridge, 2011; Chapter 6.
4. L., K.; Madic, C.; Jagdish, M. N.; Lacquement, J. In *The Chemistry of Actinide and Transactinide Elements*; Katz, J. J., Seaborg, G. T., Eds.; Springer Science & Business Media: Dordrecht, The Netherlands., 2007; Chapter 24.
5. Delage, P.; Cui, Y.; Tang, A. *J. Rock Mech. Geotech. Eng.* **2010**, *2*, 111–123.
6. Pappalardo, R. R.; Sánchez Marcos, E. *J. Phys. Chem.* **1993**, *97*, 4500–4504.
7. Martínez, J. M.; Pappalardo, R. R.; Sánchez Marcos, E. *J. Chem. Phys.* **1998**, *109*, 1445–1455.
8. Martínez, J. M.; Pappalardo, R. R.; Sánchez Marcos, E. *J. Am. Chem. Soc.* **1999**, *121*, 3175–3184.
9. Angeli, C.; Cimiraglia, R.; Evangelisti, S.; Leininger, T.; Malrieu, J.-P. *J. Chem. Phys.* **2001**, *114*, 10252–10264.
10. Angeli, C.; Cimiraglia, R.; Malrieu, J.-P. *Chem. Phys. Lett.* **2001**, *350*, 297–305.
11. Angeli, C.; Cimiraglia, R.; Malrieu, J.-P. *J. Chem. Phys.* **2002**, *117*, 9138–9153.
12. Pérez-Conesa, S.; Martínez, J. M.; Pappalardo, R. R.; Sánchez Marcos, E. *Inorg. Chem.* **2018**, *57*, 8089–8097.
13. Riddle, C.; Czerwinski, K.; Kim, E.; Paviet, P.; Weck, P.; Poineau, F.; Conradson, S. *J. Radioanal. Nucl.* **2016**, *309*, 1087–1095.

BIBLIOGRAPHY

14. Pérez-Conesa, S.; Martínez, J. M.; Sánchez Marcos, E. *J. Phys. Chem. C* **2017**, *121*, 27437–27444.
 15. Catalano, J. G.; Brown Jr, G. E. *Geochim. Cosmochim. Acta* **2005**, *69*, 2995–3005.
 16. Denecke, M. A.; Bauer, A.; Kim, J. I.; Moll, H. *Miner. Interact. Close to Equilib.* **1999**, *35*–37.
 17. Nettleton, R. E.; Green, M. S. *J. Chem. Phys.* **1958**, *29*, 1365–1370.
 18. Baranyai, A.; Evans, D. J. *Phys. Rev. A* **1989**, *40*, 3817–3822.
-



CHAPTER

1

Introduction

As you read over these lines a significant amount of the energy used by the light-bulb illuminating these pages is produced by the splitting of uranium and plutonium nuclei. 20% if you are right now in Spain, the USA or the United Kingdom, 30-40% if you are in the Czech Republic, Finland, Belgium, South Korea, Sweden or Switzerland and a world record of 77% produced by state-owned company if you are in France.¹ Even if you are reading this from Italy where nuclear energy has been forbidden, part of the energy you are consuming is nuclear since it is bought from the French nuclear industry.

Regardless of the reader's opinion on the nuclear power industry, it undoubtedly is an industrial leviathan that should be understood if only for the sake of nuclear security. In this chapter we will make an effort to overview some aspects of the industry and how understanding the chemical nature of some of its essential substances is still relevant 70 years after the first nuclear reactor developed by Enrico Fermi himself.

1.1. Nuclear Power

In 1939, Otto Hanh, Lise Meitner and Otto Robert Frisch discovered and described the fission of uranium on the basis of the “liquid drop” model of the nucleus. Hanh received the Nobel Prize in Chemistry for the experimental discovery. Unfortunately Meitner and Frisch who explained the physics behind did not. The essential idea of fission is that the nucleus of ^{235}U is metastable

and the impact of a slow neutron can split it into more stable smaller nuclei. The sum of daughter nuclei masses is lower than that of ^{235}U and the difference in mass is converted into tremendous amounts of energy according to Einstein's famous equation: $E = mc^2$. Two or three neutrons are also emitted in the process which depending on their speed might impact another ^{235}U nucleus and continue the chain reaction over and over.

If the concentration of ^{235}U is extremely high the reaction advances exponentially leading to a sudden splitting of all the fissile nuclei and a nuclear explosion occurs. To obtain this critical concentration of the nuclear material generally, another conventional explosion must be used to compress the nuclear explosive. This is the basis of a fission nuclear bomb: an explosion within the bomb compresses the fissile material (uranium or plutonium) into critical density which releases in a split second most of its nuclear energy. This was the mechanism used in the bombings of Hiroshima and Nagasaki during World War II.

The energy of fission can also be used to generate electricity by controlling the nuclear reaction. Uranium or plutonium act as fuel and not as explosives. The nuclear fuel is composed in most cases of $\text{UO}_2(\text{s})$ with varying ratios of $^{235}\text{U} / ^{238}\text{U}$. At ordinary densities it generates no energy. Spontaneous fission of ^{235}U generates neutrons that are fast and inefficient in splitting other nuclei. But if we introduce a moderator material (typically graphite, water or heavy water) the neutrons can scatter on the nuclei of the moderator slowing them down and making the thermal (slow) neutrons effective in splitting fissile nuclei. This promotes fission and a chain nuclear reaction is formed generating energy. The growth of the energy emitted is exponential and must be reduced. For this, another material captures the excess neutrons and reduces the rate of fission controlling the reaction and avoiding a nuclear accident. These materials are substances that are effective in capturing neutrons, for example cadmium or boron, and are known as control materials. In this way, the fuel is steered into steady reaction. The energy liberated heats water surrounding the reactor vessel which in the form of steam moves turbines and a generator converts the kinetic energy into electricity.

Nuclear energy is a cheap and CO_2 -free source of energy using a fuel that is fairly abundant, 40 times more than silver. In addition, unlike fossil fuels, the uranium ores are fairly evenly distributed by countries according to the Organization for Economic Co-operation and Development (OECD).² Then, why is not nuclear energy the main source of electricity in the world? The

reasons are all derived by the terrible effects that radiation and radioactivity can cause on human beings and the environment. Three main reasons can be argued:

- The sometimes reasonable and sometimes unreasonable fear of the population of anything containing the adjective “nuclear”. This is the reason why doctors ask their patients to have a Magnetic Resonance Imaging (MRI) which should actually be called Nuclear Magnetic Resonance Imaging. Ironically, unlike in other medical techniques no radioactivity is involved in MRIs.
- The occurrence of three major nuclear power accidents: Three Mile Island (1979), Chernobyl (1986) and Fukushima (2011).
- The generation of highly radioactive nuclear waste that must be processed safely and adequately to be kept afterwards for centuries undisturbed in geological facilities.

About the first two reasons this work will not dive into but we refer to the excellent books of Prof. Lozano Leyva.^{3,4}

1.2. Nuclear Fuel, Nuclear Waste and Nuclear Cemeteries

Nuclear fuel is mostly $\text{UO}_2(\text{s})$. The useful fissile isotope is ^{235}U but it is only the 0.7% of natural uranium being 99% of it ^{238}U . For this reason, many reactors run uranium enriched in ^{235}U up to 1-3%. Additionally, plutonium can also become fuel for several designs of reactors. This plutonium can be obtained from the dismantlement of thermonuclear bombs, also known as H-bombs, that use a plutonium fission explosion to initiate a fusion chain reaction of deuterium and tritium. Additionally, during power generation in a nuclear power plant, the neutron capture of uranium generates plutonium. This plutonium can be recovered from spent uranium fuel, an extraction known as reprocessing. Plutonium and depleted uranium can be used in some nuclear reactors in the form of mixed oxides in a material known as MOX. Finally, there is a high interest in the substitution of uranium and plutonium fuels by thorium⁶ which would have significant advantages: it is more abundant and efficient than uranium, produces less harmful byproducts and cannot be

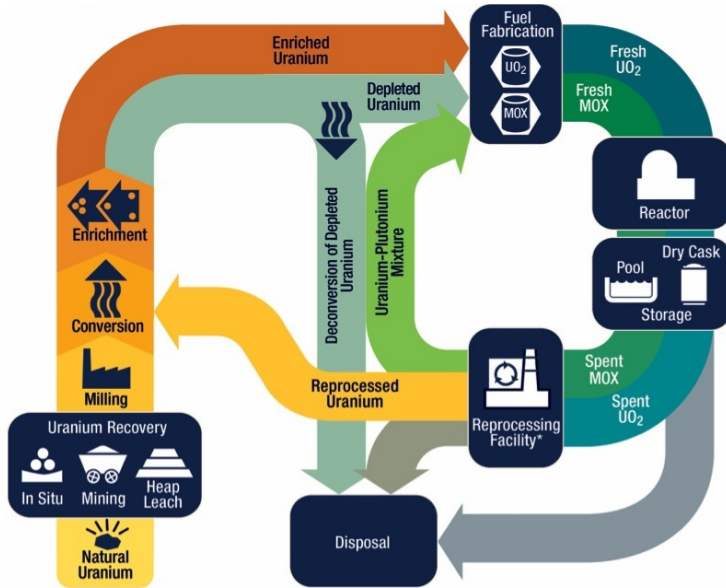


Figure 1.1 Schematic representation of the nuclear fuel cycle from the mine to disposal.⁵

used to make weapons. But the most important feature of the thorium chain reaction is that there is no possibility of a meltdown like in Chernobyl making it much safer than the uranium alternative. Unfortunately thorium technology is still under development and while uranium remains cheap the incentives to fully develop thorium technologies are low. Figure 1.1 represents the cycle of uranium from the mine to its disposal.

High level radioactive waste is made by nuclear power plant residues which are the result of the fission of the fuel. They contain unstable nuclei that emit alpha, beta or gamma radiation. Nuclear fuel is much more radioactive and dangerous when it has already been spent. For this reason reprocessing is a much more environmentally dangerous step than the actual power production. In spite of this, there has never been any accident in the handling and permanent storage of high level radioactive waste.

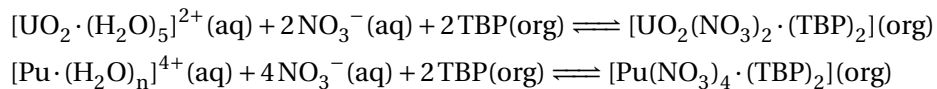
Reprocessing extracts uranium and plutonium from the waste to feed the reactor and separate radiotoxic elements for its permanent disposal. Spent nuclear fuel composition is summarized in Table 1.1. The main problem of reprocessing is the complexity of the mixture including a wide variety of

Table 1.1 Typical composition of spent nuclear fuel from a uranium nuclear power plant.³

95.6%	^{232}U : 0.1-0.3%; ^{234}U : 0.1-0.3%; ^{235}U : 0.5-1.0%; ^{236}U : 0.4-0.7%; ^{238}U : rest
2.9%	Stable elements.
0.9%	Pu.
0.3%	Cs and Sr (fission fragments).
0.1%	I and Tc (fission fragments).
0.1%	Long-lived fission fragments.
0.1%	Np, Am and Cm (long-lived transuranium elements).

elements and isotopes some of them chemically very similar like the actinoids. If reprocessing is done, which is not always the case for economical reasons, it is done normally using the PUREX method (Plutonium Uranium Redox EXtraction).^{3,7,8}

The PUREX method was developed as a part of the Manhattan project at the Oak Ridge National Laboratories and its initial goal was to purify plutonium for its use as a nuclear weapon detonant. The first step of PUREX is to dissolve the solid nuclear fuel pellets in concentrated nitric acid. Then Pu and U are extracted using liquid/liquid extraction. The original aqueous phase is exposed to a hydrocarbon phase in the presence of a complexating agent, mainly, tri n-butyl phosphine (TBP):



TBP is highly selective for oxidation states VI and IV and virtually has no affinity for states III and V (Np(V), Am(III), Cm(III), etc.). The extraction is nearly quantitative and highly selective. The organic phase is then treated with reducing agents to reduce Pu(IV) to Pu(III) which is extracted with another aqueous phase with a very high yield. The resulting Pu and U solutions are then purified, evaporated and the actinoids are converted into oxides to be reused as nuclear fuel. The key chemical point in the process is the stability of $[\text{UO}_2]^{2+}$ and the chemical and electrochemical flexibility of the Pu ions. The original aqueous phase contains all the highly radioactive elements, most importantly highly radiotoxic actinoids like Cm, Am and Np. Although the basic chemical ideas behind PUREX are simple, in practice it is a very complex chemical engineering process.

The final waste generated from PUREX contains the very radioactive but non-fissile nuclei including several transuranium actinoids (Np, Am and Cm mostly). This radioactive waste is the smallest by far in volume of all radioactive waste of industry but concentrates most of the sample radioactivity: 99.9%. For this reason they are known as High Level Radioactive Waste (HLRW).⁹

1.3. High Level Radioactive Waste Permanent Storage

HLRW is kept in waste pools close to the reprocessing or nuclear power plants allowing them to cool off with water acting as a radiation barrier. These materials can be then vitrified or solidified and introduced in stainless steel containers and allowed cooling for up to 50 years before their permanent disposal. The radioactive activity of the containers will remain terribly harmful for hundreds of thousands of years.

Several solutions have been proposed to conceal for the centuries to come the HLRW: underground geological permanent storage, deep sea ground storage, glacier storage in Antarctica, sending it to outer space or transmutation into harmless nuclei. Even though transmutation would be the ideal solution, unless major breakthroughs occur, Science is decades away from that kind of technology. The best agreed solution is storage in geological underground permanent disposal sites. Geological permanent storage sites are chambers dug deep underground in the rock where the containers will be stored safely for the centuries to come. The construction would be done in geologically stable locations and the rock would conceal the radioactive matter and its radiation. The rock acts as a passive barrier and also prevents any water from leaking in or out of the repository.

Most countries do have nuclear permanent disposal sites to keep mid and low level radioactive waste generated by the non-nuclear industry, research, radiomedicine etc. Nevertheless, even though the amount of HLRW has been growing since the beginnings of nuclear power production a fully functional HLRW permanent geological disposal site is still missing. Many countries have plans to build it. Finland will be the first country to have a geological HLRW disposal site, Onkalo, in Posiva which is expected to become operative in 2023.⁹

The security of the facilities must be extreme. Specially because the nuclear containers remain hot for hundreds of years and are exposed to severe



a)



b)

Figure 1.2 a) Montmorillonite clay rock. b) Montmorillonite clay crystals embedded in quartz.^{10,11}

radiation damage. The sites should be air-tight particularly to prevent the entrance of water that could disperse the radioelements into the underground streams.

Clays are particularly suited both as natural host rock or natural barrier for the permanent geological HLRW site and as liner material or artificial barrier to conceal the repository.¹² The most used clay rock is bentonite which is primarily composed of montmorillonite clay (Figures 1.2 and 1.3). Bentonite is compacted and mixed with sand and serves as an artificial barrier surrounding

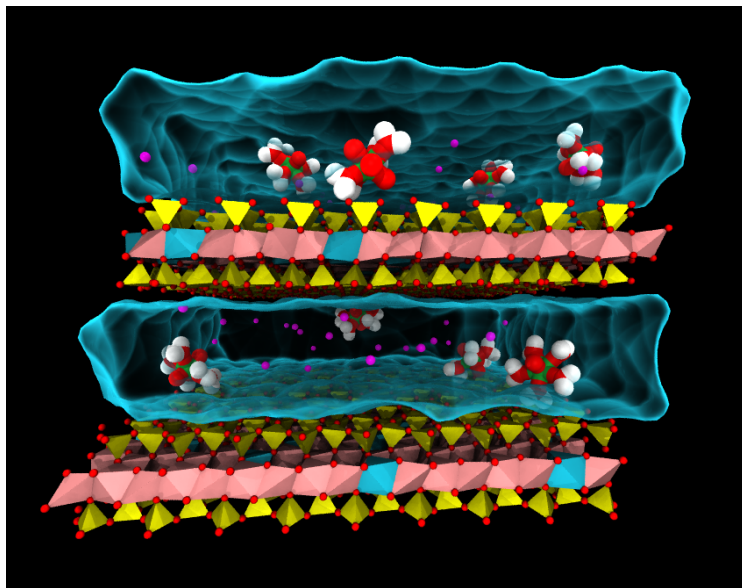


Figure 1.3 Unit cell of hydrated sodium montmorillonite clay containing uranyl hydrated ions, $[UO_2 \cdot (H_2O)_5]^{2+}$, in the interlayer. The water bulk water molecules are omitted and represented as a blue transparent surface. The uranyl cations are drawn with the “licorice” representation. SiO_4 tetrahedra (yellow), AlO_6 octahedra (pink) and MgO_6 (blue) are represented as polyhedra. The atoms are colored as follow: O (red), H (white), Na^+ (purple) and U (green).

the horizontal galleries which hold the HLRW. Clays are selected for three reasons: their high thermal conductance to dissipate the heat generated by the waste radioactivity, its low permeability to water and its high retention of radionuclides. This high retention of radioelements is due to their ionic exchange capability. If the clay is exposed to a cation containing solution it would release its harmless Na^+ cations and absorb radioactive cations such as actinyls.

1.4. Hydrophobic Solvation

In this section, we will make a small detour from the actinoids to talk about hydrophobic solvation which shall be relevant in the study of actinyl solvation and the development of the hydrophobicity and hydrophilicity fingerprint.

“Like dissolves like” is one of the first concepts a chemist learns in relation

to the solvation of compounds.¹³ It implies that solutes that are chemically like water will mimic water and be hydrophilic. Solutes that are not like water will “dislike” water and be hydrophobic. The classification of atoms and by extension molecules as hydrophilic and hydrophobic has traditionally been done based on chemical experience and heuristics which assign the character based on the chemical identity of the atoms. Hydrophobicity and hydrophilicity plays an important role in processes such as solvation, protein folding, micelle or membrane formation, phase transfer or crystallization.

Hydrophobic solvation has several peculiarities. Hydrophobic compounds have a positive free energy of hydration, a negative entropy of hydration, a negative enthalpy of hydration and a large positive specific heat of hydration.^{14,15} The word “hydrophobic” can generate the impression that the interaction of a hydrophobe with water should be repulsive and therefore its solvation enthalpy positive. Nevertheless, hydrophobic solutes interact through van der Waals interactions with water which are weak compared to water-water interactions but attractive. van der Waals interactions are non-directional so water molecules are free to form a hydrogen bond network around the solute. Figure 1.4 shows methane in liquid water and how the water molecules form their hydrogen bond network around the solute.

Hydrophobic solutes have the tendency to self-aggregate reducing their surface exposed to water. This self-assembly is known as the hydrophobic effect. Within chemistry and biochemistry it is common to talk about hydrophobic interactions or forces to describe the hydrophobic effect but this is misleading and should be avoided.¹⁶ It seems to suggest that there is an intermolecular interaction “special” to these systems which have only regular van der Waals or hydrogen bond interactions. The hydrophobic effect is a water-mediated “self-sorting” phenomenon. The free energy of water molecules is lower at bulk solution than on a hydrophobic molecule surface. The segregation of hydrophobic solutes reduces the amount of water at their surfaces producing an overall decrease of free energy of the system.

The self-assembly *is* driven by a force, but it must be considered a force only in the “potential of the mean force” sense. In other words, if there is a free energy surface which is a function of a self-assembly collective variable its derivative can be considered the hydrophobic effect force.¹⁵ Nevertheless, this terminology leads to misunderstandings and should ideally disappear.

It has long been known that for small hydrophobic solutes at room temperature the entropic term dominates the free energy of solvation and is the

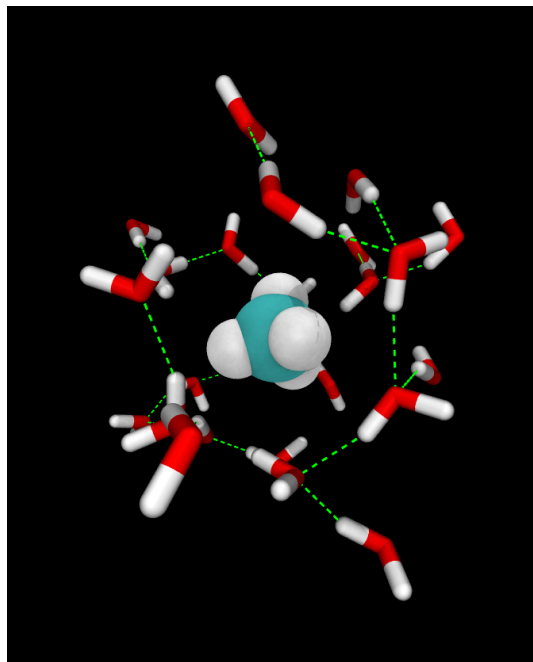


Figure 1.4 Snapshot of a MD simulation of methane in water. Only nearest water molecules are shown. The water molecule forms its hydrogen bond network around the cavity generated by methane in the solvent.

reason for the low solubility of hydrophobic molecules in water.¹⁷ This was explained theoretically in the works of Hummer et al^{18,19} on hydrophobic solvation. Their works started a body of theory known as “Information Theory” of hydrophobic solvation. Information Theory models the hydrophobic solute as a cavity in water. This cavity can be explicitly generated in solution by introducing a hard sphere particle or by the isomorphic problem of studying spontaneously generated cavities in water.

The cavity generated by hydrophobic solutes disrupts the hydrogen bond network of water decreasing the number of allowed microstates and thus the entropy of the solvent. Interestingly, this happens without affecting the average number of hydrogen bonds formed by the solvent around small solutes.^{17,20–23} For this reason the hydration entropy of small hydrophobic molecules correlates with molecular volume. This picture relates to the classical notion of hydrophobic solvation proposed by Frank and Evans in 1945, the “Iceberg” model of hydrophobic solvation. In this model, the structure of water

around a hydrophobic solute is reinforced and the dynamics slowed down by the formation of an ice-like cage of water molecules.²⁴

If the molecular size is high (~1 nm) a water/vapor-like interface is generated²⁵ and the hydration entropy correlates with the molecular surface area instead of volume.¹⁷ The reason is that water on the solute surface cannot form in this case the average number of hydrogen bonds it forms in solution.

Unlike hydrophobic solvation of small molecules at room temperature, the hydrophobic effect can be enthalpy driven, entropy driven or both.^{16,17} Quoting David Chandler:

“The increase in molecular self-assembly of hydrophobic solutes with temperature is often cited as implying that hydrophobic interactions are entropic. Entropy does indeed contribute, but the assembly process is driven by the difference between the entropically dominated solvation free energy of small molecules and the enthalpically dominated solvation free energy of large surfaces.”¹⁷

1.5. Systems Studied

The studies performed during this thesis are based on a simple scientific belief: fundamental understanding sheds light on applications. We study several systems important to the nuclear industry using fundamental science, for the sake of understanding, but bearing in mind the importance an applied scientist might give to our findings. For this reason we focus on systems that are interesting in themselves but also of potential relevance in waste reprocessing and storage or general actinoid chemistry.

We studied four elements: uranium, neptunium, plutonium and americium. These four elements lie together in the actinoid or 5f row and are crucial in nuclear industry as fuels, dangerous waste or potential pollutants if accidents happened. We have studied their actinyl form, $[AnO_2]^{2+/+}$ which correspond to oxidation states VI and V, and their main species in highly oxidizing and acidic aqueous media. Their study in solution is crucial because it is the form in which they are reprocessed and their dangerous mobile form if accidents were to occur. We also studied uranyl in clays to study its diffusion in the material and how the clay would slow down its diffusion compared to aqueous solution.

A local example can be put forward with respect to accidents, not of the

nuclear power industry, but rather of the violent use of radioactivity. In 1966, two American military aircrafts crashed and 4 termonuclear plutonium bombs were dropped in Palomares (Almería) which is a 4 hour drive away from where I am writing this Thesis.²⁶ Fortunately, only the conventional explosive of two of the bombs exploded and no nuclear explosion happened. Nevertheless, the explosion dispersed an aerosol of Pu in the nearby area. Although the bombs were recovered and part of the contamination cleaned, to this day regions around where the bombs landed are under strict nuclear control. One of the problems of Pu is its decay over time into Am which is much more volatile and radiotoxic than the rest of actinoids. For this kind of reasons, it is very important to understand the apparently obscure chemistry of americium in natural media such as clays or water.²⁷

Besides the nuclear industry, actinoids have a very interesting fundamental chemistry²⁸ in terms of bonding, electronic structure and reactivity. Understanding the chemistry of the compounds can help technological development. Neptunium as of today lacks any practical use, but who would have thought that ²⁴¹Am would be present in every household smoke detector due to its α -emission (although they were banned in Spain in 2005). Also, though it might sound shocking, uranium is a naturally occurring element which is 40 times more abundant than silver. Therefore, knowledge of its speciation and chemistry in natural waters or clays is important even when its source is geological.

Experimental information on actinoids in solution is scarce and hard to obtain.²⁹⁻³¹ The reason for this is their radioactivity which requires the use of specialized techniques and specialized facilities.²⁸ Theoretical chemistry of actinoids gives many opportunities to study them in an inexpensive and safe way. This is the point of view adopted in this thesis: the studies here reported have been devoted to the computational chemistry of several actinoid cations and their actinyl forms but also in close relation to experiment, for example, in the simulation of EXAFS spectra.

The first article of the compilation deals with the development of an *ab initio* force field based on the hydrated ion model^{32,33} (HIM) for the uranyl pentahydrate, $[\text{UO}_2 \cdot (\text{H}_2\text{O})_5]^{2+}$, in solution. The force field allowed us to run classical molecular dynamics (MD) simulations and obtain interesting in-solution properties of the complex. In particular: to describe the two solvation behaviors it exhibits as well as many spectroscopic, dynamic and thermodynamic properties. The second article extends the uranyl force field to the rest of studied actinyls: Np(V,VI), Pu(VI) and Am(VI). The simulations of

cations reveal a great chemical analogy between them with some differences between the two oxidation states of neptunyl. The third article deals with the theoretical EXAFS spectroscopy of aqueous actinyls. In particular, we compare theoretical EXAFS spectra to experiment and how increasing the level of theory of the reference quantum mechanical calculations has small structural effects with high spectroscopical impact. On the fourth article we used aqueous americium MD simulations to interpret the experimental EXAFS spectrum of a Am(III)/Am(VI) mixture³⁴ and to predict the EXAFS spectrum of a pure sample of Am(VI) in solution proposing the structural parameters of this hydrate. In the fifth article a hydrated ion-clay interaction potential is developed in order to run MD simulations of uranyl hydrated ions in a montmorillonite clay. We studied the diffusion of the uranyl cations within the clay and the effect of increasing the actinoid concentration in the interlayer. Metadynamics simulations were also run revealing the free energy surface of the uranyl cations as they diffuse in the aqueous interlayer.

In a small detour from the actinoid project, we present as the final article the work done at the group of Prof. Michele Parrinello in Università della Svizzera Italiana (Switzerland). During this six-month stay we developed a simple local fingerprint for hydrophobicity and hydrophilicity of atoms in complex solutes: from methane to amino acids. The fingerprint is inspired by the expansion of the entropy of a simple liquid in increasing terms of correlation order. We then used the fingerprint as a desolvation collective variable in a well-tempered metadynamics simulation of a host-guest system. In addition, the ability of the fingerprint to identify the hydrophobicity or hydrophilicity of the hydrated actinyl atoms was explored.

1.6. Literature Review

I will now review the literature of the field. For the sake of succinctness, the scope will be exclusively actinyl aqua-ions in solution or in montmorillonite clay in the context of statistical mechanics simulation. Many of the information left out has been reviewed elsewhere.^{35,36}

For obvious reasons, the most studied of actinyl in the literature is uranyl, $[\text{UO}_2 \cdot (\text{H}_2\text{O})_5]^{2+}$. It has been studied with all kinds of model hamiltonians from empirical force fields to Carr-Parrinello Molecular Dynamics (CPMD) and even QM/MM.

The pioneers in its study in solution were Guilbaud and Wipff.^{37,38} They developed an empirical interaction potential for uranyl with water using its free energy of hydration to validate the force field. In their MD simulations they were able to obtain coordination numbers, first shell distances as well as relative free energies of complexation to calixarene, a complexating macrocycle. The Guilbaud and Wipff non-polarizable model is still the most used in uranyl studies. Particularly, before this thesis it was the only model used in clay-uranyl simulations. In light of new free energy data Kerisit and Liu updated the model in 2013.³⁹ Empirical polarizable force fields have also been developed by Guilbaud et col.^{40,41}

Two uranyl-water force fields based on QM calculations precede the one developed in this work. The first one was developed by the Gagliardi and Roos group⁴² using the polarizable NEMO approach.⁴³ The force field was parametrized with CASPT2 calculations of the uranyl monohydrate, $[\text{UO}_2 \cdot (\text{H}_2\text{O})]^{2+}$. This model underlines the importance of charge transfer to the first solvation shell. The second and more recently developed force field was published by Maginn et al.⁴⁴ Their reference potential energy surface was obtained including four water molecules in the uranyl first shell to capture many-body effects and polarization in a non-polarizable framework. With this effective two-body model they studied a variety of structural and dynamic properties of uranyl hydration.^{44,45}

Ab initio MD simulations have also been employed. Bühl et al. ran CPMD simulations on aqueous uranyl obtaining interesting results concerning the dissociation of a water molecule out of the uranyl aqua-ion.⁴⁶ They found a clear dominance of the pentahydrate complex over the tetrahydrate. Nichols et al. ran similar simulations and were able to use ensemble configurations to generate an EXAFS spectrum that reproduced remarkably well the experiment.⁴⁷ The system has also been studied employing QM/MM simulations by Frick et al. who calculated angularly resolved radial distribution functions (RDF).⁴⁸

Although the literature regarding uranyl molecular dynamics is abundant, the rest of actinyls have not received as much attention. The reason for this is that the chemical analogy between uranyl and the rest is high except for spectroscopical and magnetic properties. The only classical force field for actinyls different than uranyl was developed by Maginn's group.^{45,49} They extended their methodology for uranyl adding the specificity of the particular actinoid by changing its partial charges, bond bending and bond stretching

parameters in accordance to quantum chemical calculations. They found all the actinyls remarkably similar in terms of hydration. The other study was carried out by Odoh et al.⁵⁰ They did CPMD-metadynamics simulations on $[\text{PuO}_2]^{2+/+}$ studying the relative stabilities of their coordination numbers.

Clay classical MD simulations have a long history. To the best of our knowledge, the first interaction potential for clays was developed by Skipper et al. in 1989 using semiempirical partial charges.⁵¹ The potential was initially used to study water (MCY model⁵²) at a talc surface but later allowed the study of more complex problems.^{53,54} The state-of-the-art clay force field is the *clayFF* force field which has been cited over a thousand times.⁵⁵ This intuitively named force field, describes the clay as a set of charged Lennard-Jones spheres which by means of non-bonded interactions conserve the clay structure reproducing several experimental properties. The *clayFF* allows the study of many hydrated and dehydrated clays, hydroxides and oxyhydroxides including its internal dynamics since it allows the aluminosilicate to be flexible. This force field will be used in this work to model montmorillonite clay. More recently, a polarizable clay force field has been proposed.⁵⁶ The literature of aluminosilicate MD simulations is very rich and is summarized in the following reviews.^{57,58}

The theoretical study of uranyl cations in montmorillonite clay has a significant amount of literature. Most of it refers to the study of the cation adsorbed on the outer pores of the clay particles exposed to bulk solution^{59–64} and only two refer to uranyl inside the clay interlayers.^{65,66}

The first study was done by Zaigan et al. who studied uranyl in montmorillonite interlayers by means of Monte Carlo simulations. They used the Wipff and Guilbaud model for uranyl^{37,38} and clay interaction potential of Skipper et al.⁵⁴ They obtained the interlayer spacing of the uranyl containing clay as a function of interlayer hydration, the dynamics of the uranyl axis orientation, the z-density profiles and uranyl radial distribution functions. The second study was done in 2005 by the same authors updating the simulation to interpret XAS spectra.⁶⁶ After these two initial works and until this thesis, the uranyl clay simulations dealt with the adsorption of the cation in bulk-solution exposed surfaces of the clay. The majority of pore-uranyl clay simulations used a combination of the *clayFF* and the Guilbaud-Wipff model for uranyl. In this set of articles a variety of effects have been studied in this system: the influence of electrolyte concentration in the pore^{59,60,63,64} including coordinating counter ions like carbonate,^{59,60} adsorption constants to the surface,^{59,60} the

z-density distribution,^{60–62,64} the average surface charge density,⁶⁴ superficial uranyl and water diffusion⁶² and superficial uranyl orientation.⁶³

1.7. Bibliography

1. World Bank, Nuclear Energy Statistics World Bank. 2015; <https://data.worldbank.org/indicator/eg.elc.nucl.zs>.
2. Organisation for Economic Co-operation Development: Nuclear Energy Agency, Distribution of Uranium Reserves. 2016; <http://www.oecd-nea.org/ndd/pubs/2016/7301-uranium-2016.pdf>.
3. Lozano Leyva, M. *Nucleares, ¿Por qué no?*; DEBOLSILLO: Barcelona, 2010.
4. Lozano Leyva, M. *Lecciones de Fukushima*; Penguin Random House: New York, 2011.
5. Wikipedia contributors, Nuclear fuel cycle — Wikipedia, The Free Encyclopedia. 2019; https://en.wikipedia.org/w/index.php?title=Nuclear_fuel_cycle&oldid=888036895, [Online; accessed 27-May-2019].
6. Allibert, M. et al. Introduction of Thorium in the Nuclear Fuel Cycle. Short-to long-term considerations. 2015; https://inis.iaea.org/search/search.aspx?orig_q=RN:46066594.
7. Herbst, R. S.; Baron, P; Nilsson, M. In *Adv. Sep. Tech. Nucl. Fuel Reprocess. Radioact. Waste Treat.*; Nash, K. L., Lumetta, G. J., Eds.; Woodhead Publishing Series in Energy; Woodhead Publishing: Cambridge, 2011; Chapter 6.
8. L., K.; Madic, C.; Jagdish, M. N.; Lacquement, J. In *The Chemistry of Actinide and Transactinide Elements*; Katz, J. J., Seaborg, G. T., Eds.; Springer Science & Business Media: Dordrecht, The Netherlands., 2007; Chapter 24.
9. Organisation for Economic Co-operation Development: Nuclear Energy Agency, The disposal of high-level radioactive waste. 2008; <https://www.oecd-nea.org/brief/brief-03.html>.
10. Wikimedia Commons, File:Montmorillonite-Quartz-ck29a.jpg — Wikimedia Commons, the free media repository. 2015; <https://commons.wikimedia.org/w/index.php?title=File:>

- Montmorillonite-Quartz-ck29a.jpg&oldid=146062115, [Online; accessed 4-July-2019].
11. Wikimedia Commons, File:Mineraly.sk - montmor.jpg — Wikimedia Commons, the free media repository. 2014; https://commons.wikimedia.org/w/index.php?title=File:Mineraly.sk_\protect\discretionary{\char\hyphenchar\font}{}{}_montmor.jpg&oldid=141760220, [Online; accessed 4-July-2019].
 12. Delage, P.; Cui, Y.; Tang, A. *J. Rock Mech. Geotech. Eng.* **2010**, *2*, 111–123.
 13. Reichardt, C.; Welton, T. *Solvents and solvent effects in organic chemistry*; John Wiley & Sons: Weinheim, Germany, 2011; Chapter 1.
 14. Harris, R. C.; Pettitt, B. M. *J. Phys. Condens. Matter* **2016**, *28*, 083003–083026.
 15. Ben-Amotz, D. *Annu. Rev. Phys. Chem.* **2016**, *67*, 617–638.
 16. Cremer, P. S.; Flood, A. H.; Gibb, B. C.; Mobley, D. L. *Nat. Chem.* **2017**, *10*, 8–16.
 17. Chandler, D. *Nature* **2005**, *437*, 640–647.
 18. Garde, S.; Hummer, G.; García, A. E.; Paulaitis, M. E.; Pratt, L. R. *Phys. Rev. Lett.* **1996**, *77*, 4966.
 19. Hummer, G.; Garde, S.; Garcia, A. E.; Pohorille, A.; Pratt, L. R. *Proc. Natl. Acad. Sci.* **1996**, *93*, 8951–8955.
 20. Pratt, L. R.; Chandler, D. *J. Chem. Phys.* **1977**, *67*, 3683–3704.
 21. Lum, K. ; David, C.; Weeks, J. D. *J. Phys. Chem. B* **1999**, *103*, 4570–4577.
 22. Huang, D. M.; Geissler, P. L.; Chandler, D. *J. Phys. Chem. B* **2001**, *105*, 6704–6709.
 23. Huang, D. M.; Chandler, D. *J. Phys. Chem.* **2002**, *106*, 2047–2053.
 24. Frank, H. S.; Evans, M. W. *J. Chem. Phys.* **1945**, *13*, 507–532.
 25. Willard, A. P.; Chandler, D. *J. Chem. Phys.* **2014**, *141*, 18C519–18C524.
 26. Izquierdo, R. M. *La historia secreta de las bombas de Palomares*; Editorial Crítica: Barcelona, 2016.
 27. Runde, W. H.; Schulz, W. W. In *The Chemistry of Actinide and Transactinide Elements*; Katz, J. J., Seaborg, G. T., Eds.; Springer Science & Business Media: Dordrecht, The Netherlands., 2007; Chapter 8.

28. Pichon, A. *Nature Chemistry* **2017**, *9*, 832.
29. Marcus, Y. *Ions in Solution and their Solvation*; John Wiley & Sons: Hoboken, NJ, 2016.
30. Choppin, G. R.; Jensen, M. P. In *The Chemistry of Actinide and Transactinide Elements*, 3rd ed.; Morss, L. R., Edelstein, N., Fuger, J., Katz, J. J., Eds.; Springer: Dordrecht, 2008; Vol. 4; Chapter 23.
31. Altmaier, M.; Gaona, X.; Fanghänel, T. *Chem. Rev.* **2013**, *113*, 901–943.
32. Pappalardo, R. R.; Sánchez Marcos, E. *J. Phys. Chem.* **1993**, *97*, 4500–4504.
33. Martínez, J. M.; Pappalardo, R. R.; Sánchez Marcos, E. *J. Chem. Phys.* **1998**, *109*, 1445–1455.
34. Riddle, C.; Czerwinski, K.; Kim, E.; Paviet, P.; Weck, P.; Poineau, F.; Conradson, S. *J. Radioanal. Nucl.* **2016**, *309*, 1087–1095.
35. Wang, D.; van Gunsteren, W. F.; Chai, Z. *Chem. Soc. Rev.* **2012**, *41*, 5836–5865.
36. Dolg, M. *Computational Methods in Lanthanide and Actinide Chemistry*; John Wiley & Sons: Chichester, UK, 2015.

37. Guilbaud, P.; Wipff, G. *J. Mol. Struc. THEOCHEM* **1996**, *366*, 55–63.
38. Guilbaud, P.; Wipff, G. *J. Phys. Chem.* **1993**, *97*, 5685–5692.
39. Kerisit, S.; Liu, C. *J. Phys. Chem. A* **2013**, *117*, 6421–6432.
40. Nguyen, T. N.; Duvail, M.; Villard, A.; Molina, J. J.; Guilbaud, P.; Dufrêche, J. F. *J. Chem. Phys.* **2015**, *142*, 024501–024511.
41. Duvail, M.; Dumas, T.; Paquet, A.; Coste, A.; Berthon, L.; Guilbaud, P. *Phys. Chem. Chem. Phys.* **2019**, *21*, 7894–7906.
42. Hagberg, D.; Karlström, G.; Roos, B. O.; Gagliardi, L. *J. Am. Chem. Soc.* **2005**, *127*, 14250–14256.
43. Wallqvist, A.; Ahlström, P.; Karlström, G. *J. Phys. Chem.* **1990**, *94*, 1649–1656.
44. Rai, N.; Tiwari, S. P.; Maginn, E. J. *J. Phys. Chem. B* **2012**, *116*, 10885–10897.
45. Tiwari, S. P.; Rai, N.; Maginn, E. J. *Phys. Chem. Chem. Phys.* **2014**, *16*, 8060–8069.
46. Bühl, M.; Kabrede, H.; Diss, R.; Wipff, G. *J. Am. Chem. Soc.* **2006**, *128*, 6357–6368.

47. Nichols, P.; Bylaska, E. J.; Schenter, G. K.; de Jong, W. *J. Chem. Phys.* **2008**, *128*, 124507–124514.
48. Frick, R. J.; Hofer, T. S.; Pribil, A. B.; Randolph, B. R.; Rode, B. M. *J. Phys. Chem. A* **2009**, *113*, 12496–12503.
49. Pomogaev, V.; Tiwari, S. P.; Rai, N.; Goff, G. S.; Runde, W.; Schneider, W. F.; Maginn, E. J. *Phys. Chem. Chem. Phys.* **2013**, *15*, 15954–15963.
50. Odoh, S. O.; Bylaska, E. J.; De Jong, W. A. *J. Phys. Chem. A* **2013**, *117*, 12256–12267.
51. Skipper, N. T.; Refson, K.; McConnell, J. *Clays and clay Miner.* **1989**, *24*, 411–425.
52. Matsuoka, O.; Clementi, E.; Yoshimine, M. *J. Chem. Phys.* **1976**, *64*, 1351–1361.
53. Greathouse, J. A.; Refson, K.; Sposito, G. *J. Am. Chem. Soc.* **2000**, *122*, 11459–11464.
54. Skipper, N. T.; Refson, K.; McConnell, J. D. C. *J. Chem. Phys.* **1991**, *94*, 7434–7445.
55. Cygan, R. T.; Liang, J.-J.; Kalinichev, A. G. *J. Phys. Chem. B* **2004**, *108*, 1255–1266.
56. Tesson, S.; Salanne, M.; Rotenberg, B.; Tazi, S.; Marry, V. *J. Phys. Chem. C* **2016**, *120*, 3749–3758.
57. Cygan, R. T.; Greathouse, J. A.; Heinz, H.; Kalinichev, A. G. *J. Mat. Chem.* **2009**, *19*, 2470–2481.
58. Greathouse, J. A.; Cygan, R. T. In *Handbook of Clay Science*; Bergaya, F., Lagaly, G., Eds.; Developments in Clay Science; Elsevier: Amsterdam, 2013; Vol. 5; Chapter 3.
59. Greathouse, J. A.; Cygan, R. T. *Phys. Chem. Chem. Phys.* **2005**, *7*, 3580–3586.
60. Greathouse, J. A.; Cygan, R. T. *Environ. Sci. Technol.* **2006**, *40*, 3865–3871.
61. Yang, W.; Zaoui, A. *J. Hazard. Mater.* **2013**, *261*, 224–234.
62. Liu, X.-y.; Wang, L.-h.; Zheng, Z.; Kang, M.-l.; Li, C.; Liu, C.-l. *J. Hazard. Mater.* **2013**, *244*, 21–28.
63. Teich-McGoldrick, S. L.; Greathouse, J. A.; Cygan, R. T. *Mol. Simul.* **2014**, *40*, 610–617.

64. Zhang, N.; Liu, X.; Li, C.; Liu, C. *Inorg. Chem. Front.* **2015**, *2*, 67–74.
 65. Zaidan, O. F.; Greathouse, J. A.; Pabalan, R. T. *Clays Clay Miner.* **2003**, *51*, 372–381.
 66. Greathouse, J. A.; Stellalevinsohn, H. R.; Denecke, M. A.; Bauer, A.; Pabalan, R. T. *Clays Clay Miner.* **2005**, *53*, 278–286.
-

Thesis Goals

The goals of this thesis were mostly planned but with some interesting surprises, new paths, tangents and occasional dead ends found during the course of research. The goals and the articles are not presented in a chronological order of publication nor in order of investigation, but following a scientifically consistent criterion. In research it is quite frequent to run projects in parallel, at other times drop all projects to focus on a single goal and all kinds of non-sequential work habits.

We had two general and main goals in mind at the beginning of this project. The first goal was to analyze and understand systems of relevance in radioactive chemistry using computational chemistry in some cases interfacing with experiment. The second goal was to fill the missing gaps in computational modelling that would allow the achievement of the aforementioned goals. These main purposes will take definite form as explained below.

The first step of this Ph. D. thesis was to study the physico-chemical properties of the $[AnO_2]^{2+/+}$ species with An=U,Np,Pu,Am in dilute aqueous solution and inserted in clay interlayers. A wide set of physico-chemical properties have been determined computationally as well as a detailed analysis of the hydration properties and X-Ray Absorption Spectroscopy of these cations in condensed media. In the clay simulations we will focus on diffusion and interactions between the hydrated ions and the clay surfaces. The methodological achievements will demand the development of *ab initio* force fields based on the hydrated ion model (HIM) that reproduce adequately the available

experimental properties. An additional goal is to give insight into the synergic experimental-theoretical procedures to analyze involved XAS problems.

The individual goals undertaken can also be associated to the different articles:

1. **“A hydrated ion model of $[\text{UO}_2]^{2+}$ in water: Structure, dynamics, and spectroscopy from classical molecular dynamics”:**

To develop an *ab initio* HIM force field for $[\text{UO}_2]^{2+}\text{-H}_2\text{O}$ in water. To study its physico-chemical properties including structural, dynamical and spectroscopical properties. To characterize the solvation structure of uranyl.

2. **“A general study of actinyl hydration by molecular dynamics simulations using ab initio force fields”:**

To extend the methodology used to develop the force field for $[\text{UO}_2]^{2+}\text{-H}_2\text{O}$ to the rest of the actinyls examining the partial transferability of the uranyl potential to the rest of actinyls. To study how the properties evolve in the series and the significance of the charge change from divalent to monovalent.

3. **“Extracting the Americyl Hydration from an Americium Cationic Mixture in Solution: A Combined X-ray Absorption Spectroscopy and Molecular Dynamics Study”:**

To interpret the experimental XAS of an $\text{Am}^{3+}/[\text{AmO}_2]^{2+}$ aqueous mixture and clarify the structural parameters fitted by the experimentalists. To generate the theoretical XAS spectrum of the mixture of species. To use the $[\text{AmO}_2]^{2+}$ contribution to the theoretical spectrum to predict the properties of the so far not measured pure americyl in aqueous solution.

4. **“Combining EXAFS and Computer Simulations to Refine the Structural Description of Actinyl in Water”:** To generate and analyze theoretical EXAFS spectra of the actinyls using the trajectories of developed in the second article. To study the effect of tiny structural changes in the spectrum and analyze the importance of including higher levels of theory to study EXAFS spectra.

5. **“Hydration and Diffusion Mechanism of Uranyl in Montmorillonite Clay: Molecular Dynamics Using an Ab Initio Potential”:**

To develop an *ab initio* HIM force field between the uranyl hydrated ion

and at the clay surface. To study the molecular dynamics of uranyl in montmorillonite clay interlayers and particularly the factors affecting its diffusion.

6. **"A local fingerprint for hydrophobicity and hydrophilicity: from methane to peptides":**

To develop a simple local fingerprint that measures the hydrophobicity and hydrophilicity of atoms in complex solutes and can serve as a collective variable in enhanced sampling simulations. To use the fingerprint as a desolvation collective variable in metadynamics simulations. To apply the fingerprint to analyze the anisotropic hydration structure of actinyls.





Methods

In this chapter we shall outline the methods used in the set of studies that form the thesis. Generic molecular dynamics and quantum chemistry methods are not included for the sake of succinctness. We focus on the contents that cannot be found in textbooks since they are either recent or rather specific to the contents of this thesis. In any case, I would like to give credit to the authors who have published those textbooks and leave them as reference for anyone seeking a fundamental training. A straightforward approach to statistical computer simulations can be achieved through the classic textbook of Frenkel¹ in addition to more unknown and modern books like those of Shclick,² Smith³ or Berendsen.⁴ To study Quantum Chemistry, the classic text of Zsabo and Osmund⁵ must be cited in addition to the more modern book of Cramer.⁶ In order to get insight into classical mechanics and statistical mechanics, the works of Marion,⁷ Goldstein,⁸ Tuckerman⁹ and McQuarrie¹⁰ must be cited.

3.1. Molecular Simulation

The coming of the digital age in the eighties up to the present produced groundbreaking transformations to most aspect of human life: culture, economics, communication, politics... Science would not be different.

Before the widespread of computation, Science was a symbiotic organism formed by two individuals: experiment and theory in the pen and paper sense.

Both parts communicated and reinforced each other in the development of the fields. With the exponential growth in computer power a third term was added to the equation: simulation.

Modelling has always been key in Science. This involves proposing a simplified image of the system and the equations that govern its behavior. After this, experimentalists would use the model to fit their data and theoreticians would solve the equations analytically. Unfortunately, this normally involves using very simple systems or doing big mathematical assumptions. With modern computers, for the first time, scientists were able to numerically solve the equations proposed by theoreticians in order to obtain detailed pictures of complex model systems. These simulations give interpretation to experiment and a predictive guide for experimentalists.

In the case of molecular simulation, a chemical system is modeled as a collection of particles which sample phase space following the evolution of a model hamiltonian. Once the sampling is finished Statistical Mechanics is applied to obtain observables that can be compared to experiment or serve to predict or interpret it. The recipe for a molecular simulation always involves three main ingredients:

The first ingredient is the Chemistry that we are studying and how we plan to represent it on the computer. For this we must choose the composition of the system and its size such that it is as representative of the real system as possible. In this thesis we simulated, among others, the actinyl hydrated ions in the solution with 1500 water molecules and inside montmorillonite clay. These systems will represent a uranyl cation at infinite dilution and a true montmorillonite infinite crystal containing uranyl cations in its interlayer.

The second ingredient is the model hamiltonian of the system. This hamiltonian will give the approximate energy of the system as a function of particle positions and velocities. If the system is small and/or the evaluation of forces and energies has to be done few times, the hamiltonian can be the quantum mechanical (QM) hamiltonian. On the contrary, if the system is large and/or many energy or force evaluations are necessary, a classical hamiltonian in the form of a force field or interaction potential must be used. In a force field the energy is given as a simple analytic function of particle coordinates (charges, bonding tensions, bending tensions, dihedrals ...) which is parametrized to reproduce experimental data (empirical force fields) or QM data (ab initio force fields) or both. If the system is very large but QM effects are explicitly needed, such as if chemical reactions or light absorption take place, a hybrid

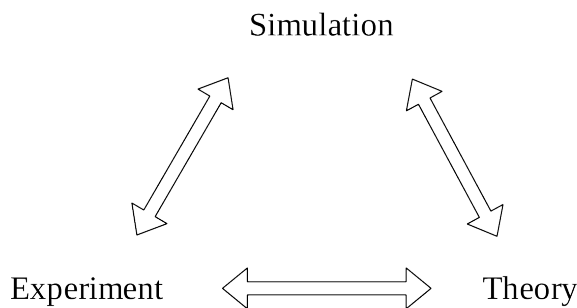


Figure 3.1 *The research triangle showing the synergy between theory, experiment and simulation.*

method must be used. These methods are known as QM/MM approaches and are based on treating a small but important part of the system quantum-mechanically and the rest using a classical force field. In this work we shall consider mostly ab initio force fields developed specifically for the systems under study. In this way we were able to work with larger systems keeping a near QM-level description at force field cost.

The third ingredient is the phase-space sampling method. The particles that constitute matter are in constant motion going from one position and velocity state to another. This continuum of states (in classical terms) is what is known as phase-space. The phase-space of most non-trivial chemical systems is too large to be studied exhaustively. Fortunately, only a limited part of this space is significant as most of these states are highly unlikely and statistically irrelevant. Therefore, we can resort to sampling only relevant areas of phase space. If the dynamics of the system are not of interest, the configuration-space rather than the phase space can be sampled.

Configuration-space is the space of all possible particle positions. Some techniques that sample configuration-space are geometry optimization and Monte Carlo simulations.

The least expensive method is geometry optimization in which the energies and geometries of the system energy minima or saddle points are obtained by an optimization procedure. This method has the limitations of only sampling states close to the initial configuration, which can be troublesome in complex potential energy surfaces, and it models entropic and solvent effects in a crude fashion.⁶ In contrast, Monte Carlo or Molecular Dynamics (MD) methods do

Boltzmann sampling of -ideally- the full configuration or phase space and includes solvent and entropic effects explicitly. Monte Carlo simulations sample stochastically configuration space by making random moves in the system and accepting them into the statistics with a probability based on their Boltzmann weight.¹ MD is based on the propagation of the equations of motion of the system and the resulting trajectory is analyzed. MD is theoretically founded on the ergodic hypothesis which states that ensemble average properties are equal to time averages properties if the phase space is sampled fully.³ In many cases this hypothesis is a reasonable assumption, but in cases with high free energy barriers between relevant states the trajectory might be stuck in one of the states and not sample the other. To have access to these states within the MD simulation approach, enhanced sampling methods like metadynamics (MetaD)^{11,12} can be used. In enhanced sampling methods a bias potential is added to the simulation hamiltonian in order to force sampling in the relevant states of the system. The extra complexity of enhanced sampling simulations is rewarded with the generation of a free energy surface of the system. Finally, in order to calculate the free energy difference between different chemical systems free energy perturbation methods can be used.¹³

3.2. Metal Ion Force Fields

Ions in solution are among the first systems to be studied with MD. The reason being that there is no question about their importance. They are present in all natural waters, in an enormous part of industrial processes, and are crucial to biochemistry (one third of pdb protein structures contain metal ions¹⁴).

The first simulation of ions in water was performed by Heinzinger and Vogel over 50 years ago studying aqueous LiCl.¹⁵ They modeled water with the ST2 model of Rahman and Stillinger¹⁶ and obtaining van der Waals parameters for the ions from their iso-electronic noble gas parameters of Hogervost.¹⁷ Despite the simulation capabilities of the time, the simulations showed good agreement between the first-shell properties and X-Ray diffraction experimental data. Furthermore, they predicted the faster rotation time of the first-shell water molecules with respect to bulk in agreement with NMR data. Other pioneers and front-runners in this research were Jorgensen et al.¹⁸⁻²⁰ and Åqvist²¹ in the eighties and nineties respectively.

The most common feature across popular aqueous ion force fields is their functional form:

$$E_{\text{int}} = \sum_{i=1}^N \sum_{j>i}^N \frac{q_i q_j}{4\pi\epsilon_0 r_{ij}} + \sum_{i=1}^N \sum_{j>i}^N 4\epsilon_{ij} \left[\left(\frac{\sigma_{ij}}{r_{ij}} \right)^{12} - \left(\frac{\sigma_{ij}}{r_{ij}} \right)^6 \right] \quad (3.1)$$

Where E_{int} is the interaction energy between all the particle pairs i, j . We shall not discuss the water force field which has been reviewed elsewhere.²² Many other functional forms exist: Born-Mayer, Mie, Morse etc.²³ Nevertheless, the one presented above is the most representative in the literature.

The first term of the equation is the electrostatic term which features the integer charge of the ion and the partial charges of the water model. This term is generally evaluated using an Ewald sum variant.¹ We neglect two effects in this force field approach: charge transfer to the first shell and polarization of the water molecules. They cannot be represented explicitly within the pair interaction approximation: all forces depend on the atom pair relative positions. This makes the force calculation algorithm computationally fast. Charge transfer and polarization are intrinsically many-body effects and not pair interaction effects. Modelling charge transfer and polarization in pair potentials remains one of the key parts of ion interaction potential development. Force fields which include many-body effects in pair potentials are known as *effective pair potentials*.

The second summation of Equation 3.1 is the van der Waals interaction between the atom pairs. In ion-water interactions they are less important in magnitude than electrostatics but crucial to the modelling. In Equation 3.1 this molecular interaction is described by the Lennard-Jones function.

Lennard-Jones based force fields have proven to be fairly robust in treating monovalent ions in a simple and inexpensive fashion. But, their performance degrades heavily on multiply-charged cations or molecular cations.^{23–25} This is a consequence of the increasing weight of charge transfer and polarization as the cation charge increases. This is the Achilles' heel of Lennard-Jones potentials.

Regardless of its functional form, the parameters of the force field are fit with respect to experimental data (empirical force fields) and/or *ab initio* calculations (*ab initio* force fields). In cation force fields the q_i are given by the water model and the charge of the ion in particular. Only the Lennard-Jones parameters remain to be fit.

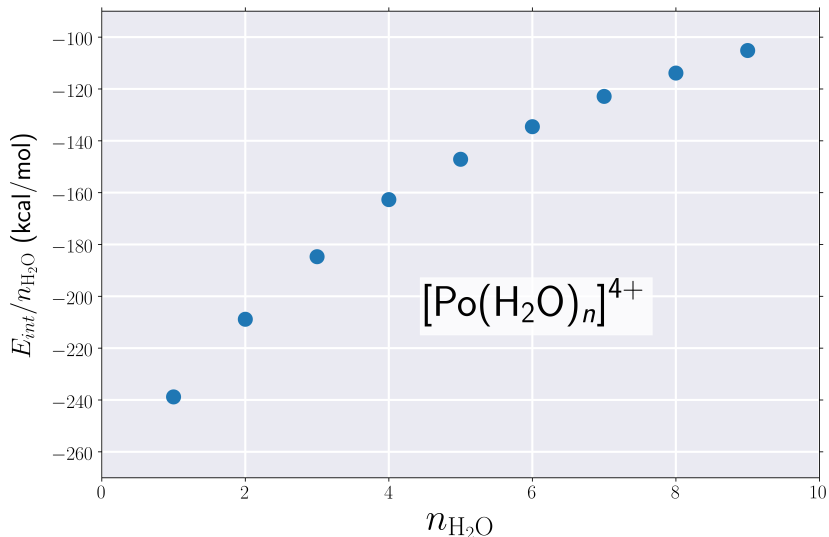


Figure 3.2 QM interaction energies of $[\text{Po}(\text{H}_2\text{O})_n]^{4+}(\text{g})$ per water molecule as a function of n at the MP2 level of theory.²⁶ This example illustrates how the interaction energy of a highly charged cation with its first shell water molecules is a many-body interaction. If this was not the case, a horizontal line would be obtained.

If the fitting is done with respect to empirical data, the force field guarantees that properties introduced in fitting data set are reproduced. It is reasonable to expect that properties that correlate with the fit data are fairly well reproduced too. Free energy of hydration and ion first-shell distance are an example of this.²⁴ Further extrapolation should be done with additional skepticism.

Ab initio force fields are parametrized with respect to energies and molecular structures obtained from quantum chemistry calculations. This strategy has several advantages. If the sampling of the system potential energy surface is exhaustive enough and at a reasonable level of theory, the prediction of information for which the force field was not specifically designed is typically better than using empirical force fields. In addition, the fitting data sets can be generated easily. Especially since medium-level calculations produce satisfactory results in most properties. This is particularly appreciated in experimentally challenging systems like radioactive elements. *Ab initio* force fields have a clear

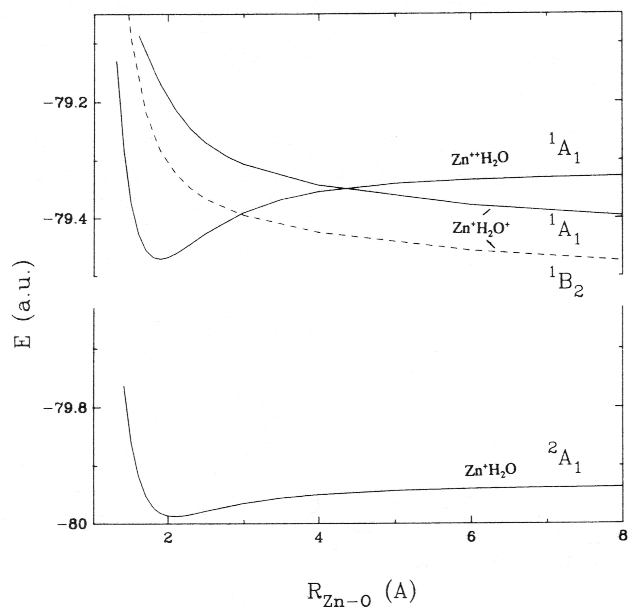


Figure 3.3 Hartree Fock energies for the ground state of $[Zn \cdot (H_2O)]^+$ (2A_1) and $[Zn \cdot (H_2O)]^{2+}$ lowest states (1A_1 and 1B_2). For the monovalent there are no low lying excited states but for the divalent there are two charge transfer states which are the lowest in energy at long distances. Reproduced with permission of the authors.²⁷

improvement path; just add more structures or improve the level of theory. For these reasons the interaction potentials developed in this thesis will all be classical force fields based on *ab initio* calculations.

The traditional strategy to obtain the QM data is to calculate the interaction energies of the monohydrate, $M^{+n} \cdot H_2O$, at different metal oxygen distances. This has two shortcomings for highly charged cations.

The first is that the average total hydration enthalpy is highly overestimated. The cause of this is that the interaction energy in the monohydrate is much more negative than the interaction energy of the individual water molecules around an ion when fully solvated. In other words, the interaction energy of the metal with its first shell is different from the interaction energy of the monohydrate times the coordination number. This is because when going from the monohydrate to the n-hydrate the polarizing capability per water molecule of the ion decreases with n. The interaction energy per water molecule decreases as you increase the number of molecules in the first shell

as is illustrated in Figure 3.2. This means that the interaction energy of a cation with its first shell is a many-body case (in this case a “body” refers to a water molecule). In addition, the water-water repulsion in the fully-hydrated ion lengthens the M-O distance decreasing the interaction energy. These effects are impossible to capture with monohydrate based potentials.^{28,29}

The second problem of monohydrate potentials is that, for highly charged cations, when scanning quantum mechanically the M-OH₂ distance there can be electronic state crossings that lead to a charge transfer state. This is shown in Figure 3.3 for the [Zn · (H₂O)]²⁺] case. The reason for this is that ionization potential of water is lower than the second ionization potential of Zn(g) but not of Zn(aq).^{27,30} This behavior has also been found in other metals like Be²⁺ and Fe³⁺.^{28,29,31}

Additionally, in the case of systems with unpaired electrons the electronic state of the ion is heavily influenced by the ligand field around it and the monohydrate cannot represent the fully hydrated ion. This is typical of most electronic states of transition metals and actinoids. The coordination of a full solvation shell stabilizes the ground state making it less sensitive to geometrical distortions.

To alleviate many of these problems our group developed about 25 years ago the Hydrated Ion Model. In this thesis we present its last extensions to the actinoid cations and its integration into a mineral matrix, montmorillonite clay.

3.3. The Hydrated Ion Model

The Hydrated Ion Model (HIM) is a modelling strategy to develop cation interaction potentials. It is inspired by the classical electrochemical concept of the hydrated ion in which the hydrated ion, [M · (H₂O)_m]ⁿ⁺, is the solute and active species in solution instead of the naked ion, Mⁿ⁺. In this way the hydrated ion becomes the solute and target of study. The ion and its first solvation shell are now considered an entity (a molecule) which has special water molecules inside and that is surrounded by different bulk water molecules. Traditionally, the picture was of a charged atom surrounded by bulk water molecules making no distinction between first and outer solvation shells.

This conceptual change has several important implications. All QM calculations must be done with the HI, [M · (H₂O)_m]ⁿ⁺. This inclusion of the full

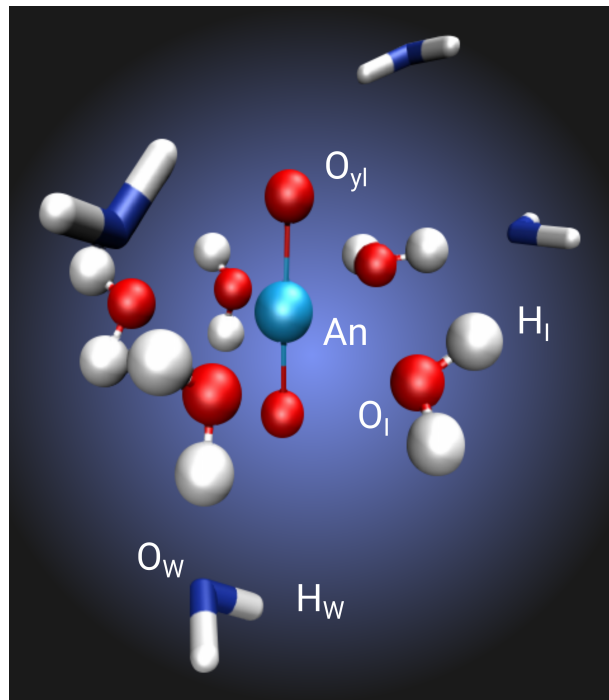


Figure 3.4 Image of an actinyl hydrated cation $[An \cdot (H_2O)_5]^{n+}$ in water. Only some bulk water molecules are drawn for clarity. Bulk water molecules are drawn with the “licorice” representation and first-shell water molecules are represented with the “ball and stick” representation.

first shell has deep consequences on the interaction QM energies used to parametrize the interaction potential and therefore in its development. Since the full shell is present there is no over-polarization of first-shell molecules like in monohydrate models. The interaction energies are similar to those in solution since the nearest-neighbor environment is the same. Many-body effects are explicitly included in the interaction energies and therefore implicitly incorporated in the force-field. Wavefunction related problems are avoided because the full shell stabilizes the electronic state with respect to electronic degeneracy and charge transfer dissociation limits. This feature is of great interest for high charge cations.

The considerations of the HI as the consistent molecular cation in solution allows us to assign different atom types (O_I and H_I) in first-shell water molecules than in the rest of bulk water molecules (O_W and H_W). Figure 3.4

illustrates this. The HIM provides great flexibility to the potential because the bulk water molecules can be modeled with conventional classical force fields (TIP4P in our case) and first-shell water molecules can be given different geometries, partial charges and interaction potentials. The first-shell water molecules can now have a higher dipole than bulk water and even be charged due to partial charge transfer from the metal center. Assignment of these partial charges can be done with conventional partial charge calculation methods like CHELPG or RESP calculated on the full HI. Charge transfer and polarization of the first-shell and its differentiation from the bulk is a feature of great interest for high-charge cations since their first-shell is specially different to bulk.

This strategy of parametrization stems from considering in a more realistic way the nature of the ion. Unfortunately, there is a price to pay. The payment is done in terms of complexity of the potential. Fortunately, this increase in complexity is manageable. Two interaction potentials must be fit and therefore two potential energy surfaces must be scanned: the first-shell ion potential energy surface which governs intra-HI motion and another for the interaction of the HI with bulk water. In addition, to capture properly all the effects that can be accessed with this model, the functional form of the force fields are typically complex. The functional forms used are a sum of r^{-n} terms and an electrostatic term:

$$E = \sum_{i=1}^{\text{HI sites}} \sum_{j>i}^{\text{water sites}} \left(\frac{C_{12}^{ij}}{r_{ij}^{12}} + \frac{C_8^{ij}}{r_{ij}^8} + \frac{C_6^{ij}}{r_{ij}^6} + \frac{C_4^{ij}}{r_{ij}^4} + \frac{q_i q_j}{4\pi\epsilon_0 r_{ij}} \right) \quad (3.2)$$

Because the number of coefficients is relatively high the potentials are more prone to over-fitting. In addition, combination rules with other atom types are impossible to use. This can hinder the recycling of potentials developed for particular systems to others, although generalizations have been done.^{32–34} Another problem associated to the functional form is that most MD programs do not allow using this functional form in a simple way limiting its use to less specialized users. Nevertheless this leads to the development of potentials that have very high accuracy, in particular in properties depending on first and second hydration shells, that can reproduce subtle experimental properties such as EXAFS spectra.^{35–39}

The problem of having new atom types for first-shell water molecules is that if they leave the first shell and diffuse into the bulk the model becomes unphysical. Fortunately, for high-charge cations this is not a problem, it is

a feature. Residence times of water molecules of most cations with charge greater than one have timescales much longer than the simulation time: any change in coordination or water exchange is unphysical anyway. The HIM considers the HI as the molecular cation in solution so the interaction between the first-shell water oxygen and the metal cation may be viewed as a flexible bond. Nevertheless, this interaction potential is not a harmonic function. The M–O_I interaction goes to zero as $r \rightarrow \infty$. The water molecules, in principle, can leave the first shell but the barrier to do it is high enough to prevent it in the simulation timescale. If this event were to happen, the potential should be reexamined. An additional advantage of having such a flexible functional form in the M–O_I interaction is that it captures anharmonicities of the bonding which a harmonic potential is unable of doing.

In some cations with low charge/radius ratio, like heavy alkalines and lanthanoids, the water exchange and the changes in coordination number are frequent. The HIM can also be used to develop potentials for these systems but some modifications must be done. Only one type of water molecules must be used and in order to capture the polarization and many body effects a polarizable potential must be used.^{35,38–40} The price to pay for this extra flexibility of the potential is that the force field becomes more computationally demanding and charge transfer to the first shell is neglected, which should be residual anyway. This model is known as the exchangeable HIM.

I will now briefly explain the historical development of the HIM across a good part of the periodic table. The HIM model started as solution to the problems found studying the potential energy surface of the Zn²⁺ monohydrate²⁷ therefore the first HI to be studied was [Zn·(H₂O)₆]²⁺.⁴¹ The HI was rigid and the parametrized interaction was the HI-bulk Water Interaction or E_{HIW} . The unprecedented agreement with the experimental hydration enthalpy obtained by Monte Carlo simulations revealed the robustness of the force field development strategy and encouraged its extension in a similar fashion to [Cr·(H₂O)₆]³⁺ with similar success.^{42,43} The next step in the progression was to make the HI flexible by parametrizing its internal degrees of freedom with the Ion First-Shell Water potential, E_{IW1} . This was initially done for Cr³⁺ but has become standard in the development of the HIM since.⁴⁴ The great advantage of internal flexibility is that it allows power spectra calculation of the aqua ion and also the X-Ray Absorption Spectra which is a subtle experimental property to reproduce due to the high structural sensitivity.^{35–39} A variety of cations were also studied using this approach, Be²⁺, Mg²⁺, Al³⁺, Rh³⁺, Ir³⁺ and

even Th^{4+} .^{32–34,45} This version of the HIM will be the one used to study actinyl pentahydrates in the thesis. The difference with previous versions is that the actinyl model will include an intramolecular cation interaction potential, E_{IMC} which will define the dynamics within the actinyl unit ($[\text{AnO}_2]^{2+}$). In this way we will deal with the fact that the cation will be molecular instead of atomic.

Another set of cations studied using the HIM are the square planar noble metals dication, $[\text{M} \cdot (\text{H}_2\text{O})_4]^{2+}$. The first two studied metals were $[\text{Pd} \cdot (\text{H}_2\text{O})_4]^{2+}$ and $[\text{Pt} \cdot (\text{H}_2\text{O})_4]^{2+}$ and its aquo-derivatives.^{46,47} A few years later the methodology was extended to study the chemotherapeutic cis-platin, $[\text{PtCl}_2(\text{NH}_3)_2]^{2+}$.^{48,49} The study of these compounds gave a picture of a single ion with two solvation environments: one equatorial that follows conventional solvation and a different axial solvation. This differentiated axial solvation was labeled the “meso-shell” since it is characterized by metal-ion distances in between the first and the second shell, with orientations and lability resembling the second shell. This behavior of a single ion having two very different solvation regions will also be encountered in actinyls.

The last category of HIM ions are studied with a polarizable ion and water model, MCDHO and MCDHO2.^{50,51} This allows the possibility for water exchanges in the first-shell and changes in coordination number. This model is known as the exchangeable HIM. The main advantage of this model is the ability to study cations with fast first-shell water exchange rates and varying coordination number. There have been numerous cations studied in this way: the alkalines, alkaline earth metals, several lanthanoids and actinoids, Sc^{3+} and Tl^+ .^{35,38,39,45,52–54} These models allow theoretically predicting the coordination numbers in solution which is experimentally challenging in some cases like Sc^{3+} .^{52,55}

3.4. X-Ray Absorption Spectroscopy

If a sample of thickness, d , and concentration, c , is irradiated by light-source of intensity, I_0 , which transmits an intensity, I , we can characterize the absorbance of the sample by its absorption coefficient, μ , according to the Lambert-Beer's Law:

$$\mu = \frac{1}{c \cdot d} \ln \frac{I_0}{I} \quad (3.3)$$

If the light source used is an X-Ray beam, the study of μ as a function of the photon energy is a technique known as X-Ray Absorption Spectroscopy (XAS).

One of humankind's most important discoveries was based on XAS: Moseley's law. In 1913, Henry Moseley discovered that the square root of the lowest frequency line of the XAS spectrum of an atom was proportional to its nuclear charge. This discovery proved that an element's position in the periodic table is due to its nuclear charge and not its mass, consolidating Bohr's model of the atom as universal across the Periodic Table.

Twenty years after Moseley's law, Krongauz discovered that the XAS spectrum of condensed matter atoms had a fine structure that could in principle be related to the structure around the absorbing atom. XAS had to wait until the seventies to become the relevant chemical and structural characterization technique it is today. Sayers, Stern and Lytle in 1971 discovered that through XAS one could have access to the pseudo radial distribution function of the absorbing atom with its neighboring atoms.⁵⁶ XAS has become widely available by the development of the intense synchrotron radiation sources used to measure the spectra.

XAS is still one of the most important techniques of structural and chemical characterization particularly of disordered materials and metals in solution. It provides highly detailed and highly accurate information of the local structure around a particular atomic center and of its oxidation state. It has the additional advantage that it is element specific. It can be used in very dilute conditions ($10^{-4} M$) becoming suitable for the study of highly radiotoxic elements like plutonium.

When increasing the energy of the incident X-Ray beam the absorption is low until at a certain energy value μ suddenly increases. At this point, the X-Ray photon has the exact energy as the ionization energy of one of the atom's core-electron, the photon is absorbed and the atom is ionized. This absorption jump is known as absorption edge. The absorption edge is element-specific and the absorbing atom is typically chosen to be the metal center. In addition, different core electrons can be ionized. This generates different edges of the element which are labeled by the principal quantum number of the ejected photoelectron ($n = 1 \rightarrow K, n = 2 \rightarrow L$ etc.).

If the absorbing atom is a monoatomic gas, increasing the energy of the photon beyond the edge causes the emission of the photoelectron with additional kinetic energy. This results in a monotonic decay of μ . If the absorbing atom is in a condensed phase the decrease in absorption is not monotonic but rather presents an oscillatory fine structure. The study of this fine structure is the basis of chemical and structural characterization using XAS. This

oscillatory behavior depends on the nature of the atom and the interaction of the ejected photoelectron with the electronic density of the nearest neighbors of the atom. The ejected photoelectron can be backscattered by the atoms surrounding the absorber doing a round trip out of the absorber and back. The constructive or destructive interference of the outgoing and ongoing photoelectron wavefunctions increases or decreases the probability of ionization generating the oscillatory behavior in μ . This effect is a consequence of the particle-wave duality of electrons.

The interference pattern is a function of the kinetic energy of the electron, the distance to the neighbors and its thermal fluctuation, the coordination number and other spectroscopical factors. Modelling this interference is the aim of XAS interpretation.

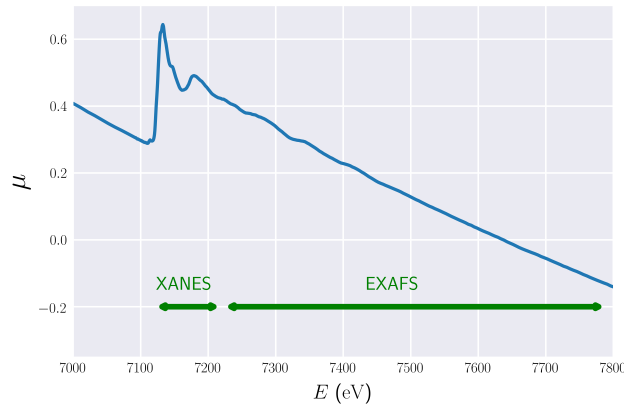


Figure 3.5 Sr L-edge X-Ray absorption spectrum in $\text{SrCO}_3(\text{s})$. The data was obtained from the XAFS spectra library of the University of Chicago. 7120 eV-7220 eV region corresponds to XANES and 7220 eV-7790 eV region to EXAFS.

Figure 3.5 shows a XAS spectrum of Sr in $\text{SrCO}_3(\text{s})$. The spectrum can be divided in two distinct regions:

- **XANES:** X-ray Absorption Near Edge Structure region of the spectrum. It extends from the absorption edge up to 100-150 keV. The photoelectron has little energy and multiple scattering processes are dominant. Quantitative analysis of XANES spectra is cumbersome due to multi-atom correlations and the complexity of the electronic problem itself. It is

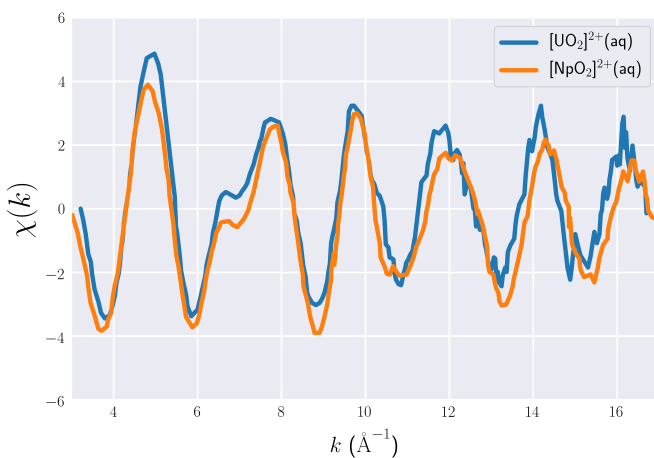


Figure 3.6 $[UO_2 \cdot (H_2O)_5]^{2+}$ (blue) and $[NpO_2 \cdot (H_2O)_5]^{2+}$ (orange) L_{III} -edge k^3 -weighted experimental EXAFS spectra.

generally interpreted qualitatively. The position of the edge itself is an indicator of the absorber oxidation state. Its shape is sensible to the symmetry of the environment and is regarded as a fingerprint of the local structure.

- **EXAFS:** Extended X-ray Absorption Fine Structure region of the spectrum. It extends from ~ 150 eV to ~ 1000 eV above the absorption edge. Since the photoelectron has higher kinetic energy, simple backscattering paths dominate. This region contains most of the structural information: bond distances, coordination numbers and dynamic and structural disorder, that can be extracted by the use of the EXAFS equation.

3.4.1. EXAFS Spectroscopy

Above the absorption edge the absorption coefficient, μ , follows the equation:

$$\mu(E) = \mu_0(E)[1 + \chi(E)] \quad (3.4)$$

Where $\mu_0(E)$ is the absorption coefficient of the gaseous monoatomic element and $\chi(E)$ is the fine structure function or EXAFS function or simply EXAFS spectrum. $\chi(E)$ contains the oscillatory fine structure of the spectrum

resulting from the constructive and destructive interference of the photoelectrons backscattering paths. The EXAFS function is written with respect to the wavenumber of the photoelectron, k :

$$k = \sqrt{2m_e(E - E_0)}/\hbar \quad (3.5)$$

Where m_e is the mass of the electron, E the photon energy and E_0 the binding energy (or work function). Figure 3.6 contains examples of experimental EXAFS spectra. The spectrum is typically weighted by k^2 or k^3 to emphasize the oscillations at high k values.

The EXAFS equation can be written as:⁵⁶

$$\chi(k) = \sum_j^{\text{path types}} \frac{N_j}{kR_j^2} S_0^2 F_j(k) e^{-\frac{-2R_j}{\lambda(k)}} e^{-2\sigma_j^2 k^2} \sin[2kR_j + \varphi_j(k)] \quad (3.6)$$

The function is the sum of the terms of the different path types. The path types are all possible closed paths that go from the absorbing atom, to one or more backscattering atoms and back to the absorber including some that go several times through the absorber. If the path has only “two legs”, a round trip to a neighbor, it is considered a single scattering path (SS). If the path has more than two legs, it is considered a multiple scattering path (MS). Figure 3.7 illustrates the kinds of paths observed. In most cases paths (round trips to a neighbor) dominate.

The Fourier Transform of $\chi(k)$ is a pseudo-radial distribution function of the absorbing atom respect to its neighbor shells. It is not a true radial distribution function because multiple scattering paths do not depend solely on the absorber-backscatterer distance.

First we will discuss the non-structural terms of Equation 3.6 which are defined *a priori* by the user or are estimated quantum-mechanically with theoretical spectroscopy packages such as FEFF.^{57,58}

- The amplitude reduction function, S_0^2 : It is a consequence of the fact that the electrons of the ionized atom experience a different potential than before the ionization and their wavefunction must relax to the ionized state. This factor must be included since only the electron and the neutral atom with a core-hole are modeled. It is typically assumed to have values from 0.85 to 1.0 but can also be estimated theoretically.

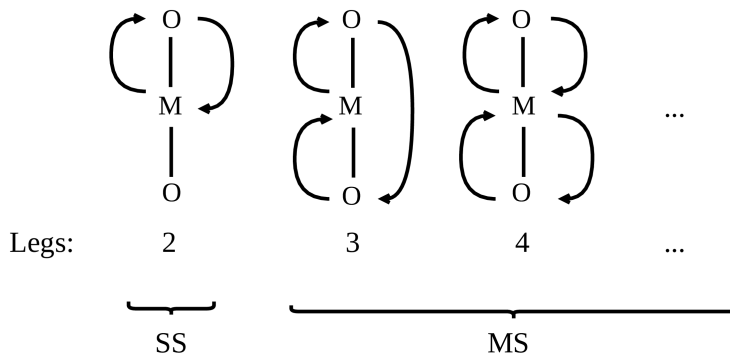


Figure 3.7 Examples of single scattering paths (SS) and multiple scattering paths (MS) with different number of legs. The absorber atom is M and the backscatterers are O. The arrows represent the paths the photoelectron travels.

- Effective amplitude function of the path, $F_j(k)$: It has a complicated dependency on k but it is determined by the atomic number of the backscattering atoms which serves as an identification method for the local environment.
- Mean free path of the photoelectron, $\lambda(k)$: The method assumes that the wavefunction of the outgoing and backscattered photoelectron are coherent. This is only true during the life-time of the excited atom's core-hole. The method also assumes inelastic scattering. The factor $e^{-2R_j/\lambda(k)}$ accounts for these two assumptions.
- Phase displacement function, $\varphi_j(k)$: Like $F_j(k)$, it has a complicated dependency on k but it is determined by the atomic number of the backscattering atoms which serves as an identification method for the local environment.

All these parameters can be nowadays calculated *ab initio* by the FEFF program based on approximate relativistic quantum-mechanical self-consistent field calculations.

Now we will discuss the equation parameters that contain the structural information:

- The distances to the backscattering atom, R_j : Actually, it is the path distance but for single scattering processes it coincides with the distance

to the backscattering neighbor atom. R_j control the frequency of the spectrum. Therefore, for systems with a single type of backscattering atoms and in the absence of significant multiple scattering contributions, the higher the frequency of $\chi(k)$ the longer the bondlength.

- The coordination number, N_j : Again, it is actually the degeneracy of the path but in single scattering processes it is equivalent to the coordination number.
- The Debye-Waller Factor, σ_j^2 : this parameter is the variance of the distance R_j and measures the thermal dispersion or disorder of the path. The factor $e^{-2\sigma_j^2 k^2}$ controls the envelop of the function and is responsible for the exponential decay of the fine structure. Therefore, a slowly decaying signal is associated with stiff structures, a small dispersion of path lengths and low Debye-Waller factors.

There are two ways of obtaining structural information out of an experimental EXAFS spectrum. One is pure experimental fitting. The spectrum is fitted to Equation 3.6 with $\{R_j, N_j, \sigma_j^2\}$ as variables. If the spectrum has many non-equivalent backscattering atoms or complex features, the fitting process can be involved. In many cases, some of the parameters are fixed. These fixed parameters are obtained from other experiments, from theoretical studies or from educated guesses. This alleviates the burden of the high dimensionality of the problem. This fitting approach is particularly complicated in actinoids since there is little available experimental information for many of them so analogy with other actinoids is used in many cases.⁵⁹

In general, it is particularly difficult to fit with high precision the Debye-Waller factors and the coordination numbers since they are highly correlated. This is the reason why experimental coordination numbers obtained from EXAFS can have uncertainties of ± 1 , while uncertainty in distances is much lower ($\sim \pm 2\%$)

The combination of theoretical information with experimental spectra is another strategy to extract structural information from EXAFS. From the atomic positions of the absorbing atom and its nearest shells the FEFF program can calculate a theoretical EXAFS spectrum. If the theoretical and experimental spectra are in good agreement, the structural parameters of the theoretical coordinates are validated and proposed to characterize the system. Theoretical modelling of EXAFS is a great tool to interpret spectra, extract structural

parameters, aid in the fitting and as a validation tool for newly developed theoretical models. In particular, computation of theoretical EXAFS spectra from statistical simulation ensembles can contribute to the interpretation of the experimental spectra.^{35,37,60–63} Conversely, reproducing the EXAFS spectrum helps to validate the quality of the simulation and the physicochemical predictions obtained.

If the theoretical spectrum is calculated from a single molecular structure the Debye-Waller factors of the paths must be guessed since a single snapshot has no dynamic bond dispersion. On the other hand, if instead of a single structure we use an statistical simulation ensemble the path length dispersion is added explicitly from the statistical thermal fluctuation. The exponential decay term containing σ_j^2 is dropped from Equation 3.6 and the theoretical EXAFS equation becomes:³⁶

$$\chi(k) = \frac{1}{N_s} \sum_i^{N_s} \sum_j \frac{N_j}{kR_j^2} S_0^2 |F_j(k)| e^{-\frac{2R_j}{\lambda}} \sin[2kR_j + \varphi_j(k)] \quad (3.7)$$

The final spectrum is the average spectrum of the set of N_s snapshots. The natural disorder introduced by the differences among the individual simulated spectra produces the exponential decay of the average function.

Both applications of the theoretical-experimental combination were done in this thesis. We used the theoretical EXAFS of an $\text{Am}^{3+}/[\text{AmO}_2 \cdot (\text{H}_2\text{O})_5]^{2+}$ mixture to interpret its experimental EXAFS spectrum and predict the structural parameters of a pure $[\text{AmO}_2 \cdot (\text{H}_2\text{O})_5]^{2+}$ solution, a solution that experimentalists have been unable to produce so far. We also used experimental EXAFS spectra to assess the quality of the actinyl force fields developed.

More information of XAS spectroscopy can be obtained from the following review articles and monographs^{58,63–67}.

3.5. Entropy In Molecular Dynamics Simulations

As we have argued in Section 1.4, entropy is one of the key factors in the hydrophobicity or hydrophilicity of a solute. Unfortunately, measuring entropic effects in simulation is a complex task. It generally involves either measuring the variation of free energy with temperature, $\left(\frac{\partial G}{\partial T}\right)_P = -S$, or by mathematically estimating how a process affects the number of microstates of a system. An example of the latter is tetrahedral entropy.⁶⁸

Liquid state theory provides an additional path. The entropy of a system can be expanded as a sum of many-body correlations:^{69,70}

$$S = S^{(1)} + S^{(2)} + S^{(3)} + \dots \quad (3.8)$$

This expansion has been used to study pure water^{71–75} and solutions of simple solutes.^{76–81} The use of the pair entropy expansion to calculate solvation entropies and free energies was formalized by Lazaridis in what is now commonly known as “Inhomogeneous Solvation Theory” (IST).⁸² Derivatives of this theory have been used to calculate the thermodynamics of structural water molecules of proteins^{83,84} or more complex solutes like amino-acids^{85–87}

We will first assume that the system consists of a single spherically symmetric solute immersed in a rigid solute like the TIP4P⁸⁸ or SPC/E⁸⁹ water models.

In Equation 3.8, $S^{(1)}$ is the self correlation term, $S^{(2)}$ is the pair correlation term, $S^{(3)}$ is the three-body correlation term, etc. Although the three-body term is expected to be significant, most of the information of the structure of the solution is in the pair term.^{69–71,90}

The first order term, $S^{(1)}$, is the translational entropy of a non-interacting system:

$$S^{(1)} = 5k_B - k_B \ln(\rho_s \lambda_s^3) - k_B \ln(\rho_w \lambda_w^3) \quad (3.9)$$

where ρ and λ are the numeric density and the thermal wavelength of the solute (s) or the solvent (w).⁷¹

The pair entropy term can be divided into three components:

$$S = S_{ss}^{(2)} + S_{sw}^{(2)} + S_{ww}^{(2)} \quad (3.10)$$

The first term is zero due to the infinite dilution of the solute. The second term equals:

$$S_{sw}^{(2)} = -\frac{k_B \rho_w}{\Omega} \int [g(r, \omega) \ln(g(r, \omega)) - g(r, \omega) + 1] dr d\omega \quad (3.11)$$

Where Ω is the integral of the Euler angles of the solvent molecule and $g(r, \omega)$ is the pair correlation function (PCF) of the atom and the solute. The PCF is a function of the distance between the centers of mass of the particles and the orientation of the solvent, ω). An analogous expression exists for the solvent-solvent term. The solute-solvent PCF can be decomposed into:⁷¹

$$g(r, \omega) = g(r) \cdot g(\omega | r) \quad (3.12)$$

Where $g(r)$ is the radial distribution function (RDF) and $g(\omega|r)$ is the conditional angular distribution function of the solute. As a consequence the solute-solvent pair entropy can be decomposed further into a translational component ($S_{\text{sw,tr}}^{(2)}$) and an orientational ($S_{\text{sw,or}}^{(2)}$) component:⁷¹

$$S_{\text{sw}}^{(2)} = S_{\text{sw,or}}^{(2)}(r, \omega) + S_{\text{sw,tr}}^{(2)}(r) \quad (3.13)$$

$$S_{\text{sw,or}}^{(2)} = -\frac{k_B \rho_w}{2\Omega} \int g(r) g(\omega|r) \ln(g(\omega|r)) dr d\omega \quad (3.14)$$

$$S_{\text{sw,tr}}^{(2)}(r) = -2\pi k_B \rho_w \int [g(r) \ln(g(r)) - g(r) + 1] dr \quad (3.15)$$

Recent work used the translational pair entropy as a fingerprint to distinguish liquid from solid local environments in metals⁹¹ and to use entropy as a collective variable to drive crystallization in enhanced sampling simulations.⁹²

In Chapter 9, as a first approach, we will only use $S_{\text{sw,tr}}^{(2)}$ to find a simple hydrophobicity and hydrophilicity fingerprint to characterize the atoms of a complex solute. Our work differs from previous uses of Equation 3.8 in that we will not be interested in calculating thermodynamic quantities as other methods do. We will develop a simple fingerprint with a very simple input like the radial distribution function which will also be a good collective variable in enhanced sampling simulations. In addition, the ability of the fingerprint to identify the hydrophobicity or hydrophilicity of the hydrated actinyl atoms will be explored.

This section has mostly been based on the following works⁷¹⁻⁸² and experience gained during my stay with Parrinello's group.

3.6. Metadynamics

The main limitation of phase space sampling in MD simulations is the discretization of the equations of motion in timesteps. The timestep for atomistically detailed systems is in the order of femtoseconds to describe the normal modes of atomic motion. Unfortunately, many of the most interesting phenomena occur in timescales of microseconds or even seconds. Some of these events are chemical reactions, protein folding, crystallization, phase changes, ligand binding etc. The long timescales are due to high kinetic barriers which are only surmounted by the system in the rare event of a fluctuation which accumulates enough of kinetic energy in the necessary degrees of freedom. For nowadays computers and, due to Moore's law, for the computers of to-

morrow, doing enough MD steps to reach such timescales is impossible in the time-span of a PhD or post-doc unless you have impressive computational resources. Parallelization can lead to study bigger systems at longer timescales, but unfortunately time by its own nature is serial.

In order to surpass the free energy barriers special enhanced sampling MD techniques must be used. Many techniques have been proposed and detailed reviews can be found in the literature.^{93–95} In enhanced sampling techniques MD simulations are carried out with some external algorithm or bias favoring non-Boltzmann sampling. After the sampling, post-processing techniques are used to obtain the Boltzmann information of the system. Enhanced sampling methods can be categorized in four groups:⁹⁴

- **Thermal Fluctuation Methods**
- **Path-Finding Methods**
- **Alchemical Methods**
- **Collective Variable Methods**

Metadynamics is a collective variable enhanced sampling technique in which one or several collective variables are biased. Collective variables (CV) are functions of the coordinates of the system which discriminate between the states of the system and are used to bias or analyze simulations. They allow the projection of the system multidimensional behavior into a small set of relevant coarse grained coordinates. CV methods like metadynamics are based on finding appropriate CVs that describe the transition and adding a bias potential on them to enhance state change. CVs should distinguish states and also capture the slow normal-modes of the system that connect states. The most challenging aspect of metadynamics and all CV-based methods is finding appropriate CVs in the high dimensional non-linear problems tackled.

The bias potential is time-dependent and is increased in the form of Gaussians added in the regions of CV space that the system visits. The Gaussians deposited accumulate in the free energy wells the system has visited filling them up as if “adding sand to fill a valley”. In the Well-Tempered version of metadynamics^{96,97} (WTMetaD) this filling of the wells converges asymptotically.⁹⁷ We shall only refer to WTMetaD which was the method used in this work. We will assume only one CV, s is being biased for simplicity but the generalization to many CVs is straightforward.

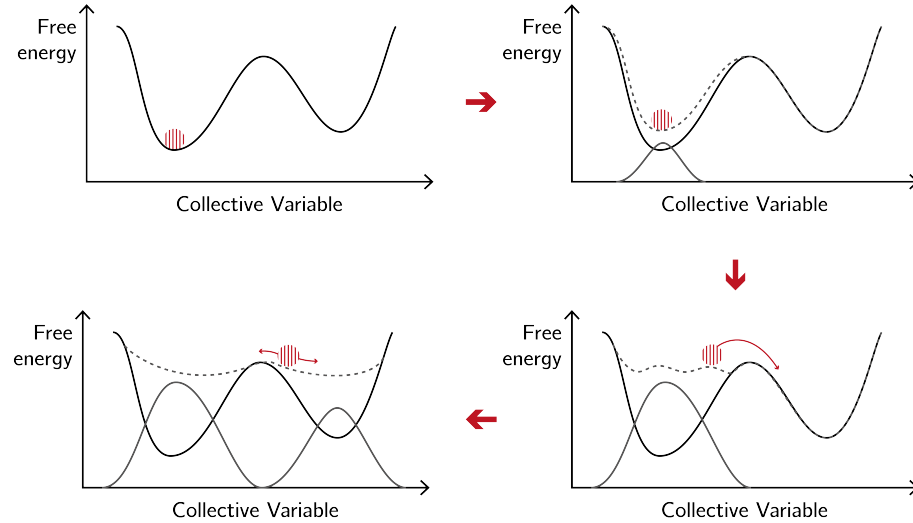


Figure 3.8 Time evolution of a system in a metadynamics simulation. The free energy surface of a system, $F(s)$, as a function of a collective variable, s , is represented as well as the biases (below the FES) and the CV-space position of the system (black circle). The dashed lines represent the FES that the biased system is experiencing due to the bias. The figure was adapted by Adriana Pérez Conesa based on the figure of Bussi and Branduardi.⁹⁸

Figure 3.8 represents schematically the evolution of a system in a metadynamics simulation. The free energy surface of a system, $F(s)$, as a function of a collective variable, s , is represented as well as the bias (below the free energy surface) and the CV-space position of the system (striped circle). A free energy surface (FES) is a projection of the free energy of the system onto a few CVs that represent its relevant states. The system is initially in the left free energy basin and if the barrier to jump to the right basin is much higher than $k_B T$, the system will only explore the left basin. In metadynamics a bias potential is added in the form of gaussians in the regions of CV-space where the system has been (Figure 3.8 top right) elevating the effective free energy surface of the system. If the right basin accumulates enough bias, the barrier is small enough for the system to jump to the right basin and start exploring it and filling it with bias (Figure 3.8 bottom right). When the right basin is also filled with bias and effective free energy of the system becomes flat enough, the system diffuses in CV-space going from one state to the other (Figure 3.8 bottom left). From the

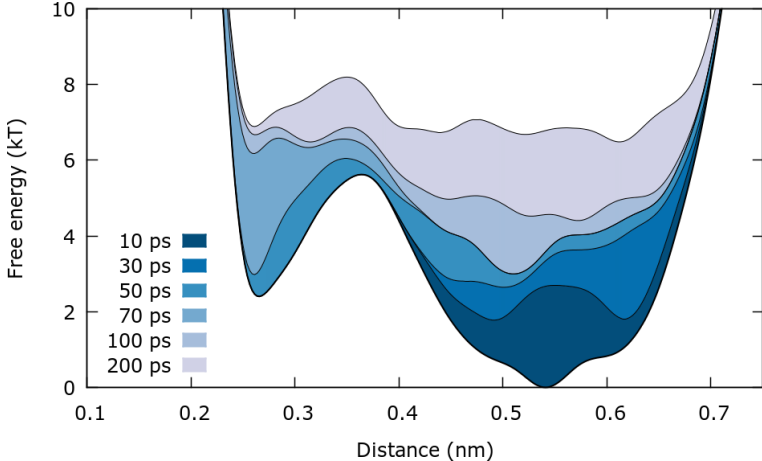


Figure 3.9 Free energy surface of a system as a function of distance (lower curve). Since the system is being simulated with metadynamics bias accumulates with time (upper curves) filling the free energy minima. Reproduced from the PLUMED2 manual.⁹⁹

deposited bias the original free energy surface of the system can be calculated.

The basis of WTMetaD is the following time-dependent bias potential:

$$V(s, t) = \sum_{k=1}^n W \exp \left[-\frac{1}{\gamma-1} \beta V_{k-1}(s_k) \right] e^{(s-s_k)^2/\sigma^2} \quad (3.16)$$

This is the bias potential added to the system hamiltonian at time t , where $n\tau < t < (n+1)\tau$. At this time it consists of n Gaussians deposited which were deposited every τ steps.

Each of the terms in the sum is a deposited gaussian ($e^{(s-s_k)^2/\sigma^2}$) at a position visited by system, s_k , with a spread σ . The initial height of the Gaussians is W but the height decays exponentially in the regions that already have bias deposited due to the factor $\exp \left[-\frac{1}{\gamma-1} \beta V_{k-1}(s_k) \right]$. The rate of decay is controlled by γ known as bias factor which is a simulation input parameter. The exponential decay of heights is the difference between the initial metadynamics algorithm to WTMetaD.

Figure 3.9 shows the free energy surface of a system as a function of one CV, distance, and how the FES is filled as a function of time. Initially the $5k_B T$ barrier makes the system oscillate within the right basin. After 50 ps so many Gaussians have been deposited in this region of the CV that the bias has reduced the $5k_B T$ barrier to $2k_B T$. This allows the system to have a fluctuation

by which it jumps to the left basin. At this point the system starts to explore the left basin and fill it with bias. Once the two states have been filled with Gaussians the FES becomes somewhat flat which allows the system to cross from one state to the other. At this point the time-evolution of the CV becomes diffusive and if the heights of the Gaussians deposited are low: the simulation has converged. At convergence the FES experienced by the system is the unbiased FES scaled by the bias factor.

In a converged simulation the free energy of the unbiased system as a function of the collective variable, $F(s)$, is:

$$F(s) = -\frac{\gamma}{\gamma-1} V(s, t) + c(t) \quad (3.17)$$

Therefore a part from an additive constant, $c(t)$, the FES can be obtained from the simulation deposited bias. Free energy differences between the states are calculated integrating the FES over their basins A and B :

$$\Delta F_{A,B} = -k_B T \log \left(\frac{\int_A e^{-\beta F(s)} ds}{\int_B e^{-\beta F(s)} ds} \right) \quad (3.18)$$

WTMetaD was proposed in order to fix a problem of the original metadynamics formulation. In the prior formulation the height of the Gaussians deposited was constant. After the filling of the free energy wells of the system the bias would keep depositing forever so that the simulation would explore higher and higher free energy regions of CV space. It was up to the user to stop the simulation. WTMetaD has been proven to converge asymptotically⁹⁷ therefore giving clear convergence conditions: the gaussian heights should be small and the CVs should have diffusive dynamics.

Access to FES is not exclusive for enhanced sampling simulations. In any ergodic MD simulation the FES as a function of a CV, s , can be obtained from its probability distribution, $P(s)$:

$$F(s) = -k_B T \log(P(s)) + c \quad (3.19)$$

If the system is not ergodic, metadynamics or some other enhanced sampling technique must be used. In the case of metadynamics, Equation 3.19 cannot be used directly since the distribution of the simulation is non-Boltzmann due to the bias. Nevertheless, the unbiased distribution can be estimated calculating a weighted histogram with the biased data in which the weights compensate biasing. This process is known as *reweighting* and it can be done

in several ways. The most accurate is the one developed recently by Tiwari and Parrinello which estimates the time dependent constant, $c(t)$, and in this way calculates exactly the bias at each step of the simulation.¹⁰⁰ This reweighting scheme uses the following weight for a given data point of value, s , sampled at time t :

$$w(s, t) \propto \exp [\beta (V_{\text{MetaD}}(s, t) - c(t) + V_{\text{ext}}(s))] \quad (3.20)$$

Where $V_{\text{MetaD}}(s, t)$ is the WTMetaD bias, $c(t)$ the time-dependent constant and $V_{\text{ext}}(s)$ any additional bias added (for example only to study a certain region of the CV). Reweighting is a very powerful technique because it allows to project the FES on collective variables different than the ones biased in the simulation. The typical metadynamics approach is to find suitable CVs to converge the simulation and then reweight on to any other CV to explore the chemistry of the system.

We will briefly enumerate the input parameters of a WTMetaD simulations and how they should be selected. In general, metadynamics is fairly robust with respect to parameter choice.

-
- **Bias factor, γ :** It regulates the decay of the gaussian heights and should be chosen to be similar to the barrier size in units of $k_B T$. In the limit of very high γ the original formulation of metadynamics is recovered. On the other hand, if γ tends to 1 unbiased MD are obtained.
 - **Initial gaussian height, W :** It should be chosen to be $1-2k_B T$. In principle it can be higher but it can make the equations of motion unstable due to very high biasing forces.
 - **Gaussian deposition frequency, τ :** It should be roughly equal to the autocorrelation time of the CV in order for the system to “equilibrate” in between depositions. This can be estimated from unbiased simulations.
 - **Gaussian widths, σ_i :** Ideally they should be as small as possible to describe more accurately the underlying FES, but the smaller the width the slower the convergence. Typically it is set to a third or a fifth of the standard deviation of the CV in the narrowest basin in an unbiased simulation.
 - **Collective variables, s_i :** The success of metadynamics simulations is mostly dependent on the choice of collective variables. Ideally, only

one should be used but two are the standard and three is also possible and necessary in some cases. Of course, the more CVs are biased the slower the convergence. The CVs should capture all the slow motions of the system such that when the bias converges there is diffusion in CV space. In many cases CV choice is cumbersome. Even if one useful CV has been chosen, there may be hidden orthogonal CVs that are not biased and prevent convergence. An example of this can be given in the context of ligand binding. Suppose the bias CV is only the distance between the pocket and the ligand. If the pocket is closed by the position of a side-chain, until there is a fluctuation and the side-chain opens the ligand will not bind. This will result in a decay of the gaussian heights which will barely be deposited and there will not be diffusion of the CV in time. To solve this, a side-chain CV should also be biased.

This section has mostly been based on the following reviews.^{11,98,101}

3.7. Bibliography

1. Frenkel, D.; Smit, B. *Understanding molecular simulation: from algorithms to applications*; Academic press: London, 2001; Vol. 1.
2. Shclick, T.; Torquato, S. *Molecular modeling and simulation: an interdisciplinary guide*, 2nd ed.; Springer Science & Business Media: New York, 2013.
3. Smith, W. In *Elements of Molecular dynamics*, 2nd ed.; Smith, W., Ed.; 2014.
4. Herman J. C. Berendsen, *Simulating the physical world: hierarchical modeling from quantum mechanics to fluid dynamics.*; Cambridge University Press: Cambridge, 2007.
5. Szabo, A.; Ostlund, N. S. *Modern quantum chemistry: introduction to advanced electronic structure theory*, 1st ed.; Courier Corporation: Mineola, New York, 2012.
6. Cramer, C. J. *Essentials of Computational Chemistry: Theories and Models*; Wiley: Chichester, UK, 2004.
7. Marion, J. B.; Thornton, S. T. *Classical dynamics of particles and systems*; Brooks/Cole Thomson Learning: Belmont, CA, 1966.

8. Goldstein, H.; Poole, C. P.; Safko, J. L. *Classical Mechanics*; Addison Wesley: Boston, MA, 2001.
9. Tuckerman, M. *Statistical mechanics: theory and molecular simulation*; Oxford University Press: Oxford, 2010.
10. McQuarrie, D. A. *Statistical thermodynamics*; Harper & Row: New York, 1973.
11. Valsson, O.; Tiwary, P.; Parrinello, M. *Annu. Rev. Phys. Chem.* **2016**, *67*, 159–184.
12. Bussi, G.; Branduardi, D. In *Rev. Comput. Chem.*; Parrill, A. L., Lipkowitz, K. B., Eds.; John Wiley & Sons Inc: Hoboken, NJ, 2015; Chapter 1.
13. Shirts, M. R.; Mobley, D. L. In *Biomolecular Simulations: Methods and Protocols*; Monticelli, L., Salonen, E., Eds.; Springer: New York, 2013; Chapter 11.
14. Solomon, E. I.; Sundaram, U. M.; Machonkin, T. E. *Chem. Rev.* **1996**, *96*, 2563–2606.

15. Heinzinger, K.; Vogel, P. *Zeitschrift für Naturforschung A* **1974**, *29*, 1164–1171.
16. Rahman, A.; Stillinger, F. H. *J. Chem. Phys.* **1971**, *55*, 3336–3359.
17. Hogervorst, W. *Physica* **1971**, *51*, 77–89.
18. Jorgensen, W. L.; Bigot, B.; Chandrasekhar, J. *J. Am. Chem. Soc.* **1982**, *104*, 4584–4591.
19. Chandrasekhar, J.; Spellmeyer, D. C.; Jorgensen, W. L. *J. Am. Chem. Soc.* **1984**, *106*, 903–910.
20. Jorgensen, W. L.; Chandrasekhar, J.; Madura, J. D.; Impey, R. W.; Klein, M. L. *J. Chem. Phys.* **1983**, *79*, 926–935.
21. Aqvist, J. *J. Phys. Chem.* **1990**, *94*, 8021–8024.
22. Vega, C.; Abascal, J. L. F. *Phys. Chem. Chem. Phys.* **2011**, *13*, 19663–19688.
23. Li, P.; Merz, K. M. *Chem. Rev.* **2017**, *117*, 1564–1686.
24. Li, P.; Song, L. F.; Merz, K. M. *J. Phys. Chem. B* **2015**, *119*, 883–895.
25. Li, P.; Roberts, B. P.; Chakravorty, D. K.; Merz, K. M. *J. Chem. Theory Comput.* **2013**, *9*, 2733–2748.

26. Ayala, R.; Martínez, J. M.; Pappalardo, R. R.; Muñoz-Páez, A.; Sánchez Marcos, E. *J. Phys. Chem. B* **2008**, *112*, 5416–5422.
27. Sánchez Marcos, E.; Pappalardo, R. R.; Barthelat, J. C.; Gadea, X. F. *J. Phys. Chem.* **1992**, *96*, 516–518.
28. Curtiss, L. A.; Halley, J. W.; Hautman, J.; Rahman, A. *J. Chem. Phys.* **1987**, *86*, 2319–2327.
29. Ayala, R.; Martínez, J. M.; Pappalardo, R. R.; and Sánchez Marcos, E. *J. Phys. Chem. A* **2000**, *104*, 2799–2807.
30. Floris, F.; Persico, M.; Tani, A.; Tomasi, J. *Chem. Phys.* **1995**, *195*, 207–220.
31. Elrod, M. J.; Saykally, R. J. *Chemical Reviews* **1994**, *94*, 1975–1997.
32. Martínez, J. M.; Pappalardo, R. R.; Sánchez Marcos, E. *J. Am. Chem. Soc.* **1999**, *121*, 3175–3184.
33. Martínez, J. M.; Sánchez Marcos, E.; Refson, K.; Pappalardo, R. R.; Merkling, P. J. *Theor. Chem. Acc.* **2004**, *111*, 101–109.
34. Carrera, F.; Torrico, F.; Richens, D. T.; Muñoz-Páez, A.; Martínez, J. M.; Pappalardo, R. R.; Sánchez Marcos, E. *J. Phys. Chem. B* **2007**, *111*, 8223–8233.
35. Galbis, E.; Hernández-Cobos, J.; den Auwer, C.; Le Naour, C.; Guillau-mont, D.; Simoni, E.; Pappalardo, R. R.; Sánchez Marcos, E. *Angew. Chem. Int. Ed. English* **2010**, *122*, 3899–3903.
36. Merkling, P. J.; Sánchez Marcos, E.; Pappalardo, R. R.; Muñoz-Páez, A. *Phys. Rev. B - Condens. Matter Mater. Phys.* **2001**, *64*, 1–4.
37. Merkling, P. J.; Adela Muñoz-Páez, A.; Sánchez Marcos, E. *J. Am. Chem. Soc.* **2002**, *124*, 10911–10920.
38. Caralampio Mínguez, D. Z. Looking for synergies in solution chemistry between first-principles intermolecular potentials and exafs and xanes spectroscopies. Ph.D. thesis, Universidad de Sevilla, Spain, 2018.
39. Morales Negrito, N. Estudio teórico de propiedades fisicoquímicas de cationes metálicos en disolución: Evolución en el grupo de los alcalinos y en la serie de los lantánidos. Ph.D. thesis, Universidad de Sevilla, Spain, 2015.
40. Galbis, E.; Hernández-Cobos, J.; Pappalardo, R. R.; Sánchez Marcos, E. *J. Chem. Phys.* **2014**, *140*, 214104.

41. Pappalardo, R. R.; Sánchez Marcos, E. *J. Phys. Chem.* **1993**, *97*, 4500–4504.
42. Pappalardo, R. R.; Martínez, J. M.; Sánchez Marcos, E. *J. Phys. Chem.* **1996**, *100*, 11748–11754.
43. Martínez, J. M.; Pappalardo, R. R.; Sánchez Marcos, E. *J. Phys. Chem. B* **1998**, *102*, 3272–3282.
44. Martínez, J. M.; Pappalardo, R. R.; Sánchez Marcos, E. *J. Chem. Phys.* **1998**, *109*, 1445–1455.
45. Yang, T.; Tsushima, S.; Suzuki, A. *J. Phys. Chem. A* **2001**, *105*, 10439–10445.
46. Martínez, J. M.; Torrico, F.; Pappalardo, R. R.; Sánchez Marcos, E. *J. Phys. Chem. B* **2004**, *108*, 15851–15855.
47. Torrico, F.; Pappalardo, R. R.; Sánchez Marcos, E.; Martínez, J. M. *Theor. Chem. Acc.* **2006**, *115*, 196–203.
48. Melchior, A.; Martínez, J. M.; Pappalardo, R. R.; Sánchez Marcos, E. *J. Chem. Theor. Comput.* **2013**, *9*, 4562–4573.
49. Melchior, A.; Tolazzi, M.; Martínez, J. M.; Pappalardo, R. R.; Sánchez Marcos, E. *J. Chem. Theory Comput.* **2015**, *11*, 1735–1744.
-
50. Saint-Martin, H.; Hernández-Cobos, J.; Bernal-Uruchurtu, M. I.; Ortega-Blake, I.; Berendsen, H. J. C. *J. Chem. Phys.* **2000**, *113*, 10899–10912.
51. Villa, A.; Hess, B.; Saint-Martin, H. *J. Phys. Chem. B* **2009**, *113*, 7270–7281.
52. Caralampio, D. Z.; Martínez, J. M.; Pappalardo, R. R.; Marcos Sánchez, E. *Theor. Chem. Acc.* **2017**, *136*, 1–8.
53. Caralampio, D. Z.; Martínez, J. M.; Pappalardo, R. R.; Sánchez Marcos, E. *Phys. Chem. Chem. Phys.* **2017**, *19*, 28993–29004.
54. Morales, N.; Galbis, E.; Martínez, J. M.; Pappalardo, R. R.; Sánchez Marcos, E. *J. Phys. Chem. Lett.* **2016**, *7*, 4275–4280.
55. Cotton, S. A. *Comm. Inorg. Chem.* **2018**, *38*, 110–125.
56. Sayers, D. E.; Stern, E. A.; Lytle, F. W. *Phys. Rev. Lett.* **1971**, *27*, 1204–1207.
57. Ankudinov, A. L.; Nesvizhskii, A. I.; Rehr, J. J. *Phys. Rev. B* **2003**, *67*, 115120–6.
58. Rehr, J. J.; Albers, R. C. *Rev. Mod. Phys.* **2000**, *72*, 621–654.
59. Denecke, M. A. *Coord. Chem. Rev.* **2006**, *250*, 730–754.

60. D'Angelo, P.; Martelli, F.; Spezia, R.; Filipponi, A.; Denecke, M. A. *Inorg. Chem.* **2013**, *52*, 10318–10324.
61. Spezia, R.; Migliorati, V.; D'Angelo, P. *J. Chem. Phys.* **2017**, *147*, 161707–161718.
62. Filipponi, A.; D'Angelo, P.; Pavel, N. V.; Di Cicco, A. *Chem. Phys. Lett.* **1994**, *225*, 150–155.
63. Palmer, B. J.; Pfund, D. M.; Fulton, J. L. *J. Phys. Chem.* **1996**, *100*, 13393–13398.
64. Gaur, A.; Shrivastava, B. D.; Nigam, H. L. *Proc. Indian Natl. Sci. Acad.* **2013**, *79*, 921–966.
65. Newville, M. *Fundamentals of XAFS, Consortium for Advanced Radiation Sources*; University of Chicago: Chicago, IL, 2004.
66. Koningsberger, D. C.; Prins, R. *X-ray Absorption: Principles, Applications, Techniques of EXAFS, SEXAFS, and XANES*; John Wiley and Sons: New York, NY, 1988.
67. Muñoz-Páez, A.; Sánchez Marcos, E. In *Comprehensive Inorganic Chemistry II From Elements to Application*; Reedijk, J., Poeppelmeier, K., Eds.; Elsevier, 2013; Chapter 5, pp 133–159.
68. Kumar, P.; Buldyrev, S. V.; Stanley, H. E. *Proc. Natl. Acad. Sci.* **2009**, *106*, 22130–22134.
69. Nettleton, R. E.; Green, M. S. *J. Chem. Phys.* **1958**, *29*, 1365–1370.
70. Baranyai, A.; Evans, D. *J. Phys. Rev. A* **1989**, *40*, 3817–3822.
71. Lazaridis, T.; Karplus, M. *J. Chem. Phys.* **1996**, *105*, 4294–4316.
72. Zielkiewicz, J. *J. Phys. Chem. B* **2008**, *112*, 7810–7815.
73. Giuffré, E.; Prestipino, S.; Saija, F.; Saitta, A. M.; Giaquinta, P. V. *J. Chem. Theory Comput.* **2010**, *6*, 625–636.
74. Agarwal, M.; Alam, M. P.; Chakravarty, C. *J. Phys. Chem. B* **2011**, *115*, 6935–6945.
75. Zhang, C.; Spanu, L.; Galli, G. *J. Phys. Chem. B* **2011**, *115*, 14190–14195.
76. Lazaridis, T.; Paulaitis, M. E. *J. Phys. Chem.* **1992**, *96*, 3847–3855.
77. Lazaridis, T.; Paulaitis, M. E. *J. Phys. Chem.* **1994**, *98*, 635–642.
78. Bergman, D. L.; Lyubartsev, A. P.; Laaksonen, A. *Phys. Rev. E* **1999**, *60*,

- 4482–4495.
79. Lazaridis, T. *J. Phys. Chem. B* **2000**, *104*, 4964–4979.
 80. Kinoshita, M.; Matubayasi, N.; Harano, Y.; Nakahara, M. *J. Chem. Phys.* **2006**, *124*, 24512–24519.
 81. Liu, M.; Besford, Q. A.; Mulvaney, T.; Gray-Weale, A. *J. Chem. Phys.* **2015**, *142*, 114117–114132.
 82. Lazaridis, T. *J. Phys. Chem. B* **1998**, *102*, 3531–3541.
 83. Li, Z.; Lazaridis, T. *Comput. Drug Discov. Des.*; Springer, 2012; pp 393–404.
 84. Abel, R.; Young, T.; Farid, R.; Berne, B. J.; Friesner, R. A. *J. Am. Chem. Soc.* **2008**, *130*, 2817–2831.
 85. Nguyen, C. N.; Kurtzman Young, T.; Gilson, M. K. *J. Chem. Phys.* **2012**, *137*, 973–980.
 86. Huggins, D. J.; Payne, M. C. *J. Phys. Chem. B* **2013**, *117*, 8232–8244.
 87. Schauperl, M.; Podewitz, M.; Waldner, B. J.; Liedl, K. R. *J. Chem. Theory Comput.* **2016**, *12*, 4600–4610.
 88. Jorgensen, W. L.; Chandrasekhar, J.; Madura, J. D.; Impey, R. W.; Klein, M. L. *J. Chem. Phys.* **1983**, *79*, 926–935.
 89. Berendsen, H. J. C.; Grigera, J. R.; Straatsma, T. P. *J. Phys. Chem.* **1987**, *91*, 6269–6271.
 90. Wallace, D. C. *J. Chem. Phys.* **1987**, *87*, 2282–2284.
 91. Piaggi, P. M.; Parrinello, M. *J. Chem. Phys.* **2017**, *147*, 114112–114116.
 92. Piaggi, P. M.; Valsson, O.; Parrinello, M. *Phys. Rev. Lett.* **2017**, *119*, 015701–015704.
 93. De Vivo, M.; Masetti, M.; Bottegoni, G.; Cavalli, A. *J. Med. Chem.* **2016**, *59*, 4035–4061.
 94. Harpole, T. J.; Delemotte, L. *Biochim. Biophys. Acta - Biomembr.* **2018**, *1860*, 909–926.
 95. Abrams, C.; Bussi, G. *Entropy* **2014**, *16*, 163–199.
 96. Barducci, A.; Bussi, G.; Parrinello, M. *Phys. Rev. Lett.* **2008**, *100*, 020603–020606.
 97. Dama, J. F.; Parrinello, M.; Voth, G. A. *Phys. Rev. Lett.* **2014**, *112*, 240602–

- 240607.
98. Bussi, G.; Branduardi, D. In *Reviews in Computational Chemistry*; Parrill, A. L., Lipkowitz, K. B., Eds.; John Wiley & Sons Inc: Hoboken, NJ, 2015; Chapter 1.
 99. Tribello, G. A.; Bonomi, M.; Branduardi, D.; Camilloni, C.; Bussi, G. *Comput. Phys. Commun.* **2014**, *185*, 604–613.
 100. Tiwary, P.; Parrinello, M. *J. Phys. Chem. B* **2015**, *119*, 736–742.
 101. Barducci, A.; Bonomi, M.; Parrinello, M. *Wiley Interdiscip. Rev. Comput. Mol. Sci.* **2011**, *1*, 826–843.
- 
-





A hydrated ion model of [UO₂]²⁺ in water: Structure, dynamics, and spectroscopy from classical molecular dynamics

4.1. *J. Chem. Phys.* 2016, **145**, 224502–224523



A hydrated ion model of $[\text{UO}_2]^{2+}$ in water: Structure, dynamics, and spectroscopy from classical molecular dynamics

Sergio Pérez-Conesa, Francisco Torrico, José M. Martínez, Rafael R. Pappalardo, and Enrique Sánchez Marcos^{a)}

Departamento de Química Física, Universidad de Sevilla, 41012 Seville, Spain

(Received 22 September 2016; accepted 21 November 2016; published online 15 December 2016)

A new *ab initio* interaction potential based on the hydrated ion concept has been developed to obtain the structure, energetics, and dynamics of the hydration of uranyl in aqueous solution. It is the first force field that explicitly parameterizes the interaction of the uranyl hydrate with bulk water molecules to accurately define the second-shell behavior. The $[\text{UO}_2(\text{H}_2\text{O})_5]^{2+}$ presents a first hydration shell U–O average distance of 2.46 Å and a second hydration shell peak at 4.61 Å corresponding to 22 molecules using a coordination number definition based on a multisite solute cavity. The second shell solvent molecules have longer mean residence times than those corresponding to the divalent monatomic cations. The axial regions are relatively de-populated, lacking direct hydrogen bonding to apical oxygens. Angle-solved radial distribution functions as well as the spatial distribution functions show a strong anisotropy in the ion hydration. The $[\text{UO}_2(\text{H}_2\text{O})_5]^{2+}$ solvent structure may be regarded as a combination of a conventional second hydration shell in the equatorial and bridge regions, and a clathrate-like low density region in the axial region. Translational diffusion coefficient, hydration enthalpy, power spectra of the main vibrational modes, and the EXAFS spectrum simulated from molecular dynamics trajectories agree fairly well with the experiment. Published by AIP Publishing. [http://dx.doi.org/10.1063/1.4971432]

I. INTRODUCTION

Actinide solution chemistry is an important challenge for many fields in science. The development of nuclear technology, its waste reprocessing, and its environmental impact involve a wide set of areas in physics, chemistry, biology, geology, and engineering.¹ Spent nuclear fuel contains many radioactive cations in the form of hydrated actinyls, $[\text{AnO}_2(\text{H}_2\text{O})_n]^{q+}$,^{2–8} that become the normal way these species are selectively separated and stored.⁹ The mobility of uranyl and other actinyls determines their speciation in natural aqueous systems, in contaminated water, in storage tanks, and their potential escape from permanent geological repositories. Due to the long lifetime of the radioactivity and the large number of environments, the problem exceeds laboratory scale. Then, the generation of appropriate inexpensive and realistic models of the phenomena becomes a challenge. Computer simulations of actinyls in solution or in other environments are a step forward in the theoretical description of radioactive materials.

With the development of accurate heavy-element quantum-mechanical (QM) techniques^{10–14} in the last decade, an increasing number of theoretical works have supplied a first-principles description of the bonding properties of these species.^{15–17} Since the early studies, solvent effects were recognized as an important factor to be considered. They were accounted either by a discrete model of one or two solvation shells,^{18–22} or by the inclusion of the hydrated ion within a

dielectric continuum,^{23–29} as had previously been proposed for other metal cation hydrations.^{30,31}

The powerful QM approach must be completed with a statistical mechanical picture of the dynamic hydration phenomenon. Even though *ab initio* molecular dynamics is ideal to this aim, in practice its computational cost limits the system size and simulation times. Fortunately, classical statistical simulations sample the ensemble in an effective way allowing to reach the necessary system sizes and simulation time scales. But this is only reliable if the interaction potentials describe properly the potential energy surface and no chemical change takes place in the system. Therefore, robust potential generation must be based on accurate experimental data and/or QM results. Due to the experimental difficulties associated with radioactive materials, information for many cations in condensed phase is scarce,³² hindering empirical potential development. *Ab initio* data can be obtained and force fields can be systematically improved by adding ion-water structures to the model potential energy surface and by increasing the level of theory.

Guilbaud and Wipff³³ pioneered in $[\text{UO}_2]^{2+}$ force field development in the 1990's. Their model is empirical and was fitted to reproduce the hydration free energy of the molecular cation. Kerisit and Liu updated the model changing the partial charges in order to reproduce a more recent value of hydration free energy.³⁴

Ab initio force fields have also been published. Hagberg *et al.*³⁵ used the NEMO approach³⁶ to generate intermolecular potentials from multireference QM computations and carried out molecular dynamics (MD) simulations. In this work the importance of introducing charge transfer terms to describe

^{a)}Electronic mail: sanchez@us.es

the hydrate of a doubly charged ion in solution, such as uranyl, was shown. Maginn *et al.*^{37,38} considered the importance of polarization and other many-body effects in the binding of water molecules to the cation. They developed another first-principles force field for uranyl by parameterizing the interaction energies of the cation in the presence of four hydration water molecules.

Bühl *et al.*³⁹ obtained interesting results associated with the dissociation process of one water molecule from the uranyl hydrate in solution by Car-Parrinello MD,⁴⁰ showing the predominance of the penta-coordination of uranyl with respect to the tetra-coordination. Nichols *et al.*⁴¹ ran a similar simulation, using an ensemble of snapshots to satisfactorily predict the EXAFS spectrum of uranyl. Frick *et al.*⁴² used a QM/MM Hartree-Fock-Mulliken charge Hamiltonian to carry out an MD simulation in which they studied the angularly resolved radial distribution functions.

All these theoretical studies along with experimental evidence^{3,43} establish a first hydration shell of five water molecules with an average D_{5h} symmetry and an experimental residence time longer than 1 μ s.^{44,45} Classical force fields have always underestimated this exchange rate by several orders of magnitude (unless particular constraints are imposed⁴⁶) and typically display water exchange. The exchange should not happen since it has an experimental period longer than the simulation time.

Most *ab initio* ion force fields are pairwise and based on the interaction of a dimer, the ion, and a single water molecule. One of the problems of the dimer description is an overestimation of the interaction as a consequence of the electrical polarization of a single solvent molecule by the cation. Maginn *et al.* showed that effective pair-wise interaction potentials are necessary to study $[UO_2]^{2+}$ in aqueous solution.³⁷ Also, for highly charged cations, the true dissociation limit of the aggregate $[M(H_2O)]^{m+}$ usually is the charge transfer state $M^{(m-1)+} + H_2O^+$ instead of the required $M^{m+} + H_2O$.⁴⁷ In addition, the electronic state of *d* and *f* series metals with partially filled orbitals can be altered during the computation of the scans needed to collect QM interaction energies for the intermolecular potential fit, since the water-ion distance has to be changed significantly.

The general and cheapest strategy to model ion-water interactions in classical MD is to represent the ion as a charged particle with a Lennard-Jones potential to incorporate van der Waals interactions (a “charged soft sphere” model). This model has the advantage of being very simple and straightforward to transfer to other systems using Lorentz-Berthelot combination rules, but has limited accuracy. For instance, it neglects charge transfer and the polarization effects on the first-shell water molecules. In addition, it treats the interaction of the first-shell water molecule with the bulk solvent as equivalent to the interactions inside the bulk, neglecting the polarization that first-shell molecules are subjected to.

The model was developed by Maginn *et al.*³⁷ and was included in their force field fitting QM structures containing $[UO_2]^{2+}$ and several solvation water molecules. In this way they depart from the dimer approach and for transferability use the “charged soft sphere” representation. Even though the first-shell exchange rates are several orders of magnitude high with

respect to experiment,⁴⁶ the model overall reproduces experimental data and gives insight into the nature of the solution.

We have taken a new step forward modelling $[UO_2]^{2+}$ as a hydrated ion which parameterizes the *ab initio* interaction of bulk water with the pentahydrate. Several years ago, our group proposed^{48–51} a specific strategy to build first-principles intermolecular potentials of highly charged metal cations in water on the basis of the old electrochemistry concept of the *hydrated ion*. It states that most metal and highly charged monatomic cations (M^{n+}) in aqueous solutions are better represented by their hydrated ion, $[M(H_2O)_n]^{n+}$.⁴⁴ The implementation of the hydrated ion concept reasonably describes structural, dynamical, energetic, and spectroscopical properties of aqueous solutions containing metal cations forming well defined *aquaions* in water.^{49,51–53} A second step was achieved when square-planar aquaions, such as $[Pd(H_2O)_4]^{2+}$ and $[Pt(H_2O)_4]^{2+}$, were studied.^{54,55} We observed that the region above and below the water molecule plane differs from the conventional first or second-shell hydration behavior. The *meso-shell* concept was proposed to describe this region.⁵⁴ For the hydrated actinyls, there are formal topological similarities with the square-planar aquaions, placing actinyl oxygens above and below the plane. There is asymmetry around the central cation, since the axial regions are quite different from the equatorial region that accommodates the first hydration shell. The aim of this work is to provide a global image of $[UO_2(H_2O)_5]^{2+}$ hydration using MD implementation of an *ab initio* force field based on the hydrated ion model.

II. METHODS

A. Hydrated ion model potential for uranyl

The implementation of the hydrated ion concept assumes there are two different types of water molecules in solution.^{48,49,56} Those of the first-shell bearing strong polarization effects and partial charge transfer from their direct interaction with the metal cation, and the rest of the water molecules belonging to the bulk solvent. Therefore, two different ion-water interaction potentials must be defined: IW1, (ion-water of the 1st shell) dealing with the ion-first-shell water molecules, and HIW, (hydrated ion-water) which describes the interaction of the hydrated ion with the bulk water molecules. Figure 1 displays a schematic representation of the regions where the different interaction potentials apply. The benefit of a refined discrimination among the first-shell and bulk water molecules has a price to pay, the water molecules of the first shell cannot exchange with the bulk water molecules. They are assumed to remain in the first shell, then this model precludes the analysis of the water exchange. Therefore, the validity of this hydrated ion model is constraint to the description of stable metal aquaions whose lifetimes are greater than simulation time. Additional to the ion-water potentials, a water model is chosen to describe the water-water interactions in the bulk. In the first shell these water-water interactions are given by the QM partial charges and the bulk water van der Waals interaction. Details of the previous development can be found elsewhere.^{50,51,56} In the case of the uranyl, an intramolecular potential for the cation is necessary, hereafter called IMC (Intra Molecular Cation), to make $[UO_2]^{2+}$ flexible.

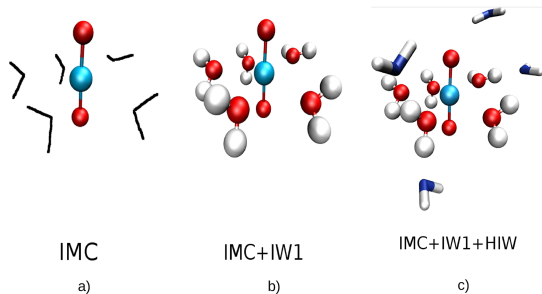


FIG. 1. Schematic representation of the different potentials describing uranyl in water. The intramolecular cation potential (IMC, (a)) corresponds to the interaction within the molecular cation. The ion-1st-shell water potential (IW1, (b)) describes the interaction of the first shell and the uranyl. The hydrated ion water potential (HIW, (c)) defines the interaction of bulk water molecules and $[\text{UO}_2(\text{H}_2\text{O})_5]^{2+}$.

QM calculations at the B3LYP level^{57,58} were used to compute the interaction energies, E_{int} , needed to build all the interaction potentials as well as the geometry optimization for the reference structure. The relativistic effective core pseudopotentials (RECP) of the Stuttgart group were used for the uranium atom with the recommended basis sets⁵⁹ [$12s11p10d8f2g]/[8s7p6d4f2g]$. The aug-cc-pVDZ basis set was employed for the rest of the atoms.⁶⁰ Several authors have shown that this hybrid functional method gives for uranyl reliable results at low computational cost.^{17,21,27} All these calculations have been performed with the Gaussian09 program.⁶¹

The basic unit for the development of the different potentials is the pentahydrated uranyl(vi) ion, $[\text{UO}_2(\text{H}_2\text{O})_5]^{2+}$, since it has been proposed to be the most stable aquaion^{6,39,62,63} even though an equilibrium with the tetrahydrate has also been suggested.⁶² The reference structure is obtained by QM geometry optimization enforcing D_{5h} symmetry. The effective partial charges on the different atoms are obtained by the Merz-Kollman method^{64,65} using the polarizable continuum model^{66,67} to represent the bulk solvent polarization in the DFT calculation. Batsanov's radii for U were used to compute the charges.⁶⁸ The partial charges used are given in Table S1 of the supplementary material.

The intermolecular potential IW1 (E_{IW1}) describes the $\text{UO}_2-(\text{H}_2\text{O})_1$. The QM energy information to fit this potential is obtained from a set of 150 structures taken from the displacement of $\text{U}-(\text{H}_2\text{O})$ distance for one of the first-shell water molecules in the range 2.10–3.10 Å, and deformations of the $[\text{UO}_2]^{2+}$ following the stretching normal vibrational modes (symmetric and asymmetric) for $\text{U}-\text{O}_{\text{yl}}$ bond-lengths of 1.55–1.85 Å, and the bending normal mode in the range 180°–150°. A schematic representation of the deformations is given in Figure S1 of the supplementary material. The QM interaction energy for a given structure i is obtained from the following expression:

$$E_{\text{int}}^i = E_{[\text{UO}_2(\text{H}_2\text{O})_5]^{2+}}^i - E_{\text{UO}_2^{2+}}^i - 5E_{(\text{H}_2\text{O})_1}. \quad (1)$$

These interaction energies, E_{int}^i , can be decomposed into two terms, one of them corresponding to the actinyl-water molecules interaction, i.e., E_{IW1} , and the other to the water molecules among them. Then Equation (2) associates the QM

interaction energy and the classical intermolecular potentials,

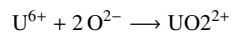
$$E_{\text{int}} = E_{\text{IW1}} + E_{(\text{H}_2\text{O})_1-(\text{H}_2\text{O})_1}. \quad (2)$$

$E_{(\text{H}_2\text{O})_1-(\text{H}_2\text{O})_1}$ is computed using for the electrostatic part the Merz-Kollman charges of the hydrated ion (Table S1 in the supplementary material) and the short-range term of the TIP4P water model. The *ab initio* interaction energy of actinyl-first-shell water molecules is then fitted to the following site-site pair potential functional form:

$$E_{\text{IW1}} = \sum_i^{\text{UO}_2 \text{ sites}} \frac{C_4^{\text{iO}}}{r_{\text{iO}}^4} + \frac{C_6^{\text{iO}}}{r_{\text{iO}}^6} + \frac{C_8^{\text{iO}}}{r_{\text{iO}}^8} + \frac{C_{12}^{\text{iO}}}{r_{\text{iO}}^{12}} + \sum_i^{\text{UO}_2 \text{ sites}} \sum_j^{\text{Water sites}} \frac{q_i q_j}{r_{ij}}. \quad (3)$$

Charges and coefficients of the fitting and root mean square error (RMSE) are given in Table S2 of the supplementary material.

The flexibility of uranyl is described by the IMC interaction potential, which models the actinyl as three particles, the two O_{yl} and the uranium cation, U(vi). The interaction energy among these three particles is computed as the formation energy of the molecular cation



The QM energy for the actinyl cation $E_{\text{UO}_2^{2+}}^i$ in one of the distorted structures used to compute E_{int}^i for the IW1 potential could be decomposed as a sum of the absolute energy of the separated atoms and the interaction energy among them,

$$E_{\text{UO}_2^{2+}}^i = E_{\text{U}^{6+}} + 2E_{\text{O}^{2-}} + E_{\text{int}}^i(\text{UO}_2^{2+}). \quad (4)$$

In this way the total interaction energy including the flexibility of the actinyl cation can be written by the following expression:

$$E_{\text{int}}^{\text{tot}} = E_{[\text{UO}_2(\text{H}_2\text{O})_5]^{2+}} - E_{\text{U}^{6+}} - 2E_{\text{O}^{2-}} - 5E_{(\text{H}_2\text{O})_1}, \quad (5)$$

where $(\text{H}_2\text{O})_1$ denotes a water molecule with the geometry of the first hydration shell. This total interaction energy may be now split into three intramolecular components,

$$\begin{aligned} E_{\text{int}}^{\text{tot}} &= E_{\text{int}} + E_{\text{int}}^i(\text{UO}_2^{2+}) \\ &= E_{\text{IMC}} + E_{\text{IW1}} + E_{(\text{H}_2\text{O})_1-(\text{H}_2\text{O})_1}. \end{aligned} \quad (6)$$

From this relationship, we derive the intramolecular interaction energy for the molecular cation in a given geometry,

$$E_{\text{IMC}} = E_{\text{int}}^{\text{tot}} - (E_{\text{IW1}} + E_{(\text{H}_2\text{O})_1-(\text{H}_2\text{O})_1}). \quad (7)$$

In this way, the intramolecular interaction inside the uranyl cation is associated with the change in the formation energy of the actinyl from their corresponding monatomic charged ions. This way of defining E_{IMC} guarantees the coupling among the different potentials. Making use of the hydrated ion concept, the flexibility of UO_2^{2+} is computed inside the hydrated ion, extracting the changes in the relative energy of the actinyl unit in the presence of the first-shell water molecules. The different deformation geometries lead to a set of values for E_{IMC} to be fitted to the following functional form:



—

$$E_{\text{IMC}} = \sum_i^{\text{O}_{\text{yl}} \text{ sites}} \left(\frac{C_4^{\text{AnO}_{\text{yl}}}}{r_{\text{AnO}_{\text{yl}}}^4} + \frac{C_6^{\text{AnO}_{\text{yl}}}}{r_{\text{AnO}_{\text{yl}}}^6} + \frac{C_8^{\text{AnO}_{\text{yl}}}}{r_{\text{AnO}_{\text{yl}}}^8} + \frac{C_{12}^{\text{AnO}_{\text{yl}}}}{r_{\text{AnO}_{\text{yl}}}^{12}} \right) \\ + \sum_i^{\text{O}_{\text{yl}} \text{ sites}} \frac{q_{\text{An}} q_{\text{O}_{\text{yl},i}}}{r_{\text{AnO}_{\text{yl},i}}}. \quad (8)$$

Coefficients of the fitting and RMSE are given in Table S3 of the [supplementary material](#).

To fulfill the description of the system, the interaction between the bulk water molecules and the hydrated actinyl must be considered, i.e., $[\text{UO}_2(\text{H}_2\text{O})_5]^{2+}-\text{H}_2\text{O}$, the HIW potential. No other force field for $[\text{UO}_2]^{2+}$ in the literature has given a specific first shell-second shell water interaction potential, the other strategies approximate this interaction by the bulk-bulk water interaction. A probe water molecule is placed at different distances and orientations with respect to the actinyl aquaion as shown in Figure 2. Around 1000 single QM points have been computed to get the interaction of a bulk water molecule with the aquaion

$$E_{\text{int}} = E_{[\text{UO}_2(\text{H}_2\text{O})_5]^{2+}-\text{H}_2\text{O}} - E_{[\text{UO}_2(\text{H}_2\text{O})_5]^{2+}} - E_{\text{H}_2\text{O}}. \quad (9)$$

Apart from the ion-dipole orientation of the probe water molecule plotted in Figure 2, three additional orientations with hydrogen atoms partially or completely pointing out to the actinide cation were included in the potential energy surface scan. The set of structures was fitted to the following site-site functional form which has been shown to behave properly in the description of the interaction of other highly charged metal cation hydrates with water molecules.^{50,51,69} The addition of two extra terms (r^{-4} , r^{-8}) to the usual Lennard-Jones formulation allows more flexibility to describe the short- and medium-range interactions in the less attracting environment close to the aquaion as the intermediate regions,

$$E_{\text{HIW}} = \sum_i^{\text{Water sites}} \sum_j^{\text{Water sites}} \left(\frac{C_{ij}^{ij}}{r_{ij}^4} + \frac{C_{ij}^{ij}}{r_{ij}^6} + \frac{C_{ij}^{ij}}{r_{ij}^8} + \frac{C_{ij}^{ij}}{r_{ij}^{12}} + \frac{q_i q_j}{r_{ij}} \right). \quad (10)$$

Fitting coefficients and RMSE are given in Table S4 of the [supplementary material](#).

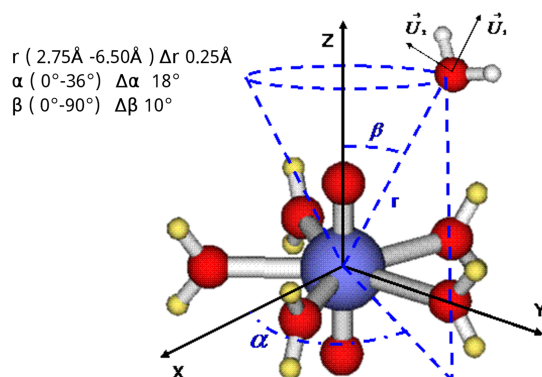


FIG. 2. Intermolecular geometrical parameters scanned in developing the HIW potential $[\text{UO}_2(\text{H}_2\text{O})_5]^{2+}-\text{H}_2\text{O}$.

Once described the methodology proposed to build the set of intermolecular potentials of the uranyl cation in water, it is worth underlining the fact that the procedure is independent of the QM calculation level. This means that the choice of the computational level for a given molecular cation must be determined by the cost/accuracy ratio as a function of the physicochemical properties to be studied.

B. Molecular dynamics simulations

MD simulations were run using the DL_POLY4 package.⁷⁰ The system was composed of one $[\text{UO}_2(\text{H}_2\text{O})_5]^{2+}$ and 1495 TIP4P⁷¹ H_2O which corresponds to a concentration $\sim 0.04 \text{ mol kg}^{-1}$. Simulations were run using a 14 Å cutoff for short-range interactions and particle mesh Ewald for the long-range Coulomb interactions. A 1 fs time step was used. The equations of motion were integrated using the velocity Verlet⁷² and the NOSQUISH⁷³ quaternion algorithms. The system was initially minimized and then thermalized to 300 K for 0.5 ns with the Hoover thermostat. Then, a 0.5 ns NPT equilibration trajectory at 300 K and 1 bar was run using the Hoover barostat and thermostat with characteristic times of 0.5 ps on both. Finally, a 5 ns production run was performed. The final average density of the system was 1.001 g cm^{-3} .

III. RESULTS AND DISCUSSION

A. Hydration enthalpy

The hydration enthalpy (ΔH_{hyd}) of $[\text{UO}_2]^{2+}$ was computed according to

$$\Delta H_{\text{hyd}} = H_{[\text{UO}_2]^{2+}(\text{aq})} - H_{\text{H}_2\text{O}} - H_{[\text{UO}_2]^{2+}(\text{g})}. \quad (11)$$

The different enthalpy values correspond to the average simulation enthalpy of: the aquaion in a box with 1495 water molecules, an equilibrated water box with the same total number of H_2O molecules and $[\text{UO}_2]^{2+}$ in gas phase.

Our estimation of $\Delta H_{\text{hyd}}(\text{UO}_2^{2+})$ is $-333 \pm 14 \text{ kcal mol}^{-1}$ which is within the range of experimental data. From the literature, an experimental ΔH_{hyd} interval between $-401 \pm 15 \text{ kcal mol}^{-1}$ obtained by Gibson *et al.*⁷⁴ and $-325 \pm 5 \text{ kcal mol}^{-1}$ given by Marcus⁷⁵ is defined. The difficulties associated with the accurate quantification of gas phase formation enthalpy of actinides may be behind this substantial gap between experimental measurements.⁷⁶

The TIP4P water model aside, we must point out that the $H_{[\text{UO}_2]^{2+}(\text{aq})}$ estimation might be missing a small many-body contribution due to the first-second shell hydration.⁴⁹ Therefore, our ΔH_{hyd} could be slightly overestimated, which suggested that our theoretical estimation is much closer to Marcus' value.

B. Hydration structure of uranyl in aqueous solution

The uranium-oxygen RDF (Figure 3) shows three well defined peaks. The two first sharp peaks correspond to the two O_{yl} and the five first shell oxygen atoms, O_{l} , at 1.76 Å and 2.46 Å, respectively. The third peak centered at 4.62 Å and extending up to ~ 6 Å corresponds to the second hydration shell.

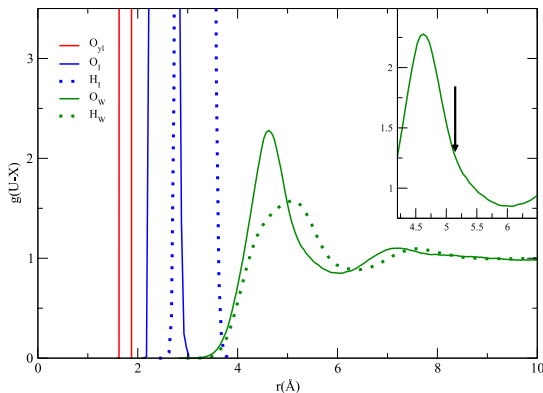


FIG. 3. U–O (solid lines) and U–H (dotted lines) radial distribution functions. Oxo oxygens (red), O_{y1}, first-shell H_I and O_I (blue) and second-shell H_w and O_w (green).

The main structural results in the literature and those of this study have been summarized in Table I. Our results are within the range of values for the U–O_{y1}, U–O, and U–H distances in the literature. In particular, they are quite similar to those reported by Bühl *et al.* from their CPMD simulation⁷⁷ and agree quite well with the experimental values reported from different techniques.^{3,7,43,78}

The solvent effects on the $[UO_2(H_2O)_5]^{2+}$ induce opposite effects on the U–O bonds: the U–O_{y1} bond-length is increased from 1.75 Å in gas phase to an average value of 1.76 Å in solution but the U–O_I is shortened from 2.50 Å in the isolated cluster to 2.46 Å in solution. CPMD simulations⁷⁷ and QM studies^{21,31} when a second hydration shell is added to the metal hydrate show the same effect.

The running coordination number (CN) of the second hydration shell obtained using the U–O_w RDF (Figure 3) is 29. This striking value compelled us to revise the analysis. For most highly charged monatomic cations, it is a number slightly bigger than twice the CN of the first shell, because, on average, they can form two hydrogen bonds (HB) with two different second-shell water molecules and some additional packing water molecules.^{32,44,51} However, we obtain three times this value. Due to the non-spherical symmetry of uranyl, one could wonder if the second peak in the RDF collects

non-second-shell water molecules which artificially increase the CN.

The molecular axis formed by the U–O_{y1} bonds and the perpendicular plane defined by the first-shell oxygen water molecules allow us to examine contributions to U–O_w (and U–H_w) RDFs from different regions around the hydrated uranyl. Figure 4(b) plots the three selected regions: the equatorial one corresponds to the volume obtained by the rotation of the generatrix with azimuthal angles in the range 60°–90°; the axial region corresponds to the cone obtained when the azimuthal angle is 0°–30°, and the intermediate region corresponds to the volume obtained by the angles 30°–60°. A detailed description of this type of decomposition of the total RDF in angle-solved contributions can be found elsewhere.⁸² Figure 4(a) plots the U–O_w and U–H_w angle-solved distribution functions. The maxima corresponding to the second-shell peak appear at 4.65 Å for the equatorial region, 4.35 Å for the intermediate region, and 4.85 Å for the axial region with integration numbers (for both hemispheres) of 10, 12, and 4, respectively. The relative position of the peak for the U–H_w partial RDFs indicates that the water molecules in the equatorial region follow mainly an ion-dipole orientation since their tilt angle is close to 180°. This value is reduced in the intermediate region and the U–H_w maximum appears at a shorter distance than the U–O_w in the axial region. The peak minimum for the axial and intermediate regions appears at 6.0–6.4 Å which is about 1 Å higher than in the equatorial region (~5.3 Å). Thus, the second-shell minimum of the total RDF (~6.0 Å in Figure 3) encompasses not only the water molecules interacting with the first shell but additionally the O_{y1} solvation. The equatorial RDF integrates to a number of H₂O molecules which correspond to the typical hydration of monatomic cations. Furthermore, if we compute the average number of HB of the first-shell water molecules with second-shell water molecules (according to Chandler's definition⁸³) we obtain 1.9 per water molecule, i.e., the classical cation hydration picture.

There is some discrepancy on the structure adopted by the solvent in the axial region. Wipff and Guibaud^{33,79} and Keristi and Liu³⁴ from MD using empirical interaction potentials, and Siboulet *et al.*²¹ from QM computations found one hydrogen atom at around 1.8 Å from the uranyl oxygen forming typical hydrogen bonding. On the contrary, Roos *et al.*³⁵ and Maginn *et al.*^{37,38} with classical MD using *ab initio* potentials;

TABLE I. Structural parameters corresponding to the hydration of $UO_2^{2+} \cdot n H_2O$ water derived from different experimental and theoretical sources. Distances are given in Å.

Source	R(U–O _{y1})	R(U–O _I)	N _I	R(U–O _{II})	N _{II}	R(U–H _I)	R(U–H _{II})	R(O _{y1} –O)	R(O _{y1} –H)
This work	1.76	2.46	5 ^a	4.62	22 ^b	3.13	5.09	3.43	5.9
CPMD ^{41,42,77}	1.77–1.81	2.44–2.48	5	4.59–4.6	14–16				
<i>Ab initio</i> CMD ^{35,37,38}	1.71–1.76	2.40–2.46	5	4.6–4.7	16–19			3.0	3.7
Empirical CMD ^{33,34,79}	1.80–1.89	2.40–2.5	5	4.3–4.7	15–19		5.2 ^c	2.96–3.01	1.8–2.08
QM gas phase clusters ^{21,80}	1.77–1.79	2.42–2.43	5 ^a	4.5–4.6	10 ^a			1.8–1.92	
High energy x-ray scattering ^{3,7}	1.702–1.77	2.42	5 ^d	4.46	15				
EXAFS ^{43,78}	1.76	2.41	5.2–5.3						

^aFixed value.

^bUsing the multisite solute hydration number definition.⁸¹

^cN_H = 31–42.

^dAn equilibrium 88:12 five:four coordination is proposed.

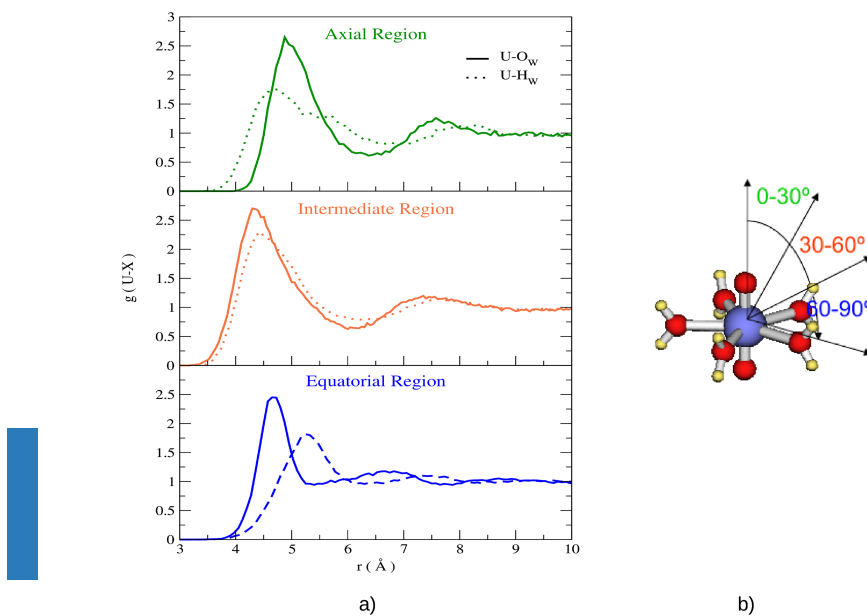


FIG. 4. (a) shows the RDF for the axial region (0° - 30°), the intermediate region (30° - 60°), for the equatorial region (60° - 90°). $g(U-O_w)$ (solid lines) and $g(U-H_w)$ (dotted lines). (b) defines the hydration angular regions.

Bühl *et al.*,⁷⁷ Frick *et al.*,⁴² and Nichols *et al.*⁴¹ using *ab initio* MD did not find preferential HB formation; furthermore, a low density number region is obtained, which led them to propose a rather *hydrophobic* behaviour in the uranyl axial region.

Our model clearly supports the non-hydrophilic structure of the axial region. In the 0° - 90° O_{yl} angle solved RDF (Figure 5(b)) the H and O first peak overlap. If the O_{yl} atom had anionic character, the H maximum would be closer to the reference atom than the O maximum due to the formation of a H bond. The Spatial Distribution Function (SDF)⁵⁴ of the simulation is displayed in Figure 6. Water molecules occupy mainly the equatorial and intermediate regions, and the axial region is de-populated. Each axial region contains an average of 2.5 molecules at a distance of 3.35 Å. A snapshot of the simulation in Figure 7 depicts the hydration in that region. Axial water molecules H-bond preferentially

among them than to the O_{yl} atom, this reinforcement of the water structure is a typical characteristic of the hydrophobic hydration.^{84,85} The SDF also shows that the hydration structure of $[UO_2(H_2O)_5]^{2+}$ resembles a sphere with the poles cut due to the lack of hydration of the O_{yl} atoms.

The fact that the intermolecular potentials developed are based on the explicit QM assumption of a hydrated uranyl as the key species in solution allows a fine tuning of the interactions of the first and second hydration shell with the molecular cation and among them. This gives an even-tempered description of all the interactions in the close environment of the uranyl. As a result, it is found that the axial hydration mainly adopts a solvent structure, slightly perturbed by the presence of the uranyl oxygen and the cation charge, whereas in the equatorial region the strongly polarized uranyl-first shell water mediated an ordered second-shell structure in its environment.

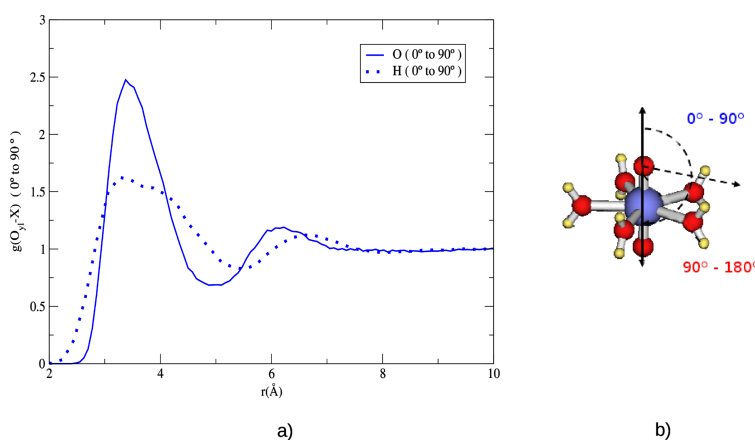


FIG. 5. (b) shows the RDF for the 0° - 90° . (a) defines the hydration angular regions. $g(O_{yl}-O)$ (solid lines) and $g(O_{yl}-H)$ (dotted lines).

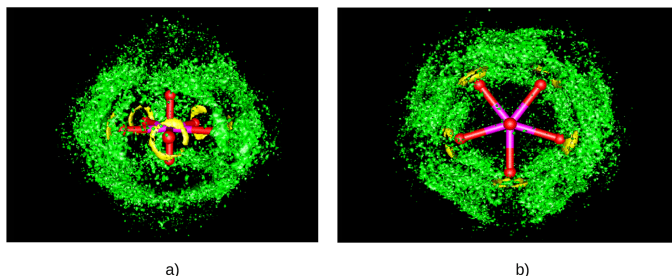


FIG. 6. $[UO_2(H_2O)_5]^{2+}(aq)$ spatial distribution function from the MD simulation: first shell H probability density (yellow) and bulk O water probability density (green). The isodensity surfaces contain 20% of the total probability.

The CNs of the second shell obtained with high energy x-ray scattering and most MD simulations are quite smaller than the value obtained from the total U–O_w RDF integration. Nevertheless, this high value is a direct consequence of using a radial distribution function that is spherically averaged to measure coordination in non-spherically symmetric environments. Our RDFs are complex, for example, having an inflection point at ~ 5 Å in the U–O_w RDF (see inset in Figure 3). Its integration assigns bridge water molecules to the coordination of O_{y1} and O_t artificially. The computation of the solute CN based on the multisite cavity definition developed by our group for asymmetric coordination environments avoids this artifact.⁸¹ This CN is defined as the average number of water molecules within the cavity formed by the overlapping of spheres centered on solvent exposed atoms (O_t and O_{y1}, in our case), whose radii correspond to the minima of angle-solved X–O_w RDFs. Employing this definition, we obtain a second coordination shell value of 22 which is closer to the range of literature values and is consistent with our angle-solved analysis. In order to test this multisite cavity method and the intermolecular potentials developed, a similar MD simulation to the one presented here was carried out using the potential of

Maginn *et al.*³⁷ The multisite-cavity CN was in this case 20, and the cavity volume was 730 \AA^3 , whereas our cavity had a volume of 697 \AA^3 . Figure 8 shows the solute multisite-cavity that encloses the water molecules counted to obtain the CNs. Finally, the second-shell CN in high energy x-ray scattering experiment can only be considered a lower bound of the value for a dilute solution because the samples have an $UO_2(ClO_4)_2$ concentration of 0.5 mol kg^{-1} .

C. Water mean residence time

In Table II we present the mean residence time (MRT) of solvent molecules in the second shell computed by the method of Impey *et al.*⁸⁶ The MRT of a water molecule in the first shell of another water molecule in a TIP4P water simulation is included for comparison. We allow two possible time intervals (t^*) for the water molecule to leave the shell and return still ascribing it to the shell, $t_{2ndshell}^* = 0 \text{ ps}$ and $t_{2ndshell}^* = 2 \text{ ps}$. These values are generally accepted to provide a good range in the literature.^{86,87} We have also studied the residence times in the regions defined by the angle-solved distribution functions defined in Figure 5.

The total MRT of a water molecule in the $[UO_2]^{2+}$ second shell has a value of 8 and 17 ps for $t_{2ndshell}^* = 0 \text{ ps}$ and $t_{2nd}^* = 2 \text{ ps}$, respectively. The MRT is much higher than the 0.4 ps and 5.6 ps obtained in QMCF *ab initio* MD by Frick *et al.*⁴² Additionally, our value is greater than that for other divalent cation aqueous solutions like that of Mg^{2+} having values of 3 ps and 14 ps.⁵¹ This is likely due to the much higher volume of the second hydration shell of a molecular cation, such as $[UO_2]^{2+}$. The comparison of the angle-solved and the total MRT shows that

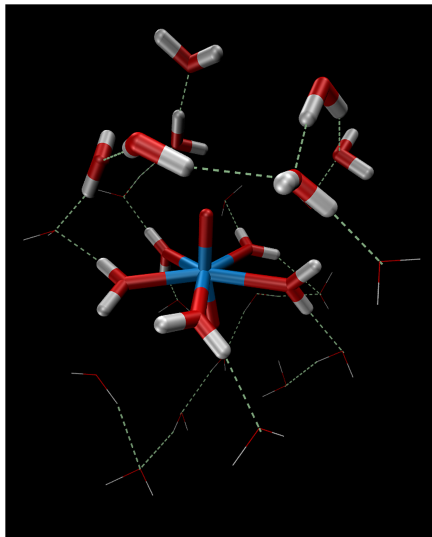


FIG. 7. $[UO_2(H_2O)_5]^{2+}$ MD snapshot showing only some water molecules with an axial view and HB according to Chandler's definition.⁸³

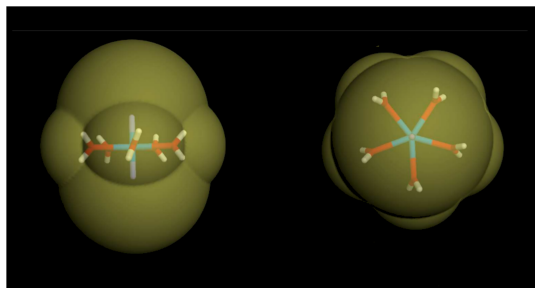


FIG. 8. Multisite solute cavity for the hydrated ion model of $[UO_2(H_2O)_5]^{2+}$ with a volume of 697 \AA^3 .

TABLE II. Mean residence times (ps) of H_2O in the second shell of $[\text{UO}_2]^{2+}$ with maximum transient period out of the shell $t^* = 0$ ps and $t^* = 2$ ps and its decomposition in the angular regions of Figure 4(a). For comparison the MRT of TIP4P water in the first shell of another water molecule in a pure water simulation is included.

Region	$t_{2\text{ndshell}}^* = 0$ ps	$t_{2\text{ndshell}}^* = 2$ ps
Total MRT (2nd shell)	8 ± 1	17 ± 1
$0^\circ\text{-}30^\circ$ (2nd shell)	1 ± 1	6 ± 1
$30^\circ\text{-}60^\circ$ (2nd shell)	1 ± 1	8 ± 1
$60^\circ\text{-}90^\circ$ (2nd shell)	2 ± 1	10 ± 1
H_2O (1st shell)	1.39 ± 0.02	4.19 ± 0.06

the equatorial second shell has lower exchange rates with bulk solvent molecules than the axial second shell. Solvent motion within the different angular regions of the second shell explains the difference between total and partial MRTs.

The solvent MRT in the axial regions is higher than in the first-shell of a bulk water molecule. This indicates that the water-water interactions around the hydrophobic O_{yl} region are reinforced with respect to solution. The enhancement of the water structure around a hydrophobic solute is a dynamical characteristic of a clathrate-like hydration.^{84,85}

D. Self-diffusion coefficient

The self-diffusion coefficient, D_0 , for the $[\text{UO}_2(\text{H}_2\text{O})_5]^{2+}$ in the MD simulation was computed using the Einstein formula. An initial value of $(0.8 \pm 0.1) 10^{-5} \text{ cm}^2 \text{ s}^{-1}$ was obtained. Due to the use of periodic boundary conditions, diffusion coefficients from MD simulations are always underestimated. The neighboring images of each atom couple viscously reducing their motion and reducing D_0 . This effect can be corrected for a cubic cell using the Yeh and Hummer expression,⁸⁸

$$D_0^{\text{corr}} = D_0 + \frac{k_B T \xi}{6\pi\eta L}, \quad (12)$$

where η is the solvent viscosity, L the average simulation box size, and ξ the so called self-term which for a cubic lattice at room temperature is 2.837 298. Using the TIP4P water viscosity at 300 K, a $D_0^{\text{corr}} = (1.1 \pm 0.1) 10^{-5} \text{ cm}^2 \text{ s}^{-1}$ value is obtained. The experimental self-diffusion coefficient for $[\text{UO}_2]^{2+}$ at infinite dilution is $(0.67 \pm 0.01) 10^{-5} \text{ cm}^2 \text{ s}^{-1}$.^{89,90} The simulated value only has the right order of magnitude of the experimental. The TIP4P water model overestimates the self-diffusion coefficient of water by ~50%; therefore

TABLE III. Normal mode frequencies, $\bar{\nu}$ (cm^{-1}) for $[\text{UO}_2(\text{H}_2\text{O})_5]^{2+}$ with different models and experiment. The uncertainties in our theoretical results are $\pm 5 \text{ cm}^{-1}$.

System	Method	E_1	2A_1	1A_1	A_2
$[\text{UO}_2(\text{H}_2\text{O})_5]^{2+}(\text{g})$	B3LYP	224	314	945	1028
$[\text{UO}_2(\text{H}_2\text{O})_5]^{2+}(\text{g})$	MD 5 K	181	298	982	1080
$[\text{UO}_2(\text{H}_2\text{O})_5]^{2+}(\text{g})$	MD 300 K	256	286	977	1027
$[\text{UO}_2(\text{H}_2\text{O})_5]^{2+}(\text{aq})$	MD 300 K, 1 bar	252	338	1004	1101
$[\text{UO}_2(\text{H}_2\text{O})_5]^{2+}(\text{aq})$	Experimental	253 ± 10^{93}		$874 \pm 10^{93,94}$	965 ± 10^{94}

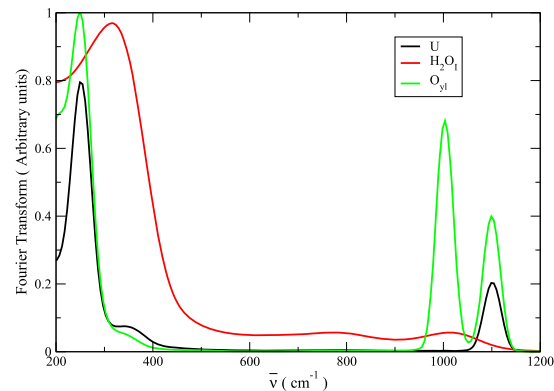


FIG. 9. Power spectra of the velocity autocorrelation function of the U , O_{yl} , and H_2O_1 atom types of the MD simulation.

since the water molecules around the cation move too fast, the cation is more free to move than if the water dynamics was more accurate. A usual correction, employed by several authors,^{34,46,91} is the normalization of the obtained diffusion coefficient by the pure water model diffusion coefficient, in our case $D_0^{\text{corr}}/D_0^{\text{TIP4P}} = 0.4 \pm 0.1$. This value is close to the normalized experimental diffusion coefficient, $D_0^{\text{exp}}/D_0^{\text{wat}} = 0.3 \pm 0.01$, revealing that our $[\text{UO}_2]^{2+}$ dynamics is partly biased by the water model diffusion.

E. Power spectra

The power spectra of the velocity autocorrelation (VAC) functions of the atoms of $[\text{UO}_2(\text{H}_2\text{O})_5]^{2+}$ from the simulation trajectory have been computed and plotted in Figure 9. To make easier the assignment of the bands, internal coordinates associated with a particular normal mode have been defined.^{51,92} For the $[\text{UO}_2]^{2+}$ bending motion, with irreducible representation E_1 , ϕ was defined as the $\text{O}_{\text{yl}}\text{-U-O}_{\text{yl}}$ angle and its cosine function used to compute its autocorrelation function,

$$\langle (\cos(\phi) - \overline{\cos(\phi)}) \cdot (\cos(\phi) - \overline{\cos(\phi)}) \rangle. \quad (13)$$

The Fourier transform of the autocorrelation function is performed to obtain the normal mode frequencies. The rest of the internal coordinates for the symmetric (1A_1) and antisymmetric (A_2) U-O_{yl} stretching as well as the water breathing symmetric U-O_1 stretching (2A_1) are defined in the [supplementary material](#). Table III presents the frequencies obtained with several simulation conditions and models, together with experimental data.

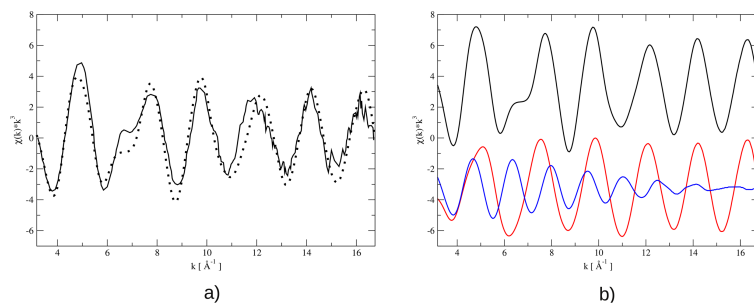


FIG. 10. $[\text{UO}_2(\text{H}_2\text{O})_5]^{2+}$ L_{III}-edge k^3 -weighted EXAFS spectra. (a) Experimental⁴³ 0.01M $[\text{UO}_2]^{2+}$, 0.1M HClO_4 EXAFS data (solid line), and simulated spectrum (dotted line). (b) Simulated spectrum (black), $\text{O}_{\text{y}1}$ path (red line) contributions to the simulated spectrum, and O_{i} path contributions (blue line) to the simulated spectrum.

The normal mode frequencies obtained in solution are close to the experimental ones, with a maximum 15% error for the $1A_1$. The fact that the stretching modes are overestimated is due in part to the B3LYP potential energy surface that biases our frequencies in that sense, particularly for $1A_1$ and A_2 , and to the performance of the intermolecular potentials developed.

The normal mode frequencies are a measure of the fit of the classical potential to the QM potential energy surface. It is worth pointing out that the interaction potential contains no harmonic terms, unlike the majority of force fields. Therefore, simulation frequencies contain all the anharmonicities that the surface presents since, unlike static standard QM methods, no harmonic model is assumed.

Bearing in mind these facts, the comparison of the $[\text{UO}_2(\text{H}_2\text{O})_5]^{2+}$ frequencies in gas phase using the B3LYP harmonic normal modes and those obtained from low temperature MD simulation (Table III) supports the good potential performance. Gas phase room temperature MD simulation frequencies shift with respect to their low temperature counterparts. This shifting is partly due to the anharmonicities of the potential energy surface explored at higher temperatures and to the coupling of the modes to the bulk water motion. Running the high temperature simulation with the water molecules frozen yields frequencies (not shown) nearly identical to those at low temperature, therefore, the coupling of the first shell water motions to the molecular cation normal modes is the main responsibility of the shifts.

The $[\text{UO}_2(\text{H}_2\text{O})_5]^{2+}$ frequencies obtained from MD simulations at 300 K in solution and in the gas phase have only small change for the modes involving uranyl, which reflects the small perturbation induced by solvation on the $[\text{UO}_2]^{2+}$ entity. Contrarily, the $\text{U}-\text{O}_{\text{i}}$ stretching is more affected in relative terms due to the second shell effects.

F. EXAFS spectrum simulation

X-ray absorption spectroscopy is a powerful technique to obtain accurate short range structural information around a metal ion in solution.^{95,96} The comparison between the experimental EXAFS spectrum of a given sample and the simulated one derived from a set of configurations extracted from a statistical computer simulation has become a useful tool for intramolecular potential assessment.^{52,97,98} The simulated EXAFS spectrum for uranyl in water has been computed as the average of the individual spectra of 200 configurations of $[\text{UO}_2]^{2+}$ including its two first coordination shells from the MD trajectory using the FEFF 9.0 code.⁹⁹ The average

L_{III} -edge k^3 -weighted spectrum including multiple scattering up to four-legged paths was computed. Figure 10 compares the simulated spectrum with the experimental spectrum of a 0.01M $[\text{UO}_2]^{2+}$ (aq) solution in 0.1 M perchloric acid.⁴³ Details of the method to simulate the EXAFS spectrum can be found elsewhere.^{52,69} The similarity between the main features of the simulated and experimental spectra validates our atomistic representation of the uranyl aqueous solution. The calculated spectra reproduce satisfactorily the experimental frequency, and slightly underestimate the signal decay. The spectrum is unchanged if only the first hydration shell is included in the calculations. This means that the second shell cannot be detected by EXAFS for this system.

We obtain Debye-Waller factors of $6.5 \cdot 10^{-4} \text{ \AA}^2$ and $6.8 \cdot 10^{-3} \text{ \AA}^2$ for $\text{U}-\text{O}_{\text{y}1}$ and $\text{U}-\text{O}_{\text{w}}$, respectively, which are close to the experimental values⁴³ of $1.6 \cdot 10^{-3} \text{ \AA}^2$ and $7.1 \cdot 10^{-3} \text{ \AA}^2$.

The shoulder at $\sim 6.5 \text{ \AA}^{-1}$ has a lower intensity in the simulated spectrum than in the experimental. To study this, we decomposed this complex spectrum into its $\text{U}-\text{O}_{\text{y}1}$ and $\text{U}-\text{O}_{\text{i}}$ contributions (together with multiple scattering paths where $\text{O}_{\text{y}1}$ and O_{i} backscatters are included) in Figure 10. Both contributions are produced mainly by the single-scattering paths. The $\text{U}-\text{O}_{\text{y}1}$ paths (red line) have a slow decay and high intensity due to the small disorder associated with the strong covalent bonds $\text{U}-\text{O}_{\text{y}1}$. In contrast, contributions due to the O_{i} involved paths (blue line) generate a weaker signal with a damped oscillation which decays faster than its counterpart. The frequency of the latter contribution is higher since the $\text{U}-\text{O}_{\text{i}}$ distance is larger than that of the $\text{U}-\text{O}_{\text{y}1}$ bond. The shoulder is a feature produced by the superposition of single scattering paths and not a multiple scattering phenomenon that other structures with planar backscattering configurations present.

IV. CONCLUDING REMARKS

We have extended the hydrated ion model for the development of intermolecular potentials to the case of molecular metal cation, including its flexibility. The set of intermolecular potentials represents correctly the model potential energy surface and the properties derived from the analysis of the MD trajectory are in agreement with experimental data. It is worth mentioning that the broad scope of spectroscopic, energetic, dynamical, and structural properties are well described. The second-shell CNs obtained from RDFs are overestimated since they count bridge water molecules and even third-shell

water molecules as the angle-solved RDFs have shown. Using the definition of a multisite cavity for the solute to compute the CN, the overestimated value is eliminated obtaining a CN closer to previously published results. These RDFs also show a very weak solvation of the O_{y1} atoms implying a hydrophobic behavior without preferential H bond formation with the solute, but reinforcement of the water network. This fact, in addition to the reinforcement of the axial water structure shown by the MRT, gives evidence of clathrate-like solvation around the O_{y1} atoms. Their weak solvation is also manifested by the absence of frequency shifts in the uranyl stretching and bending normal modes of the pentahydrate isolated or in solution. In contrast, the equatorial solvation structure resembles that of monatomic divalent cations. The hydration structure of the [UO₂]²⁺ cation is striking since its hydrophilic and hydrophobic regions are very close together on a small solute in contrast to most amphiphilic solutes. The intermediate hydration region contains a set of water molecules which fit both regions smoothly. The hydration structure of [UO₂]²⁺ is strongly anisotropical, being the result of coupling a conventional hydration sphere in the equatorial region with clathrate-like caps, mediated by bridge water molecules in the intermediate region. Based on previous experience with the hydrated ion model,⁵¹ the generalization of the set of intermolecular potentials for [UO₂]²⁺ in water could be easily extended to the series of actinyls, [AnO₂]^{q+}. Therefore, the set of new potentials presented here will be the starting point for the description of other actinyls in solution or confined condensed media, e.g., layered silicates.

SUPPLEMENTARY MATERIAL

See supplementary material for the atomic partial charges and Merz-Kollman radii; deformations of the pentahydrate to fit the force field; interaction potential coefficients and quality of fit parameters; and normal mode internal coordinate definition.

ACKNOWLEDGMENTS

This work was financially supported by Junta de Andalucía of Spain (Proyecto de Excelencia, No. P11-FQM 7607) and the Spanish Ministry of Education, Culture and Sports for the Ph.D. scholarship FPU (Formación de Profesorado Universitario) awarded to SPC.

- ¹S. Cotton, *Lanthanide and Actinide Chemistry* (Wiley, London, 2006).
- ²N. Bardin, P. Rubini, and C. Madic, *Radiochim. Acta* **83**, 189 (1998).
- ³M. Åberg, D. Ferri, J. Glaser, and I. Grenthe, *Inorg. Chem.* **22**, 3986 (1983).
- ⁴W. D. Loveland, D. J. Morrissey, and G. T. Seaborg, *Modern Nuclear Chemistry* (John Wiley & Sons, 2006).
- ⁵S. D. Conradson, *Appl. Spectrosc.* **52**, 252 (1998).
- ⁶U. Wahlgren, H. Moll, I. Grenthe, B. Schimmelpfennig, L. Maron, V. Vallet, and O. Gropen, *J. Phys. Chem. A* **103**, 8257 (1999).
- ⁷J. Neufeld, L. Soderholm, and S. Skanthakumar, *J. Phys. Chem. A* **108**, 2733 (2004).
- ⁸K. L. Nash and G. J. Lumetta, *Advanced Separation Techniques for Nuclear Fuel Reprocessing and Radioactive Waste Treatment* (Woodhead, 2011).
- ⁹J. M. McKibben, *Radiochim. Acta* **36**, 3 (1984).
- ¹⁰M. Dolg, *Lanthanides and Actinides* (John Wiley, Chichester, 1999), p. 1478.
- ¹¹L. Seijo, Z. Barandiaran, and E. Harguindegay, *J. Chem. Phys.* **114**, 118 (2001).
- ¹²P. J. Hay and R. L. Martin, *J. Chem. Phys.* **109**, 3875 (1998).

- ¹³P. A. Malmqvist, B. O. Roos, and B. Schimmelpfennig, *Chem. Phys. Lett.* **357**, 230 (2002).
- ¹⁴V. Vallet, L. Maron, C. Teichsel, and J.-P. Flament, *J. Chem. Phys.* **113**, 1391 (2000).
- ¹⁵N. Kaltsoyannis, P. J. May, J. Li, J. P. Blaudeau, and B. E. Bursten, *The Chemistry of Actinide and Transactinide Elements*, 3rd ed. (Springer, Dordrecht, 2006), Chap. 17, p. 1893.
- ¹⁶L. Gagliardi and B. Roos, *Nature* **433**, 848 (2005).
- ¹⁷V. Vallet, P. Macak, U. Wahlgren, and I. Grenthe, *Theor. Chem. Acc.* **115**, 145 (2006).
- ¹⁸S. Tsushima and A. Suzuki, *J. Mol. Struct.: THEOCHEM* **487**, 33 (1999).
- ¹⁹S. Tsushima and A. Suzuki, *J. Mol. Struct.: THEOCHEM* **529**, 21 (2000).
- ²⁰J. P. Blaudeau, S. A. Zygmunt, L. A. Curtiss, D. T. Reed, and B. E. Bursten, *Chem. Phys. Lett.* **310**, 347 (1999).
- ²¹B. Siboulet, C. Marsden, and P. Vitorge, *Chem. Phys.* **326**, 289 (2006).
- ²²K. Ingram, L. Jonas, L. Häller, and N. Kaltsoyannis, *Dalton Trans.* 2403 (2006).
- ²³S. Spencer, L. Gagliardi, N. C. Handy, A. G. Ioannou, and A. Simper, *J. Phys. Chem. A* **103**, 1831 (1999).
- ²⁴P. J. Hay, R. L. Martin, and G. Schreckenbach, *J. Phys. Chem. A* **104**, 6259 (2000).
- ²⁵S. Tsushima, T. Yang, and A. Suzuki, *Chem. Phys. Lett.* **334**, 365 (2001).
- ²⁶L. V. Moskaleva, S. Krüger, A. Spörl, and N. Rösch, *Inorg. Chem.* **43**, 4080 (2004).
- ²⁷Z. Cao and K. Balasubramanian, *J. Chem. Phys.* **123**, 114309 (2005).
- ²⁸M. S. K. Fuchs, A. M. Shor, and N. Rösch, *Int. J. Quantum Chem.* **86**, 487 (2002).
- ²⁹G. Shamov and G. Schreckenbach, *J. Phys. Chem. A* **109**, 10961 (2005).
- ³⁰E. Sánchez Marcos, R. R. Pappalardo, and D. Rinaldi, *J. Phys. Chem.* **95**, 8928 (1991).
- ³¹J. M. Martínez, R. R. Pappalardo, and E. Sánchez Marcos, *J. Phys. Chem. A* **101**, 4444 (1997).
- ³²Y. Marcus, *Ions in Solution and Their Solvation*, 1st ed. (John Wiley & Sons, 2015).
- ³³P. Guilbaud and G. Wipff, *J. Phys. Chem.* **97**, 5685 (1993).
- ³⁴S. Kerisit and C. Liu, *J. Phys. Chem. A* **117**, 6421 (2013).
- ³⁵D. Hagberg, G. Karlström, B. O. Roos, and L. Gagliardi, *J. Am. Chem. Soc.* **127**, 14250 (2005).
- ³⁶A. Wallqvist, P. Ahlström, and G. Karlström, *J. Phys. Chem.* **94**, 1649 (1990).
- ³⁷N. Rai, S. P. Tiwari, and E. J. Maginn, *J. Phys. Chem. B* **116**, 10885 (2012).
- ³⁸V. Pomogaev, S. P. Tiwari, N. Rai, G. S. Goff, W. Runde, W. F. Schneider, and E. J. Maginn, *Phys. Chem. Chem. Phys.* **15**, 15954 (2013).
- ³⁹M. Bühl, R. Diss, and G. Wipff, *J. Am. Chem. Soc.* **127**, 13506 (2005).
- ⁴⁰R. Car and M. Parrinello, *Phys. Rev. Lett.* **55**, 2471 (1985).
- ⁴¹P. Nichols, E. J. Bylaska, G. K. Schenter, and W. de Jong, *J. Chem. Phys.* **128**, 124507 (2008).
- ⁴²R. J. Frick, T. S. Hofer, A. B. Pribil, B. R. Randolph, and B. M. Rode, *J. Phys. Chem. A* **113**, 12496 (2009).
- ⁴³C. Hennig, K. Schmeide, V. Brendler, H. Moll, S. Tsushima, and A. C. Scheinost, *Inorg. Chem.* **46**, 5882 (2007).
- ⁴⁴D. T. Richens, *The Chemistry of Aqua Ions* (John Wiley, West Sussex, England, 1997).
- ⁴⁵L. Helm and A. E. Merbach, *Chem. Rev.* **105**, 1923 (2005).
- ⁴⁶S. P. Tiwari, N. Rai, and E. J. Maginn, *Phys. Chem. Chem. Phys.* **16**, 8060 (2014).
- ⁴⁷E. Sánchez Marcos, R. R. Pappalardo, J. C. Barthelat, and F. Xavier Gadea, *J. Phys. Chem.* **96**, 516 (1992).
- ⁴⁸R. R. Pappalardo and E. Sánchez Marcos, *J. Phys. Chem.* **97**, 4500 (1993).
- ⁴⁹R. R. Pappalardo, J. M. Martínez, and E. Sánchez Marcos, *J. Phys. Chem.* **100**, 11748 (1996).
- ⁵⁰J. M. Martínez, R. R. Pappalardo, and E. Sánchez Marcos, *J. Chem. Phys.* **109**, 1445 (1998).
- ⁵¹J. M. Martínez, R. R. Pappalardo, and E. Sánchez Marcos, *J. Am. Chem. Soc.* **121**, 3175 (1999).
- ⁵²P. J. Merkling, A. Muñoz-Páez, and E. Sánchez Marcos, *J. Am. Chem. Soc.* **124**, 10911 (2002).
- ⁵³E. Galbis, J. Hernández-Cobos, C. den Auwer, C. Le Naour, D. Guillaumont, E. Simoni, R. R. Pappalardo, and E. Sánchez Marcos, *Angew. Chem.* **122**, 3899 (2010).
- ⁵⁴J. M. Martínez, F. Torrico, R. R. Pappalardo, and E. Sánchez Marcos, *J. Phys. Chem. B* **108**, 15851 (2004).
- ⁵⁵F. Torrico, R. R. Pappalardo, E. Sánchez Marcos, and J. M. Martínez, *Theor. Chem. Acc.* **115**, 196 (2006).

- 56 J. M. Martínez, R. R. Pappalardo, E. Sánchez Marcos, K. Refson, S. Díaz-Moreno, and A. Muñoz-Páez, *J. Phys. Chem. B* **102**, 3272 (1998).
- 57 A. D. Becke, *J. Chem. Phys.* **98**, 5648 (1993).
- 58 P. J. Stephens, F. J. Devlin, C. F. Chabalowski, and M. J. Frisch, *J. Phys. Chem.* **98**, 11623 (1994).
- 59 W. Küchle, M. Dolg, H. Stoll, and J. Preuss, *J. Chem. Phys.* **100**, 7535 (1994).
- 60 D. E. Woon and T. H. Dunning, Jr., *J. Chem. Phys.* **98**, 1358 (1993).
- 61 M. J. Frisch, G. W. Trucks, H. B. Schlegel, G. E. Scuseria, M. A. Robb, J. R. Cheeseman, G. Scalmani, V. Barone, B. Mennucci, G. A. Petersson, H. Nakatsuji, M. Caricato, X. Li, H. P. Hratchian, A. F. Izmaylov, J. Bloino, G. Zheng, J. L. Sonnenberg, M. Hada, M. Ehara, K. Toyota, R. Fukuda, J. Hasegawa, M. Ishida, T. Nakajima, Y. Honda, O. Kitao, H. Nakai, T. Vreven, J. A. Montgomery, Jr., J. E. Peralta, F. Ogliaro, M. Bearpark, J. J. Heyd, E. Brothers, K. N. Kudin, V. N. Staroverov, R. Kobayashi, J. Normand, K. Raghavachari, A. Rendell, J. C. Burant, S. S. Iyengar, J. Tomasi, M. Cossi, N. Rega, J. M. Millam, M. Klene, J. E. Knox, J. B. Cross, V. Bakken, C. Adamo, J. Jaramillo, R. Gomperts, R. E. Stratmann, O. Yazev, A. J. Austin, R. Cammi, C. Pomelli, J. W. Ochterski, R. L. Martin, K. Morokuma, V. G. Zakrzewski, G. A. Voth, P. Salvador, J. J. Dannenberg, S. Dapprich, A. D. Daniels, Ö. Farkas, J. B. Foresman, J. V. Ortiz, J. Cioslowski, and D. J. Fox, *gaussian* 09, Revision D.01, Gaussian, Inc., Wallingford, CT, 2009.
- 62 L. Soderholm, S. Skanthakumar, and J. Neuefeind, *Anal. Bioanal. Chem.* **383**, 48 (2005).
- 63 L. Sémon, C. Boeheme, I. Billard, C. Hennig, K. Lützenkirchen, T. Reich, A. Roßberg, I. Rossini, and G. Wipff, *ChemPhysChem* **2**, 591 (2001).
- 64 U. C. Singh and P. A. Kollman, *J. Comput. Chem.* **5**, 129 (1984).
- 65 B. H. Besler, K. M. Merz, and P. A. Kollman, *J. Comput. Chem.* **11**, 431 (1990).
- 66 S. Miertus, E. Scrocco, and J. Tomasi, *Chem. Phys.* **55**, 117 (1981).
- 67 B. Mennucci, E. Cancès, and J. Tomasi, *J. Phys. Chem. B* **101**, 10506 (1997).
- 68 S. Batsanov, *Inorg. Mat.* **37**, 871 (2001).
- 69 F. Carrera, F. Torrico, D. T. Richens, A. Muñoz-Páez, J. M. Martínez, R. R. Pappalardo, and E. Sánchez Marcos, *J. Phys. Chem. B* **111**, 8223 (2007).
- 70 I. Todorov, W. Smith, K. Trachenko, and M. T. Dove, *J. Mater. Chem.* **16**, 1911 (2006).
- 71 W. L. Jorgensen, J. Chandrasekhar, J. D. Madura, R. W. Impey, and M. L. Klein, *J. Chem. Phys.* **79**, 926 (1983).
- 72 W. C. Swope, H. C. Andersen, P. H. Berens, and K. R. Wilson, *J. Chem. Phys.* **76**, 637 (1982).
- 73 T. Miller, M. Eleftheriou, P. Pattnaik, A. Ndirango, D. Newns, and G. Martyna, *J. Chem. Phys.* **116**, 8649 (2002).
- 74 J. K. Gibson, R. G. Haire, M. Santos, J. Maralo, and A. Pires de Matos, *J. Phys. Chem. A* **109**, 2768 (2005).
- 75 Y. Marcus and A. Loewenschuss, *J. Chem. Soc., Faraday Trans. 1* **82**, 2873 (1986).
- 76 L. V. Moskaleva, A. V. Matveev, S. Krüger, and N. Rösch, *Chem. - Eur. J.* **12**, 629 (2006).
- 77 M. Bühl, H. Kabrede, R. Diis, and G. Wipff, *J. Am. Chem. Soc.* **128**, 6357 (2006).
- 78 P. Allen, J. Bucher, D. Shuh, N. Edelstein, and T. Reich, *Inorg. Chem.* **36**, 4676 (1997).
- 79 P. Guillaud and G. Wipff, *J. Mol. Struct.: THEOCHEM* **366**, 55 (1996).
- 80 K. E. Gutowski and D. A. Dixon, *J. Phys. Chem. A* **110**, 8840 (2006).
- 81 A. Melchior, J. M. Martínez, R. R. Pappalardo, and E. Sánchez Marcos, *J. Chem. Theory Comput.* **9**, 4562 (2013).
- 82 E. C. Beret, J. M. Martínez, R. R. Pappalardo, E. Sánchez Marcos, N. L. Doltsinis, and D. Marx, *J. Chem. Theory Comput.* **4**, 2108 (2008).
- 83 A. Luzar and D. Chandler, *Phys. Rev. Lett.* **76**, 928 (1996).
- 84 P. Ball, *Chem. Rev.* **108**, 74 (2008).
- 85 E. I. Martín, J. M. Martínez, and E. Sánchez Marcos, *J. Chem. Phys.* **143**, 044502 (2015).
- 86 R. Impey, P. Madden, and I. McDonald, *J. Phys. Chem.* **87**, 5071 (1983).
- 87 A. E. García and L. Stiller, *J. Comput. Chem.* **14**, 1396 (1993).
- 88 I.-C. Yeh and G. Hummer, *J. Phys. Chem. B* **108**, 15873 (2004).
- 89 J.-P. Simonin, I. Billard, H. Hendrawan, O. Bernard, K. Lützenkirchen, and L. Sémon, *Phys. Chem. Chem. Phys.* **5**, 520 (2003).
- 90 D. Kern and E. Orlemann, *J. Am. Chem. Soc.* **71**, 2102 (1949).
- 91 M. Chopra and N. Choudhury, *J. Phys. Chem. B* **118**, 14373 (2014).
- 92 R. J. H. Clark and R. E. Hester, *Advances in Infrared and Raman Spectroscopy* (Hayden, 1983), Chap. 6.
- 93 M. Gál, P. Goggins, and J. Mink, *Spectrochim. Acta, Part A* **48**, 121 (1992).
- 94 C. Tait, in *Symposium of Heavy Element Complexes*, 217th ACS National Meeting, Anaheim, CA, 1999.
- 95 D. Koningsberger and R. Prins, *X-Ray Absorption: Principles, Applications, Techniques of EXAFS, SEXAFS, and XANES* (John Wiley and Sons, New York, NY, 1988).
- 96 M. A. Denecke, *Coord. Chem. Rev.* **250**, 730 (2006).
- 97 A. Filippini, P. D'Angelo, N. V. Pavel, and A. Di Cicco, *Chem. Phys. Lett.* **225**, 150 (1994).
- 98 B. J. Palmer, D. M. Pfund, and J. L. Fulton, *J. Phys. Chem.* **100**, 13393 (1996).
- 99 A. L. Ankudinov, A. I. Nesvizhskii, and J. J. Rehr, *Phys. Rev. B* **67**, 115120 (2003).





SUPPLEMENTARY MATERIAL

**A Hydrated Ion Model of $[\text{UO}_2]^{2+}$ in water:
Structure, dynamics and spectroscopy from
classical Molecular Dynamics**

Sergio Pérez-Conesa, Francisco Torrico, José M. Martínez, Rafael R. Pappalardo
and Enrique Sánchez Marcos

*Departamento de Química Física, Universidad de Sevilla,
41012 Sevilla, Spain. e-mail:sanchez@us.es*



—



—

Normal mode internal coordinate definition

For the bending motion of $[\text{UO}_2\cdot(\text{H}_2\text{O})_5]^{2+}(\text{aq})$, with irreducible representation E_1 , ϕ was defined as the $\text{O}_{\text{yl}}\text{-U-O}_{\text{yl}}$ angle and its cosine function is used to compute its autocorrelation function.

$$\langle (\cos(\phi) - \overline{\cos(\phi)}) \cdot (\cos(\phi) - \overline{\cos(\phi)}) \rangle \quad (1)$$

For the symmetric tension of $[\text{UO}_2\cdot(\text{H}_2\text{O})_5]^{2+}(\text{aq})$, $1A_1$, the following normal mode internal coordinate was defined, $R_{\text{sym}} = \sum_{i=1}^2 R_i(\text{U} - \text{O}_{\text{yl}})$ and it is used to compute its autocorrelation function:

$$\langle (R_{\text{sym}}(0) - \overline{R_{\text{sym}}}) \cdot (R_{\text{sym}}(t) - \overline{R_{\text{sym}}}) \rangle \quad (2)$$

For the asymmetric tension of $[\text{UO}_2\cdot(\text{H}_2\text{O})_5]^{2+}(\text{aq})$, A_2 , the following normal mode internal coordinate was defined, $R_{\text{asym}} = R_i(\text{U} - \text{O}_{\text{yl},1}) - R_i(\text{U} - \text{O}_{\text{yl},2})$ and it is used to compute its autocorrelation function:

$$\langle (R_{\text{asym}}(0) - \overline{R_{\text{asym}}}) \cdot (R_{\text{asym}}(t) - \overline{R_{\text{asym}}}) \rangle \quad (3)$$

For the breathing tension of $[\text{UO}_2\cdot(\text{H}_2\text{O})_5]^{2+}(\text{aq})$, A_1 , the following normal mode internal coordinate was defined, $R_{\text{br}} = \frac{1}{5} \sum_{i=1}^5 R_i(\text{U} - \text{O}_i)$ and it is used to compute its autocorrelation function:

$$\langle (R_{\text{br}}(0) - \overline{R_{\text{br}}}) \cdot (R_{\text{br}}(t) - \overline{R_{\text{br}}}) \rangle \quad (4)$$

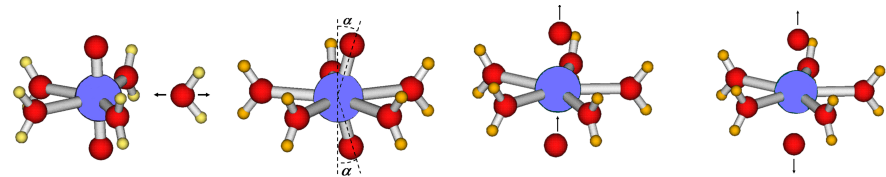


Figure 1: Deformations from the reference structure of the pentahydrated actinyl considered to build the intermolecular potential IW1 and intramolecular IMC.

Table 1: Effective Merz-Kollmann charges of $[\text{UO}_2 \cdot (\text{H}_2\text{O})_5]^{2+}(\text{aq})$ using PCM to model the bulk solvent.

	Partial Charge (a.u.)	Radius (\AA)
q_{U}	2.80	2.65
q_{O}	-1.05	1.40
$q_{\text{O}_{\text{y}1}}$	-0.55	1.40
q_{H}	0.55	1.20

Table 2: Coefficients from the fitting of the IW1 interaction potential and root mean square error (RMSE).

Coefficients	$\text{kcal mol}^{-1} \text{\AA}^{-n}$
$C_4^{\text{UO}_1}$	-6388.86
$C_6^{\text{UO}_1}$	52787.05
$C_8^{\text{UO}_1}$	-131984.94
$C_{12}^{\text{UO}_1}$	476950.29
$C_4^{\text{O}_{\text{y}1}\text{O}_1}$	1696.66
$C_6^{\text{O}_{\text{y}1}\text{O}_1}$	-8196.99
$C_8^{\text{O}_{\text{y}1}\text{O}_1}$	18165.85
$C_{12}^{\text{O}_{\text{y}1}\text{O}_1}$	-30202.92
RMSE	0.61 kcal mol^{-1}

Table 3: Coefficients from the fitting of the IMC interaction potential, RMSE_{total} and RMSE_{partial} which is computed for points lower than 15 kcal mol⁻¹.

Coefficients	kcal mol ⁻¹ Å ⁻ⁿ
$C_4^{UO_{yl}}$	-133370.94
$C_6^{UO_{yl}}$	668178.78
$C_8^{UO_{yl}}$	-1059978.49
$C_{12}^{UO_{yl}}$	949717.97
$C_4^{O_{yl}O_{yl}}$	-167679.49
$C_6^{O_{yl}O_{yl}}$	4369622.37
$C_8^{O_{yl}O_{yl}}$	-33177820.27
$C_{12}^{O_{yl}O_{yl}}$	605633365.20
RMSE _{total}	3.37 kcal mol ⁻¹
RMSE _{partial}	0.42 kcal mol ⁻¹

Table 4: Coefficients from the fitting of the HIW interaction potential, RMSE_{total} and RMSE_{partial} which is computed for points lower than 15 kcal mol⁻¹.

Coefficients	kcal mol ⁻¹ Å ⁻ⁿ	Coefficients	kcal mol ⁻¹ Å ⁻ⁿ
C_4^{UOW}	18578.27	$C_4^{O_lOW}$	-830.40
C_6^{UOW}	-288922.08	$C_6^{O_lOW}$	6718.50
C_8^{UOW}	1481816.44	$C_8^{O_lOW}$	-4208.51
C_{12}^{UOW}	-12631787.76	$C_{12}^{O_lOW}$	-3888.10
C_4^{UHW}	-5094.89	$C_4^{O_lHW}$	28.22
C_6^{UHW}	65098.47	$C_6^{O_lHW}$	100.59
C_8^{UHW}	-268274.37	$C_8^{O_lHW}$	-40.17
C_{12}^{UHW}	1482339.87	$C_{12}^{O_lHW}$	1.06
$C_4^{O_{yl}OW}$	-1503.86	$C_4^{H_lOW}$	-64.73
$C_6^{O_{yl}OW}$	10373.23	$C_6^{H_lOW}$	166.44
$C_8^{O_{yl}OW}$	-15794.55	$C_8^{H_lOW}$	-57.00
$C_{12}^{O_{yl}OW}$	12403.99	$C_{12}^{H_lOW}$	1.25
$C_4^{O_{yl}HW}$	187.28	$C_4^{H_lHW}$	4.63
$C_6^{O_{yl}HW}$	-314.50	$C_6^{H_lHW}$	-0.29
$C_8^{O_{yl}HW}$	213.54	$C_8^{H_lHW}$	0.07
$C_{12}^{O_{yl}HW}$	-22.69	$C_{12}^{H_lHW}$	0.00
RMSE _{total}		1.94 kcal mol ⁻¹	
RMSE _{partial}		1.15 kcal mol ⁻¹	

A general study of actinyl hydration by molecular dynamics simulations using ab initio force fields

5.1. *J. Chem. Phys.* 2019, **150**, 104504–104514



A general study of actinyl hydration by molecular dynamics simulations using *ab initio* force fields

Cite as: J. Chem. Phys. 150, 104504 (2019); doi: 10.1063/1.5083216

Submitted: 29 November 2018 • Accepted: 26 February 2019 •

Published Online: 13 March 2019



Sergio Pérez-Conesa, Francisco Torrico, José M. Martínez, Rafael R. Pappalardo, and Enrique Sánchez Marcos^a

AFFILIATIONS

Departamento de Química Física, Universidad de Sevilla, 41012 Sevilla, Spain

^a Electronic mail: sanchez@us.es

ABSTRACT

A set of new *ab initio* force fields for aqueous $[AnO_2]^{2+/+}$ ($An = Np(vi,v)$, $Pu(vi)$, $Am(vi)$) has been developed using the Hydrated Ion (HI) model methodology previously used for $[UO_2]^{2+}$. Except for the non-electrostatic contribution of the HI-bulk water interaction, the interaction potentials are individually parameterized. Translational diffusion coefficients, hydration enthalpies, and vibrational normal mode frequencies were calculated from the MD simulations. Physico-chemical properties satisfactorily agree with experiments validating the robustness of the force field strategy. The solvation dynamics and structure for all hexavalent actinoids are extremely similar and resemble our previous analysis of the uranyl cation. This supports the idea of using the uranyl cation as a reference for the study of other minor actinyls. The comparison between the NpO_2^{2+} and NpO_2^{+} hydration only provides significant differences in first and second shell distances and second-shell mean residence times. We propose a single general view of the $[AnO_2]^{2+/+}$ hydration structure: aqueous actinyls are amphiphilic anisotropic solutes which are equatorially conventional spherically symmetric cations capped at the poles by clathrate-like water structures.

Published under license by AIP Publishing. <https://doi.org/10.1063/1.5083216>

I. INTRODUCTION

The solution chemistry of actinoid cations is a challenging yet important technological and environmental issue. Nuclear technology draws knowledge from many fields: physics, chemistry, environmental science, engineering, etc.¹ Actinyl aqua ion $[AnO_2(H_2O)_m]^{2+}$ chemistry is very important in spent nuclear fuel reprocessing and storage.^{2–8} For instance, U and Pu are under their actinyl form in the PUREX method which is a liquid-liquid extraction process used to separate U and Pu from minor actinoids in dissolved nuclear fuel.⁹ Their diffusion, redox, acid-base and solubility properties determine their speciation and presence in natural systems as well as their risk management in permanent geological facilities.

Actinyls are *trans*-dioxo molecular cations with chemical formula $[AnO_2]^{2+/+}$, the actinide atom being in a pentavalent or hexavalent oxidation state. The elements that form stable actinyls are uranium, neptunium, plutonium, and americium.¹⁰ For Am, the

most stable form is its $Am(III)$ aquaion, but $Am(V,VI)$ also exist and are relatively stable, in highly acidic and oxidizing media.¹¹ The most stable species for Np is $[NpO_2]^+$, but $[NpO_2]^{2+}$ has also been reported.¹⁰ Plutonium can be found in oxidation states from III to VI, being the $Pu(IV)$ aquaion the most stable although the $Pu(VI)$ actinyl form is also technologically and environmentally important.¹² In this work, we focus on U(vi), Pu(vi), Np(vi), and Am(vi) but as well as on Np(v) for comparison with a singly charged actinyl cation. The aqueous coordination chemistry of these species in acid media is very similar for all of them and are mainly pentahydrated ions, $[AnO_2(H_2O)_5]^{2+/+}$.

Statistical simulation of aqueous uranyl has a long and successful history.^{13–21} By contrast, there are only two studies that extend the computational study of uranyl to other elements. Odoh *et al.*²² carried out Car-Parrinello Molecular Dynamics²³ (CPMD) on aqueous $[PuO_2]^{2+/+}$ studying the relative stability of different coordination numbers and hydrolysis. The only force field for actinyls beyond uranium is the one developed by the Maginn group²⁴ in

which they extend their previous uranyl model.¹⁷ They developed Lennard-Jones parameters for a general $[AnO_2]^{2+/+}$ (aq) system, and the partial charges and bonding terms of the molecular cation specify the element and oxidation state.

The most common force field model of an ion in solution is to consider the ion as a charged particle with Lennard-Jones parameters that are combined with those of the solvent (a “charged soft sphere model”). This model benefits from being very simple and easy to transfer to new systems applying combination rules without further parameterization. But its accuracy is limited especially for highly charged or polarizing cations. It neglects charge transfer and polarization effects suffered by first-shell solvent molecules. Therefore, it treats first-shell-bulk water molecule interactions as regular bulk water molecule interactions.

In the 1990s, our group proposed a strategy to parameterize *ab initio* interaction potentials for highly charged metal ions based on the old electrochemistry concept of the *Hydrated Ion* (HI).^{25–28} Its key idea is that highly charged metal cations (M^{q+}) are better represented in solution by their hydrated form $[M(H_2O)_m]^{q+}$.²⁹ HI models for a diverse set of ions have been developed providing a reasonable description of the energetic, structural, spectroscopic, and dynamic properties of cations forming well defined aqua ions in water.^{28,30–32} The recent development of the $[UO_2(H_2O)_5]^{2+}$ -H₂O force field²¹ was the first time that the HI model was applied to a molecular cation. The derived MD simulations provided some interesting insights into its solvation structure and dynamics.²¹ Considering the similar chemical nature of An(v,vi), it is easy to anticipate that most of the methodology and knowledge of the previous U(vi) system could be transferred to broaden our knowledge of actinyl cations as done in the past with monoatomic cations of more dissimilar nature such as Be²⁺, Mg²⁺, Ir³⁺, Rh³⁺, Pt³⁺, and Pd²⁺.^{28,30–32} In fact, recently we extended this approach to Am(vi) to study the nature of the first EXAFS measurement of an Am(vi)/Am(III) mixture solution.³³ We were able to simulate independently EXAFS spectra of both the americyl cation and the Am(III) aqua ion and combine them to simulate the theoretical EXAFS spectrum of an ion mixture in solution.

We present in this work a set of new *ab initio* interaction potentials for $[AnO_2(H_2O)_5]^{2+/+}$ based on the HI model to provide a global picture of the influence that the oxidation state and element nature have on their aqua ion properties.

II. METHODS

A. Hydrated ion model potential for actinyls

The set of *ab initio* interaction potentials developed is based on the $[AnO_2(H_2O)_5]^{2+/+}$ model for An = Np(v,vi), Pu(vi), Am(vi). We follow the methodology that has already been successful in our $[UO_2(H_2O)_5]^{2+}$ study. Each actinyl potential has been developed as a particular case of the general method established for the uranyl case.²¹

The main feature of the HI model force fields is to consider two different types of water molecules: first-shell and bulk.^{25,26} The first one bears strong polarization effects and partial charge transfer due to the direct interaction with the cation. The latter water molecules are bulk molecules, in this case modeled by the TIP4P potential.³⁴ First-shell water molecules will have different atom

types, partial charges, geometries, and non-electrostatic interactions than bulk water molecules. The main limitation in this model is that the release of a water molecule from the first shell renders the simulation system unphysical. Because, the actinyls studied have first-shell mean residence times (MRTs) much longer than the simulation time,^{29,35,36} the HI model is very appropriate for these systems. All MD simulations carried out in this work have been monitored to check that the first-shell water molecules stay in their shell along the whole simulation. This monitorization is a requirement to guarantee the correct behavior of the potential when the model is employed.

All H₂O molecules are treated as rigid bodies. Nevertheless, the hydrated ion is flexible in its first shell and also within the $[AnO_2]^{2+/+}$ unit. The potential energy of the whole simulation system is partitioned as follows:

$$E = E_{IMC} + E_{IW1} + E_{W1-W1} + E_{HIW} + E_{TIP4P}. \quad (1)$$

The terms that are fitted to the quantum mechanical (QM) information are E_{IMC} (Intra-Molecular Cation) which accounts for the interactions within the $[AnO_2]^{2+/+}$ unit, E_{IW1} (Ion-Water of the 1st shell) that provides the interaction of the molecular cation with its first shell, and E_{HIW} (Hydrated Ion Water) which describes the interaction energy of bulk water molecules and $[AnO_2(H_2O)_5]^{2+/+}$. The remaining terms are the Lennard-Jones plus the electrostatic interactions among bulk water molecules (E_{TIP4P}) and first-shell solvent molecules (E_{W1-W1}). The fitted terms have an electrostatic contribution in addition to a non-electrostatic component defined by a polynomial functional form where $n = 4, 6, 8, 12$. The expressions for the potential terms are

$$E_{IMC} = \sum_i^{\text{sites}} \left(\frac{C_4^{\text{AnO}_i}}{r_{\text{AnO}_i}^4} + \frac{C_6^{\text{AnO}_i}}{r_{\text{AnO}_i}^6} + \frac{C_8^{\text{AnO}_i}}{r_{\text{AnO}_i}^8} + \frac{C_{12}^{\text{AnO}_i}}{r_{\text{AnO}_i}^{12}} \right) + \sum_i^{\text{sites}} \frac{q_{\text{An}} q_{\text{O}_{i,1}}}{r_{\text{AnO}_i}^n}, \quad (2)$$

$$E_{IW1} = \sum_i^{\text{AnO}_2} \frac{C_4^{\text{iO}_i}}{r_{\text{iO}_i}^4} + \frac{C_6^{\text{iO}_i}}{r_{\text{iO}_i}^6} + \frac{C_8^{\text{iO}_i}}{r_{\text{iO}_i}^8} + \frac{C_{12}^{\text{iO}_i}}{r_{\text{iO}_i}^{12}} + \sum_i^{\text{AnO}_2} \sum_j^{\text{1st shell Water}} \frac{q_i q_j}{r_{ij}}, \quad (3)$$

$$E_{HIW} = \sum_i^{\text{HI sites}} \sum_j^{\text{Water sites}} \left(\frac{C_4^{ij}}{r_{ij}^4} + \frac{C_6^{ij}}{r_{ij}^6} + \frac{C_8^{ij}}{r_{ij}^8} + \frac{C_{12}^{ij}}{r_{ij}^{12}} + \frac{q_i q_j}{r_{ij}} \right). \quad (4)$$

The structures used to parameterize the IMC and IW1 potentials always contain the pentahydrate in the gas phase and are deformations following the normal modes of bending and symmetric or antisymmetric stretching. The fact of including first-shell water molecules in the QM calculations guarantees the polarization of the actinyl and the first-shell water molecules of the hydrated ion entity as present in solution. In the case of the HIW potential, the structures to parameterize the potential consist of the pentahydrate and a single bulk water molecule. The additional polarization of the rest of the solution will be provided in the simulation by the HIW term. Details of the procedure can be found elsewhere.²¹

Due to the low degree of polarization and charge transfer in the case of $[NpO_2(H_2O)_5]^+$, the first-shell water molecules bear

the same charges and geometry as the TIP4P water model (including the massless point charge). Nevertheless, they are still different from bulk water molecules due to the non-electrostatic part of the IW1 and HIW interaction potentials. The IW1 and IMC interaction potentials were fitted specifically for each of the actinyl species, whereas the non-electrostatic part of the HIW potential developed for $[UO_2 \cdot (H_2O)_5]^{2+}$ was transferred for all actinyls. This assumption was based on the previous experience of the group with other cations^{28,30-33} and the fact that actinyls have a similar coordination chemistry. To test this, in Fig. 1, we present scans of the interaction energy of a second-shell water molecule with the HI obtained from QM calculations and the HIW potential. The ions $[NpO_2 \cdot (H_2O)_5]^{2+}$ and $[NpO_2 \cdot (H_2O)_5]^+$ were chosen as representatives of the set, but analogous results were obtained for the other actinyls. The approximation is reasonable since the difference between the curves has the same magnitude as the typical uncertainty associated with the fitting of the *ab initio* interaction potentials. Furthermore, the error of the pentavalent case is nearly constant, as a consequence the equations of motion are not altered given that these equations are propagated using the gradient of the potential.

All the parameters of the interaction potentials can be found in Tables S1-S5 of the [supplementary material](#).

The level of theory of the PES used to fit the interaction potentials is the same as in our previous work: B3LYP^{27,38}/aug-cc-PVDZ³⁹ with Stuttgart relativistic effective core pseudopotentials⁴⁰ using Gaussian09.⁴¹ Partial charges were calculated using the Merz-Kollman^{42,43} method polarizing previously the electronic density with the Polarizable Continuum Model (PCM) of solvation.⁴⁴ The B3LYP functional has given reliable interaction energies and molecular geometries for actinyls⁴⁵⁻⁴⁷ even if they have an open-shell nature.^{48,49} Some NEVPT2⁵⁰⁻⁵² geometrical scans were carried out using the ORCA package⁵³ in order to test this issue. The ground state multiplicities of the aqua ions are a doublet for

NpO_2^{2+} , a triplet for NpO_2^+ and PuO_2^{2+} , and a quartet for AmO_2^{2+} . The active space chosen was four π/π^* and two σ/σ^* molecular orbitals formed by actinoid f-orbitals and p-orbitals of the O_{yl} atoms and 4 atomic-like non-bonding f-orbitals of the actinoid. This led to CASSCF(n,10) configurations where n is 6 plus the number of actinoid unpaired electrons. The addition of bonding and antibonding molecular orbitals is motivated by the fact that f-orbitals participate in the formation of the oxo-bond. These orbitals were obtained from small-base set unrestricted Density Functional Theory (DFT) calculation using the Becke-Perdew (BP) functional and using the “stable” keyword as recommended in the ORCA CASSCF tutorial (http://www.molphys.org/orca_tutorial/orca_hands_on.html). Since the ground states are degenerate, the calculations were run using a state average over the degenerate states excluding excited states. The perturbational step of the calculation was done using quasi-degenerate perturbation theory. The basis sets used were ma-def2-TZVP for O, def2-SVP for H, and SD(60,MWB)//DEF-TZVP for actinides.^{40,54} The calculations were accelerated using the RI and RIJK pseudospectral methods with “autoaux” auxiliary basis sets. Figure S1 of the [supplementary material](#) shows four geometry scans at both levels of theory. In all cases, the differences using B3LYP or NEVPT2 level of calculation were in the range of the typical fit root mean square error of our *ab initio* force fields. Furthermore, the optimized geometry bond lengths at the NEVPT2 level differ less than 3% which is irrelevant for most solution properties. These small differences are in part due to the fact that unrestricted DFT computations include static electron correlation using a mean field approach which seems sufficient for our purposes.

B. Molecular dynamics simulations

For each of the actinyl species, the simulated system consisted of a hydrated ion, $[AnO_2 \cdot (H_2O)_5]^{2+/+}$, and 1495 TIP4P water molecules initially at pure water density and an approximate ion concentration of $\sim 0.04 \text{ mol kg}^{-1}$. A 5 ns NPT trajectory was integrated using the velocity Verlet and the NOSQUISH⁵⁵ quaternion algorithms with a 1 fs time step. 0.5 ns of equilibration was performed. The average temperature and pressure were kept constant at 300 K and 1 atm using the Nosé Hoover barostat and thermostat with characteristic times of 0.5 ps. Short range interactions were truncated at 14 Å, and electrostatic interactions were calculated using the Ewald sum. The simulations were performed using a modified version of DL_POLY Classic⁵⁶ which includes the functional forms of the new potential developed.

III. RESULTS AND DISCUSSION

A. Hydration enthalpies

The hydration enthalpies, ΔH_{hyd} , of $[AnO_2]^{2+/+}$ were obtained by the following expression:

$$\Delta H_{\text{hyd}} = H_{[AnO_2]^{2+/+}(\text{aq})} - H_{H_2O(\text{aq})} - H_{[AnO_2]^{2+/+}(\text{g})}, \quad (5)$$

where $H_{[AnO_2]^{2+/+}(\text{aq})}$, $H_{H_2O(\text{aq})}$, and $H_{[AnO_2]^{2+/+}(\text{g})}$ are the MD simulation enthalpies of the aqua ion solution (one ion and 1500 solvent molecules), a 1500 H₂O box, and $[AnO_2]^{2+/+}(\text{g})$. Table I contains the results.

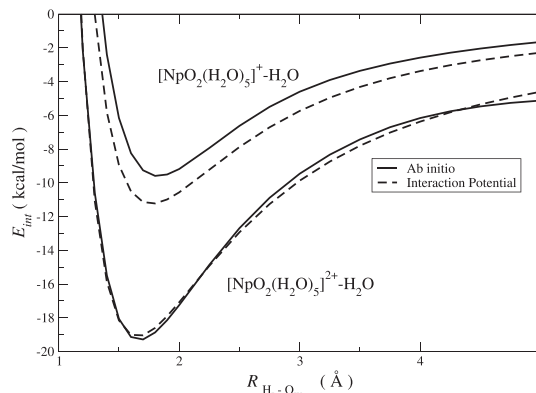


FIG. 1. Interaction energy scans of a bulk water molecule with $[NpO_2 \cdot (H_2O)_5]^+$ (top) and $[NpO_2 \cdot (H_2O)_5]^{2+}$ (bottom) obtained with B3LYP calculations (solid lines) or the HIW potential (dashed lines). The HIW potential was parameterized for $[UO_2 \cdot (H_2O)_5]^{2+}$ in our previous work²¹ and was extrapolated to other hexavalent and pentavalent actinyls.

TABLE I. Energetic, structural, and dynamical properties calculated from the molecular dynamics simulations. Uncertainties are standard errors.

Property	U(vi)	Np(vi)	Np(v)	Pu(vi)	Am(vi)
ΔH_{hyd} (kcal mol ⁻¹)	-333 ± 14	-337 ± 14	-190 ± 16	-350 ± 16	-342 ± 16
$D_{An}(10^{-5})$ cm ² s ⁻¹	1.2 ± 0.2	1.2 ± 0.2	1.2 ± 0.1	1.2 ± 0.1	1.3 ± 0.1
D_{An}/D_W	0.37 ± 0.04	0.38 ± 0.03	0.36 ± 0.06	0.38 ± 0.03	0.39 ± 0.03
$r_{An-O_{ij}}$ (Å)	1.77	1.73	1.79	1.72	1.72
r_{An-O_i} (Å)	2.46	2.43	2.58	2.43	2.44
$r_{An-O_{ii}}$ (Å)	4.61	4.63	4.74	4.60	4.64
$CN_{An-O_{ii}}$	22	25	22	22	22
MRT _W (ps), $t^* = 0$ ps	8 ± 1	6.9 ± 0.2	5.1 ± 0.3	8 ± 1	8 ± 1
MRT _W (ps), $t^* = 2$ ps	17 ± 1	15.9 ± 0.5	13.4 ± 0.5	16 ± 1	16 ± 1

All the hexavalent enthalpies are statistically identical and vary around -340 kcal/mol. In the case of $[NpO_2]^{+}$, ΔH_{hyd} is -190 kcal/mol, about 40% less than the corresponding $[NpO_2]^{2+}$ value.

Gibson *et al.*⁵⁷ measured the hydration enthalpies of all the hexavalent actinyls studied, obtaining values around -400 kcal/mol. Marcus⁵⁸ obtained a value of -325 ± 5 kcal mol⁻¹ for $[UO_2]^{2+}$, 75 kcal mol⁻¹ smaller than Gibson's value. The difficulty of measuring the formation enthalpy of gas phase actinyl ions might be, in part, the cause of this discrepancy.⁵⁹ This difficulty is even stronger in the case of the dication since it involves measuring the second ionization energy of the gas phase actinyl. Our value for the hexavalent actinyls approaches the value of Marcus especially since our $H_{[AnO_2]^{2+/+}}$ could be missing a small many-body contribution in the first-second shell interaction.²⁶ The $[NpO_2]^{+}$ hydration enthalpy from MD matches Gibson's value experimental value of -180 ± 20 kcal mol⁻¹. Rai *et al.*¹⁷ have computed ΔG_{hydr} for the uranyl based on an integration path split into two steps, growth and charging of the actinyl cation in water. Their ΔG_{hydr} values obtained for different water models are in between the reported experimental data.^{57,58}

B. Self-diffusion coefficient

The translational self-diffusion coefficients, D_0 , of the actinyls were calculated using the Einstein equation and correcting for finite box-size effects with the formula of Yeh and Hummer,⁶⁰

$$D_{An}^{\text{corr}} = D_{An}^0 + \frac{k_B T \xi}{6\pi\eta L}, \quad (6)$$

where η is the TIP4P water viscosity, L is the box length, and ξ is the self-term for a cubic box (2.8373 at room temperature). This correction is significant in the absolute value, and thus uncorrected D_{An}^0 values are in the range $0.8-0.9 \times 10^{-5}$ cm² s⁻¹, whereas size-corrected diffusion data are in the range $1.2-1.3 \times 10^{-5}$ cm² s⁻¹ (Table I). Uncorrected D_{An}^0 values obtained by Tiwari *et al.*⁶¹ are in the range $0.6-0.7 \times 10^{-5}$ cm² s⁻¹ using SPC/E for the water model. The diffusion coefficient of a solute correlates strongly with the solvent diffusion. Bearing in mind that the TIP4P water model overestimates the water mobility, the comparison between ion mobilities derived from this work and that of Tiwari *et al.*⁶¹ is satisfactory. For the particular case of uranyl, Kerisit and Liu⁶²

using three different potentials and the SPC/E model for water give uncorrected D_{An}^0 values in the range $0.85-0.94 \times 10^{-5}$ cm² s⁻¹. To supply a less dependent D_{An} on the water mobility, it is common practice in the literature⁶¹⁻⁶³ that the solute diffusion coefficients are normalized by the water self-diffusion coefficient.

The experimental self diffusion coefficients of the different actinyls range from 0.55×10^{-5} cm² s⁻¹ to 0.8×10^{-5} cm² s⁻¹.⁶⁴⁻⁶⁶ Considering TIP4P water mobility is too high, the aqua ion translates more freely than it should as well. The normalization corrects this effect, and then the data agree within the error with the experimental normalized range, 0.24-0.35,^{64,65} using 2.3×10^{-5} cm² s⁻¹ for water.⁶⁷

We observe once again how our MD results reflect the physico-chemical similarity among the different actinyls. Surprisingly, the difference in D^0 for the Np(vi)/Np(v) pair is small experimentally⁶⁴ (~ 0.8 and $\sim 0.7 \times 10^{-5}$ cm² s⁻¹) and in our model, a common value ($\sim 1.2 \times 10^{-5}$ cm² s⁻¹), despite the difference in the solute-solvent interaction strength manifested by the ΔH_{hyd} values. Thus, the hydrodynamic radius dominates actinyl diffusion, which is very similar for both mono- and di-valent cations, in fact the minimum for the Np-O radial distribution functions (RDFs) enclosing the first hydration shell are 6.3 and 6.0 Å for Np(v) and Np(vi), respectively.

C. Normal mode frequencies

The MD and experimental normal mode frequencies of the aqua ions in solution are presented in Table II. The selected normal modes are the symmetric and antisymmetric An-O_{yl} stretching of the irreducible representation $1A_1$ and A_2 , respectively; the actinyl bending, E_1 , and the water breathing stretching $2A_1$. The frequencies were calculated from the Fourier transforms of the velocity autocorrelation functions of generalized coordinates associated with these motions. Details of the procedure can be found elsewhere.²¹ Unlike most force fields, our normal mode frequencies incorporate all the anharmonicities of the *ab initio* potential energy surface.

Our frequencies agree reasonably with the experiment having a maximum relative error of 15%. All the frequencies overestimate the infrared and Raman spectroscopy data. A bias of the B3LYP potential energy surface could cause this. The hydrated uranyl ion

TABLE II. Experimental and MD normal mode frequencies in cm^{-1} . The uncertainty of the results is $\pm 5 \text{ cm}^{-1}$. All experimental symmetric and antisymmetric values are from Refs. 68 and 69, respectively.

System	Method	E_1	$2A_1$	$1A_1$	A_2
$[\text{UO}_2\cdot(\text{H}_2\text{O})_5]^{2+}(\text{aq})$	MD	252	338	1004	1101
	Expt.	253 ± 10		870 ± 10	965 ± 1
$[\text{NpO}_2\cdot(\text{H}_2\text{O})_5]^{2+}(\text{aq})$	MD	265	374	976	1073
	Expt.			863 ± 5	969 ± 1
$[\text{NpO}_2\cdot(\text{H}_2\text{O})_5]^+(\text{aq})$	MD	295	270	839	875
	Expt.			824 ± 4	863 ± 5
$[\text{PuO}_2\cdot(\text{H}_2\text{O})_5]^{2+}(\text{aq})$	MD	297	361	890	1048
	Expt.			835 ± 5	962 ± 1
$[\text{AmO}_2\cdot(\text{H}_2\text{O})_5]^{2+}(\text{aq})$	MD	309	353	882	957
	Expt.				939 ± 1

gas phase QM frequencies (within the harmonic approximation) are 224 cm^{-1} , 314 cm^{-1} , 945 cm^{-1} , and 1028 cm^{-1} for E_1 , $2A_1$, $1A_1$, and A_2 , respectively. If the frequencies are calculated from a gas phase simulation of hydrated uranyl using the classical force field at 300 K, the values obtained are 256 cm^{-1} , 286 cm^{-1} , 977 cm^{-1} , and 1027 cm^{-1} for E_1 , $2A_1$, $1A_1$, and A_2 , respectively. The comparison between these two sets of frequencies proves that the bias in the frequencies is due to the level of theory and not to the ability of the potential to reproduce the PES. The frequencies of the interaction potential even in a perfect fit situation are always going biased by the quantum-mechanical level used to calculate the PES. This means, if it was necessary to improve normal mode frequencies prediction, our force field development procedure could be used with a higher level of theory.

D. Hydration structure of actinyls in aqueous solution

The properties involving the second hydration shell of the hexavalent actinyls are statistically equivalent since all An(vi) present similar An–O distances (Table I) and their radial distribution functions nearly overlap (see Fig. S2 in the supplementary material). Our An–O distances agree with those obtained by Maginn and col.²⁴ from molecular dynamic simulations using their model force field within the hundredth of an angstrom. Due to this strong analogy of the hexavalent aqua ions, the conclusions of our previous work on uranyl²¹ generalize to all actinyl dicitations as we have found for diffusion and hydration enthalpies. Our model describes the hydration of hexavalent actinyls as cations which equatorially have conventional monoatomic cation solvation and axially hydrophobic caps around the O_{y1} oxygens. Figure 2 depicts this behavior where two simulation snapshots of U(vi) with second-shell equatorial water molecules colored in blue [Fig. 2(a)] and axial water molecules in orange [Fig. 2(b)] are shown. Equatorial water molecules form typical hydrogen bonds (HBs) with first-shell water molecules as present in most metal cations. By contrast, axial solvent molecules form HB with other solvent molecules around the O_{y1} atoms but without directly interacting with it. This last type of solvation is analogous to that of *hydrophobic* solutes like methane.⁷⁰ Figure 3 shows the Spatial Distribution Function (SDF) of bulk water oxygen atoms around

the hydrated ion, and the presence of different solvation zones is clear.

We will now compare the hydration structure of the Np(vi)/Np(v) revealing the effect of the charge. Figure 4 shows the Np–O and Np–H radial distribution functions (RDFs) of the neptunyl aqua ion in both oxidation states. Np–O RDFs [Fig. 4(a)] show the intense peaks corresponding to first-shell atom types: O_{y1}, O₁. Both radial distributions have very similar shapes except for a slightly lower intensity and a shift toward longer distances in Np(v). The Np–O distances are longer for Np(v) than for Np(vi) as a consequence of the smaller charge. This effect is more pronounced for the first and second hydration shells which lengthen their Np–O distances 0.15 Å and 0.11 Å, when going from NpO_2^{2+} to NpO_2^+ , than for the Np–O_{y1} distance that only increases 0.06 Å. This may be understood on the basis that the Np–O interactions are mostly electrostatic, whereas the Np–O_{y1} oxo bonds are mostly covalent.

The integration of the Np–O_W RDFs up to their second shell minima (6.0 Å for NpO_2^{2+} and 6.3 Å NpO_2^+) gives running integration numbers of 29 for Np(vi) and 32 for Np(v). As happened in $[\text{UO}_2]^{2+}$,²¹ the Np(vi) value is higher than for the rest of

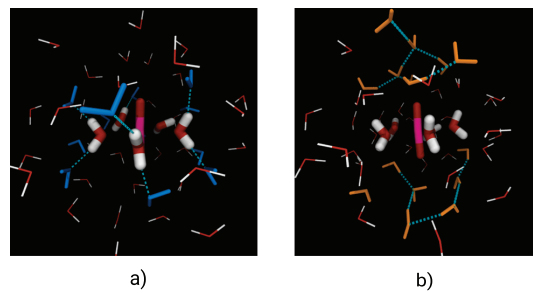


FIG. 2. Images (a) and (b) are snapshots of the MD trajectory highlighting equatorial (blue) and axial (orange) second-shell water molecules of the actinyl hexavalent aquaion.

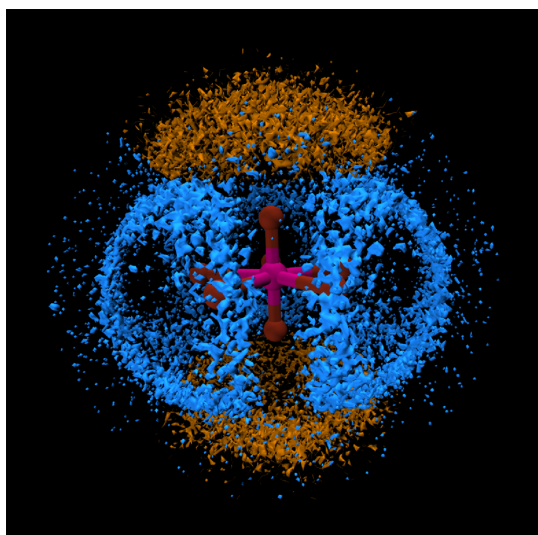


FIG. 3. Spatial distribution function (SDF) of solvent molecules around the actinyl hexavalent aquaion. The axial solvation shell is colored in orange and the equatorial solvation shell in blue.

literature values, both theoretical^{1 3-1 5 18-20,24} and experimental^{3,16} which oscillate between 14 and 19. No experimental values are available for Np(v), the CPMD simulation of Odoh *et al.*²² on $[\text{PuO}_2]^{+}$ gives a value of ~ 22 . First-shell water molecules of typical highly

charged monoatomic cations are expected on average to form two HBs with the second shell therefore having in the second shell about twice the number of first-shell water molecules.^{71,72} Our values are about three times the first-shell coordination number.

Actinyls have a non-spherically symmetric complex hydration structure. The use of a spherically averaged function like the total RDF may lead to a misinterpretation, in the present case overestimating the CN. If the total An-O RDF is integrated up to $\sim 6.3 \text{ \AA}$ [see Fig. 4(a)], it will include the true first shell of water molecules (axial and equatorial) but also the intermediate ones which may be assigned to either. A proper CN can be computed avoiding this artifact by using the multisite cavity CN definition which is adequate for non-spherical solvation environments.⁷³ The multisite cavity CN is defined as the average number of water molecules within overlapping spheres centered on solvent-exposed atoms (O_{yl} and O_{l}). The radii of these spheres correspond to the minima above the first peak of angle-solved X-Ow RDFs. This multisite cavity contains the molecules that must be considered primarily to be solvating the $[\text{AnO}_2(\text{H}_2\text{O})_5]^{2+/+}$ cation. With this definition, the second shell CN for Np(vi)/Np(v) is, respectively, 22 and 25. We attribute the difference in CN to the uncertainty in the definition of the cavity radii. These values are close to the values of the literature obtained by integrating the total RDF and are consistent with our analysis of the angle-solved RDFs. Our actinyl models have more anisotropic hydration than those of the literature which creates a larger discrepancy between RDF-CN and multisite cavity CN. The cause for this is the specific charge transfer and polarization suffered by the first-shell water molecules which unlike other classical potentials are different from bulk water molecules. The other possible way to explicitly include this charge transfer in simulation would be to use *ab initio* MD simulations, but its computational cost is too high to study systems big enough to accommodate a well defined second

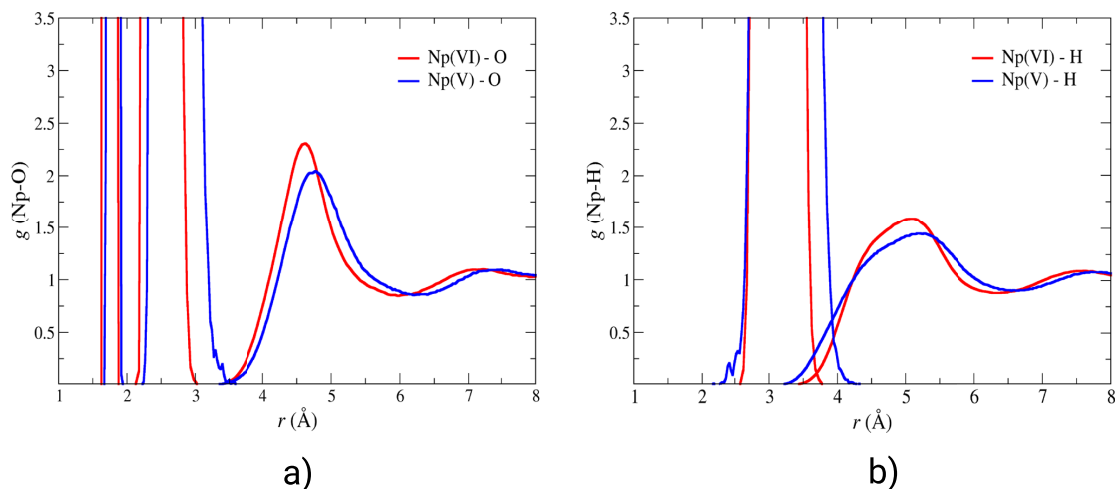


FIG. 4. An-O (a) and An-H (b) RDFs for $[\text{NpO}_2(\text{H}_2\text{O})_5]^{2+}$ (red) and $[\text{NpO}_2(\text{H}_2\text{O})_5]^+$ (blue).

shell. This issue has been examined in greater detail in our previous studies.^{21,73}

As previously discussed, portraying actinyls with total RDFs can lead to artifacts in the analysis. Therefore, three hydration regions are defined using the molecular axis of the actinyl as reference. The axial region is defined by azimuthal angles from 0° to 30° with respect to both $\text{Np}-\text{O}_{\text{yl}}$ [Fig. 5(c)]. Likewise, the intermediate and equatorial regions scan the angular ranges of 30° - 60° and 60° - 90° , respectively. The $\text{Np}-X$ angle-solved RDFs and the region definitions are given in Fig. 5.

The equatorial $\text{Np}-\text{O}_w$ RDFs have maxima at 4.62 \AA for $\text{Np}(\text{vi})$ and 4.74 \AA for $\text{Np}(\text{v})$ both integrating to 10 water molecules. The relative position of the equatorial $\text{Np}-\text{H}_w$ RDFs with respect to O_w shows that equatorial second-shell water molecules form well defined HBs with the first hydration shell. Both these facts depict an equatorial solvation shell that follows the typical monoatomic cation structure. The main differences between the RDFs of $\text{Np}(\text{vi})$ and $\text{Np}(\text{v})$ is that the RDF of the pentavalent cation second-shell peaks 0.1 \AA further away and that ends with an inflection point at 5.5 \AA , and not a minimum, lacking a third solvation shell [see bottom of Fig. 4(b)]. The inflection point evidences that the water structure becomes bulk-like immediately after the second-shell as is the case for other monovalent cations.^{74,75} For $\text{Np}(\text{vi})$, the structure-making effect of the cation is more long ranged and even a third solvation shell is weakly observed.

The axial and intermediate angle-solved RDFs are similar for both oxidation states (see top and center plots in Fig. 5). Their main difference is that the axial $\text{Np}(\text{v})-\text{H}_w$ angle-solved RDF is broader and approaches more the central atom. The coordination numbers for the axial and intermediate regions are 4 and 12 regardless of the aqua ion charge. For both valencies, the equatorial second-shell ends at shorter distances than the total RDF. Thus the integration of the total RDF captures hydration not only from the equatorial region but also from the axial and intermediate shells whose RDFs finish more than 1 \AA further away. The intermediate region plays the role of a bridge that smoothly transitions the solvent behavior from axial to equatorial.

The absence or presence of solvent HBs with the O_{yl} atom is an ongoing debate in the literature^{13-20,24} because it would define the O_{yl} atom as *hydrophobic* or *hydrophilic*. In our $[\text{UO}_2\cdot(\text{H}_2\text{O})_5]^{2+}(\text{aq})$ model,²¹ there was no HB formation and clathrate-like structures were observed in the axial regions. In these structures, water molecules form HB among them rather than with the O_{yl} atom [see Fig. 2(b)]. In Fig. 6, we present the angle-solved $\text{O}_{\text{yl}}-\text{X}$ RDFs for the 0° - 90° region of $[\text{NpO}_2\cdot(\text{H}_2\text{O})_5]^{2+/+}(\text{aq})$. For both oxidation states, the overall shapes are similar. The RDFs have features that led to the same conclusion: the water molecules are far away from the O_{yl} atom ($\sim 3.5 \text{ \AA}$) and the $\text{O}_{\text{yl}}-\text{H}_w$ and $\text{O}_{\text{yl}}-\text{O}_w$ overlap significantly, i.e., there is no preferential water orientation involving HBs with O_{yl} . In summary, across the series and for both oxidation states, the axial

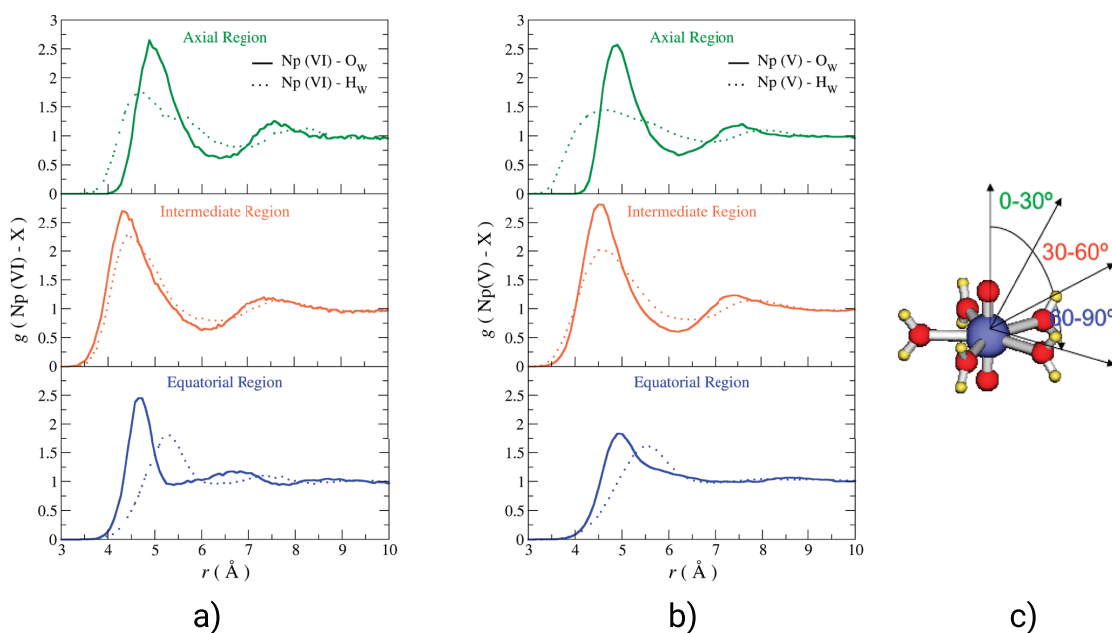


FIG. 5. $\text{An}-\text{O}_w$ (solid lines) and $\text{An}-\text{H}_w$ (dotted lines) angle-solved (0° - 90°) RDF for $[\text{NpO}_2\cdot(\text{H}_2\text{O})_5]^{2+}$ (a) and $[\text{NpO}_2\cdot(\text{H}_2\text{O})_5]^+$ (b) for their axial, intermediate, and equatorial regions. (c) defines the angular regions of $[\text{AnO}_2]^{2+/+}$.

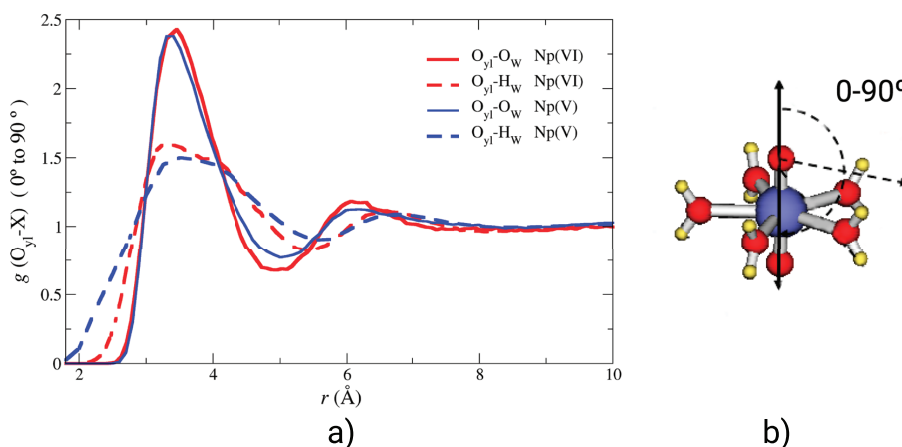


FIG. 6. (a) $O_{yl}-O_w$ (solid lines) and $O_{yl}-H_w$ (dotted lines) angle-solved RDFs (0-90°) in $[NpO_2 \cdot (H_2O)_5]^{2+}$ (red) and $[NpO_2 \cdot (H_2O)_5]^+$ (blue). (b) defines the angular regions of the O_{yl} atom.

region is *hydrophobic* and no HB formation with the O_{yl} atom is observed.

The overall picture of the actinyls studied in this work is similar to $[UO_2 \cdot (H_2O)_5]^{2+}$. The aqua ion has the typical monoatomic cation second-shell hydration structure equatorially and is capped at the poles by clathrate-like regions.

E. Second-shell water mean residence times

Mean residence times (MRTs) for the second-shell water molecules were calculated using the method of Impey *et al.*⁷⁶ With this method, the water molecules are allowed for leaving the shell and return for a time t^* without losing their assignment to the region. We use the values of $t_{2nd\ shell}^* = 0$ ps and 2 ps which are the most common values in the literature^{76,77} and allow us to establish a reasonable range to estimate this property. The MRTs of the different hexavalent actinyls are statistically identical (see Table I). Therefore, as we have established

for most of the properties, the conclusions obtained previously for uranyl²¹ apply to the other elements. We will now compare Np(vi) and Np(v) to discuss the charge effect on the MRT, and their values are collected in Table III.

The total MRT for second-shell water molecules of $[NpO_2 \cdot (H_2O)_5]^{2+}$ is higher than for other doubly charged atomic cations like Mg^{2+} where typical values are 3 ps and 14 ps for $t_{2nd\ shell}^* = 0$ ps and 2 ps, respectively.²⁸ But it is surprising that despite its lower charge, $[NpO_2 \cdot (H_2O)_5]^+$ also has total MRTs higher than Mg^{2+} . This is mostly likely due to the large volume of the $[NpO_2]^{2+/+}$ second shell which is comparable for both oxidation states.

If we compare the angle-solved MRTs of the two oxidation states, we obtain the same ordering of the regions. For $t_{2nd\ shell}^* = 2$ ps, in particular, the region with the highest MRT is the equatorial region, followed by the intermediate region and the axial region, since the equatorial and bridge regions can form HBs with the first shell and the axial region is dominated by water-water interactions. The most remarkable feature of the MRTs is that in both cases for

TABLE III. Mean residence times (ps) of H_2O in the second shell of $[NpO_2]^{2+/+}$ obtained with the method of Impey *et al.*⁷⁶ and their decomposition in the angular regions of Fig. 5(c). MRTs of TIP4P water in the first shell of another water molecule in pure water are ~1.4 ps and ~4.2 ps for $t^* = 0$ ps and $t^* = 2$ ps, respectively. The uncertainties are standard errors.

System	$[NpO_2 \cdot (H_2O)_5]^{2+}$		$[NpO_2 \cdot (H_2O)_5]^+$	
	$t_{2nd\ shell}^* = 0$ ps	$t_{2nd\ shell}^* = 2$ ps	$t_{2nd\ shell}^* = 0$ ps	$t_{2nd\ shell}^* = 2$ ps
Total	6.9 ± 0.2	15.9 ± 0.5	5.1 ± 0.3	13.4 ± 0.5
$0^\circ-30^\circ$ (axial)	0.79 ± 0.04	4.8 ± 0.4	0.60 ± 0.02	4.6 ± 0.2
$30^\circ-60^\circ$ (intermediate)	0.60 ± 0.01	6.88 ± 0.07	0.47 ± 0.01	6.9 ± 0.6
$60^\circ-90^\circ$ (equatorial)	1.41 ± 0.04	8.6 ± 0.2	1.66 ± 0.06	9.9 ± 0.2

$t_{2\text{nd shell}}^*$ = 2 ps, the axial MRT is larger than the MRT of a TIP4P water molecule in the first-shell of another water molecule. Therefore, there is a local reinforcement of the water structure around the O_{yl} atom without direct interaction with it. This is a dynamical property characteristic of clathrate-like hydration around a hydrophobic solute.^{70,78}

IV. CONCLUSIONS

We have successfully applied the hydrated ion methodology developed for U(vi)²¹ to the actinyl series by changing both the charge and the actinide element. The IW1 and IMC interaction potentials in addition to a transferred HIW potential from [UO₂]²⁺ correctly model the potential energy surface.

The simulation results agree satisfactorily with experimental evidence of multiple nature: structural, dynamical, and thermodynamical, validating therefore interaction potentials for further studies. Besides first-shell distances, the solvation properties of all hexavalent actinyls are indistinguishable, despite the specificity of the IW1 potential and partial charges. This suggests the possibility of using the uranyl cation as a reference for the study of systems where other actinyls are involved as long as the integrity of the aqua ion is preserved. Comparing Np(vi) and Np(v), we found that their structure and dynamics are rather similar apart from the logical small lengthening of An–O_{yl} and An–O_w distances and a small shortening in second shell MRTs due to the decrease in the total charge.

The hydration picture of a general An(v,vi) is remarkably similar to that of U(vi). Actinyls are anisotropic amphiphilic solutes which display a conventional metal ion equatorial solvation shell capped at the poles by clathrate-like solvent structures, mediated by bridge water molecules in the intermediate regions.

SUPPLEMENTARY MATERIAL

See [supplementary material](#) for all the actinyl hydrated ion force field parameters, additional RDFs, and interaction energy scans.

ACKNOWLEDGMENTS

This work was financially supported Junta de Andalucía of Spain (No. FQM-282) and the Spanish Ministry of Education, Culture, and Sports for Sergio Pérez-Conesa's Ph.D. scholarship FPU (Formación de Profesorado Universitario).

REFERENCES

- ¹S. Cotton, *Lanthanide and Actinide Chemistry* (Wiley, London, 2006).
- ²C. M. N. Bardin and P. Rubini, *Radiochim. Acta* **83**, 189 (1998) and references therein.
- ³M. Aaberg, D. Ferri, J. Glaser, and I. Grenthe, *Inorg. Chem.* **22**, 3986 (1983).
- ⁴P. G. Allen, J. J. Bucher, D. K. Shuh, N. M. Edelstein, and T. Reich, *Inorg. Chem.* **36**, 4676 (1997).
- ⁵S. D. Conradson, *Appl. Spectrosc.* **52**, 252A (1998).
- ⁶U. Wahlgren, H. Moll, I. Grenthe, B. Schimmelpfennig, L. Maron, V. Vallet, and O. Groen, *J. Phys. Chem. A* **103**, 8257 (1999).
- ⁷J. Neufeind, L. Soderholm, and S. Skanthakumar, *J. Phys. Chem. A* **108**, 2733 (2004).
- ⁸L. Soderholm, S. Skanthakumar, and J. Neufeind, *Anal. Bioanal. Chem.* **383**, 48 (2005).
- ⁹J. M. McKibben, *Radiochim. Acta* **36**, 3 (1984).
- ¹⁰M. Altmaier, X. Gaona, and T. Fanghänel, *Chem. Rev.* **113**, 901 (2013).
- ¹¹C. Riddle, K. Czerwinski, E. Kim, P. Paviet, P. Weck, F. Poineau, and S. Conradson, *J. Radioanal. Nucl. Chem.* **309**, 1087 (2016).
- ¹²K. Maher, J. R. Bargar, and G. E. Brown, *Inorg. Chem.* **52**, 3510 (2013).
- ¹³P. Guillaud and G. Wipff, *J. Phys. Chem.* **97**, 5685 (1993).
- ¹⁴P. Guillaud and G. Wipff, *J. Mol. Struct.: THEOCHEM* **366**, 55 (1996).
- ¹⁵S. Kerisit and C. Liu, *Geochim. Cosmochim. Acta* **74**, 4937 (2010).
- ¹⁶D. Hagberg, G. Karlström, B. O. Roos, and L. Gagliardi, *J. Am. Chem. Soc.* **127**, 14250 (2005).
- ¹⁷N. Rai, S. P. Tiwari, and E. J. Maginn, *J. Phys. Chem. B* **116**, 10885 (2012).
- ¹⁸P. Nichols, E. J. Bylaska, G. K. Schenter, and W. de Jong, *J. Chem. Phys.* **128**, 124507 (2008).
- ¹⁹R. J. Frick, T. S. Hofer, A. B. Pribil, B. R. Randolph, and B. M. Rode, *J. Phys. Chem. A* **113**, 12496 (2009).
- ²⁰M. Bühl, H. Kabrede, R. Diss, and G. Wipff, *J. Am. Chem. Soc.* **128**, 6357 (2006).
- ²¹S. Pérez-Conesa, F. Torrico, J. M. Martínez, R. R. Pappalardo, and E. Sánchez Marcos, *J. Chem. Phys.* **145**, 224502 (2016).
- ²²S. O. Odoh, E. J. Bylaska, and W. A. De Jong, *J. Phys. Chem. A* **117**, 12256 (2013).
- ²³R. Car and M. Parrinello, *Phys. Rev. Lett.* **55**, 2471 (1985).
- ²⁴V. Pomogaev, S. P. Tiwari, N. Rai, G. S. Goff, W. Runde, W. F. Schneider, and E. J. Maginn, *Phys. Chem. Chem. Phys.* **15**, 15954 (2013).
- ²⁵R. R. Pappalardo and E. Sánchez Marcos, *J. Phys. Chem.* **97**, 4500 (1993).
- ²⁶R. R. Pappalardo, J. M. Martínez, and E. Sánchez Marcos, *J. Phys. Chem.* **100**, 11748 (1996).
- ²⁷J. M. Martínez, R. R. Pappalardo, and E. Sánchez Marcos, *J. Chem. Phys.* **109**, 1445 (1998).
- ²⁸J. M. Martínez, R. R. Pappalardo, and E. Sánchez Marcos, *J. Am. Chem. Soc.* **121**, 3175 (1999).
- ²⁹D. T. Richens, *The Chemistry of Aqua Ions* (J. Wiley, West Sussex, England, 1997).
- ³⁰J. M. Martínez, F. Torrico, R. R. Pappalardo, and E. Sánchez Marcos, *J. Phys. Chem. B* **108**, 15851 (2004).
- ³¹F. Torrico, R. R. Pappalardo, E. S. Marcos, and J. M. Martínez, *Theor. Chem. Acc.* **115**, 196 (2006).
- ³²F. Carrera, F. Torrico, D. T. Richens, A. Muñoz-Páez, J. M. Martínez, R. R. Pappalardo, and E. Sánchez Marcos, *J. Phys. Chem. B* **111**, 8223 (2007).
- ³³S. Pérez-Conesa, J. M. Martínez, R. R. Pappalardo, and E. Sánchez Marcos, *Inorg. Chem.* **57**, 8089 (2018).
- ³⁴W. L. Jorgensen, J. Chandrasekhar, J. D. Madura, R. W. Impey, and M. L. Klein, *J. Chem. Phys.* **79**, 926 (1983).
- ³⁵L. Helm and A. E. Merbach, *Chem. Rev.* **105**, 1923 (2005).
- ³⁶A. F. Panasci, "Ligand exchange kinetics of environmentally relevant metals," Ph.D. thesis, University of California, Davis, 2014.
- ³⁷A. D. Becke, *J. Chem. Phys.* **98**, 5648 (1993).
- ³⁸P. J. Stephens, F. J. Devlin, C. F. Chabalowski, and M. J. Frisch, *J. Phys. Chem.* **98**, 11623 (1994).
- ³⁹D. E. Woon and T. H. Dunning, Jr., *J. Chem. Phys.* **98**, 1358 (1993).
- ⁴⁰W. Küchle, M. Dolg, H. Stoll, and J. Preuss, *J. Chem. Phys.* **100**, 7535 (1994).
- ⁴¹M. J. Frisch, G. W. Trucks, H. B. Schlegel, G. E. Scuseria, M. A. Robb, J. R. Cheeseman, G. Scalmani, V. Barone, B. Mennucci, G. A. Petersson, H. Nakatsuji, M. Caricato, X. Li, H. P. Hratchian, A. F. Izmaylov, J. Bloino, G. Zheng, J. L. Sonnenberg, M. Hada, M. Ehara, K. Toyota, R. Fukuda, J. Hasegawa, M. Ishida, T. Nakajima, Y. Honda, O. Kitao, H. Nakai, T. Vreven, J. A. Montgomery, Jr., J. E. Peralta, F. Ogliaro, M. Bearpark, J. J. Heyd, E. Brothers, K. N. Kudin, V. N. Staroverov, R. Kobayashi, J. Normand, K. Raghavachari, A. Renndell, J. C. Burant, S. S. Iyengar, J. Tomasi, M. Cossi, N. Rega, J. M. Millam, M. Klene, J. E. Knox, J. B. Cross, V. Bakken, C. Adamo, J. Jaramillo, R. Gomperts, R. E. Stratmann, O. Yazyev, A. J. Austin, R. Cammi, C. Pomelli, J. W. Ochterski, R. L. Martin, K. Morokuma, V. G. Zakrzewski, G. A. Voth, P. Salvador, J. J. Dannenberg, S. Dapprich, A. D. Daniels, Ö. Farkas, J. B. Foresman, J. V. Ortiz, J. Cioslowski, and D. J. Fox, GAUSSIAN09 Revision D.01, 2009.
- ⁴²U. C. Singh and P. A. Kollman, *J. Comput. Chem.* **5**, 129 (1984).
- ⁴³B. H. Besler, K. M. Merz, and P. A. Kollman, *J. Comput. Chem.* **11**, 431 (1990).

- ⁴⁴J. Tomasi, B. Mennucci, and R. Cammi, *Chem. Rev.* **105**, 2999 (2005).
- ⁴⁵B. Siboulet, C. J. Marsden, and P. Vitorge, *Chem. Phys.* **326**, 289 (2006).
- ⁴⁶V. Vallet, P. Macak, U. Wahlgren, and I. Grentle, *Theor. Chem. Acc.* **115**, 145 (2006).
- ⁴⁷K. Balasubramanian and Z. Cao, *Inorg. Chem.* **46**, 10510 (2007).
- ⁴⁸C. Clavaguera-Sarrio, V. Vallet, D. Maynau, and C. J. Marsden, *J. Chem. Phys.* **121**, 5312 (2004).
- ⁴⁹D. Majumdar, K. Balasubramanian, and H. Nitsche, *Chem. Phys. Lett.* **361**, 143 (2002).
- ⁵⁰C. Angeli, R. Cimiraglia, S. Evangelisti, T. Leininger, and J.-P. Malrieu, *J. Chem. Phys.* **114**, 10252 (2001).
- ⁵¹C. Angeli, R. Cimiraglia, and J.-P. Malrieu, *Chem. Phys. Lett.* **350**, 297 (2001).
- ⁵²C. Angeli, R. Cimiraglia, and J.-P. Malrieu, *J. Chem. Phys.* **117**, 9138 (2002).
- ⁵³F. Neese, *Wiley Interdiscip. Rev.: Comput. Mol. Sci.* **2**, 73 (2012).
- ⁵⁴A. Schäfer, C. Huber, and R. Ahlrichs, *J. Chem. Phys.* **100**, 5829 (1994).
- ⁵⁵T. F. Miller, M. Eleftheriou, P. Pattnaik, A. Ndirango, D. Newns, and G. J. Martyna, *J. Chem. Phys.* **116**, 8649 (2002).
- ⁵⁶I. T. Todorov, W. Smith, K. Trachenko, and M. T. Dove, *J. Mater. Chem.* **16**, 1911 (2006).
- ⁵⁷J. K. Gibson, R. G. Haire, M. Santos, J. Marçalo, and A. de Matos, *J. Phys. Chem. A* **109**, 2768 (2005).
- ⁵⁸Y. Marcus and A. Loewenschuss, *J. Chem. Soc., Faraday Trans.* **82**, 2873 (1986).
- ⁵⁹L. V. Moskaleva, A. V. Matveev, S. Krüger, and N. Rösch, *Chem. - Eur. J.* **12**, 629 (2006).
- ⁶⁰I.-C. Yeh and G. Hummer, *J. Phys. Chem. B* **108**, 15873 (2004).
- ⁶¹S. P. Tiwari, N. Rai, and E. J. Maginn, *Phys. Chem. Chem. Phys.* **16**, 8060 (2014).
- ⁶²S. Kerisit and C. Liu, *J. Phys. Chem. A* **117**, 6421 (2013).
- ⁶³M. Chopra and N. Choudhury, *J. Phys. Chem. B* **118**, 14373 (2014).
- ⁶⁴I.-P. Simonin, I. Billard, H. Hendrawan, O. Bernard, K. Lützenkirchen, and L. Semon, *Phys. Chem. Chem. Phys.* **5**, 520 (2003).
- ⁶⁵G. Marx, R. Gauglitz, V. Friehmelt, and K. H. Feldner, *J. Less-Common Met.* **122**, 185 (1986).
- ⁶⁶D. M. H. Kern and E. F. Orlemann, *J. Am. Chem. Soc.* **71**, 2102 (1949).
- ⁶⁷J.-M. Andanson, M. Traïkia, and P. Husson, *J. Chem. Thermodyn.* **77**, 214 (2014).
- ⁶⁸L. H. Jones and R. A. Penneman, *J. Chem. Phys.* **21**, 542 (1953).
- ⁶⁹L. J. Basile, J. C. Sullivan, J. R. Ferraro, and P. LaBonville, *Appl. Spectrosc.* **28**, 142 (1974).
- ⁷⁰P. Ball, *Chem. Rev.* **108**, 74 (2008).
- ⁷¹H. Ohtaki and T. Radnai, *Chem. Rev.* **93**, 1157 (1993).
- ⁷²Y. Marcus, *Chem. Rev.* **88**, 1475 (1988).
- ⁷³A. Melchior, J. M. Martínez, R. R. Pappalardo, and E. Sánchez Marcos, *J. Chem. Theory Comput.* **9**, 4562 (2013).
- ⁷⁴M. L. San-Román, M. Carrillo-Tripp, H. Saint-Martin, J. Hernández-Cobos, and I. Ortega-Blake, *Theor. Chem. Acc.* **115**, 177 (2006).
- ⁷⁵K. Morimoto, M. Kato, H. Uno, A. Hanari, T. Tamura, H. Sugata, T. Sunaoshi, and S. Kono, *J. Phys. Chem. Solids* **66**, 634 (2005).
- ⁷⁶R. W. Impey, P. A. Madden, and I. R. McDonald, *J. Phys. Chem.* **87**, 5071 (1983).
- ⁷⁷A. E. García and L. Stiller, *J. Comput. Chem.* **14**, 1396 (1993).
- ⁷⁸E. I. Martín, J. M. Martínez, and E. Sánchez Marcos, *J. Chem. Phys.* **143**, 044502 (2015).

SUPPORTING INFORMATION

A general study of actinyl hydration by molecular dynamics simulations using *ab initio* force fields.

Sergio Pérez-Conesa, Francisco Torrico, José M. Martínez, Rafael R. Pappalardo

and Enrique Sánchez Marcos

*Departamento de Química Física, Universidad de Sevilla,
41012 Sevilla, Spain. e-mail:sanchez@us.es*



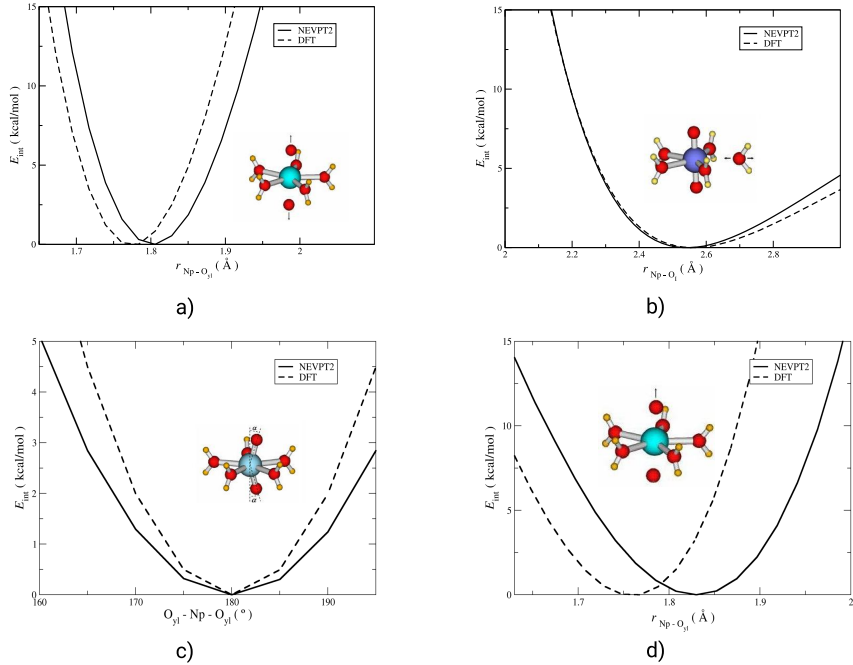


Figure S1: Interaction energy scans of $[\text{NpO}_2 \cdot (\text{H}_2\text{O})_5]^+$ obtained with NEVPT2 calculations (solid line) and DFT (dashed line). In scan a) the oxo-bonds are varied symmetrically and in scan, b) the water molecule is moved radially, c) the O_{y1} -Np- O_{y1} angle is varied, d) one of the oxo-bonds is varied and the other kept at the equilibrium distance. NEVPT2 calculations which incorporate both dynamical and static electronic correlation explicitly were carried out. We remind the reader that B3LYP also includes static electron correlation but within a mean field approximation.

Table S1: First-shell water geometry in Å and degrees. For Np(V) the first shell water molecules have the geometry (including the massless particle) of TIP4P.

	First-shell geometry				
	U	Np(VI)	Np(V)	Pu(VI)	Am(VI)
R(O _I – H _I)	0.97	0.97	0.95723	0.97	0.97
H _I O _I H _I	106.6	106.6	104.52	106.6	106.2

Table S2: Effective Merz-Kollmann charges of [AnO₂·(H₂O)₅]^{+/2+}(aq) using the PCM to model the bulk solvent using as radii 2.65 Å, 1.40 Å and 1.20 Å for An, O and H respectively. For [NpO₂·(H₂O)₅]⁺ the first shell water molecules have the same structure and partial charges as the TIP4P model.

	Partial Charge (a.u.)				
	U	Np(VI)	Np(V)	Pu(VI)	Am(VI)
q_{An}	2.80	2.71	2.52	2.62	2.59
$q_{\text{O}_{\text{y}1}}$	-0.55	-0.50	-0.76	-0.47	-0.38
q_{O}	-1.05	-1.04	0.0	-1.04	-1.06
q_{H}	0.55	0.55	0.52	0.55	0.55
q_{q}	-	-	-1.04	-	-

Table S3: Coefficients of the IW1 interaction potentials, root mean square error (RMSE) of the fit and shift values. Their units are kcal mol⁻¹ Å⁻ⁿ and kcal mol⁻¹.

Coefficients	U	Np(VI)	Np(V)	Pu(VI)	Am(VI)
$C_4^{\text{AnO}_1}$	-6388.86	781.099	0.0	-6343.16	-3847.25
$C_6^{\text{AnO}_1}$	52787.05	-14881.6	-21667.67	63274.85	28895.08
$C_8^{\text{AnO}_1}$	-131984.94	75576.2	139543.16	-188099.67	-56776.53
$C_{12}^{\text{AnO}_1}$	476950.29	-247512	-761189.70	714067.88	180662.05
$C_4^{\text{O}_{\text{y}1}\text{O}_1}$	1696.66	-2989.75	0.0	4225.93	1329.48
$C_6^{\text{O}_{\text{y}1}\text{O}_1}$	-8196.99	39404.6	17317.38	-70487.33	-5640.56
$C_8^{\text{O}_{\text{y}1}\text{O}_1}$	18165.85	-140671	-101999.72	365255.74	318.75
$C_{12}^{\text{O}_{\text{y}1}\text{O}_1}$	-30202.92	637345	756412.76	-2718499.04	235669.93
RMSE	0.6	1.4	0.6	1.6	0.8

Table S4: Coefficients from the fitting of the IMC interaction potentials, RMSE_{total}, RMSE_{partial} which is computed for points with energy lower than 15 kcal mol⁻¹ with respect to the interaction energy of the minimum and shift values. Their units are kcal mol⁻¹ Å⁻ⁿ and kcal mol⁻¹.

Coefficients	U	Np(VI)	Np(V)	Pu(VI)	Am(VI)
$C_4^{\text{AnO}_y}$	-133370.94	-136859.23	-74453.49	842.00	-141079.35
$C_6^{\text{AnO}_y}$	668178.78	676835.56	403271.32	-28267.67	691027.72
$C_8^{\text{AnO}_y}$	-1059978.49	-1067029.16	-695592.42	74562.59	-1078152.49
$C_{12}^{\text{AnO}_y}$	949717.97	953580.31	754700.69	94491.15	938322.18
$C_4^{\text{O}_y\text{O}_y}$	-167679.49	-210487.33	-1270195.07	-4881731.10	-305210.33
$C_6^{\text{O}_y\text{O}_y}$	4369622.37	6034823.14	29013046.5	102789274.00	7544789.67
$C_8^{\text{O}_y\text{O}_y}$	-33177820.27	-45743307.84	-207350887	-680306326.00	-53292782.03
$C_{12}^{\text{O}_y\text{O}_y}$	605633365.20	779053537.28	3673600800	10352292900	840547323.14
RMSE _{total}	3.4	3.6	3.3	1.3	2.3
RMSE _{partial}	0.4	1.0	1.4	0.9	0.6

Table S5: Coefficients of the HIW interaction potential from previous work. They are used for all actinyls. RMSE_{total} and RMSE_{partial} which is computed for points with energy lower than 15 kcal mol⁻¹ with respect to the interaction energy of the minimum. The units are kcal mol⁻¹ Å⁻ⁿ and kcal mol⁻¹.

Coefficients	An(VI,V)	Coefficients	An(VI,V)
$C_4^{\text{UO}_w}$	18578.27	$C_4^{\text{O}_i\text{O}_w}$	-830.40
$C_6^{\text{UO}_w}$	-288922.08	$C_6^{\text{O}_i\text{O}_w}$	6718.50
$C_8^{\text{UO}_w}$	1481816.44	$C_8^{\text{O}_i\text{O}_w}$	-4208.51
$C_{12}^{\text{UO}_w}$	-12631787.76	$C_{12}^{\text{O}_i\text{O}_w}$	-3888.10
$C_4^{\text{UH}_w}$	-5094.89	$C_4^{\text{O}_i\text{H}_w}$	28.22
$C_6^{\text{UH}_w}$	65098.47	$C_6^{\text{O}_i\text{H}_w}$	100.59
$C_8^{\text{UH}_w}$	-268274.37	$C_8^{\text{O}_i\text{H}_w}$	-40.17
$C_{12}^{\text{UH}_w}$	1482339.87	$C_{12}^{\text{O}_i\text{H}_w}$	1.06
$C_4^{\text{O}_y\text{O}_w}$	-1503.86	$C_4^{\text{H}_i\text{O}_w}$	-64.73
$C_6^{\text{O}_y\text{O}_w}$	10373.23	$C_6^{\text{H}_i\text{O}_w}$	166.44
$C_8^{\text{O}_y\text{O}_w}$	-15794.55	$C_8^{\text{H}_i\text{O}_w}$	-57.00
$C_{12}^{\text{O}_y\text{O}_w}$	12403.99	$C_{12}^{\text{H}_i\text{O}_w}$	1.25
$C_4^{\text{O}_y\text{H}_w}$	187.28	$C_4^{\text{H}_i\text{H}_w}$	4.63
$C_6^{\text{O}_y\text{H}_w}$	-314.50	$C_6^{\text{H}_i\text{H}_w}$	-0.29
$C_8^{\text{O}_y\text{H}_w}$	213.54	$C_8^{\text{H}_i\text{H}_w}$	0.07
$C_{12}^{\text{O}_y\text{H}_w}$	-22.69	$C_{12}^{\text{H}_i\text{H}_w}$	0.00
RMSE _{total}	1.9		
RMSE _{partial}	1.2		

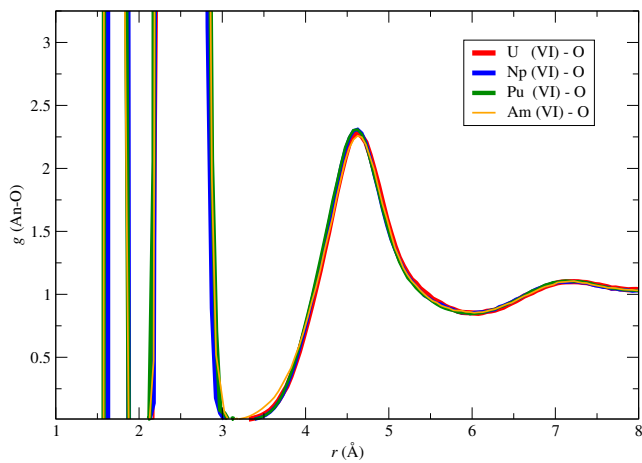


Figure S2: MD simulations An-O radial distribution functions for $[AnO_2 \cdot (H_2O)_5]^{2+}$
An = U,Np,Pu,Am



Extracting the Americyl Hydration from an Americium Cationic Mixture in Solution: A Combined X-ray Absorption Spectroscopy and Molecular Dynamics Study

6.1. *Inorg. Chem.* 2018, 57, 8089–8097

CHAPTER 6. EXTRACTING THE AMERICYL HYDRATION FROM AN AMERICIUM
CATIONIC MIXTURE IN SOLUTION: A COMBINED X-RAY ABSORPTION
SPECTROSCOPY AND MOLECULAR DYNAMICS STUDY



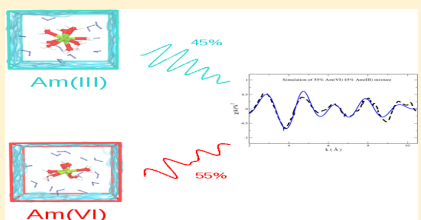
Extracting the Americyl Hydration from an Americium Cationic Mixture in Solution: A Combined X-ray Absorption Spectroscopy and Molecular Dynamics Study

Sergio Pérez-Conesa, José M. Martínez, Rafael R. Pappalardo,^{IP} and Enrique Sánchez Marcos^{*}

Department of Physical Chemistry, University of Seville, 41012 Seville, Spain

 Supporting Information

ABSTRACT: Am(VI) solution chemistry differs from that of lighter actinoids, as U, Pu, and Np, where the actinyl $[AnO_2]^{2+}$ is the most stable form and plays an important role in nuclear fuel technology. The behavior of americium in solution shows the trend to stabilize lower oxidation states, mainly Am(III). Riddle and co-workers recently reported the EXAFS and first XANES spectra of an americium-containing aqueous solution where the americyl species is detected in a mixture. We have developed $Am^{3+} - H_2O$ and $[AmO_2]^{2+} - H_2O$ intermolecular potentials based on quantum-mechanical calculations to carry out classical MD simulations of these two cations in water. Structural information extracted from the statistical trajectories has been used to simulate EXAFS and XANES spectra of both solutions. For the Am^{3+} case the theoretical–experimental agreement for both EXAFS and XANES spectra is satisfactory. This is not the case for the $[AmO_2]^{2+}$ aqueous solutions. However, when an aqueous solution mixture of both cationic forms in a 55/45 $[AmO_2]^{2+}/Am^{3+}$ ratio is considered, the theoretical–experimental agreement is recovered. EXAFS and XANES spectra which would correspond to a pure $[AmO_2]^{2+}$ aqueous solution are proposed. In the XANES case, the main features characterizing the simulated spectrum are consistent with those previously found in the experimental XANES spectra of stable $[UO_2]^{2+}$ and $[PuO_2]^{2+}$ in water.



INTRODUCTION

Americium is formed as a byproduct of the irradiation of uranium by neutrons as well as of Pu decay.¹ It is of great interest, since it is one of the main species responsible for the high radiotoxicity of minor actinoids in nuclear fuel waste.^{2–4} To engineer such a waste recycling process, to understand the biological hazard of americium, or to study its geochemical speciation, detailed knowledge of its complex solution chemistry is necessary. Unlike lanthanoids, the aqueous chemistry of actinoids is very rich, since each element has a distinct behavior with different stable oxidation states and species.⁵ The An(VI) solution chemistry of lighter actinoids, such as U, Pu, and Np, is dominated by the actinyl species, $[AnO_2]^{2+}$, which is stable and plays an important role in nuclear fuel technology. However, the behavior of Am in solution tends to stabilize lower oxidation states, mainly Am(III), adopting the monoatomic form Am^{3+} . The stabilization of americyl species requires the presence of highly oxidizing media.⁶ The ability to examine this higher oxidation state solution chemistry would yield relevant information on how these forms could be incorporated in new separation processes of minor actinoids in nuclear fuel recycling.^{1–4}

Structural information on aqueous americium ionic solutions has been obtained by means of extended X-ray absorption fine structure spectroscopy (EXAFS).^{6–9} This technique provides accurate short-range structural information around metal ions^{10,11} at concentrations as low as 10^{-4} M, typical values found in actinoid solutions.¹² Unfortunately, the radiotoxicity

of americium makes experimental information highly resource demanding and scarce. Extracting information and interpreting the spectra becomes an involved task, since experimental structural information obtained from other techniques is limited, so that structural models to help in the EXAFS fitting are lacking. This leads in many cases to assumptions about the model system based on analogies with other lighter actinoids¹² or to find out synergies with theoretical tools.^{13–17}

The most stable species of Am in solution is its aqua ion, $[Am(H_2O)_n]^{3+}$, whose EXAFS spectrum has been measured by Allen et al.⁷ and Stumpf et al.^{7,8} These studies established Am^{3+} hydration numbers in the range of 7.4–10 with an Am–O distance range of 2.477–2.494 Å. Riddle et al.⁶ have very recently obtained the first EXAFS spectrum of Am(VI), $[AmO_2]^{2+}$, in a 1 M HNO_3 aqueous solution containing $NaBiO_3$. These authors reported that the sample solution must be an Am(VI)/Am(III) mixture having a 70/30 ratio on the basis of UV-vis spectroscopy, although radiolysis degradation and sample stability may affect these values during the sample preparation, transportation, and measuring.⁶ Because of the low americium concentration (below 0.015 M) in the sample, we can assume that the recorded spectrum can be envisaged as a weighted sum of the two individual and independent contributions, provided the absence of significant interactions among the americium ions. Thus, Riddle et al.⁶ obtained

Received: January 18, 2018

Published: April 10, 2018

DOI: 10.1021/acs.inorgchem.8b00164
Inorg. Chem. 2018, 57, 8089–8097

structural parameters of the present species, assuming a complex model including contributions from the two oxidation states Am(III) and Am(VI). For americyl, these authors reported $\text{Am}-\text{O}_{\text{yl}}$ and $\text{Am}-\text{O}_1$ distances of 1.69 and 2.44 Å, respectively. These values were obtained from a fitting of a solution mixture composed of 70% Am(VI), ~29% Am(III), and a marginal presence of Am(V) (~1%). First-shell coordination numbers of 1.3 for O_{yl} , which results from the main contribution of two O_{yl} backscatters weighted by the percentage of americyl in the sample (~70%), and 4.1 ± 0.8 , which roughly results from the backscattering contribution of five oxygen atoms of the first hydration shell weighted by the same percentage of americyl in the sample, were obtained. Debye–Waller factors, which reflect the structural and dynamic disorder of a given shell of backscatters surrounding the metal cation, surprisingly shows smaller stiffness for the $\text{Am}=\text{O}_{\text{yl}}$ covalent bonds than for the $\text{Am}-\text{OH}_2$ intermolecular bonds, 0.006 and 0.002 Å², respectively, a fact that is difficult to rationalize. Because the EXAFS spectrum corresponds to a mixture of oxidation states as opposed to the most common EXAFS fitting scenario involving only one well-defined species as absorber, this is a challenging experiment which needs additional information to fully resolve the hydration structure of the cation mixture present in the sample.

Computational modeling of actinoids has become an interesting alternative or complement to experiment and is currently a well-established tool.¹⁸ Nevertheless, published theoretical studies^{15,17,19–22} on americium compounds in solution are scarce in comparison to other actinoids, although the experience from other actinoids should be partially transferable. Computation of EXAFS spectra from the structural information obtained by statistical simulations can contribute, as previously shown, to the interpretation of the experimental spectra.^{13,15,17,23–25} Conversely, the agreement with experimental results supports the interaction potentials employed as well as the physicochemical properties derived from the simulation.

The aim of this work is to rationalize the experimental XAS spectra⁵ of the $[\text{AmO}_2]^{2+}/\text{Am}^{3+}$ mixture in solution from a theoretical view, identifying individual contributions. For this purpose, XAS spectra will be computed from the structural information provided by MD simulations. In this case, both cations form stable aqua ions in solution, $[\text{AmO}_2(\text{H}_2\text{O})_n]^{2+}$ and $[\text{Am}(\text{H}_2\text{O})_m]^{3+}$, with $n = 5$ and $m = 8, 9$. The first task is the development of specific ab initio interaction potentials of these cations with water. To fulfill this requirement, we use our hydrated ion model,²⁶ which is based on the assumption that the cationic reference species in solution is the aqua ion; i.e., the hydrated ion.^{13,26,27} Recently we have published¹⁶ a classical interaction potential, on the basis of first-principles calculations, to describe uranyl in water considering the hydrated uranyl $[\text{UO}_2(\text{H}_2\text{O})_5]^{2+}$ instead of the naked ion $[\text{UO}_2]^{2+}$ in aqueous solution. From classical MD simulations, we were able to successfully simulate its EXAFS spectrum and investigate the hydration dynamics, structure, and thermodynamics of aqueous uranyl. The performance of this potential has been shown recently in the description of uranyl in the liquid vein of a clay.²⁸

■ COMPUTATIONAL METHODS

The hydrated ion model is a classical electrochemical concept developed to better describe the physicochemical properties of highly charged metal cations.^{29,30} This model recognizes the hydrated ion as

the representative solute instead of the naked ion. This is necessary because the polarization exerted by the ion on its first shell is such that first-shell water molecules must be considered to be molecular species different from bulk water molecules.³¹ Therefore, first-shell water molecules must have a different description than bulk water molecules and their charges and interaction potential parameters must be developed specifically for them. This imposes a restriction: the model is only applicable to hydrated ions whose first-shell residence times are longer than the simulation time. This restriction is due to the fact first-shell water release would lead to an arrangement where one or several water molecules with fitted parameters to be in the first shell are in the bulk. To get the ab initio interaction energies, all QM calculations were carried out in the presence of the full first hydration sphere. This procedure has two main advantages: the first is completely general, as it avoids the overpolarization that would occur if only one water molecule was considered to describe the ion–water interaction, and the second concerns the case of open-shell metal cations, where the ion is in the correct electronic state in solution due to the presence of the ligand field provided by the hydration shell. Additional information about the hydrated ion model and its extension allowing the first-shell water molecule exchange on the basis of a polarizable model can be found elsewhere.^{13,16,32,35}

B3LYP^{36,37} reproduces reasonably well the properties of actinyl cations,^{38,39} treating the multireference problem in an effective way. In order to be consistent with the previous uranyl potential, the level of theory chosen for $[\text{AmO}_2(\text{H}_2\text{O})_5]^{2+}$ was B3LYP employing the semirelativistic Stuttgart pseudopotential⁴⁰ with its recommended basis for americium and aug-cc-PVDZ for light atoms.⁴¹ The americyl pentahydrate is a quartet and B3LYP wave function shows low spin contamination, $\langle S(S + 1) \rangle = 3.84$ instead of 3.75, the pure-spin eigenvalue. To check the structural and energy results, we have carried out a NEVPT2^{42–44} computation of the americyl hydrate including 9 electrons and 10 orbitals in the active space. Basis sets ma-def2-TZVP⁴⁵ on the oxygen atom, def2-SVP⁴⁶ on the hydrogen atom, and DEF-TZVP⁴⁷/SD(60,MWB) pseudopotential for Am^{40} were used. Our B3LYP optimizations produce $\text{Am}-\text{O}_{\text{yl}}$ and $\text{Am}-\text{O}_1$ bond lengths of 1.71 and 2.48 Å, respectively, and an interaction energy of -226.2 kcal mol⁻¹ including counterpoise correction. NEVPT2 as implemented in the ORCA program⁴⁸ provides very similar results: optimized distances of 1.75 and 2.42 Å for $\text{Am}-\text{O}_{\text{yl}}$ and $\text{Am}-\text{O}_1$ bond lengths, respectively, and an interaction energy of -239.4 kcal mol⁻¹ including counterpoise correction. If the structural disagreement was substantial, the simulated EXAFS, which will be presented later on, would deviate strongly from experiment. Since such is not the case, B3LYP seems to be an adequate computational level for the purposes of this article: i.e., to understand the nature of the Am(VI)/Am(III) mixture. The optimized geometries and interaction energies of Am(VI) at both levels of series are included in Table S1 of the Supporting Information.

The method used to develop the interaction potential of uranyl,¹⁶ which is a general strategy for any hydrated actinyl cation, was applied on the americyl pentahydrate. The total interaction potential of an actinyl in solution within the hydrated ion model, as developed for the uranyl case,¹⁶ is the result of combining three interaction potentials: one to describe the flexibility of the actinyl molecular cation $\text{O}=\text{An}=\text{O}$, a second intermolecular potential between the actinyl and the water molecules forming the hydrate $[\text{AnO}_2]^{2+}-\text{H}_2\text{O}$, which defines the intrinsic dynamic of the pentahydrated actinyl $[\text{AnO}_2(\text{H}_2\text{O})_5]^{2+}$, and a third intermolecular potential to describe the interaction of bulk water molecules with the actinyl hydrate, $[\text{AnO}_2(\text{H}_2\text{O})_5]^{2+}-\text{H}_2\text{O}$. This implies that the model considers two types of water molecules in solution: first-shell and bulk water molecules. The intramolecular interaction potential within the $[\text{AmO}_2]^{2+}$ hydrated ion was developed specifically for this species. The nonelectrostatic interaction contribution between bulk water molecules and the hydrated ion is the same as for the uranyl case, since it was found to be fairly unspecific to the actinoid (Figure S1 of the Supporting Information). The interaction potential parameters can be found in Tables S2–S6 of the Supporting Information.

Table 1. Simulation and Experimental Results of Am(III) and Am(VI) in Solution^a

	[AmO ₂ (H ₂ O) ₅] ²⁺		[Am(H ₂ O) _n] ³⁺	
	MD	exptl	MD, n = 8	MD, n = 9
D _i (10 ⁵ cm ² s ⁻¹)	1.3 ± 0.1		0.7 ± 0.2	0.8 ± 0.2
ΔH _{hydr} (kcal mol ⁻¹)	-342	~−325, ~−401	-870	-886
r(Am–O _{yl}) (Å)	1.72	1.69		
CN(Am–O _{yl})	2 ^b	1.3		
DW(Am–O _{yl}) (Å ²)	0.0007	0.006		
r(Am–O _l) (Å)	2.44	2.48	2.47	2.53
CN(Am–O _l)	5 ^b	4.1	8 ^b	9 ^b
r(Am–O _{ll}) (Å)	4.64		4.66	4.72
CN(Am–O _{ll})	29 ^b		19	19
DW(Am–O _l) (Å ²)	0.007	0.002	0.006	0.007
				0.007, 0.009

^aThe properties displayed are translational self diffusion coefficient (D_i),⁶¹ hydration enthalpy (ΔH_{hydr}),³⁰ metal–oxygen distances (r),^{7–9} coordination numbers (CN),^{7–9} and Debye–Waller factors (DW).^{7–9} ^bFixed.

The level of theory chosen to develop the potential for [Am(H₂O)₈]³⁺ was MP2 using the Stuttgart semirelativistic pseudopotential,⁴⁹ which was specifically developed to treat the Am³⁺ cation, with its recommended basis set on americium and cc-PVTZ^{41,50–52} on light atoms. All quantum-mechanical calculations were run with Gaussian09.⁵³ Dolg and co-workers⁴⁹ developed a series of specific pseudopotentials for the trivalent cations of the actinoid series, including the f electrons in the pseudopotential. In this way the challenging issue of the f electron open shell is no longer found. This series of pseudopotentials is particularly convenient to deal with the actinoid hydration, as Dolg and co-workers⁵⁴ showed by studying the actinoid hydration of the whole An³⁺ series with the semicontinuum model. Am³⁺, like most large trivalent cations, must have a first-shell water mean residence time in the range of 2–10 ns.^{17,55} The aim of the Am³⁺–H₂O interaction potential is to get a reasonable representation of the solution structure validated by realistic simulated EXAFS and XANES spectra. Therefore, for Am³⁺ the coordination number of the first shell was kept fixed at a given hydration number following our hydrated ion model.^{26,34} Because the coordination number along the actinoid series is known to change from 9 to 8, we have considered both Am³⁺ hydrates, [Am(H₂O)_m]³⁺ for $m = 8, 9$, to develop an intermolecular potential with water. This gives us a reasonable range of possible Am³⁺ hydrates in solution. The gas-phase optimized Am–O distances for the octahydrate and enneahydrate are 2.51 and 2.56 Å, respectively. The optimized geometries and interaction energies of Am(III) with both coordination numbers are included in Table S1 of the Supporting Information. The first-shell water molecule geometry was that of the gas-phase QM optimization of [Am(H₂O)_m]³⁺. RESP⁵⁶ effective charges obtained from PCM^{57,58} polarized wave functions were assigned to the first-shell water molecules. The employed water models are not polarizable, and therefore polarization of the charges of the hydrated ion by the bulk solvent is included in a mean field sense with the PCM method. All water–water van der Waals interactions were described by the TIP4P⁵⁹ Lennard–Jones parameters. Additionally, angular harmonic interaction potentials (O–Am–O) for first-shell oxygen atoms were incorporated. The first-shell water oxygen–metal interaction was modeled as a harmonic bonding potential. The angular and bonding harmonic interaction terms are included in order to preserve the first-shell coordination integrity. The interaction potential parameters can be found in Tables S2, S3, S7, and S8 of the Supporting Information.

Five nanosecond molecular dynamics simulations were run for each of the americium species. Simulation boxes contained the ion and 1500 water molecules including first-shell water molecules. The TIP4P⁵⁹ model was employed for bulk water molecules. The simulation ensemble was NPT at 300 K and 1 atm. The time step chosen was 1 fs, and all water molecules were kept rigid. Electrostatic interactions were calculated using the Ewald summation method with a cutoff radius of 14 Å and 10^{−6} for relative error. The program used was DL_POLY CLASSIC.⁶⁰ Details of the simulation can be found elsewhere.¹⁶

RESULTS AND DISCUSSION

Table 1 summarizes the main results of our simulations and the published experimental works. In the rest of the section we detail our results.

Figure 1 displays the Am–O and Am–H RDFs for the simulations of Am³⁺ in water (top), which includes the results

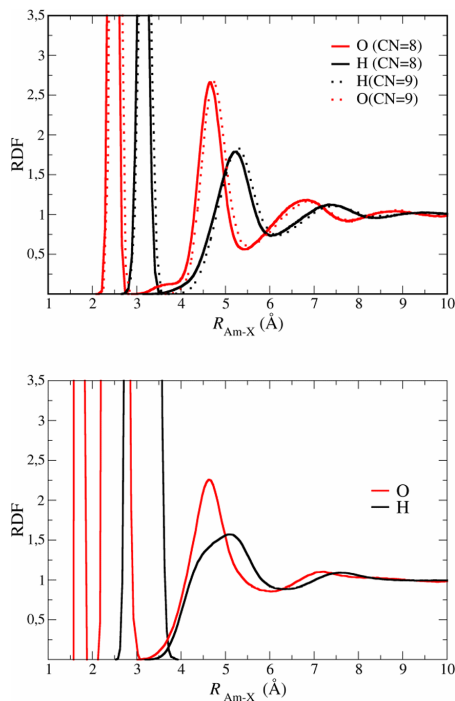


Figure 1. Am–O and Am–H RDFs for Am³⁺ (top) and [AmO₂]²⁺ (bottom) aqueous solutions derived from MD simulations.

derived from the intermolecular potentials assuming the Am(III) octahydrate (solid lines), and enneahydrate (dashed lines) and [AmO₂]²⁺ (bottom). The Am(III) hydration structure derived from the [Am(H₂O)₈]³⁺–H₂O potential is dominated by a well-defined first hydration shell with two sharp

peaks centered at 2.47 Å for Am–O and 3.15 Å for Am–H pairs. The second shell is formed by 19–20 water molecules with Am–O and Am–H peaks centered at 4.64 and 5.21 Å, respectively. When the $[\text{Am}(\text{H}_2\text{O})_9]^{3+}$ –H₂O potential is employed, as expected, an Am–water lengthening is observed; thus, the two first Am–O peaks are centered at 2.53 and 4.74 Å, and a similar shifting occurs for the Am–H peaks. In the americyl case, Am–O RDF (Figure 1 bottom) shows a sharp peak centered at 1.72 Å and integrating to 2, which corresponds to the O_{yl} atoms. A second well-defined peak, broader than the previous one, is centered at ~2.45 Å and integrates to 5. This is the equatorial hydration shell of the americyl cation. A third Am–O peak centered at 4.64 Å and integrating to ~30 collects the second-shell water molecules of the equatorial region together with water molecules solvating the axial region and intermediate region between axial and equatorial. This complex combination of hydrating water molecules around the americyl pentahydrate is also reflected in the Am–H RDF. The second Am–H peak overlaps with the Am–O peaks. This indicates the different orientations of water molecules in the axial, equatorial, and intermediate regions. This complex hydration structure was already observed in the $[\text{UO}_2]^{2+}$ case, and we refer to that work for a deeper description of this hydration structure on the basis of angle-solved RDFs,¹⁶ as well as to the analysis carried out by Maginn's group.^{20,21} Figures S2 and S3 of the Supporting Information plot the angle-solved RDFs for americyl pentahydrate.

To calculate the Am^{3+} hydration enthalpy, $\Delta H_{\text{hydr}}^{\text{theor}}(\text{Am}^{3+})$, we have computed two contributions:

$$\begin{aligned}\Delta H_{\text{hydr}}^{\text{theor}}(\text{Am}^{3+}) \\ = \Delta H_{\text{hydr}}^{\text{MD}}([\text{Am}(\text{H}_2\text{O})_8]^{3+}) + \Delta H_{\text{form}}^{\text{QM}}([\text{Am}(\text{H}_2\text{O})_8]^{3+})\end{aligned}$$

The first contribution is the hydration enthalpy of the $[\text{Am}(\text{H}_2\text{O})_8]^{3+}$ aqua ion in water that is computed from MD simulations of the Am^{3+} aqua ion in water, pure water, and the aqua ion in gas phase at the same temperature:

$$\begin{aligned}\Delta H_{\text{hydr}}^{\text{MD}}([\text{Am}(\text{H}_2\text{O})_8]^{3+}) \\ = H^{\text{MD}}([\text{Am}(\text{H}_2\text{O})_8]^{3+} \text{ in water}) - H^{\text{MD}}(\text{water}) \\ - H^{\text{MD}}([\text{Am}(\text{H}_2\text{O})_8]^{3+})\end{aligned}$$

The second contribution corresponds to the formation enthalpy of the $[\text{Am}(\text{H}_2\text{O})_8]^{3+}$ aqua ion. This is computed at the quantum-mechanical level used to build the potential energy surface which was employed further to generate the Am^{3+} –water intermolecular potential. Thermal corrections were included using the ideal gas rotational and translational partition functions at 300 K. The zero point energy was included using the harmonic oscillator model. The relaxation energy of water molecules from the gas phase to solution was neglected, since it is very small in comparison to ΔH_{hydr} .

$$\begin{aligned}\Delta H_{\text{form}}^{\text{QM}}([\text{Am}(\text{H}_2\text{O})_8]^{3+}) \\ = H^{\text{QM}}([\text{Am}(\text{H}_2\text{O})_8]^{3+}) - H^{\text{QM}}(\text{Am}^{3+}) \\ - 8H^{\text{QM}}(\text{H}_2\text{O})\end{aligned}$$

The theoretical hydration enthalpy for Am^{3+} is $-870 \text{ kcal mol}^{-1}$, which agrees reasonably with the experimental estimation of $-823 \text{ kcal mol}^{-1}$ (6% relative error),³⁰ bearing in mind the typical uncertainty of ionic hydration for highly

charged cations, and particularly for heavy actinoids.³⁰ Martelli et al.⁶² from their classical MD simulation of Am^{3+} obtained a value of $-869 \pm 11 \text{ kcal mol}^{-1}$, which matches the value obtained in this work. When the case of the enneahydrate is considered, the estimated hydration enthalpy for $\text{Am}^{(III)}$ is $-886 \text{ kcal mol}^{-1}$.

There is no experimental hydration enthalpy for $[\text{AmO}_2]^{2+}$, but there are estimations for other lighter actinyls on the basis of empirical models which range between -325 ± 5 and $-401 \pm 15 \text{ kcal mol}^{-1}$.^{63,64} We computed the $[\text{AmO}_2]^{2+}$ hydration enthalpy as the difference between the enthalpies derived from MD simulations of $[\text{AmO}_2]^{2+}$ in water and that of the sum of the TIP4P bulk water and $[\text{AmO}_2]^{2+}$ in the gas phase.

$$\begin{aligned}\Delta H_{\text{hydr}}^{\text{theor}}([\text{AmO}_2]^{2+}) &= H^{\text{MD}}([\text{AmO}_2]^{2+} \text{ in water}) \\ &- H^{\text{MD}}(\text{water}) - H^{\text{MD}}([\text{AmO}_2])^{2+}\end{aligned}$$

The theoretical estimation is $-342 \pm 16 \text{ kcal mol}^{-1}$, which is consistent with the estimation from empirical models.^{63,64}

Regarding the dynamics of the cations, self-translational diffusion coefficients have been computed from their MD trajectories as done in a previous work.¹⁶ Their D_i finite-size corrected⁶⁵ values are $(1.3 \pm 0.1) \times 10^{-5} \text{ cm}^2 \text{ s}^{-1}$ for $[\text{AmO}_2]^{2+}$, $(0.7 \pm 0.2) \times 10^{-5} \text{ cm}^2 \text{ s}^{-1}$ for $[\text{Am}(\text{H}_2\text{O})_8]^{3+}$, and $(0.8 \pm 0.2) \times 10^{-5} \text{ cm}^2 \text{ s}^{-1}$ for $[\text{Am}(\text{H}_2\text{O})_9]^{3+}$. The experimental diffusion coefficient⁶¹ of Am^{3+} is $(0.625 \pm 0.003) \times 10^{-5} \text{ cm}^2 \text{ s}^{-1}$, which agrees within the statistical uncertainty with our estimation. Martelli et al.⁶² have computed from classical MD simulations that used a polarizable interaction potential the diffusion coefficient of Am^{3+} , $(0.63 \pm 0.2) \times 10^{-5} \text{ cm}^2 \text{ s}^{-1}$. The diffusion coefficient of $[\text{AmO}_2]^{2+}$ is similar to our result for $[\text{UO}_2]^{2+}$, as can be expected due to the physicochemical similarity of these two species.¹⁶ To the best of our knowledge, the diffusion coefficient of $\text{Am}^{(VI)}$ has not been reported. In any case, the value obtained for $\text{Am}^{(VI)}$, as expected, resembles our $\text{U}^{(VI)}$ value¹⁶ of $(1.2 \pm 0.1) \times 10^{-5} \text{ cm}^2 \text{ s}^{-1}$. The comparison of the diffusion coefficient of our actinyl model with experiments has been previously discussed.¹⁶ To understand these results, we must realize that the diffusional behavior of these cations is mediated by their hydrated ions rather than by their bare ions. Then, the hydrates of $[\text{AmO}_2]^{2+}$ and Am^{3+} are the real species determining the ion mobility in aqueous solution. Am^{3+} hydrate has a size similar to that of the $[\text{AmO}_2]^{2+}$ hydrate, but its higher charge justifies its smaller diffusion coefficient value.

The Am L₃-edge EXAFS and XANES spectra were computed as the average of the individual spectra of 500 snapshots evenly taken from the MD trajectories. The spectra were obtained using FEFF9.^{66,67} (examples of FEFF input files are included in the Supporting Information). These snapshots included two hydration shells. EXAFS spectra include multiple scattering paths up to four legs and XANES spectra full multiple scattering contributions. To simulate the spectrum of the $[\text{AmO}_2]^{2+}$ /Am³⁺ mixture, the individual spectra were summed using the weighting factor of each oxidation state.

Figure 2 (top) shows the comparison of the experimental k^2 -weighted Am L₃ edge of an acidic aqueous Am(III) solution (black dashed line) recorded by Stumpf et al.⁷ and the simulated spectrum derived from our $[\text{Am}(\text{H}_2\text{O})_8]^{3+}$ MD simulation (green line). The shape of the experimental EXAFS signal indicates a rather simple contribution, mainly due to the single scattering paths of the first-hydration shell water molecules. The simulated spectrum (green line) reproduces rather well the frequency and intensity of the signal. This

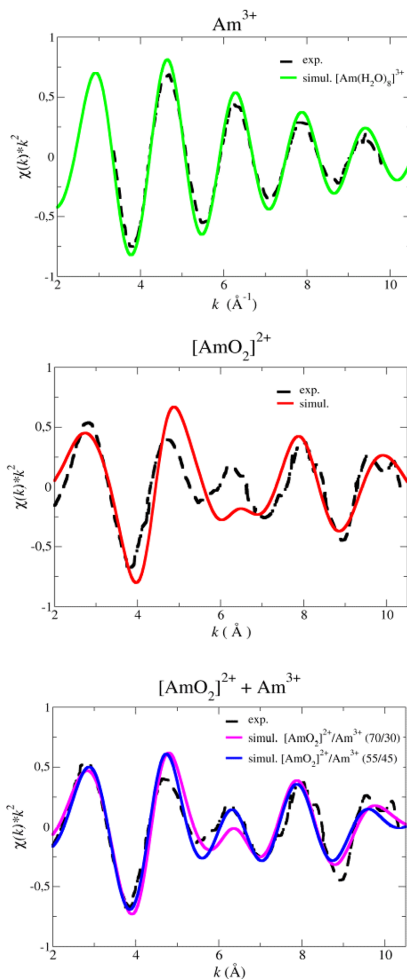


Figure 2. Experimental (dashed lines) vs simulated (solid lines) Am L₃-edge k^2 -weighted EXAFS spectra: (top) experimental (ref 7) and simulated Am³⁺ aqueous solution; (middle) experimental Am ionic mixture (ref 6) and simulated spectrum of [AmO₂]²⁺ (red line); (bottom) experimental Am ionic mixture (ref 6) and simulated spectra with 70/30 (magenta line) and a 55/45 (blue line) [AmO₂]²⁺/Am³⁺ ratios.

agreement allows the assignment of an octacoordination for Am(III) with a first-shell Am–O distance of 2.47 Å and a DW factor for the first hydration shell of 0.0055 Å². An analogous simulated EXAFS spectrum was carried out from the MD simulation containing the enneahydrated Am(III). The comparison between the Am(III) EXAFS spectra of the two coordination numbers with the experimental spectrum is given in Figure S4 (top) of the Supporting Information. The difference in the EXAFS is noticeable, since the change in coordination and M–O distance has a strong effect on the EXAFS. A similar or larger discrepancy for CN = 7.4, 10 must be expected.

Stumpf et al.^{7,8} and Allen et al.⁹ from their experimental EXAFS analysis obtained the same Am–O distance of 2.48 Å and coordination numbers of 7.4 and 10, respectively. DW factors of 0.0069 and 0.0090 Å², respectively, were fixed in the fitting. Spezia et al.^{15,17} have studied Am(III) by means of two approaches, revisiting the EXAFS analysis and using MD simulations, obtaining Am–O distances in the range 2.47–2.49 Å, although they found an enneacoordination. These authors also obtained a fair agreement between the experimental spectrum and that simulated. As they pointed out, the ±1 uncertainty in coordination numbers for aqua ions is intrinsic to EXAFS spectroscopy.

Figure 2 (middle) plots the experimental EXAFS spectrum recorded by Riddle and co-workers of an aqueous solution (black dashed line) containing several Am cationic forms, americyl being the most abundant. The simulated EXAFS spectrum corresponding to a pure sample of [AmO₂]²⁺ in water (red line) is also in the same figure. Both signals are complex, indicating several contributions out of phase with different intensities. This might be inherent to the [AmO₂(H₂O)₅]²⁺ species, where there are contributions from Am=O_{y1} and Am–O_l paths with quite different distances. DW factors computed from our MD simulations are 0.00074 Å² for Am–O_{y1} and 0.0072 Å² for Am–O_l. Both factors may justify such a peculiar EXAFS spectrum shape. However, the agreement between the experimental and simulated spectra is not satisfactory. As suggested by Riddle et al.,⁶ the relative instability of the Am(VI) oxidation state leads to a mixture of Am(VI) and Am(III) in the solution and a marginal presence of Am(V). Figure 2 (bottom) shows the comparison of the experimental (dashed black line) with the theoretical spectra (blue and magenta lines) obtained from two different weighted sums of the Am³⁺ and [AmO₂]²⁺ simulated spectra shown in the two upper plots. The much better agreement gives evidence for the presence of an Am cationic mixture in the aqueous solutions recorded by Riddle et al.⁶ In our case, the best [AmO₂]²⁺/Am³⁺ ratio matching as much as possible the experimental signal was achieved with a 55/45 value (blue line), whereas the suggested experimental value was 70/30 (magenta line). Although both ratios give simulated spectra similar to the experimental spectrum, our proposed ratio performs better. The observed discrepancy of ratios is probably a consequence of the uncertainty in both the theoretical procedure and the experimental determination of the Am species concentration in the measured sample. The MD simulation used for the Am³⁺ contribution to the simulated spectrum was that using the [Am(H₂O)₈]³⁺ hydrate. The comparison of the experimental results with the simulated spectrum obtained using the Am(III) enneahydrate MD simulation is plotted in Figure S4 (bottom) of the Supporting Information. The better theoretical–experimental agreement derived from the use of the Am(III) octahydrate EXAFS spectrum is clear. Two conclusions can be derived from the analysis of Figure 2 and Figure S4 of the Supporting Information. The first one is that, even with the highly oxidizing character of the medium, the experimental spectrum clearly is the combination of the two Am cationic species regardless of the cation ratio applied and the Am(III) hydrate selected to combine. The second conclusion is that the best agreement obtained with a cation ratio different from that experimentally proposed, but not too much, suggests some uncertainty in the individual Am species population really present in the measured sample. As a consequence of this analysis we can establish that the simulated EXAFS spectrum

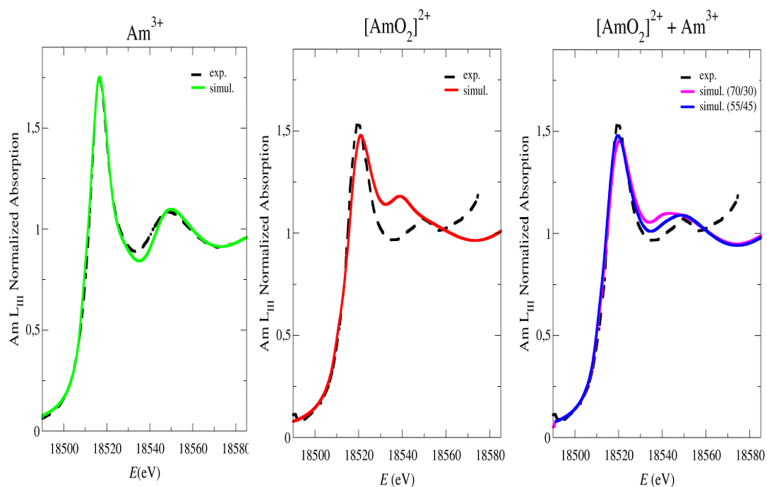


Figure 3. Experimental (dashed lines) vs simulated (solid lines) Am L_3 -edge XANES spectra: (top) experimental (ref 7) and simulated Am^{3+} aqueous solution; (middle) experimental Am ionic mixture (ref 6) and simulated spectrum of $[\text{AmO}_2]^{2+}$ (red line); (bottom) experimental Am ionic mixture (ref 6) and simulated spectra with 70/30 (magenta line) and 55/45 (blue line) $[\text{AmO}_2]^{2+}/\text{Am}^{3+}$ ratios.

(red line) in the middle of Figure 2 is our theoretical proposal for the spectrum of an $[\text{AmO}_2]^{2+}$ dilute aqueous solution.

An additional test of the cationic mixture aqueous solution can be made by the theoretical–experimental comparison of the XANES spectra of the same samples. Figure 3 displays such a test for the $\text{Am}(\text{III})$ sample (left part) and $\text{Am}(\text{VI})$ sample (middle part). The agreement between the experiment (black dashed line) and the theoretical model using $[\text{Am}(\text{H}_2\text{O})_8]^{3+}$ (green line) is remarkable. In contrast, there is poor agreement of the experimental XANES (black dashed line in the center part) of the sample containing the $\text{Am}(\text{VI})$ oxidation state and the simulated spectrum derived from the pure $[\text{AmO}_2]^{2+}$ MD simulation. However, when the spectrum is computed considering the $[\text{AmO}_2]^{2+}/\text{Am}^{3+}$ mixture, the agreement is clearly improved. Again the 55/45 ratio (blue line in the right part of Figure 3) performs better than the 70/30 experimental proposal (magenta line). If we accept that this satisfactory result is not a consequence of fortuitous error cancellations, the model suggests that the experimental ratio of the mixture might be reconsidered. Furthermore, as in the EXAFS case, we propose the red line in the center of Figure 3 as the XANES spectrum of a pure sample of $[\text{AmO}_2]^{2+}$ in water, something that up to the present has not been measured. The greater stability of higher oxidation states in water for $[\text{UO}_2]^{2+}$ and $[\text{PuO}_2]^{2+}$ allows the experimental determination of the XANES for aqueous solutions only containing those actinyls.^{68,69} The energy gap between the white line and the first resonance is ~ 18 and ~ 21 eV for $[\text{UO}_2]^{2+}$ and $[\text{PuO}_2]^{2+}$ XANES spectra, respectively. In the case of our simulated pure $[\text{AmO}_2]^{2+}$ aqueous solution this gap is 23 eV, which corroborates the global consistency among experimental and theoretical results. It is interesting to point out that this gap in the experimental spectrum of the mixture is ~ 30 eV. The energy position of the edge in XANES has long been used as a semiquantitative index on the absorber atom oxidation state. For systems with O atoms in the first hydration shell there is a linear correlation between the oxidation state and the edge energy, with an increase of ~ 1.5 eV per formal oxidation state.⁷⁰ FEFF9.6

computations of the XANES spectra of aqueous solutions of the $\text{Am}(\text{III})$ and $\text{Am}(\text{VI})$ oxidation states (left green line and middle red line in Figure 3) predicts 4.0 eV to compare with the empirically estimated value of 4.5 eV. However, when the experimental XANES spectra (dashed lines in Figure 3, left $\text{Am}(\text{III})$, middle or right $\text{Am}(\text{VI})$) are analyzed, the difference is 2.0 eV, whereas the value from the theoretical XANES spectra of $\text{Am}(\text{III})$ (left green line) and the cationic mixture (right blue line) is 2.5 eV.

In conclusion, this study has established a spectroscopic–theoretical procedure to deal with an aqueous solution mixture of two americium cations, Am^{3+} and $[\text{AmO}_2]^{2+}$, which contribute separately to a sole X-ray absorption spectrum. From this global experimental signal, the individual contributions to the XANES and EXAFS spectra corresponding to the pure aqueous solutions of each individual ionic species is achieved on the basis of reliable intermolecular potentials and ab initio methods of multiple scattering theory. Discarding error cancellations, if the sum of the two contributions leads to a fair agreement with experiment, we could assume as correct the individual contributions and consequently support the simulated EXAFS and XANES spectra of $[\text{AmO}_2]^{2+}$ as the expected Am L_3 -edge spectra of a pure $[\text{AmO}_2]^{2+}$ aqueous solution. This may be envisaged as a challenge for new experiments intended to design appropriate medium conditions to stabilize selectively the $[\text{AmO}_2]^{2+}$ species in water. The combined experimental–theoretical strategy opens possibilities to the analysis of involved mixture solutions of species containing a particular absorber atom present in different oxidation states.

ASSOCIATED CONTENT

Supporting Information

The Supporting Information is available free of charge on the ACS Publications website at DOI: [10.1021/acs.inorgchem.8b00164](https://doi.org/10.1021/acs.inorgchem.8b00164).

Cartesian coordinates of optimized structures of $[Am(H_2O)_8]^{3+}$, $[Am(H_2O)_9]^{3+}$, and AmO_2^{2+} , EXAFS and XANES FEFF input files, interaction energy scans of a bulk water molecule with $[AmO_2(H_2O)_5]^{2+}$ given by DFT and the developed classical potential, gas-phase quantum-mechanical optimized geometries of the Am^{3+} and $[AmO_2]^{2+}$ hydrates, interaction potential parameters, angle-solved RDFs, and theoretical–experimental comparison of the EXAFS spectrum corresponding to simulated spectra built from $[Am(H_2O)_8]^{3+}$ and $[Am(H_2O)_9]^{3+}$ MD simulations and simulated spectra built with the 55/45 ratio using for Am(III) the $[Am(H_2O)_5]^{2+}$ MD simulation (PDF)

AUTHOR INFORMATION

Corresponding Author

*E.S.M.: e-mail, sanchez@us.es; tel, +34 955421005.

ORCID

Rafael R. Pappalardo: [0000-0003-3751-2395](https://orcid.org/0000-0003-3751-2395)

Enrique Sánchez Marcos: [0000-0002-8367-9105](https://orcid.org/0000-0002-8367-9105)

Notes

The authors declare no competing financial interest.

ACKNOWLEDGMENTS

We thank Prof. Steven Conradson for providing some of the experimental spectra. This work was financially supported by the Consejería de Economía, Innovación, Ciencia y Desarrollo, Junta de Andalucía of Spain (Proyecto de Excelencia, P11-FQM7607), and the Spanish Ministry of Education, Culture and Sports for the Ph.D. scholarship FPU (Formación de Profesorado Universitario) granted to SPC.

REFERENCES

- (1) Runde, R. W.; Schulz, W. W. In *The Chemistry of the Actinide and Transactinide Elements*, 3rd ed.; Morss, L. R., Edelstein, N., Fuger, J., Katz, J. J., Eds.; Springer: Berlin, 2008; Vol. 2; Chapter 8, pp 1265–1395.
- (2) Morimoto, K.; Kato, M.; Uno, H.; Hanari, A.; Tamura, T.; Sugata, H.; Sunaoshi, T.; Kono, S. Preparation and Characterization of (Pu, U, Np, Am, simulated FP) O_{2-x} . *J. Phys. Chem. Solids* **2005**, *66*, 634–638.
- (3) Yoshimochi, H.; Nemoto, M.; Mondo, K.; Koyama, S.; Namekawa, T. Fabrication Technology for MOX Fuel Containing AmO_2 by an in-Cell Remote Process. *J. Nucl. Sci. Technol.* **2004**, *41*, 850–856.
- (4) Prieur, D.; Carvajal-Nunez, U.; Vitova, T.; Somers, J. Local and Electronic Structure of Americium-Bearing PuO_2 . *Eur. J. Inorg. Chem.* **2013**, *2013*, 1518–1524.
- (5) Choppin, G. R.; Jensen, M. P. In *The Chemistry of the Actinide and Transactinide Elements*, 3rd ed.; Morss, L. R., Edelstein, N., Fuger, J., Katz, J. J., Eds.; Springer: Berlin, 2008; Vol. 4; Chapter 23, pp 2524–2621.
- (6) Riddle, C.; Czerwinski, K.; Kim, E.; Paviet, P.; Weck, P.; Poineau, F.; Conradson, S. Characterization of Pentavalent and Hexavalent Americium Complexes in Nitric Acid Using X-Ray Absorption Fine Structure Spectroscopy and First-Principles Modeling. *J. Radioanal. Nucl. Chem.* **2016**, *309*, 1087–1095.
- (7) Stumpf, S.; Stumpf, T.; Dardenne, K.; Hennig, C.; Foerstendorf, H.; Klenze, R.; Fanghänel, T. Sorption of Am (III) Onto 6-Line-Ferrhydrite and its Alteration Products: Investigations by EXAFS. *Environ. Sci. Technol.* **2006**, *40*, 3522–3528.
- (8) Stumpf, T.; Hennig, C.; Bauer, A.; Denecke, M. A.; Fanghänel, T. An EXAFS and TRLFS Study of the Sorption of Trivalent Actinides Onto Smectite and Kaolinite. *Radiochim. Acta* **2004**, *92*, 133–138.
- (9) Allen, P.; Bucher, J.; Shuh, D.; Edelstein, N.; Craig, I. Coordination Chemistry of Trivalent Lanthanide and Actinide Ions in Dilute and Concentrated Chloride Solutions. *Inorg. Chem.* **2000**, *39*, 595–601.
- (10) Koningsberger, D.; Prins, R. *X-ray Absorption: Principles, Applications, Techniques of EXAFS, SEXAFS, and XANES*; Wiley: New York, NY, 1988.
- (11) Muñoz-Páez, A.; Sánchez Marcos, E. In *Comprehensive Inorganic Chemistry II: From Elements to Applications*, 2nd ed.; Reedijk, J., Poeppelmeier, K., Eds.; Elsevier: Amsterdam, 2013; Vol. 9; pp 133–159.
- (12) Denecke, M. A. Actinide Speciation Using X-Ray Absorption Fine Structure Spectroscopy. *Coord. Chem. Rev.* **2006**, *250*, 730–754.
- (13) Galbis, E.; Hernández-Cobos, J.; den Auwer, C.; Le Naour, C.; Guillaumont, D.; Simoni, E.; Pappalardo, R. R.; Sánchez Marcos, E. Solving the Hydration Structure of the Heaviest Actinide Aqua Ion Known: The Californium (III) Case. *Angew. Chem.* **2010**, *122*, 3899–3903.
- (14) Atta-Fynn, R.; Bylaska, E. J.; Schenter, G. K.; de Jong, W. A. Hydration Shell Structure and Dynamics of Curium(III) in Aqueous Solution: First Principles and Empirical Studies. *J. Phys. Chem. A* **2011**, *115*, 4665–4677.
- (15) D'Angelo, P.; Martelli, F.; Spezia, R.; Filippioni, A.; Denecke, M. A. Hydration Properties and Ionic Radii of Actinide (III) Ions in Aqueous Solution. *Inorg. Chem.* **2013**, *S2*, 10318–10324.
- (16) Pérez-Conesa, S.; Torrico, F.; Martínez, J. M.; Pappalardo, R. R.; Sánchez Marcos, E. a Hydrated Ion Model of $[UO_2]^{2+}$ in Water: Structure, Dynamics, and Spectroscopy from Classical Molecular Dynamics. *J. Chem. Phys.* **2016**, *145*, 224502.
- (17) Spezia, R.; Migliorati, V.; D'Angelo, P. On the Development of Polarizable and Lennard-Jones Force Fields to Study Hydration Structure and Dynamics of Actinide(III) Ions Based on Effective Ionic Radii. *J. Chem. Phys.* **2017**, *147*, 161707.
- (18) Dolg, M. *Computational Methods in Lanthanide and Actinide Chemistry*; Wiley: Cologne, Germany, 2015.
- (19) Vallet, V.; Privalov, T.; Wahlgren, U.; Grenthe, I. The Mechanism of Water Exchange in $AmO_2(H_2O)_5^{2+}$ and in the Isoelectronic $UO_2(H_2O)_5^{2+}$ and $NpO_2(H_2O)_5^{2+}$ Complexes as Studied by Quantum Chemical Methods. *J. Am. Chem. Soc.* **2004**, *126*, 7766–7767.
- (20) Pomogaev, V.; Tiwari, S. P.; Rai, N.; Goff, G. S.; Runde, W.; Schneider, W. F.; Maginn, E. J. Development and Application of Effective Pairwise Potentials for UO_2^n , NpO_2^n , PuO_2^n , and AmO_2^n ($n=1, 2$) Ions With Water. *Phys. Chem. Chem. Phys.* **2013**, *15*, 15954–15963.
- (21) Tiwari, S. P.; Rai, N.; Maginn, E. J. Dynamics of Actinyl Ions in Water: A Molecular Dynamics Simulation Study. *Phys. Chem. Chem. Phys.* **2014**, *16*, 8060–8069.
- (22) Fabrizio, A.; Rotzinger, F. P. Quantum Chemical Study of the Water Exchange Mechanism of the Americyl (VI) Aqua Ion. *Inorg. Chem.* **2016**, *S5*, 11147–11152.
- (23) Filippioni, A.; D'Angelo, P.; Pavel, N. V.; Di Cicco, A. Triplet Correlations in the Hydration Shell of Aquaiions. *Chem. Phys. Lett.* **1994**, *225*, 150–155.
- (24) Palmer, B. J.; Pfund, D. M.; Fulton, J. L. Direct Modeling of EXAFS Spectra from Molecular Dynamics Simulations. *J. Phys. Chem.* **1996**, *100*, 13393–13398.
- (25) Merkling, P. J.; Muñoz-Páez, A.; Sánchez Marcos, E. Exploring the Capabilities of X-Ray Absorption Spectroscopy for Determining the Structure of Electrolyte Solutions: Computed Spectra for Cr^{3+} or Rh^{3+} in Water Based on Molecular Dynamics. *J. Am. Chem. Soc.* **2002**, *124*, 10911–10920.
- (26) Martínez, J. M.; Pappalardo, R. R.; Sánchez Marcos, E. First-Principles Ion-Water Interaction Potentials for Highly Charged Monoatomic Cations. Computer Simulations of Al^{3+} , Mg^{2+} and Be^{2+} . *J. Am. Chem. Soc.* **1999**, *121*, 3175–3184.
- (27) Morales Negrito, N. Estudio Teórico de Propiedades Fisicoquímicas de Cationes Metálicos En Disolución: Evolución en

- el Grupo de los Alcalinos y en la Serie de los Lantánidos. Ph.D. thesis, Universidad de Sevilla, Sevilla, Spain, 2015.
- (28) Pérez-Conesa, S.; Martínez, J. M.; Sánchez Marcos, E. Hydration and Diffusion Mechanism of Uranyl in Montmorillonite Clay: Molecular Dynamics Using an Ab Initio Potential. *J. Phys. Chem. C* **2017**, *121*, 27437–27444.
- (29) Frank, H. S.; Evans, M. W. Free Volume and Entropy in Condensed Systems III. *J. Chem. Phys.* **1945**, *13*, 507–532.
- (30) Marcus, Y. *Ions in Solution and their Solvation*; Wiley: Hoboken, NJ, 2015; pp 107–116.
- (31) Taube, H. Use of Oxygen Isotope Effects in Study of Hydration of Ions. *J. Phys. Chem.* **1954**, *58*, 523–528.
- (32) Pappalardo, R. R.; Sánchez Marcos, E. Recovering the concept of the hydrated ion for modeling ionic solutions: a Monte Carlo study of zinc(2+) in water. *J. Phys. Chem.* **1993**, *97*, 4500–4504.
- (33) Pappalardo, R. R.; Martínez, J. M.; Sánchez Marcos, E. Application of the Hydrated Ion Concept for Modeling Aqueous Solutions Containing Highly Charged Ions: A Monte Carlo Simulation of Cr3+ in Water Using an ab Initio Intermolecular Potential. *J. Phys. Chem.* **1996**, *100*, 11748–11754.
- (34) Martínez, J. M.; Pappalardo, R. R.; Sánchez Marcos, E.; Refson, K.; Díaz-Moreno, S.; A, M. Dynamics of a Highly Charged Ion in Aqueous Solutions: Molecular Dynamics Simulations of Dilute CrCl₃ Aqueous Solutions Using Interaction Potentials Based on the Hydrated Ion Concept. *J. Phys. Chem. B* **1998**, *102*, 3272–3282.
- (35) Galbis, E.; Hernández-Cobos, J.; Pappalardo, R.; Sanchez Marcos, E. Collecting High-order Interactions in an Effective Pairwise Intermolecular Potential Using the Hydrated Ion Concept: The Hydration of Cf(III). *J. Chem. Phys.* **2014**, *140*, 214104.
- (36) Becke, A. D. Density-Functional Thermochemistry. III. The Role of Exact Exchange. *J. Chem. Phys.* **1993**, *98*, 5648–5652.
- (37) Stephens, P. J.; Devlin, F. J.; Chabalowski, C. F.; Frisch, M. J. Ab Initio Calculation of Vibrational Absorption and Circular Dichroism Spectra Using Density Functional Force Fields. *J. Phys. Chem.* **1994**, *98*, 11623–11627.
- (38) Clavaguera-Sarrio, C.; Vallet, V.; Maynau, D.; Marsden, C. J. Can Density Functional Methods Be Used for Open-Shell Actinide Molecules? Comparison With Multiconfigurational Spin-Orbit Studies. *J. Chem. Phys.* **2004**, *121*, 5312–5321.
- (39) Averkiev, B. B.; Mantina, M.; Valero, R.; Infante, I.; Kovacs, A.; Truhlar, D. G.; Gagliardi, L. How Accurate are Electronic Structure Methods for Actinoid Chemistry? *Theor. Chem. Acc.* **2011**, *129*, 657–666.
- (40) Küchle, W.; Dolg, M.; Stoll, H.; Preuss, J. Energy-Adjusted Pseudopotentials for the Actinides. Parameter Sets and Test Calculations for Thorium and Thorium Monoxide. *J. Chem. Phys.* **1994**, *100*, 7535–7542.
- (41) Kendall, R. A.; Dunning, T. H., Jr.; Harrison, R. J. Electron Affinities of the First-Row Atoms Revisited. Systematic Basis Sets and Wave Functions. *J. Chem. Phys.* **1992**, *96*, 6796–6806.
- (42) Angeli, C.; Cimiraglia, R.; Malrieu, J.-P. N-electron valence state perturbation theory: a fast implementation of the strongly contracted variant. *Chem. Phys. Lett.* **2001**, *350*, 297–305.
- (43) Angeli, C.; Cimiraglia, R.; Malrieu, J.-P. n-electron valence state perturbation theory: A spinless formulation and an efficient implementation of the strongly contracted and of the partially contracted variants. *J. Chem. Phys.* **2002**, *117*, 9138–9153.
- (44) Jung, J.; Atanasov, M.; Neese, F. Ab Initio Ligand-Field Theory Analysis and Covalency Trends in Actinide and Lanthanide Free Ions and Octahedral Complexes. *Inorg. Chem.* **2017**, *56*, 8802–8816.
- (45) Zheng, J.; Xu, X.; Truhlar, D. G. Minimally augmented Karlsruhe basis sets. *Theor. Chem. Acc.* **2011**, *128*, 295–305.
- (46) Weigend, F.; Ahlrichs, R. Balanced basis sets of split valence, triple zeta valence and quadruple zeta valence quality for H to Rn: Design and assessment of accuracy. *Phys. Chem. Chem. Phys.* **2005**, *7*, 3297–3305.
- (47) Eichhorn, K.; Weigend, F.; Treutler, O.; Ahlrichs, R. Auxiliary basis sets for main row atoms and transition metals and their use to approximate Coulomb potentials. *Theor. Chem. Acc.* **1997**, *97*, 119–124.
- (48) Neese, F. The ORCA program system. *Wiley Interdiscip. Rev. Comput. Mol. Sci.* **2012**, *2*, 73–78.
- (49) Moritz, A.; Cao, X.; Dolg, M. Quasirelativistic Energy-Consistent 5f-In-Core Pseudopotentials for Trivalent Actinide Elements. *Theor. Chem. Acc.* **2007**, *117*, 473–481.
- (50) Dunning, T. H., Jr. Gaussian Basis Sets for Use in Correlated Molecular Calculations. I. the Atoms Boron Through Neon and Hydrogen. *J. Chem. Phys.* **1989**, *90*, 1007–1023.
- (51) Woon, D. E.; Dunning, T. H., Jr. Gaussian Basis Sets for Use in Correlated Molecular Calculations. III. the Atoms Aluminum Through Argon. *J. Chem. Phys.* **1993**, *98*, 1358–1371.
- (52) Woon, D. E.; Dunning, T. H., Jr. Gaussian Basis Sets for Use in Correlated Molecular Calculations. IV. Calculation of Static Electrical Response Properties. *J. Chem. Phys.* **1994**, *100*, 2975–2988.
- (53) Frisch, M. J., et al. *Gaussian 09, Revision D.01*; Gaussian Inc.: Wallingford, CT, 2009.
- (54) Wiebke, J.; Moritz, A.; Cao, X.; Dolg, M. Approaching actinide(+III) hydration from first principles. *Phys. Chem. Chem. Phys.* **2007**, *9*, 459–465.
- (55) Helm, L.; Merbach, A. Inorganic and Bioinorganic Solvent Exchange Mechanisms. *Chem. Rev.* **2005**, *105*, 1923–1960.
- (56) Bayly, C. I.; Cieplak, P.; Cornell, W.; Kollman, P. A. A Well-Behaved Electrostatic Potential Based Method Using Charge Restraints for Deriving Atomic Charges: The RESP Model. *J. Phys. Chem.* **1993**, *97*, 10269–10280.
- (57) Miertuš, S.; Scrocino, E.; Tomasi, J. Electrostatic Interaction of a Solute With a Continuum. A Direct Utilization of Ab Initio Molecular Potentials for the Revision of Solvent Effects. *Chem. Phys.* **1981**, *55*, 117–129.
- (58) Cancès, E.; Mennucci, B.; Tomasi, J. A New Integral Equation Formalism for the Polarizable Continuum Model: Theoretical Background and Applications to Isotropic and Anisotropic Dielectrics. *J. Chem. Phys.* **1997**, *107*, 3032–3041.
- (59) Jorgensen, W. L.; Chandrasekhar, J.; Madura, J. D.; Impey, R. W.; Klein, M. L. Comparison of Simple Potential Functions for Simulating Liquid Water. *J. Chem. Phys.* **1983**, *79*, 926–935.
- (60) Todorov, I. T.; Smith, W.; Trachenko, K.; Dove, M. T. DL_POLY_3: New Dimensions in Molecular Simulations Via Massive Parallelism. *J. Mater. Chem.* **2006**, *16*, 1911–1918.
- (61) Fourest, B.; Duplessis, J.; David, F. Comparison of Diffusion Coefficients and Hydrated Radii for some Trivalent Lanthanide and Actinide Ions in Aqueous Solution. *Radiochim. Acta* **1984**, *36*, 191–195.
- (62) Martelli, F.; Abadie, S.; Simonin, J.-P.; Vuilleumier, R.; Spezia, R. Lanthanoids(III) and actinoids(III) in water: Diffusion coefficients and hydration enthalpies from polarizable molecular dynamics simulations. *Pure Appl. Chem.* **2012**, *85*, 237–246.
- (63) Marcus, Y.; Loewenschuss, A. Standard Thermodynamic Functions of the Gaseous Actinyl Ions MO₂²⁺ and for Their Hydration. *J. Chem. Soc., Faraday Trans. 1* **1986**, *82*, 2873–2886.
- (64) Gibson, J. K.; Haire, R. G.; Santos, M.; Maralo, J.; Pires de Matos, A. Oxidation Studies of Dipositive Actinide Ions, An²⁺ (An = Th, U, Np, Pu, Am) in the Gas Phase: Synthesis and Characterization of the Isolated Uranyl, Neptunyl, and Plutonyl Ions UO₂²⁺(g), NP₂²⁺(g) and PuO₂²⁺(g). *J. Phys. Chem. A* **2005**, *109*, 2768–2781.
- (65) Yeh, I.-C.; Hummer, G. System-Size Dependence of Diffusion Coefficients and Viscosities from Molecular Dynamics Simulations with Periodic Boundary Conditions. *J. Phys. Chem. B* **2004**, *108*, 15873–15879.
- (66) Ankudinov, A. L.; Nesvizhskii, A. I.; Rehr, J. J. Dynamic Screening Effects in X-Ray Absorption Spectra. *Phys. Rev. B: Condens. Matter Mater. Phys.* **2003**, *67*, 115120.
- (67) Rehr, J. J.; Albers, R. Theoretical Approaches to X-Ray Absorption Fine Structure. *Rev. Mod. Phys.* **2000**, *72*, 621–654.
- (68) Conradson, S. D.; Clark, D. L.; Neu, M. P.; Runde, W. H.; Tait, C. D. Characterizing the Plutonium Aquo Ions by XAFS Spectroscopy. *Los Alamos Science* **2000**, *26*, 418–421.

(69) den Auwer, C.; Drot, R.; Simoni, E.; Conradson, S. D.; Gailhanou, M.; Mustre de Leon, J. Grazing Incidence XAFS Spectroscopy of Uranyl Sorbed Onto TiO₂ Rutile Surfaces. *New J. Chem.* **2003**, *27*, 648–655.

(70) Runde, W. H.; Mincher, B. J. Higher Oxidation States of Americium: Preparation, Characterization and Use for Separations. *Chem. Rev.* **2011**, *111*, 5723–5741.

CHAPTER 6. EXTRACTING THE AMERICYL HYDRATION FROM AN AMERICIUM
CATIONIC MIXTURE IN SOLUTION: A COMBINED X-RAY ABSORPTION
SPECTROSCOPY AND MOLECULAR DYNAMICS STUDY



SUPPLEMENTARY MATERIAL

**Extracting the Americyl Hydration from an
Americium Cationic Mixture in Solution: a
Combined X-ray Absorption Spectroscopy and
Molecular Dynamics Study**

Sergio Pérez-Conesa, José M. Martínez, Rafael R. Pappalardo and Enrique
Sánchez Marcos

*Departamento de Química Física, Universidad de Sevilla,
41012 Sevilla, Spain. e-mail:sanchez@us.es*



Cartesian coordinate files of the QM optimized structures.

18

[AmO₂·(H₂O)₅]²⁺
Am 0.000000 0.000000 0.039248
Oyl 0.000000 0.000000 1.745248
Oyl 0.000000 0.000000 -1.666753
O₁ 2.360600 0.739936 0.164123
H₁ 2.952612 0.973002 0.896313
H₁ 2.866433 0.891641 -0.649522
O₁ 0.000000 2.476716 0.001752
H₁ 0.000000 3.059801 0.776938
H₁ 0.000000 3.059801 -0.773433
O₁ -2.355497 0.765347 0.001752
H₁ -2.910043 0.945531 0.776938
H₁ -2.910043 0.945531 -0.773433
O₁ -1.455777 -2.003706 0.001752
H₁ -1.798505 -2.475431 0.776938
H₁ -1.798505 -2.475431 -0.773433
O₁ 1.455777 -2.003706 0.001752
H₁ 1.798506 -2.475431 0.776938
H₁ 1.798506 -2.475431 -0.773433

25

[Am(H₂O)₈]³⁺
Am 0.000000 0.000000 0.000000
O₁ 0.000000 2.124334 1.352560
H₁ 0.566354 2.336487 2.110749
H₁ -0.554699 2.911204 1.235908
O₁ 1.502132 1.502132 -1.352560
H₁ 2.052619 1.251673 -2.110749
H₁ 1.666301 2.450765 -1.235908
O₁ 0.000000 -2.124334 1.352560
H₁ -0.566354 -2.336487 2.110749
H₁ 0.554699 -2.911204 1.235908
O₁ -1.502132 -1.502132 -1.352560
H₁ -2.052619 -1.251673 -2.110749
H₁ -1.666301 -2.450765 -1.235908
O₁ -1.502132 1.502132 -1.352560
H₁ -1.251673 2.052619 -2.110749
H₁ -2.450765 1.666301 -1.235908
O₁ 1.502132 -1.502132 -1.352560
H₁ 1.251673 -2.052619 -2.110749
H₁ 2.450765 -1.666301 -1.235908
O₁ -2.124334 0.000000 1.352560

S2

H_I -2.911204 -0.554699 1.235908

H_I -2.336487 0.566354 2.110749

O_I 2.124334 0.000000 1.352560

H_I 2.336487 -0.566354 2.110749

H_I 2.911204 0.554699 1.235908

28

[Am(H₂O)9]3+

Am 0.024223 -0.012098 0.048730

O_I 2.077156 0.836889 1.298111

H_I 2.120819 1.603332 1.888744

H_I 2.966936 0.455277 1.322700

OI -0.687163 1.514491 1.980244

HI -0.872206 2.464345 1.945179

HI -0.830174 1.268518 2.905847

OI 1.823482 -1.799365 -0.209074

HI 2.460753 -1.880506 -0.933982

HI 2.049147 -2.518054 0.399618

OI 1.812461 0.768954 -1.612177

HI 1.799959 0.683630 -2.576679

HI 2.648961 1.214701 -1.413980

OI -0.798646 -0.319657 -2.344248

HI -1.007392 -1.157779 -2.782614

HI -1.006603 0.360987 -3.001074

OI -1.051452 -2.321783 -0.224646

HI -1.989367 -2.549975 -0.147525

HI -0.608947 -3.158892 -0.427472

OI 0.106628 -1.284203 2.256088

HI 0.697199 -1.142736 3.010517

HI -0.432750 -2.049286 2.504913

OI -2.515924 0.184100 0.122230

HI -3.053482 0.477435 0.872680

HI -3.152677 0.022699 -0.589413

OI -0.548697 2.312029 -0.827509

HI 0.056395 2.936076 -1.254854

HI -1.410791 2.752988 -0.844858



Feff input files for EXAFS.

```
Backscattering Potential calculation Am(VI)
EDGE L3
S02 0.0
CONTROL 1 0 0 0 0 0
PRINT 0 0 0 3 0 0
COREHOLE RPA
EXAFS 18.0
CRITERIA 4.0 2.5
RPATH 6.0
NLEG 4
RPATH 6.0
TDLDA 1
SCF 6.0
EXCHANGE 0 -7.0 0.
POTENTIALS
0 95 Am 3 3
1 8 Oyl 3 3
2 8 OW 3 3
3 8 O 3 3
4 1 H 2 2
ATOMS
0.0000000 0.0000000 0.0000000 0 Am 0.0000000
1.0248800 -0.9132700 -1.0163530 1 Oyl 1.7080441
...
Paths calculation of Am(VI)
EDGE L3
S02 0.0
CONTROL 0 1 1 1 1 1
PRINT 0 0 0 3 0 0
COREHOLE RPA
EXAFS 18.0
CRITERIA 4.0 2.5
RPATH 6.0
NLEG 4
RPATH 6.0
TDLDA 1
SCF 6.0
EXCHANGE 0 -7.0 0.
POTENTIALS
0 95 Am 3 3
1 8 Oyl 3 3
2 8 OW 3 3
3 8 O 3 3
ATOMS
0.0000000 0.0000000 0.0000000 0 Am 0.0000000
1.0248800 -0.9132700 -1.0163530 1 Oyl 1.7080441
...
```

Feff input files for XANES.

```
Backscatering Potential calculation Am(VI)
CONTROL 1 0 0 0 0
PRINT 0 0 3 0 0
XANES
FMS 6.0 1
AFOLP
OPCONS
MPSE 2
COREHOLE RPA
TDLDA 1
SCF 6.0 0
EXCHANGE 0 0.0 0.0 2
POTENTIAL
0 95 Am 3 3
1 8 Oyl 3 3
2 8 OW 3 3
3 8 O 3 3
4 1 H 2 2
ATOMS
0.0000000 0.0000000 0.0000000 0 Am 0.0000000
1.0248800 -0.9132700 -1.0163530 1 Oyl 1.7080441
...
Paths calculation of Am(VI)
CONTROL 0 1 1 1 1
PRINT 0 0 3 0 0
XANES
FMS 6.0 1
AFOLP
OPCONS
MPSE 2
COREHOLE RPA
TDLDA 1
SCF 6.0 0
EXCHANGE 0 0.0 0.0 2
POTENTIALS
0 95 Am 3 3
1 8 Oyl 3 3
2 8 OW 3 3
3 8 O 3 3
ATOMS
0.0000000 0.0000000 0.0000000 0 Am 0.0000000
1.0248800 -0.9132700 -1.0163530 1 Oyl 1.7080441
...
```

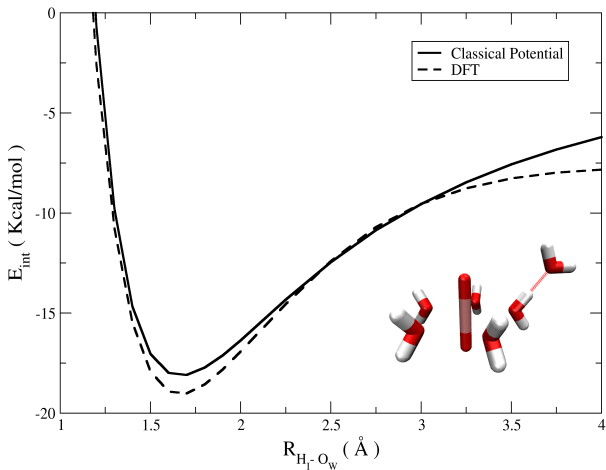


Figure S1: Interaction energy scans of a bulk water molecule with $[AmO_2 \cdot (H_2O)_5]^{2+}$ calculated with the classical potential and with DFT. The Americyl Hydrate-water potential was parametrized from the $[UO_2 \cdot (H_2O)_5]^+ \cdot H_2O$ potential developed in our previous paper (J. Chem. Phys. **2016**, *145*, 224502) and is extrapolated to the americyl case by changing the atomic charges (Table S3).

Table S1: Quantum chemistry optimization geometries of gas phase hydrated ions. The QM interaction energy of the first shell with the Am^{3+} or $[AmO_2]^{2+}$ are also included. Energies are given in kcal mol⁻¹ and distances in Å. All interaction energies include the counterpoise correction for the basis set superposition error.

	$[AmO_2 \cdot (H_2O)_5]^{2+}$			$[Am \cdot (H_2O)_8]^{3+}$		$[Am \cdot (H_2O)_9]^{3+}$	
	$r(Am-O_I)$	$Am-O_I$	E_{int}	$r(Am-O_I)$	E_{int}	$r(Am-O_I)$	E_{int}
B3LYP	1.71	2.48	-226.2	-	-	-	-
NEVPT2*	1.75	2.42	-239.4	2.51	-477.83	2.56	-502.2

*The level of theory for $[Am \cdot (H_2O)_n]^{3+}$ is MP2 which is essentially equivalent to NEVPT2 since the system has a closed shell when the Dolg pseudopotentials are used.

Table S2: First-shell water geometry in Å and degrees for Am(III) and Am(VI) as used in the simulations.

	First-shell geometry		
	Am(III) CN=8	Am(III) CN=9	Am(VI)
$r(O_I - H_I)$	0.97	0.97	0.97
$\widehat{H_I O_I H_I}$	104.5	104.8	106.2

Table S3: Effective charges of $[AmO_2 \cdot (H_2O)_5]^{2+}(aq)$ using the PCM to model the bulk solvent. The radii used are 2.65 Å, 1.40 Å and 1.20 Å for Am, O and H respectively. For Am(III) and Am(VI) the RESP and Merz-Kollman were respectively used to obtain these charges.

	Partial Charge (a.u.)		
	Am(III) CN=8	Am(III) CN=9	Am(VI)
q_{An}	3.0	3.0	2.71
$q_{O_{y1}}$	-	-	-0.50
q_{O_I}	-1.04	-0.97	-1.04
q_{H_I}	0.52	0.485	0.55

Table S4: Coefficients of the Americyl-water first shell interaction potential of americyl and root mean square error (RMSE) of the fit. Their units are $kcal\ mol^{-1}\ \text{\AA}^{-n}$ and $kcal\ mol^{-1}$ respectively.

Coefficients	Am(VI)
$C_4^{AnO_I}$	-3847.25
$C_6^{AnO_I}$	28895.08
$C_8^{AnO_I}$	-56776.53
$C_{12}^{AnO_I}$	180662.05
$C_4^{O_{y1}O_I}$	1329.48
$C_6^{O_{y1}O_I}$	-5640.56
$C_8^{O_{y1}O_I}$	318.75
$C_{12}^{O_{y1}O_I}$	235669.93
RMSE	0.8

Table S5: Coefficients from the fitting of the intramolecular cation interaction potential of americyl, RMSE_{total} and RMSE_{partial} which is computed for points with energy lower than $15\ kcal\ mol^{-1}$ with respect to the interaction energy of the minimum. Their units are $kcal\ mol^{-1}\ \text{\AA}^{-n}$ and $kcal\ mol^{-1}$ respectively.

Coefficients	Am(VI)
$C_4^{AmO_{y1}}$	-141079.35
$C_6^{AmO_{y1}}$	691027.72
$C_8^{AmO_{y1}}$	-1078152.49
$C_{12}^{AmO_{y1}}$	938322.18
$C_4^{O_{y1}O_{y1}}$	-305210.33
$C_6^{O_{y1}O_{y1}}$	7544789.67
$C_8^{O_{y1}O_{y1}}$	-53292782.03
$C_{12}^{O_{y1}O_{y1}}$	840547323.14
RMSE _{total}	2.3
RMSE _{partial}	0.6

Table S6: Coefficients of the $[\text{UO}_2 \cdot (\text{H}_2\text{O})_5]^{2+}$ - H_2O interaction potential from previous work (J. Chem. Phys. **2016**, *145*, 224502) also used for americyl. $\text{RMSE}_{\text{total}}$ and $\text{RMSE}_{\text{partial}}$ which is computed for points with energy lower than 15 kcal mol⁻¹ with respect to the interaction energy of the minimum. The units are kcal mol⁻¹ Å⁻ⁿ and kcal mol⁻¹.

Coefficients	Am(VI)	Coefficients	Am(VI)
C_4^{AmOW}	18578.27	$C_4^{\text{O}_1\text{OW}}$	-830.40
C_6^{AmOW}	-288922.08	$C_6^{\text{O}_1\text{OW}}$	6718.50
C_8^{AmOW}	1481816.44	$C_8^{\text{O}_1\text{OW}}$	-4208.51
C_{12}^{AmOW}	-12631787.76	$C_{12}^{\text{O}_1\text{OW}}$	-3888.10
C_4^{UHW}	-5094.89	$C_4^{\text{O}_1\text{HW}}$	28.22
C_6^{UHW}	65098.47	$C_6^{\text{O}_1\text{HW}}$	100.59
C_8^{UHW}	-268274.37	$C_8^{\text{O}_1\text{HW}}$	-40.17
C_{12}^{UHW}	1482339.87	$C_{12}^{\text{O}_1\text{HW}}$	1.06
$C_4^{\text{O}_1\text{OW}}$	-1503.86	$C_4^{\text{H}_1\text{OW}}$	-64.73
$C_6^{\text{O}_1\text{OW}}$	10373.23	$C_6^{\text{H}_1\text{OW}}$	166.44
$C_8^{\text{O}_1\text{OW}}$	-15794.55	$C_8^{\text{H}_1\text{OW}}$	-57.00
$C_{12}^{\text{O}_1\text{OW}}$	12403.99	$C_{12}^{\text{H}_1\text{OW}}$	1.25
$C_4^{\text{O}_1\text{HW}}$	187.28	$C_4^{\text{H}_1\text{HW}}$	4.63
$C_6^{\text{O}_1\text{HW}}$	-314.50	$C_6^{\text{H}_1\text{HW}}$	-0.29
$C_8^{\text{O}_1\text{HW}}$	213.54	$C_8^{\text{H}_1\text{HW}}$	0.07
$C_{12}^{\text{O}_1\text{HW}}$	-22.69	$C_{12}^{\text{H}_1\text{HW}}$	0.00
RMSE _{total}	1.9		
RMSE _{partial}	1.2		

$$E_{\text{HIW}} = \sum_i^{\text{HI sites}} \sum_j^{\text{Water sites}} \left(\frac{C_4^{ij}}{r_{ij}^4} + \frac{C_6^{ij}}{r_{ij}^6} + \frac{C_8^{ij}}{r_{ij}^8} + \frac{C_{12}^{ij}}{r_{ij}^{12}} + \frac{q_i q_j}{r_{ij}} \right)$$

Table S7: Coefficients of the intramolecular potential of $[\text{Am}\cdot(\text{H}_2\text{O})_8]^{3+}$ (aq). The bonding interaction is given by $E_{\text{AmO}_i} = k_r (r_{\text{AmO}_i} - r_0)^2$ and the angular interaction by $E_{\text{O}_j\text{O}_i} = k_\theta (\theta_{\text{O}_j\text{AmO}_i} - \theta_{\text{O}_j\text{AmO}_i}^0)^2 + E_{ij}^{\text{vdwTIP4P}} + E_{ij}^{\text{coul}}$. In addition, the electrostatic interactions of the H_I must be included.

Coefficients	
k_r (kcal mol ⁻¹ Å ⁻²)	49.0
r_0 (Å)	0.1
k_θ (kcal mol ⁻¹)	130.0
$\theta_{\text{O}_j\text{AmO}_i}^0$ (°)	Gas phase min. angles

Table S8: Coefficients of the intramolecular potential of $[Am \cdot (H_2O)_9]^{3+}$ (aq). The bonding interaction is given by $E_{AmO_i} = k_r (r_{AmO_i} - r_0)^2$ and the angular interaction by $E_{O_jO_i} = k_\theta (\theta_{O_jAmO_i} - \theta_{O_jAmO_i}^0)^2 + E_{ij}^{\text{vdwTIP4P}} + E_{ij}^{\text{coul}}$. In addition, the electrostatic interactions of the H_I must be included.

Coefficients	
k_0 (kcal mol ⁻¹ Å ⁻²)	45.5
r_0 (Å)	0.1
k_θ (kcal mol ⁻¹)	120.0
$\theta_{O_jAmO_i}^0$ (°)	Gas phase min. angles

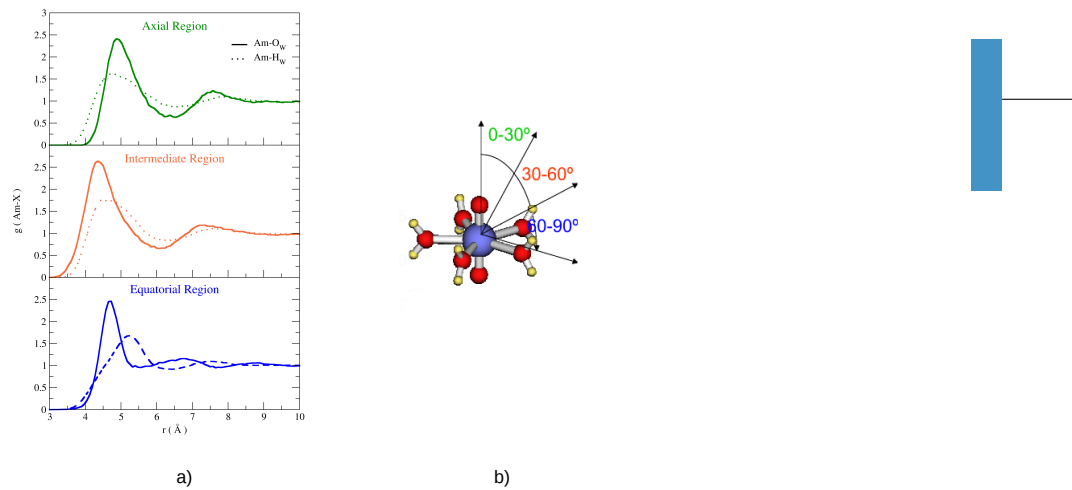


Figure S2: Figure S2a shows angle-resolved Am(VI)-Ow/Hw RDF for the axial region (0-30°), the intermediate region (30-60°), for the equatorial region (60-90°). g(Am-O) (solid lines) and g(Am-H) (dotted lines). Figure S2b defines the hydration angular regions. The analysis of this figure is analogous to that found in J. Chem. Phys. **2016**, *145*, 224502.

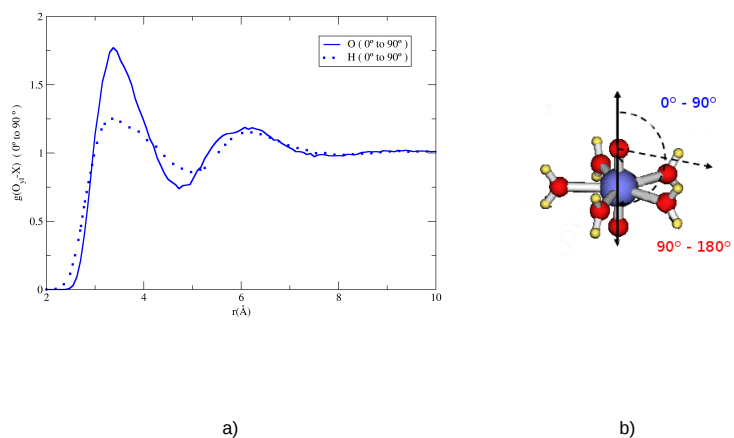


Figure S3: Figure S3a shows the angle-resolved $O_{\text{yl}}\text{-O}_W/\text{H}_W$ RDF for the $0\text{-}90^{\circ}$ for the Am(VI) system. Figure S3b defines the hydration angular regions. $g(O_{\text{yl}}\text{-O})$ (solid lines) and $g(O_{\text{yl}}\text{-H})$ (dotted lines). The analysis of this figure is analogous to that found in J. Chem. Phys. **2016**, *145*, 224502

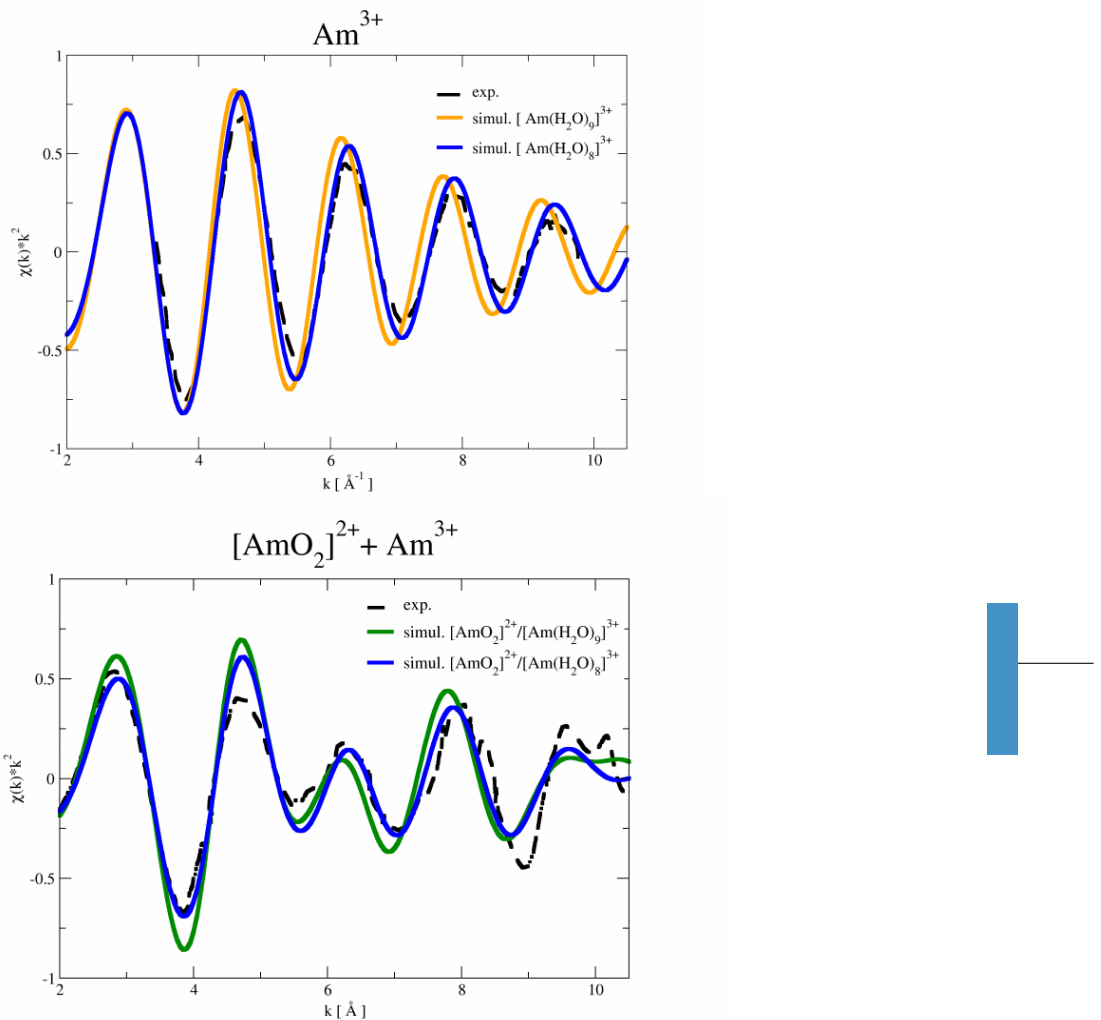
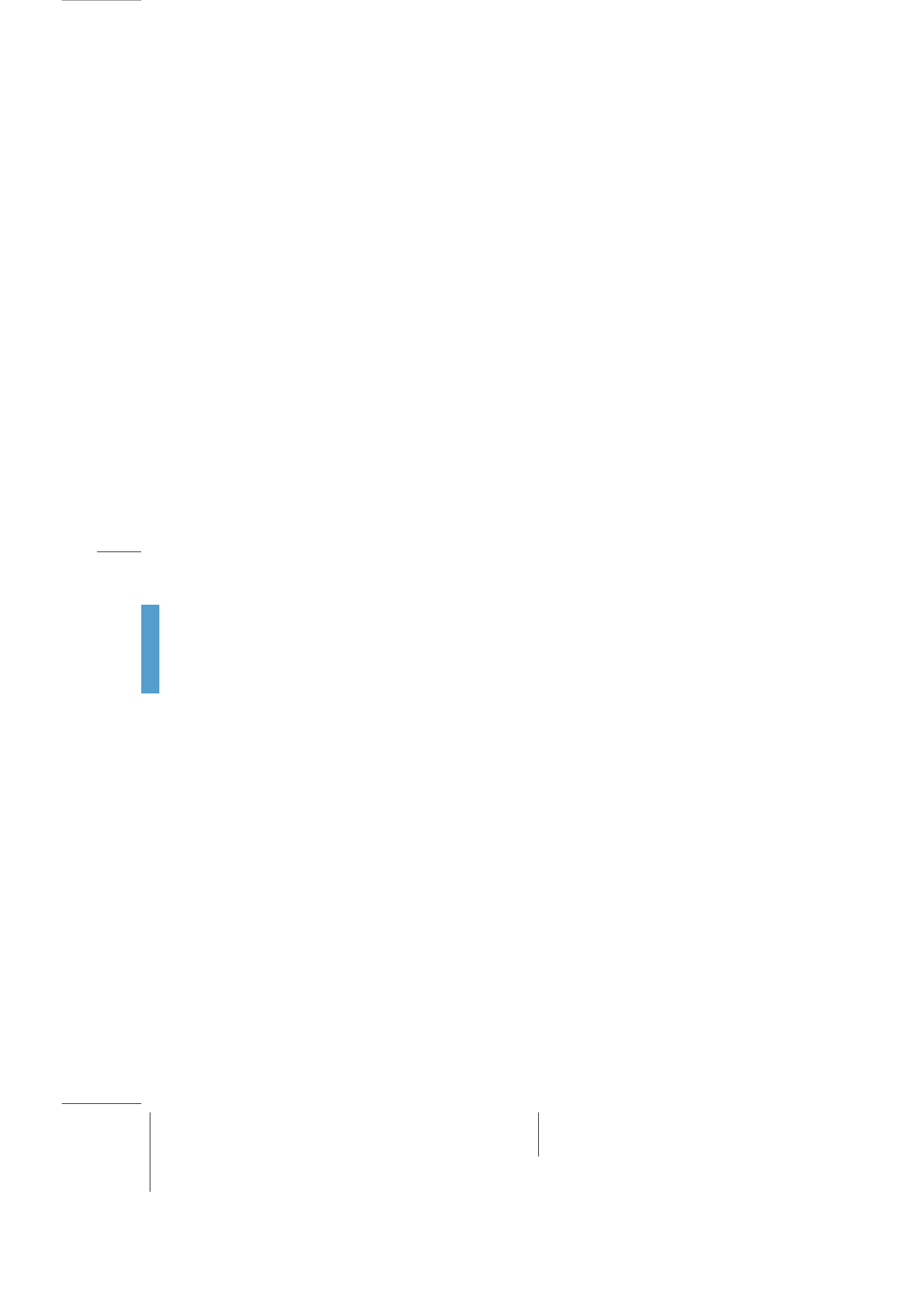


Figure S4: Experimental (dashed) vs. simulated (solid line) Am L₃-edge k²-weighted EXAFS spectra of Am aqueous solutions containing only Am(III) (top) or an Am(VI)/Am(III) mixture (bottom). In the Am(III) simulated spectra, the Am(III) hydrated with 8 (green) or 9 (orange) has been considered. In the case of Am(VI)/Am(III) mixture (55/45 ratio), the simulated spectrum using the Am^{3+} octahydrate (blue) or the Am^{3+} eneahydrate (dark green) is plotted.



Combining EXAFS and Computer Simulations to Refine the Structural Description of Actinyl in Water

7.1. Pending on publication

Combining EXAFS and Computer Simulations to Refine the Structural Description of Actinyl in Water.

Sergio Pérez-Conesa, José M. Martínez,

Rafael R. Pappalardo and Enrique Sánchez Marcos*

Departamento de Química Física, Universidad de Sevilla,

41012 Sevilla, Spain. e-mail:sanchez@us.es

Abstract

EXAFS spectroscopy is one of the most used techniques to solve the actinoid solution structure. In this work a systematic analysis of the EXAFS spectra of four actinyl cations, $[UO_2]^{2+}$, $[NpO_2]^{2+}$, $[NpO_2]^+$ and $[PuO_2]^{2+}$ has been carried out by comparing experimental results with simulated spectra. These were obtained by averaging individual contributions from snapshots taken from classical Molecular Dynamics simulations which employed recently developed $[AnO_2]^{2+/+}-H_2O$ *ab initio* force field based on the hydrated ion model.

Analysis of the complex EXAFS signal shows that both single scattering An-O_{yl} and An-O_w paths as well as multiple scattering paths involving $[AnO_2]^{+/2+}$ molecular cation are relevant. Theoretical EXAFS are in reasonable agreement for most cases, although the EXAFS region between 6 and 9 Å⁻¹ is hard to reproduce theoretically in some cases. Except uranyl, all studied actinyls are open-shell electron configurations, therefore it has been investigated how simulated EXAFS spectra are affected by minute changes of An-O bond distances produced by the inclusion of static and dynamic electron correlation in the quantum mechanical calculations.

We have developed a $[\text{NpO}_2]^+ - \text{H}_2\text{O}$ force field based on a NEVPT2 potential energy surface. In this way, the importance of including small structural changes in the force field and the Debye-Waller factors associated to the simulation has been checked, revealing them as crucial in XAS spectroscopy.

1 Introduction

Actinoid cations have a rich solution chemistry even in pure water which is very important technologically and environmentally.^{1,2} Reprocessing of spent nuclear fuel involves several actinoids mainly under the form of actinyl aqua ions $[\text{AnO}_2(\text{H}_2\text{O})_m]^{q+}$.^{3–10} In the actinyl motif, the actinoid cation, in oxidation state V or VI, bonds covalently to two oxygen atoms (“O-yl”) forming a linear unit. In aqueous solution, the equatorial plane perpendicular to this axis contains typically 5 water molecules coordinated to the metal atom. Knowledge of the chemistry of actinyl cations is key in the recovery of minor actinoids of high radiotoxicity from spent nuclear fuel.¹⁰

X-ray absorption spectroscopy, particularly Extended X-ray absorption fine structure (EXAFS), is a powerful experimental technique to characterize the solvation around metal ions, given that it provides short range structural information around metal ions in solution with remarkable accuracy and sensitivity,^{11,12} among them actinoids.¹³ In particular, EXAFS has a structural precision in the hundredth of an angstrom in determining coordination distances around an absorbing atom. In addition, the technique is element specific and can handle submillimolar concentrations of the analyte. Unfortunately, the price to pay for its high precision is the difficulty in the fitting and interpretation of complex signals exhibiting multiple contributions, as those of actinyls. In many cases analogies with lighter lanthanoids are made¹³ or theoretical tools are used giving rise to many interesting insights.^{11,14–17} In addition, the simulation of XAS spectra from molecular dynamics (MD) trajectories and its comparison to experiment has proven to be an useful tool to assess the accuracy of the intermolecular potentials employed in the simulation and to

interpret experimental results.^{18–21}

In 2016 we presented a new DFT-level classical interaction potential for the $[UO_2]^{2+}$ pentahydrate¹⁶ based on the Hydrated Ion model.^{11,22} With the developed force field we carried out classical MD simulations in which we were able to reproduce a variety of experimental data.¹⁶ Particularly, the model satisfactorily reproduces the experimental EXAFS spectrum of uranyl. We decomposed the spectrum in two main single scattering path components: an intense, high frequency and slowly decaying signal corresponding to U-O_{y1} paths, and another less intense, lower frequency and fast-decaying signal corresponding to U-O_w paths. Multiple scattering paths involving crossed U-O_{y1} and U-O_w paths were found to be minor contributions. The methodology developed was extended to other actinyl cations - $[NpO_2]^{2+}$, $[NpO_2]^+$, $[PuO_2]^{2+}$ and $[AmO_2]^{2+}$ providing a general view of actinyl hydration and the effect of changing properties when going from the dication to the monocation.²³ Using the americyl hydrated ion model we were able to study the nature of the first Am(VI)/Am(III) mixture spectrum recorded²⁴ by Riddle et al.²⁵ Despite the importance of XAS spectroscopy in actinyl chemistry, to the best of our knowledge there are no MD simulated spectra obtained for actinyls different from uranyl in the literature,^{16,26} some of them devoted to their complexation and behavior in organic phases.^{27,28} The only exception are the XANES spectra calculated for neptunyl by den Auwer et al.²⁹ with a rigid aqua ion structural model.

This work pursues the systematic study of the MD-based simulated EXAFS spectra obtained by means of the application of our actinyl force fields in solution for the series of actinyls cations, $[UO_2]^{2+}$, $[NpO_2]^{2+}$, $[NpO_2]^+$ and $[PuO_2]^{2+}$. Figure 1 shows the experimental k^3 -weighted EXAFS spectra of the actinyls recorded by different groups during the last twenty years in different independent experiments. Except for $[PuO_2]^{2+}$ where only one spectrum is presented, the comparison among spectra is quite similar for uranyl^{5,30} and neptunyl(VI),^{31,32} but in the Np(V) case a larger discrepancy is found between the two spectra, even when both groups recorded the Np(V) spectrum^{31,32} in the

same experiment where that of the Np(VI) was recorded. In both cases dilute aqueous solutions were measured and no complexation or other medium effects could be responsible of this discrepancy, but rather the intrinsic difficulty to carry out measurements of this type of highly-radioactive samples.

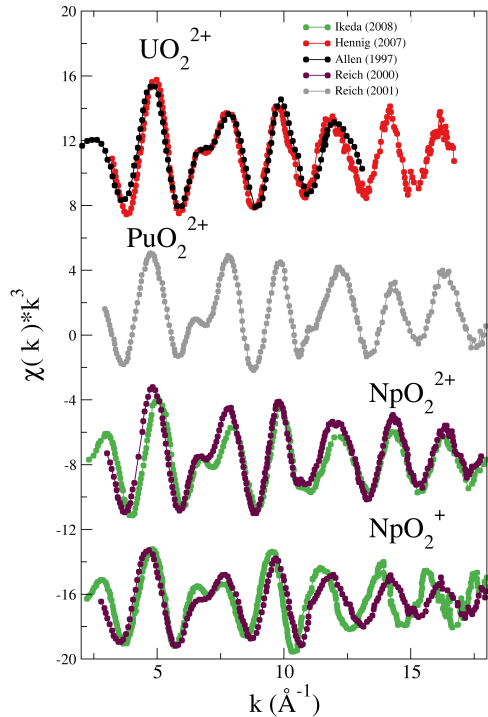


Figure 1: Experimental k^3 -weighted EXAFS spectra recorded for aqueous solutions of $[\text{UO}_2]^{2+}$ (Allen (1997)⁵ -black dotted line- and Hennig (2007)³⁰ -red dotted line-), $[\text{PuO}_2]^{2+}$ (Reich (2001)³³ -grey dotted line-), $[\text{NpO}_2]^{2+}$ and $[\text{NpO}_2]^+$ (Ikeda (2008)³² - green dotted line- and Reich (2000)³¹ -magenta dotted line-)

Except uranyl all the actinyls of this study have open-shell electron configurations. We will evaluate how good is the DFT mean field treatment of static electronic correlation effects to provide an accurate enough EXAFS spectrum prediction for open-shell actinyls, since DFT has shown the ability of our model to reproduce many other experimental properties.^{23,34,35} To get insight into this question and check the EXAFS sensitivity to minute

structural changes, multi-reference NEVPT2^{36–38} computations have been performed to build a force field potential based on this quantum-mechanical level.

2 Computational Methods

2.1 Quantum Chemical Calculations

The interaction potentials published in our previous article²³ were parameterized at a DFT level of theory: B3LYP^{39,40}/aug-cc-PVDZ⁴¹ with Stuttgart relativistic effective core pseudopotentials⁴² using Gaussian09.⁴³ The B3LYP functional has given reasonable interaction energies and molecular geometries for actinyls^{44–46} both open and closed shell.^{47,48} In our previous work we showed that an interaction potential parameterized at that level of theory was able to reproduce satisfactorily many experimental properties.

To get insight into the impact that static and dynamical electron correlation may have on the geometrical structure and dynamical and structural disorder of the close environment of the actinyl, NEVPT2 calculations, which incorporate both dynamical and static electronic correlation were carried out using the ORCA⁴⁹ program. Although these calculations are too expensive to envisage the full force field development for every case, we shall use them to check the influence of electron correlation in the actinyl geometry and the structural and dynamical disorder, and as a result their simulated EXAFS spectra. The active space chosen was the set of atomic-like f-orbitals in addition to the molecular orbitals resulting from combining actinide f-orbitals and O_{y1} p-orbitals. This resulted in CASSCF(n,10) configurations where n is 6 plus the number of actinoid unpaired electrons. Since the ground states are degenerate, calculations were carried out using a state average over the degenerate states excluding excited states. The perturbational step of the calculation was done using quasi-degenerate perturbation theory. The basis sets used were ma-def2-TZVP for O, def2-SVP for H and SD(60,MWB)//DEF-TZVP for actinoids.^{50–52} The calculations were accelerated using the RI and RIJK pseudospectral methods with

“autoaux” auxiliary basis sets. Geometry optimizations due to the lack of analytical gradients were performed numerically by evenly changing the M-O_{yl} and M-O_W distances in a 2D grid with an interval of $\sim 0.005\text{\AA}$.

2.2 Molecular Dynamics Simulations

MD simulations were run in a similar way to our previous studies on actinyls.^{16,23,24} A single pentahydrated actinyl ion, $[\text{AnO}_2(\text{H}_2\text{O})_5]^{2+}$, ($\text{An}=\text{U(VI),Np(VI),Np(V),Pu(VI)}$) and 1495 TIP4P water molecules were placed in a cubic box at liquid water density. The simulations were run at 300 K and 1 atm in the NPT ensemble using the Nosé-Hoover thermostat and barostat with $\tau = 0.5$ ps. Non-bonded interactions were cut at 14\AA and electrostatic interactions were computed using Ewald summation. The equations of motion were integrated using a 1 fs timestep for a total time of 5 ns. All simulations were run using DL_POLY Classic.⁵³



The first set of interaction potentials used in this work were developed previously.^{16,23,24} They are based on the hydrated ion model proposed by our group over 20 years ago.²² In this model we consider the ion and its first hydration shell as the solute rather than the naked ion. In this way first-shell water molecules have different atom types and interaction potentials than bulk water molecules. This allows the first-shell molecules to have different partial charges (even with charge transfer from the metal) and different non-bonded interactions with the metal and bulk water molecules. In this way we are able to incorporate charge transfer and polarization effects into an effective non-polarizable site-site interaction potential. The caveat to this model is that if a first-shell water molecule were to leave the first shell it would render the system unphysical. Nevertheless, for many ions, as is the case for actinyls, the characteristic time for this phenomenon is much longer than the simulation time.

The interaction potentials were all parameterized from B3LYP quantum chemical calculations. The interaction within the molecular ion (IMC, intramolecular cation) and

the interaction of the molecular ion with its first shell (IW1, ion first-shell water) were parameterized specifically for each ion. The interaction of the hydrated ion and bulk water molecules (HIW, hydrated ion water) was parameterized only for the uranyl case. For the rest of the actinoids the non-electrostatic component of the HIW of uranyl was used since it has proven to be fairly similar across the actinoids studied.²³ Non-electrostatic water-water interactions within the first shell were modeled in the same way as in the TIP4P model. Finally, the TIP4P water model was used to model bulk water molecules. Therefore the energy of the system is defined by the following expression:

$$E = E_{\text{IMC}} + E_{\text{IW1}} + E_{\text{W}_1-\text{W}_1} + E_{\text{HIW}} + E_{\text{TIP4P}} \quad (1)$$

The parameterized terms of the potential were given the functional form of r^{-n} with $n = 4, 6, 8, 12$ plus the coulombic term. As an example we present below the functional form of the IW1 potential:

$$E_{\text{IW1}} = \sum_i^{\text{AnO}_2 \text{ sites}} \frac{C_4^{\text{iO}}}{r_{\text{iO}}^4} + \frac{C_6^{\text{iO}}}{r_{\text{iO}}^6} + \frac{C_8^{\text{iO}}}{r_{\text{iO}}^8} + \frac{C_{12}^{\text{iO}}}{r_{\text{iO}}^{12}} + \sum_i^{\text{AnO}_2 \text{ sites}} \sum_j^{\text{Water sites}} \frac{q_i q_j}{r_{ij}} \quad (2)$$

Due to the paramagnetic nature of the actinyls, except the uranyl case, in this work we have explored how the inclusion of static and dynamic electron correlation in the wavefunction used to fit the force field may affect to the solution properties and the shape of the simulated EXAFS spectra. To fulfill this task we have reparametrized the NpO_2^+ interaction potential using NEVPT2 calculations rather than B3LYP. All the parameters of the interaction potentials including the new Np(V) full NEVPT2 potential can be found in the Supporting Information.

2.3 Simulated XAS spectra

Molecular dynamics simulations are a useful tool to interpret and analyze complex EXAFS spectra.^{15,21,54} In addition, comparison of experimental spectra with simulated ones generated from an ensemble of MD configurations is a useful and sensitive tool to validate force fields.^{18,21} 200 configurations of $[AnO_2]^{2+/+}$ were extracted from the MD trajectories. The configurations included water molecules up to the first solvation shell since we have found the second shell to have no-influence in the spectra. Average L_{III} -edge spectra were obtained from the individual spectra using the FEFF 9.6 code⁵⁵ including multiple scattering up to four-legged paths. Details of the spectrum simulation method can be found elsewhere.^{11,21} In addition, the FEFF input files can be found in the supplementary information. A value of $S_0^2 = 0.9$ has been assumed for the simulated spectra, and $\Delta E_0 = -8$ eV has been applied in order to match the first resonance of the experimental spectrum.

All experimental EXAFS spectra were obtained at highly acidic pH, with non-coordinating counterions and an actinyl concentration of $\sim 50\text{-}10$ mM.^{5,30-33}

3 Results and Discussion

Figures 2 and 3 shows the comparison between the experimental spectra of the different actinyls,^{5,30-33} and the simulated spectra obtained with the force field derived from B3LYP potential energy surfaces (blue lines) developed in our previous works on actinyls.^{16,23}

The cases of the UO_2^{2+} and NpO_2^{2+} collected in Figure 2 show a good general agreement with experiment, in particular bearing in mind that there are two different experimental spectra to compare for each actinyl. When considering the comparison for the cases of PuO_2^{2+} and NpO_2^+ , shown in Figure 3, deviations from experimental spectra are significant, in particular in the case of the Np(V) actinyl. Actinyls in aqueous solution have complex EXAFS spectra due to the superposition of several scattering paths of rather different in nature. Two single scattering (SS) signals are ascribed to a slowly

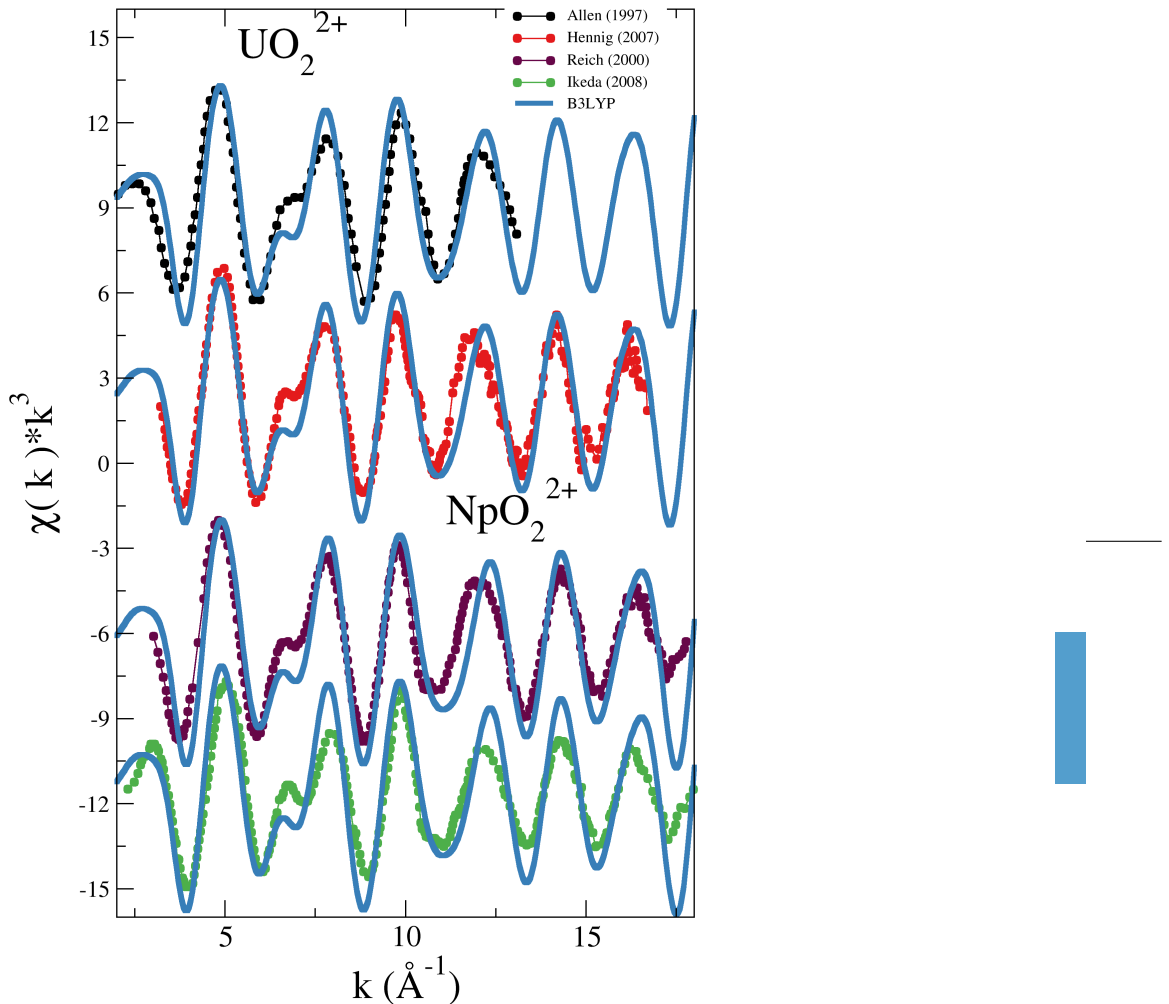


Figure 2: Simulated (blue solid line) and experimental (dots) Li_{III}-edge k^3 -weighted EXAFS spectra for UO_2^{2+} and NpO_2^{2+} in water. The experimental conditions are low pH, with non-coordinating counter-ions and an actinyl concentration of $\sim 10\text{mM}$. The experimental EXAFS are taken from Allen (1997)⁵ (black dotted line) and Hennig (2007)³⁰ (red dotted line) for uranyl, and from Reich (2000)³¹ (magenta dotted line) and Ikeda (2008)³² (green dotted line).

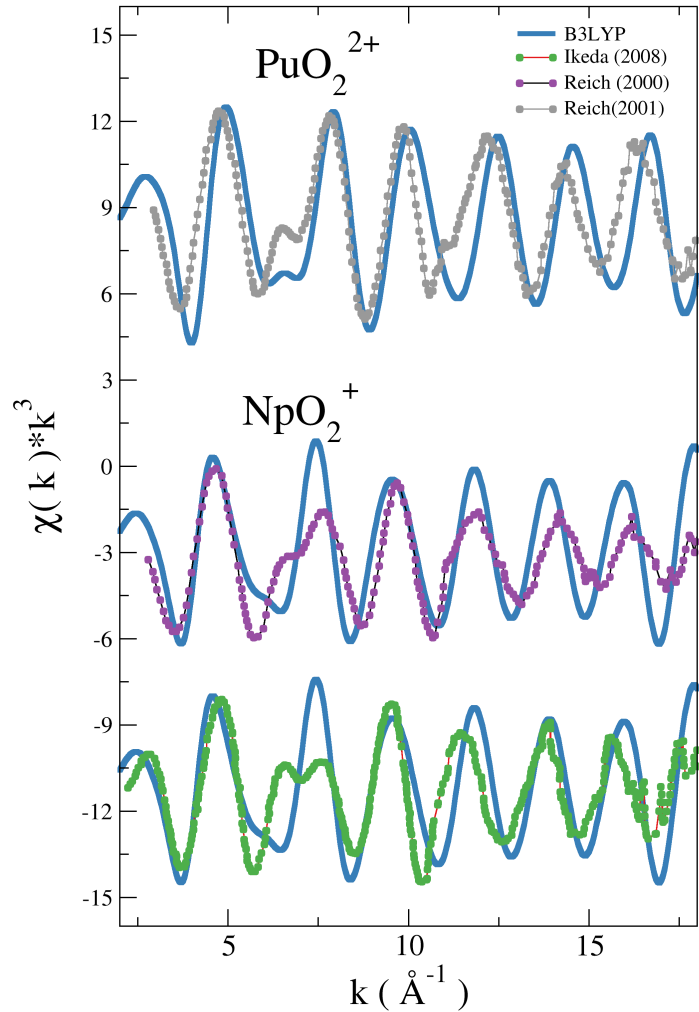


Figure 3: Simulated (blue solid line) and experimental (dots) L_{III}-edge k³-weighted EXAFS spectra for PuO₂²⁺ and NpO₂⁺ in water. The experimental conditions are low pH, with non-coordinating counter-ions and an actinyl concentration of ~10mM. The experimental EXAFS are taken from Reich (2001)³³ (grey dotted line) for plutonyl, and from Reich (2000)³¹ (magenta dotted line) and Ikeda (2008)³² (green dotted line).

decaying high frequency An-O_{y1} contribution with high intensity and a lower frequency fast decaying An-O_w signal. In addition a set of multiple scattering paths associated to the AnO₂²⁺ cation.^{16,56} Destructive interference of the two components generates the characteristic shoulder around 6.5 Å⁻¹. At high k values the spectrum is mostly the An-O_{y1} component. This phenomenon is demonstrated in Figure 4 where the B3LYP-based simulated EXAFS spectrum corresponding to the uranyl has been decomposed in two SS U-O_{y1} and U-O_w paths and the MS paths involving the uranyl unit. It is observed how the hump and its surrounding region, 6-8 Å⁻¹, is mainly the result of the SS U-O_w and MS paths (see pink and magenta vertical lines), whereas the high k-region is dominated by the SS U-O_{y1} paths (see green vertical lines).

Once analyzed the main structural factors responsible of the EXAFS spectrum, since the differences between simulated and experimental spectra differ became larger as the series progresses and the spin multiplicity of the complex increases, it became apparent that a multireference PES including static and dynamic correlation should help to solve the problem. We hypothesized that the B3LYP An-O_{y1} distances were systematically short and, probably as a consequence of the larger congestion around the metal center, the An-O_w B3LYP distances were too long. The oxo-bond is markedly covalent in character, as a consequence an underestimation of its static electronic correlation causes a shortening of the An-O_{y1}.

3.1 Simulated EXAFS spectrum based on a NEVPT2 force field for NpO₂⁺ in aqueous solution

To prove the hypothesis that the lower quality of the spectra of NpO₂⁺ and PuO₂²⁺ with respect to uranyl was due to the lack of a multireference representation for both actinyls, we developed a classical interaction potential for Np(V) based on a NEVPT2 level PES. The spectrum derived from the set of MD-simulation snapshots using the NEVPT2 force field is presented in Figure 5 (yellow solid line). It is clearly superior to the B3LYP-level

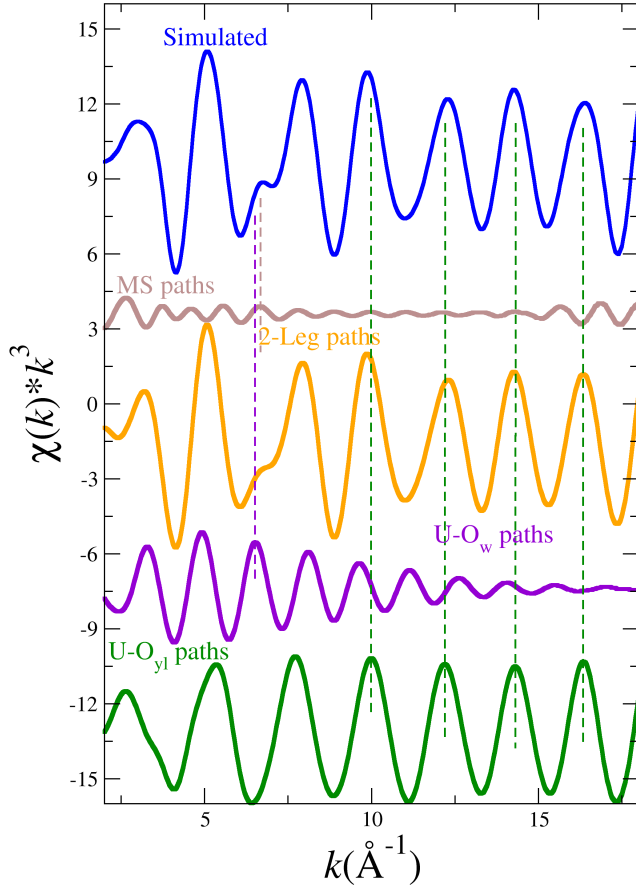


Figure 4: Simulated L_{III}-edge k^2 -weighted EXAFS spectrum for U(VI) (blue line) and its decomposition in MS scattering (brown line) and SS scattering (yellow line) contributions, as well as the U-O_w (purple line) and U-O_{yl} (green line) SS contributions.

counterpart (see Figure 3).

Table 1 collects the optimized An-O_{y1} and An-O_w distances obtained at the QM level (B3LYP-opt, MP2-opt/NEVPT2-opt) for the isolated actinyl aqua ion, as well as the values derived from the use of the developed force field (B3LYPPOT-opt, NEVPOT-opt) and the most likely distances and their corresponding Debye-Waller factors derived from the MD simulations (MD-B3LYP, MD-NEVPT2, MD-fit). The geometry of the [NpO₂(H₂O)₅]⁺ at the B3LYP-level has Np-O_{y1} and Np-O_w distances of 1.78 Å and 2.59 Å respectively. As anticipated the NEVPT2-level optimized geometry has longer Np-O_{y1} bonds (1.83 Å) and shorter Np-O_w distances (2.52 Å), this is also reflected in the distances obtained in the MD simulations. We conclude for Np-O_{y1}⁺ that the problem of our initial spectrum was that the reference DFT hydrated ion minimum energy geometry is not accurate enough for appropriate EXAFS prediction. EXAFS spectrum is so sensitive to structure that changes in a few hundredths of angstrom imply noticeable modifications in the EXAFS spectrum shape. A multireference QM method including both static and dynamic electron correlation is therefore necessary.

The change in distances of [NpO₂(H₂O)₅]⁺ when going from B3LYP to NEVPT2 is also found in the cases of the other open-shell actinyl aqua ions, although this effect is less pronounced.

3.1.1 EXAFS fitting.

After producing the spectra above mentioned, we decided to take one step further into obtaining the best possible structural parameters. We tried to condense all the knowledge gained in the previous EXAFS simulation to look for structural parameters of the actinyls producing simulated spectra very similar to experiment but from a single structure of the actinyl pentahydrate and not from a MD trajectory. The EXAFS of actinyls are mainly defined by An-O_{y1} and An-O_w single scattering path contributions of a pentahydrate. Therefore, in a first approximation the total signal can be obtained by summing the

Table 1: EXAFS spectra, gas-phase QM optimization and MD first-shell distances, and Debye-Waller factors (σ^2) for the studied actinyl aqua ions. All experimental EXAFS spectra are obtained at highly acidic pH, with non-coordinating counterions and an actinyl concentration of \sim 50-10 mM. The MD values are obtained from the RDF-maxima and variance. Distances are given in Å and DW in Å²

System	r_{AnO_1}	$\sigma_{\text{AnO}_1}^2$	r_{AnO_1}	$\sigma_{\text{AnO}_1}^2$
$[\text{UO}_2]^{2+}(\text{aq})$				
B3LYP-opt	1.74		2.49	
MP2-opt	1.77		2.50	
B3LYPPOT-opt	1.76		2.49	
MD-B3LYP	1.76	0.0004	2.48	0.007
Exp (Hennig 2007) ³⁰	1.76 \pm 0.02	0.002	2.41 \pm 0.02	0.007
Exp (Allen 1997) ⁵	1.76 \pm 0.01	0.002	2.41 \pm 0.01	0.007
$[\text{NpO}_2]^{2+}(\text{aq})$				
B3LYP-opt	1.73		2.48	
NEVPT2-opt	1.77		2.42	
B3LYPPOT-opt	1.74		2.47	
MD-B3LYP	1.74	0.0004	2.46	0.007
MD-fit	1.77	0.0008	2.41	0.004
Exp (Ikeda 2008) ³²	1.76 \pm 0.01	0.002	2.42 \pm 0.01	0.006
Exp (Reich 2000) ³¹	1.754 \pm 0.003	0.002	2.414 \pm 0.006	0.006
$[\text{NpO}_2]^+(\text{aq})$				
B3LYP-opt	1.78		2.59	
NEVPT2-opt	1.83		2.52	
B3LYPPOT-opt	1.78		2.59	
NEVPOT-opt	1.83		2.52	
MD-B3LYP	1.79	0.0007	2.61	0.012
MD-fit	1.82	0.0008	2.47	0.005
MD-NEVPT2	1.84	0.0007	2.54	0.011
Exp (Ikeda 2008) ³²	1.84 \pm 0.01	0.002	2.49 \pm 0.01	0.007
Exp (Reich 2000) ³¹	1.822 \pm 0.003	0.002	2.488 \pm 0.009	0.006
$[\text{PuO}_2]^{2+}(\text{aq})$				
B3LYP-opt	1.71		2.46	
NEVPT2-opt	1.76		2.43	
B3LYPPOT-opt	1.71		2.47	
MD-B3LYP	1.71	0.0006	2.45	0.009
MD-fit	1.76	0.0006	2.43	0.005
Exp (Reich 2001) ³³	1.74 \pm 0.01	0.001	2.42 \pm 0.01	0.005

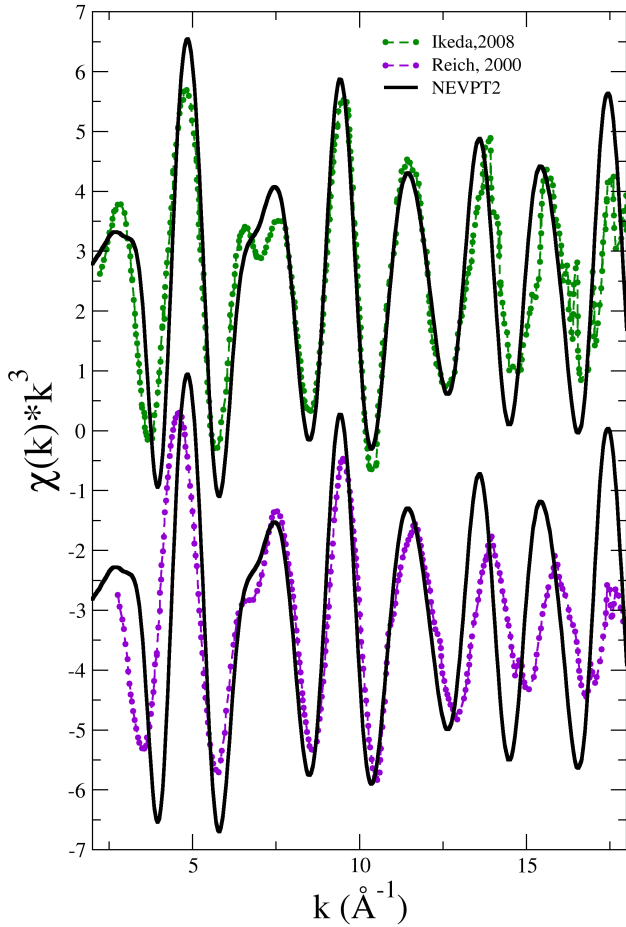


Figure 5: Simulated (black solid line) vs. experimental^{31,32} (dots) L_{III}-edge k^3 -weighted EXAFS spectra for NpO_2^+ . The simulated spectra is obtained using the NEVPT2-level interaction potential developed for neptunyl.

simulated EXAFS of a single structure of the hydrate without the O_{yI} atoms and the simulated EXAFS of the actinyl without the water molecules. This approximation neglects cross paths. Of course since the calculations are generated from a single structure, both components should be multiplied by an exponential decay term to include the DW factor and the thermal dispersion of the distances. Four parameters are unknown: the two An-O distances and their corresponding DW factors.

In our procedure, we varied first the An-O_{yI} distance such that the An-O_{yI} component would match the experimental spectrum at high k values where the other component is negligible due to its fast decay. In addition, we assumed as starting DW factor values those derived from the MD simulations. These values were modified slightly to get computed spectra close to the experimental ones. This assumption is sound given the good correspondence of the MD simulated and experimental spectra at high k . Finally, we varied the An-O_w distance and DW factor in a 2D grid and searched for the pair of parameters that qualitatively gave the spectrum more similar to the experimental EXAFS. The simulated spectra obtained with this procedure are presented in Figure 6. Our computed spectra are capable of reproducing most of the features of the experiment and reassure us that the structural parameters obtained are sound.

In Table 1, we summarize the EXAFS parameters obtained in this study and their experimental counterparts. It is clear that our theoretical parameters are significantly improved including the static correlation effects in the simulation, in the case of NpO₂⁺, or as a result of the formal fitting procedure. This improvement is particularly strong for the An-O_{yI} distance which is the dominant contribution to the spectra.

4 Conclusions

Regardless of the overall well behavior of our previously developed interaction potentials, based on B3LYP potential energy surfaces, with most experimental properties,^{16,23,24} their simulated EXAFS spectra do not reproduce adequately the experimental ones in all cases.

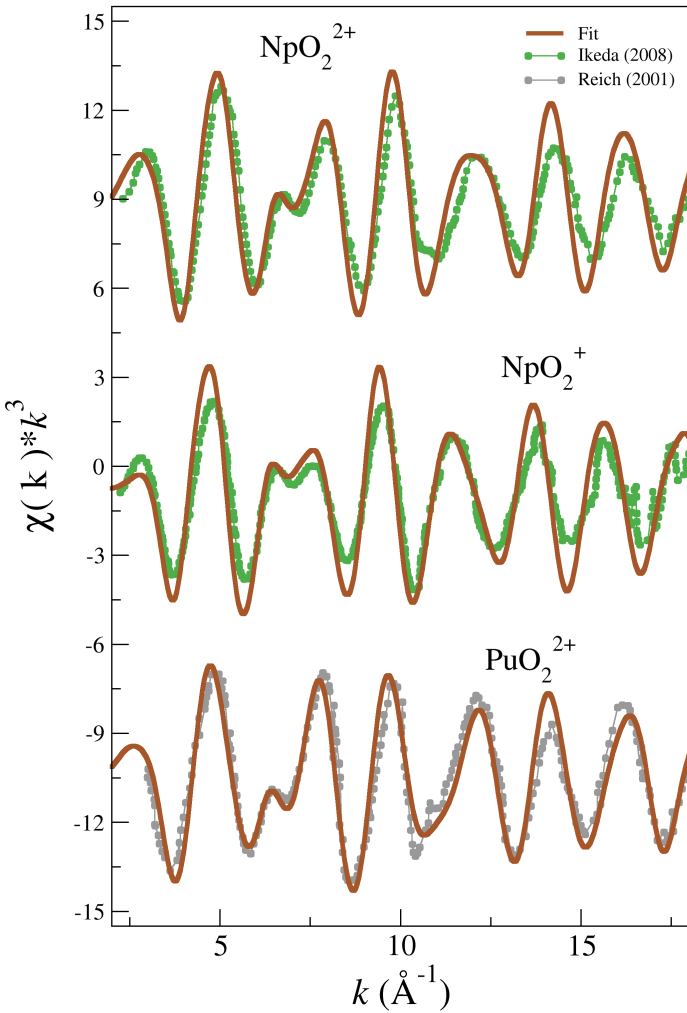


Figure 6: Simulated (brown solid line) and experimental^{30,32,57} (dotted line) L_{III}-edge k²-weighted EXAFS spectra for Np(VI), Np(V) and Pu(VI). The simulated spectra are obtained using the procedure described in the text.

We have shown in the NpO_2^+ case that, at least, one of the main reason is the lack of static correlation in the B3LYP PES used to parametrize the potentials. This absence of static correlation generates small structural changes in the actinyl aqua ions which produces noticeable changes in the EXAFS spectra.

Using the understanding gained from our simulations we decided to fit the HI structural model in order to gain precision in the prediction of experimental parameters. To fit the experimental EXAFS spectrum, the theoretical $\chi(k)$ was obtained as the sum of the two main single scattering paths: one concerning the actinyl cation and another involving the metal atom and its first-shell water molecules. In order to fit the spectrum, the M-O_{yl} DW was assumed to be the one obtained in the MD simulation. Then the M-O_{yl} was adjusted in order to reproduce the high- k part of the spectrum that has minimal contribution of the Ow -involving paths. Finally the M-Ow distance and the DW associated to the calculation were scanned in a 2D grid to find the spectrum with the best fit to the experimental spectrum.

In conclusion, we found out that for actinyl aqua ions the structural precision of EXAFS is so high that in order to properly simulate their EXAFS spectrum the impact of static correlation effects on the actinyl structure must be taken into account.

5 Acknowledgments.

This work was financially supported by the Spanish Ministry of Science, Innovation and Universities (PGC2018-099366-B-I00). SPC acknowledges a PhD scholarship FPU (Formación de Profesorado Universitario) for the Spanish Education Ministry.

References

- [1] Choppin, G. R.; Jensen, M. P. In *Chem. Actin. Trans. Elem.*, 3rd ed.; Morss, L. R., Edelstein, N., Fuger, J., Katz, J. J., Eds.; Springer: Dordrecht, 2008; Vol. 4; Chapter

23, pp 2524–2621.

- [2] Cotton, S. *Lanthanide & Actinide Chemistry*; Wiley: London, 2006.
- [3] Bardin, N.; Rubini, P.; Madic, C. *Radiochim. Acta* **1998**, *83*, 189 and references therein.
- [4] Aaberg, M.; Ferri, D.; Glaser, J.; Grenthe, I. *Inorg. Chem.* **1983**, *22*, 3986–3989.
- [5] Allen, P. G.; Bucher, J. J.; Shuh, D. K.; Edelstein, N. M.; Reich, T. *Inorg. Chem.* **1997**, *36*, 4676–4683.
- [6] Conradson, S. D. *Appl. Spectrosc.* **1998**, *52*, 252A–279A.
- [7] Wahlgren, U.; Moll, H.; Grenthe, I.; Schimmelpfennig, B.; Maron, L.; Vallet, V.; Gropen, O. *J. Phys. Chem. A* **1999**, *103*, 8257–8264.
- [8] Neuefeind, J.; Soderholm, L.; Skanthakumar, S. *J. Phys. Chem. A* **2004**, *108*, 2733–2739.
- [9] Soderholm, L.; Skanthakumar, S.; Neuefeind, J. *Anal. Bioanal. Chem.* **2005**, *383*, 48–55.
- [10] McKibben, J. M. *Radiochim. Acta* **1984**, *36*, 3–15.
- [11] Galbis, E.; Hernández-Cobos, J.; den Auwer, C.; Le Naour, C.; Guillaumont, D.; Simoni, E.; Pappalardo, R. R.; Sánchez Marcos, E. *Angew. Chem. Int. Ed. English* **2010**, *122*, 3899–3903.
- [12] Altmaier, M.; Gaona, X.; Fanghänel, T. *Chem. Rev.* **2013**, *113*, 901–943.
- [13] Denecke, M. A. *Coord. Chem. Rev.* **2006**, *250*, 730–754.
- [14] Atta-Fyn, R.; Bylaska, E. J.; Schenter, G. K.; de Jong, W. A. *J. Phys. Chem. A* **2011**, *115*, 4665–4677.

- [15] D'Angelo, P.; Martelli, F.; Spezia, R.; Filippone, A.; Denecke, M. A. *Inorg. Chem.* **2013**, *52*, 10318–10324.
- [16] Pérez-Conesa, S.; Torrico, F.; Martínez, J. M.; Pappalardo, R. R.; Sánchez Marcos, E. *J. Chem. Phys.* **2016**, *145*, 224502.
- [17] Spezia, R.; Migliorati, V.; D'Angelo, P. *J. Chem. Phys.* **2017**, *147*, 161707.
- [18] Palmer, B. J.; Pfund, D. M.; Fulton, J. L. *J. Phys. Chem. Chem.* **1996**, *100*, 13393–13398.
- [19] Campbell, L.; Rehr, J.; Schenter, G.; McCarthy, M.; Dixon, D. *J. Synchrotron. Rad.* **1999**, *6*, 310–312.
- [20] Chilemi, G.; D'Angelo, P.; Pavel, N. V.; Sanna, N.; Barone, V. *J. Am. Chem. Soc.* **2002**, *124*, 1968–1976.
-
- [21] Merkling, P. J.; Adela Muñoz-Páez, A.; Sánchez Marcos, E. *J. Am. Chem. Soc.* **2002**, *124*, 10911–10920.
-
- [22] Martínez, J. M.; Pappalardo, R. R.; Sánchez Marcos, E. *J. Am. Chem. Soc.* **1999**, *121*, 3175–3184.
- [23] Pérez-Conesa, S.; Martínez, J. M.; Pappalardo, R. R.; Sánchez Marcos, E. *J. Chem. Phys.* **2019**, *150*, 104504(1)–(10).
- [24] Pérez-Conesa, S.; Martínez, J. M.; Pappalardo, R. R.; Sánchez Marcos, E. *Inorg. Chem.* **2018**, *57*, 8089–8097.
- [25] Riddle, C.; Czerwinski, K.; Kim, E.; Paviet, P.; Weck, P.; Poineau, F.; Conradson, S. *J. Radioanal. Nucl.* **2016**, *309*, 1087–1095.
- [26] Nichols, P.; Bylaska, E. J.; Schenter, G. K.; de Jong, W. *J. Chem. Phys.* **2008**, *128*, 124507.

- [27] Duvail, M.; Dumas, T.; Paquet, A.; Coste, A.; Berthon, L.; Guilbaud, P. *Phys. Chem. Chem. Phys.* **2019**, *21*, 7894–7906.
- [28] Sukhbaatar, T.; Duvail, M.; Dumas, T.; Dourdain, S.; Arrachart, G.; Solari, P. L.; Guilbaud, P.; Pellet-Rostainga, S. *Chem. Comm.* **2019**, *55*, 7583–7586.
- [29] den Auwer, C.; Drot, R.; Simoni, E.; Conradson, S. D.; Gailhanou, M.; Mustre de Leon, J. *New J. Chem.* **2003**, *27*, 648–655.
- [30] Hennig, C.; Schmeide, K.; Brendler, V.; Moll, H.; Tsushima, S.; Scheinost, A. C. *Inorg. Chem.* **2007**, *46*, 5882–5892.
- [31] Reich, T.; Bernhard, G.; Geipel, G.; Funke, H.; Hennig, C.; Roßberg, A.; Matz, W.; Schell, N.; Nitsche, H. *Radiochim. Acta* **2000**, *88*, 633–637.
- [32] Ikeda-Ohno, A.; Hennig, C.; Rossberg, A.; Funke, H.; Scheinost, A. C.; Bernhard, G.; Yaita, T. *Inorg. Chem.* **2008**, *47*, 8294–8305.
- [33] Reich, T.; Geipel, G.; Funke, H.; Hennig, C.; Roßberg, A.; Bernhard, G. *ESRF Highlights (Biannual Report 1999/2000)* **2001**, 27–32.
- [34] Rai, N.; Tiwari, S. P.; Maginn, E. J. *J. Phys. Chem. B* **2012**, *116*, 10885–10897.
- [35] Pomogaev, V.; Tiwari, S. P.; Rai, N.; Goff, G. S.; Runde, W.; Schneider, W. F.; Maginn, E. J. *Phys. Chem. Chem. Phys.* **2013**, *15*, 15954–15963.
- [36] Angeli, C.; Cimiraglia, R.; Evangelisti, S.; Leininger, T.; Malrieu, J.-P. *J. Chem. Phys.* **2001**, *114*, 10252–10264.
- [37] Angeli, C.; Cimiraglia, R.; Malrieu, J.-P. *Chem. Phys. Lett.* **2001**, *350*, 297–305.
- [38] Angeli, C.; Cimiraglia, R.; Malrieu, J.-P. *J. Chem. Phys.* **2002**, *117*, 9138–9153.
- [39] Becke, A. D. *J. Chem. Phys.* **1993**, *98*, 5648–5652.

- [40] Stephens, P. J.; Devlin, F. J.; Chabalowski, C. F.; Frisch, M. J. *J. Phys. Chem.* **1994**, *98*, 11623–11627.
- [41] Woon, D. E.; Dunning Jr., T. H. *J. Chem. Phys.* **1993**, *98*, 1358–1371.
- [42] Küchle, W.; Dolg, M.; Stoll, H.; Preuss, J. *J. Chem. Phys.* **1994**, *100*, 7535–7542.
- [43] Frisch, M. J. et al. Gaussian09 Revision D.01. 2009.
- [44] Siboulet, B.; Marsden, C. J.; Vitorge, P. *Chem. Phys.* **2006**, *326*, 289–296.
- [45] Vallet, V.; Macak, P.; Wahlgren, U.; Grenthe, I. *Theor. Chem. Acc.* **2006**, *115*, 145–160.
- [46] Balasubramanian, K.; Cao, Z. *Inorg. Chem.* **2007**, *46*, 10510–10519.
-
- [47] Clavaguéra-Sarrio, C.; Vallet, V.; Maynau, D.; Marsden, C. J. *J. Chem. Phys.* **2004**, *121*, 5312–5321.
- [48] Majumdar, D.; Balasubramanian, K.; Nitsche, H. *Chem. Phys. Lett.* **2002**, *361*, 143–151.
- [49] Neese, F. *Wiley Interdiscip. Rev. Comput. Mol. Sci.* **2012**, *2*, 73–78.
- [50] Zheng, J.; Xu, X.; Truhlar, D. *Theor. Chem. Acc.* **2011**, *128*, 295–305.
- [51] Weigend, F.; Ahlrichs, R. *Phys. Chem. Chem. Phys.* **2005**, *7*, 3297–3305.
- [52] Cao, X.; Dolg, M.; Stoll, H. *J. Chem. Phys.* **2003**, *118*, 487–496.
- [53] Todorov, I. T.; Smith, W.; Trachenko, K.; Dove, M. T. *J. Mat. Chem.* **2006**, *16*, 1911–1918.
- [54] Muñoz-Páez, A.; Sánchez Marcos, E. In *Compr. Inorg. Chem. {II} From Elem. to Appl.*, 2nd ed.; Reedijk, J., Poeppelmeier, K., Eds.; Elsevier: Leiden, 2013; Vol. 9; pp 133–159.

- [55] Rehr, J. J.; Kas, J. J.; Vila, F. D.; Prange, M. P.; Jorissen, K. *Phys. Chem. Chem. Phys.* **2010**, *12*, 5503–5513.
- [56] Hudson, E.; Rehr, J.; Bucher, J. J. *Phys. Rev. B* **1995**, *52*, 13815–13826.
- [57] Panak, P. J.; Booth, C. H.; Caulder, D. L.; Bucher, J. J.; Shuh, D. K.; Nitsche, H. *Radiochim. Acta* **2002**, *90*, 315–321.

SUPPLEMENTARY INFORMATION

**Combining EXAFS and Computer Simulations to
Refine the Structural Description of Actinyl in
Water**

Sergio Pérez-Conesa, José M. Martínez, Rafael R. Pappalardo and Enrique
Sánchez Marcos

*Departamento de Química Física, Universidad de Sevilla,
41012 Sevilla, Spain. e-mail:sanchez@us.es*



Table S1: First-shell water geometry in Å and degrees. For Np(V) the first shell water molecules have the geometry (including the massless particle) of TIP4P.

	First-shell geometry				
	U	Np(VI)	Np(V)	Np(V) (NEV)	Pu(VI)
$R(O_I - H_I)$	0.97	0.97	0.9572	0.9572	0.97
$\widehat{H_I O_I H_I}$	106.6	106.6	104.52	104.52	106.6

Table S2: Effective Merz-Kollmann charges of $[AnO_2 \cdot (H_2O)_5]^{+/2+}$ (aq) using the PCM to model the bulk solvent using as radii 2.65 Å, 1.40 Å and 1.20 Å for An, O and H respectively. For $[NpO_2 \cdot (H_2O)_5]^+$ the first shell water molecules have the same structure and partial charges as the TIP4P model. The electron density used is that of B3LYP (unless otherwise stated)

	Partial Charge (a.u.)				
	U	Np(VI)	Np(V)	Np(V) (NEV)	Pu(VI)
q_{An}	2.80	2.71		2.52	2.62
$q_{O_{vi}}$	-0.55	-0.50		-0.76	-0.47
q_O	-1.05	-1.04	0.0	0.0	-1.04
q_H	0.55	0.55	0.52	0.52	0.55
q_q	-	-	-	-1.04	-

Table S3: Coefficients of the DFT-level (unless otherwise stated) IW1 interaction potentials and root mean square error (RMSE) of the fit. Their units are kcal mol⁻¹ Å⁻ⁿ, kcal mol⁻¹ and Å respectively.

Coefficients	U	Np(VI)	Np(V)	Np(V) (NEV)	Pu(VI)
$C_4^{AnO_I}$	-6388.86	781.099	0.0	0.0	-6343.16
$C_6^{AnO_I}$	52787.05	-14881.6	-21667.67	-12254	63274.85
$C_8^{AnO_I}$	-131984.94	75576.2	139543.16	72991	-188099.67
$C_{12}^{AnO_I}$	476950.29	-247512	-761189.70	-247770	714067.88
δ_{AnO_I}	0.007	-0.057	-0.072	-	-0.040
$C_4^{O_{vi}O_I}$	1696.66	-2989.75	0.0	-702.86	4225.93
$C_6^{O_{vi}O_I}$	-8196.99	39404.6	17317.38	17282	-70487.33
$C_8^{O_{vi}O_I}$	18165.85	-140671	-101999.72	-75128	365255.74
$C_{12}^{O_{vi}O_I}$	-30202.92	637345	756412.76	756410	-2718499.04
RMSE	0.6	1.4	0.6	0.2	1.6

Table S4: Coefficients from the fitting of the DFT-level IMC interaction potentials, RMSE_{total}, RMSE_{partial} which is computed for points with energy lower than 15 kcal mol⁻¹ with respect to the interaction energy of the minimum. Their units are kcal mol⁻¹ Å⁻ⁿ, kcal mol⁻¹ and Å respectively.

Coefficients	U	Np(VI)	Np(V)	Np(V) (NEV)	Pu(VI)
$C_4^{\text{AnO}_{\text{y}1}}$	-133370.94	-136859.23	-74453.49	-16380	842.00
$C_6^{\text{AnO}_{\text{y}1}}$	668178.78	676835.56	403271.32	81524	-28267.67
$C_8^{\text{AnO}_{\text{y}1}}$	-1059978.49	-1067029.16	-695592.42	-125340	74562.59
$C_{12}^{\text{AnO}_{\text{y}1}}$	949717.97	953580.31	754700.69	122600	94491.15
$C_4^{\text{O}_{\text{y}1}\text{O}_{\text{y}1}}$	-167679.49	-210487.33	-1270195.07	-0.33976E+07	-4881731.10
$C_6^{\text{O}_{\text{y}1}\text{O}_{\text{y}1}}$	4369622.37	6034823.14	29013046.5	0.80706E+08	102789274.00
$C_8^{\text{O}_{\text{y}1}\text{O}_{\text{y}1}}$	-33177820.27	-45743307.84	-207350887	-0.60584E+09	-680306326.00
$C_{12}^{\text{O}_{\text{y}1}\text{O}_{\text{y}1}}$	605633365.20	779053537.28	3673600800	0.11936E+11	10352292900
RMSE _{total}	3.4	3.6	3.3	0.3	1.3
RMSE _{partial}	0.4	1.0	1.4	0.001	0.9

Table S5: Coefficients of the HIW interaction potential from previous work. They are used for all actinyls. RMSE_{total} and RMSE_{partial} which is computed for points with energy lower than 15 kcal mol⁻¹ with respect to the interaction energy of the minimum. The units are kcal mol⁻¹ Å⁻ⁿ and kcal mol⁻¹.

Coefficients	An(VI,V)	Coefficients	An(VI,V)
C_4^{UOw}	18578.27	$C_4^{\text{O}_1\text{Ow}}$	-830.40
C_6^{UOw}	-288922.08	$C_6^{\text{O}_1\text{Ow}}$	6718.50
C_8^{UOw}	1481816.44	$C_8^{\text{O}_1\text{Ow}}$	-4208.51
C_{12}^{UOw}	-12631787.76	$C_{12}^{\text{O}_1\text{Ow}}$	-3888.10
C_4^{UHW}	-5094.89	$C_4^{\text{O}_1\text{Hw}}$	28.22
C_6^{UHW}	65098.47	$C_6^{\text{O}_1\text{Hw}}$	100.59
C_8^{UHW}	-268274.37	$C_8^{\text{O}_1\text{Hw}}$	-40.17
C_{12}^{UHW}	1482339.87	$C_{12}^{\text{O}_1\text{Hw}}$	1.06
$C_4^{\text{O}_{\text{y}1}\text{Ow}}$	-1503.86	$C_4^{\text{H}_1\text{Ow}}$	-64.73
$C_6^{\text{O}_{\text{y}1}\text{Ow}}$	10373.23	$C_6^{\text{H}_1\text{Ow}}$	166.44
$C_8^{\text{O}_{\text{y}1}\text{Ow}}$	-15794.55	$C_8^{\text{H}_1\text{Ow}}$	-57.00
$C_{12}^{\text{O}_{\text{y}1}\text{Ow}}$	12403.99	$C_{12}^{\text{H}_1\text{Ow}}$	1.25
$C_4^{\text{O}_{\text{y}1}\text{Hw}}$	187.28	$C_4^{\text{H}_1\text{Hw}}$	4.63
$C_6^{\text{O}_{\text{y}1}\text{Hw}}$	-314.50	$C_6^{\text{H}_1\text{Hw}}$	-0.29
$C_8^{\text{O}_{\text{y}1}\text{Hw}}$	213.54	$C_8^{\text{H}_1\text{Hw}}$	0.07
$C_{12}^{\text{O}_{\text{y}1}\text{Hw}}$	-22.69	$C_{12}^{\text{H}_1\text{Hw}}$	0.00
RMSE _{total}	1.9		
RMSE _{partial}	1.2		

Feff input files for EXAFS.

```
##### POTENTIALS FILE #####
TITLE_Np B3LYP Oyl+1st shell
```

```
EDGE L3
S02 1.0 # S02 fixed a posteriori
```

```
CONTROL 1 0 0 0 0 0
```

```
PRINT 0 0 0 3 0 0
```

```
COREHOLE RPA
EXAFS 18.0
```

```
CRITERIA 4.0 2.5
RPATH 6.0
NLEG 4
```

```
TDLDA 1
SCF 6.0
EXCHANGE 0 -8.0 0.
POTENTIALS
```

0	93	Np	3	3
1	8	Oyl	3	3
2	8	O	3	3
3	1	H	2	2

ATOMS



```
##### PATHS FILE #####
TITLE_Np B3LYP Oyl+1st shell
```

```
EDGE L3
S02 1.0 # S02 fixed a posteriori
```

```
CONTROL 0 1 1 1 1 1
```

```
PRINT 0 0 0 3 0 0
```

```
COREHOLE RPA
EXAFS 18.0
```

```
CRITERIA 4.0 2.5
```

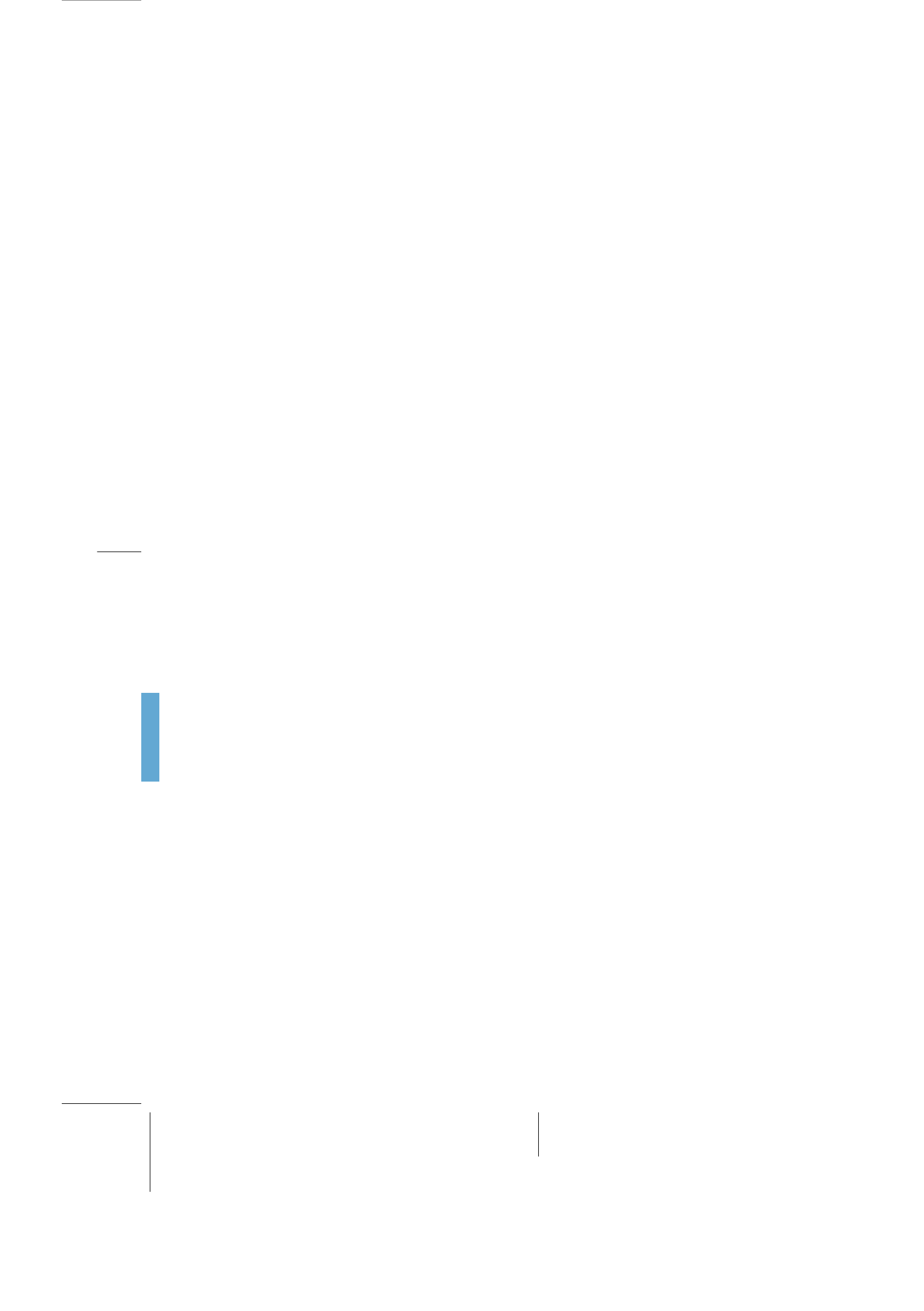


RPATH 6.0
NLEG 4

TDLDA 1
SCF 6.0
EXCHANGE 0 -8.0 0.
POTENTIALS

0	93	Np	3	3
1	8	Oyl	3	3
2	8	O	3	3

ATOMS



Hydration and Diffusion Mechanism of Uranyl in Montmorillonite Clay: Molecular Dynamics Using an Ab Initio Potential

8.1. *J. Phys. Chem. C* 2017, 121, 27437–27444

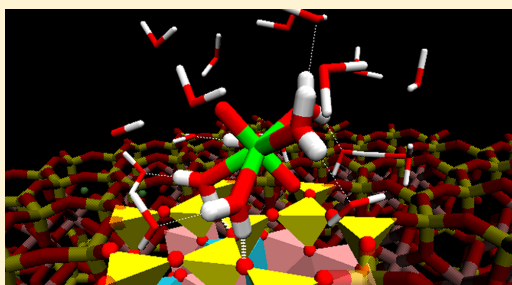
Hydration and Diffusion Mechanism of Uranyl in Montmorillonite Clay: Molecular Dynamics Using an Ab Initio Potential

Sergio Pérez-Conesa, José M. Martínez, and Enrique Sánchez Marcos*

Department of Physical Chemistry, University of Seville, 41012 Seville, Spain

Supporting Information

ABSTRACT: Permanent geological repositories lined with bentonite, a montmorillonite-containing clay, is one of the options considered for the storage of high-level radioactive waste. If the fuel rods were dissolved by a water leak, the clay would exchange its cations with the radioactive cations, slowing down their diffusion to the environment. We present an ab initio force field for the uranyl–montmorillonite interaction based on the hydrated ion model, i.e., recognizing the $[UO_2(H_2O)_5]^{2+}$ as the cationic species. This new interaction potential was used to run molecular dynamics simulations of the hydrated clay system. The uranyl aqua ion formed outer-sphere complexes with the clay layers, in agreement with EXAFS data. The hydrate is strongly bound, forming 1.4 hydrogen bonds between the first shell and clay oxygens. Uranyl–clay interaction sites were identified as groups of three Mg substitutions. Increasing the uranyl concentration enhances mobility due to partial surface coverage. Uranyl diffuses by means of a hopping mechanism. The constrictivity factor, δ_{int} , from the simulation self-diffusion coefficient of $[UO_2]^{2+}$ was calculated. A semiquantitative agreement with the experimental datum was obtained.



INTRODUCTION

Use of a geological high-level radioactive waste repository is one of the most considered options for the permanent storage of spent nuclear fuel. The repositories are lined with natural and artificial clay materials, particularly montmorillonite-containing clays like bentonite.^{1,2} Montmorillonite is an aluminosilicate consisting of octahedral sheets of AlO_6 sandwiched by sheets of SiO_4 tetrahedra forming a solid layer. The layers have isomorphic substitutions of Al by Mg or Si by Al, producing a net negative charge on the layers. The interlayers are filled with different amounts of aqueous solutions containing cations, such as Na^+ or Ca^{2+} , compensating the layer charge. Their use as liner material is based on their cation exchange capability. If water were to breach the nuclear fuel rods and dissolve the radionuclides, the clay would exchange its interlayer cations for the radioactive cations, slowing down their release to the environment.

Uranium is the main component of spent nuclear fuel. At low pH and ionic strength its most stable form in solution is the uranyl cation, $[UO_2]^{2+}$, in particular its pentacoordinated hydrated ion,³ $[UO_2(H_2O)_5]^{2+}(aq)$. EXAFS experiments infer that $[UO_2(H_2O)_5]^{2+}$ confined in the montmorillonite interlayer forms outer-sphere complexes.⁴ Apart from its intrinsic interest, the $[UO_2]^{2+}$ cation is representative of actinyls, $[AnO_2]^{2+}$, one of the forms adopted in nuclear fuel waste by highly radioactive minor actinides, such as Pu, Np, and Am.⁵

Classical molecular dynamics has proven to be a useful tool to interpret experimental information on these systems.^{1,6} It

also provides microscopic details of the phenomena since this type of information is usually hard to obtain directly or unambiguously. Several works have been published employing MD and Monte Carlo simulations of montmorillonite–uranyl systems. Most of them study $[UO_2]^{2+}$ at the outer surfaces of clay particles,^{7–13} although some of them study it in the interlayer.^{14,15} To our knowledge, none of the works compute the constrictivity factor (δ_{int}) from the self-diffusion coefficient, which is an important macroscopic experimental parameter to quantify the radioactive cation mobility inside the clay.

Current classical interaction potentials fitted to first-principles calculations benefit from a systematic improvement, a higher robustness to extrapolation, and the fact that high-level quantum mechanical calculations are becoming more affordable.¹⁶ All clay MD simulations in the literature use the original Wipff and Guillaud empirical force field for $[UO_2]^{2+}$ ¹⁷ or derived ones. Even though using this model has given many insights,^{7,10,11,14,15} ab initio interaction potentials for molecular cation–water and molecular cation–clay interactions could give a new and refined view of the system. Several years ago, we proposed the hydrated ion model (HIM)^{18–20} as a method to design interaction potentials of highly charged cations in water. The model is based on the classical electrochemical concept of the hydrated ion, in which the species that interacts with the

Received: August 24, 2017

Revised: October 20, 2017

Published: October 20, 2017

bulk water molecules is the cation and its first hydration shell and not the naked ion, $M^{n+}-H_2O$. This model alleviates several problems of traditional ab initio cation–water potentials: overestimation of the ion–first shell interaction, incorrect quantum mechanical dissociation limit, and neglect of charge transfer to the first shell.^{20,21} The approach has proven to be applicable to cations of different nature.^{19,22,23} Recently, we published an ab initio potential for $[UO_2]^{2+}$ in water based on the HIM, considering the $[UO_2(H_2O)_5]^{2+}$ as the central flexible species acting in solution.²⁴ In the present work we aim (1) to build the first ab initio $[UO_2(H_2O)_5]^{2+}$ –clay interaction potential based on the HIM and use it in MD simulations of $[UO_2]^{2+}$ in confined media; (2) to compute for the first time the constrictivity factor (δ_{int}) from MD self-diffusion coefficients; (3) to interpret, at the microscopic level, the aqua ion diffusion mechanism and its interaction with the clay, as well as the hydration structure and dynamics of the interlayer.

METHODS

System Definition. We defined our model system as a Na-montmorillonite clay, with unit formula $Na_{0.66}[Al_{3.33}Mg_{0.66}]_-[Si_8]O_{20}[OH]_4n(H_2O)$. The montmorillonite was derived from an X-ray triclinic pyrophyllite structure.²⁵ The simulation box contains two clay layers and two interlayers. The layers of this mineral consist of a plane of Al or Mg octahedra sandwiched by Si tetrahedra planes, known as the TOT structure. Each layer consists of a 9×5 supercell with random octahedral substitutions of Al^{3+} by Mg^{2+} , excluding the possibility of substituting two vertex-sharing octahedra following the procedure of Holmboe.²⁶ Relative displacements of the clay layers is prevented by fixing one Al atom of each clay layer.

Three monolayers of water fill the interlayer. This hydration state, known as 3W, corresponds to 15 H_2O molecules per unit cell and an interlayer spacing of $\approx 18.8 \text{ \AA}$.²⁶ The 3W hydration state is among the most common in high level waste repositories.²⁷ The final system box size is $\approx 47 \times 45 \times 37.6 \text{ \AA}^3$. The system is oriented with the z axis normal to the surface, such that interlayers are parallel to the xy plane. Na^+ ions balance the negative charge of the layers. Eight Na^+ atoms and 20 H_2O were substituted in each interlayer by 4 $[UO_2(H_2O)_5]^{2+}$, then the simulation box contained 8 uranyl aqua ions, as displayed in Figure 1. To account for the effect of concentration, another simulation box was built with a single aqua ion per interlayer. Unless otherwise stated, all analysis will refer to the eight uranyl system.

Interaction Potentials. The CLAYFF flexible force field²⁸ was used to describe the clay. This force field assigns to each atom type a partial charge and Lennard-Jones parameters. Even though CLAYFF was developed for SPC water, for compatibility with the hydrated ion model of $[UO_2]^{2+}$, the TIP4P water model was used.³⁹ The dynamics and structural properties of CLAYFF–TIP4P simulations are very similar to those of SPC model simulations. The Na^+ model of Jorgensen et al. was chosen, since it was built using TIP4P water.³⁰ Lorentz–Bertzeltot combination rules were used to model the van der Waals interaction of atoms with different atom types, except those belonging to $[UO_2(H_2O)_5]^{2+}$. Uranyl pentahydrate interactions with bulk H_2O are described by the HIM interaction potential recently developed by our group.²⁴ The intramolecular interactions of the uranyl pentahydrate $[UO_2(H_2O)_5]^{2+}$ are described by the ion–water first-shell potential

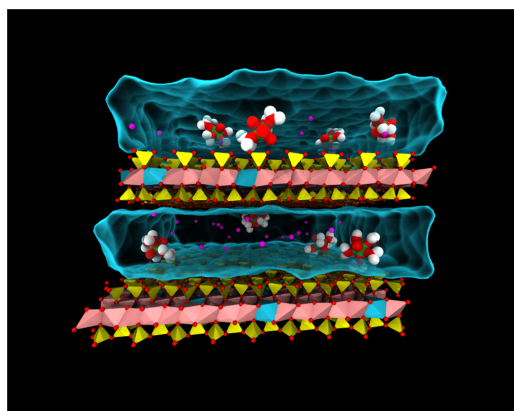


Figure 1. Simulation box. The color scheme is H (white), O (red), Na (purple), Mg octahedra (blue), Al octahedra (pink), Si tetrahedra (yellow), and U (green), and bulk water molecules are represented as the blue surface. Clay H atoms are omitted.

(IW1), a site–site potential including several r^{-n} terms, allowing first-shell water molecules to exchange with bulk, unlike in an harmonic bonding potential case. The finite energy barrier preventing water-release naturally appears when fitting the quantum-mechanical surface. Since first-shell H_2O molecules have a different definition than bulk water, our model would not work properly if an exchange occurred during simulation. Therefore, this model is valid if the water exchange time in the studied system is longer than the simulation time, which is the case for $[UO_2]^{2+}$ in water.³¹

$[UO_2(H_2O)_5]^{2+}$ –Montmorillonite Interaction Potential, the Hydrated Ion–Clay Interaction. All QM calculations were carried out using ORCA³² at the MP2 level of theory. For U, Si, and Al atoms, Stuttgart semirelativistic pseudopotentials were used to remove respectively 60, 10, and 10 electrons from the core and their recommended basis sets.^{33,34} The rest of atoms used Dunning's cc-aug-PVDZ basis set.^{35–39} The RI^{40–44} and RIJCOSX⁴⁵ scaling reduction techniques were employed to accelerate the calculations.

All system interactions can be obtained from the literature except for the interaction of the hydrated ion with the clay, denoted as the hydrated ion–clay interaction, HIC. The development of this force field is crucial to reach the goals of this study.

To model the surface we carved small molecular clusters from the two surface interaction centers. QM calculations of clay clusters interacting with uranyl have been reported in the literature.^{46,47} To deal with a reasonable cluster size (~ 100 atoms), they contained part of the octahedral AlO_6 sheets and part of one of the tetrahedral SiO_4 sheets. The cluster was carved of the crystal structure, and the relative atomic positions were unchanged. Some oxygen atoms were saturated with hydrogen atoms. Our model stands on the reasonable assumption that the nonelectrostatic component of the interaction is fairly local and can be approximated by a surface cluster, since the known models provide the long-range electrostatics. To obtain a set of QM structures to be fitted, unrelaxed scans were performed with the aqua ion in its gas-phase minimum geometry. Examples of these scans are depicted in Figure 2.

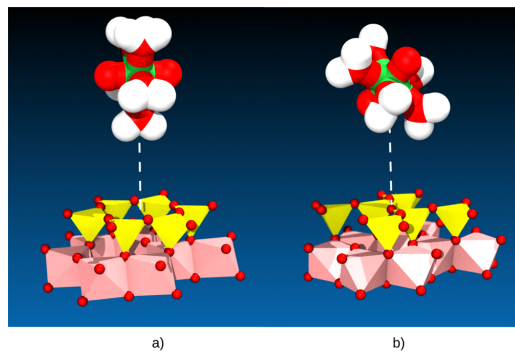


Figure 2. Two of the cluster–aqua ion scans used to parametrize the HIC interaction. (a) Hexagonal center scan with 90° tilt angle, defined by the actinyl axis and the surface normal. (b) O-Center scan with tilt angle 45°. Al octahedra (pink), Si tetrahedra (yellow), O atoms (red), uranium atoms (green), and H atoms (white) are displayed. Clay H atoms are omitted.

The hydrated ion–clay interaction energy is defined as

$$\begin{aligned} E_{\text{int}}^i &= E_{[\text{UO}_2(\text{H}_2\text{O})_5]^{2+}-\text{clay}}^i - E_{[\text{UO}_2(\text{H}_2\text{O})_5]^{2+}} - E_{\text{clay}} \\ &= E_{\text{Coul}}^i + E_{\text{non-Coul}}^i \end{aligned} \quad (1)$$

E_{int}^i splits into a purely electrostatic interaction term and a non-Coulomb term. We fitted only the non-Coulomb interactions between U, O_{yl} (oxo bond oxygen), and O_l (first-shell water molecule oxygen) atom types of the hydrated ion with the O and O_H (hydroxyl oxygen) atom types of the clay, to which we shall refer collectively as O_{clay}. It was necessary to include additionally an O_{yl}–Si term. To fit the interactions, r^{-n} polynomials were used. The full HIC functional form is presented below:

$$\begin{aligned} E_{\text{int}} &= E_{\text{Coul}}^i + E_{\text{non-Coul}}^i \\ &= \sum_{i \in \text{aqua ion}} \sum_{j \in \text{clay}} \frac{q_i q_j}{r_{ij}} + \sum_{i \in \text{U, O}_{\text{yl}}, \text{O}_l} \sum_{j \in \text{O}_{\text{clay}}} \frac{C_4^{ij}}{r_{ij}^4} + \frac{C_6^{ij}}{r_{ij}^6} + \frac{C_8^{ij}}{r_{ij}^8} \\ &\quad + \frac{C_{12}^{ij}}{r_{ij}^{12}} + \sum_{i \in \text{O}_{\text{yl}}} \sum_{j \in \text{Si}} \frac{C_4^{ij}}{r_{ij}^4} + \frac{C_6^{ij}}{r_{ij}^6} + \frac{C_8^{ij}}{r_{ij}^8} + \frac{C_{12}^{ij}}{r_{ij}^{12}} \end{aligned} \quad (2)$$

The HIC interaction potential developed is the first ab initio force field for clay–uranyl interactions. Details of the interaction potential development and the coefficients (Table S1) can be found in the Supporting Information (SI).

Molecular Dynamics Simulation. Molecular dynamics (MD) simulations were run using DL_POLY_CLASSIC.⁴⁸ An integration time step of 1 fs was used. The water molecules and hydroxyl groups were kept rigid using quaternion dynamics. The Ewald sum was used to calculate the electrostatic interactions. The van der Waals interactions were truncated at a cutoff radius of 14 Å. The Nosé–Hoover thermostat with a target temperature of 300 K was applied with a characteristic time of 0.5 ps. For NPT simulations, in addition to the thermostat, the Nosé–Hoover barostat with orthorhombic constraint with a characteristic time of 0.5 ps was applied to keep the average pressure at 1 atm. With orthorhombic constraints only the diagonal terms of the stress tensor are coupled to the barostat, preserving cell shape. A total number

of 9028 atoms were explicitly considered in the simulation box. The system was minimized, and an NPT run to relax the simulation box was performed. A 75 ns NVT production simulation was run for the two systems with different numbers of [UO₂]²⁺ aqua ions.

Uncertainties of all simulated properties are given as standard error.

Diffusion Modeling. The translational self-diffusion coefficient, $D_{\text{interlayer}}^{\text{MD}}$, for [UO₂]²⁺ in the MD simulation was computed using the Einstein formula.⁴⁹ Self-diffusion coefficients were not corrected for viscous self-coupling, since Holmboe et al.²⁶ proved its weakness in an analogous system.

Unfortunately, $D_{\text{interlayer}}^{\text{MD}}$ cannot be compared directly to the experimental diffusion parameters obtained in clay diffusion experiments. Experimentalists measure the effective diffusion coefficient, D^*

$$\vec{J} = -c D^* \vec{\nabla} C_U \quad (3)$$

where \vec{J} is the mass flux, c is the porosity of the material (volume of pores over total volume), and C_U is the mass concentration of uranium. Bourg and Sposito⁵⁰ proposed the following model of the apparent diffusion coefficient

$$\epsilon \frac{D^*}{D_0} = \frac{\alpha_{\text{macropore}} + \alpha_{\text{int}} \delta_{\text{int}}}{G_i} \quad (4)$$

where α is the molar fraction in the interlayer or the macropores; G_i is a “geometric” factor addressing tortuosity, pore irregularity, and connectivity;⁵¹ D_0 is the self-diffusion coefficient of uranyl in water; and δ_{int} is a “constrictivity” factor.⁵² δ_{int} is a measure of the change in diffusivity of a species in the interlayer with respect to solution. This parameter can be calculated from experiment or using self-diffusion coefficients obtained from MD with the expression⁵⁰

$$\delta_{\text{int}} = \frac{D_{\text{int}}^{\text{MD}}}{D_0^{\text{MD}}} \quad (5)$$

Thus, δ_{int} assesses the validity of theoretical diffusion dynamics and the microscopic conclusions predicted. In addition, $\delta_{\text{int}}^{\text{H}_2\text{O}}$ and $\delta_{\text{int}}^{\text{M}^+}$ of a clay with a given dry bulk density, ρ_d , allows numerical modeling of self-diffusion coefficient ratios over the whole range of ρ_d .

RESULTS AND DISCUSSION

Structure of the Interlayer. The z -density profile, $\rho(z)$, of the simulation (Figure 3) shows that outer-sphere complexes are formed between the uranyl pentahydrate and the solid surface, since first-shell water molecules (O_l) stand between the uranyl and the clay surface. In addition, the uranyl pentahydrate entity is preserved throughout the simulation, i.e., the simulation agrees with EXAFS results,⁴ and with previous theoretical MD simulation studies.^{14,15} In the HIM description of [UO₂(H₂O)₅]²⁺, the first-shell molecules could leave the first-shell, since these water molecules are treated as independent particles in the simulation, but they remain coordinated due to the potential energy barrier. This satisfies the requirement of our HIM model about no exchange of first-shell water molecules. Likewise, it shows the good behavior of the potential coupling.

The hydrated ions stay on the clay surface, forming outer-sphere complexes for most of the simulation. Only one of the uranyls travels to the other surface, although others make

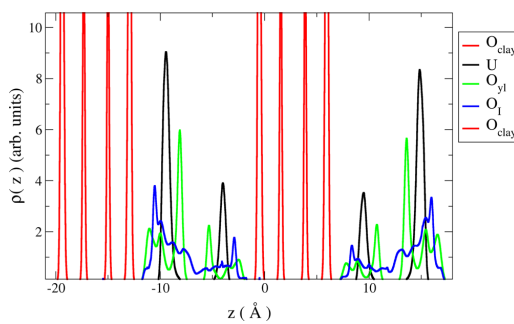


Figure 3. z -Density profile for $[\text{UO}_2]^{2+}$ –clay in the 8HI simulation. The red lines correspond to the O_{clay} atom and delimit the solid surface position.

occasional back and forth displacements. Transition times take a few picoseconds. The clay layer with $-0.5 \text{ \AA} < z < 5.8 \text{ \AA}$ has one uranyl bound on each of its two surfaces, whereas the other layer has six. Since both layers contain the same number of substitutions, the different arrangement of the Mg substitutions in the two layers is the cause of the uranyl z -density asymmetry.

The O_{yl} z -density shows peaks on both sides of the uranium curve because the $\text{O}_{\text{yl}}\text{—U—O}_{\text{yl}}$ axis is not parallel to the surface. The O_{yl} z -density has a split peak close to the surface. Thus, two preferential tilt angles with the surface exist. The tilt angle distribution calculated is found to be bimodal with $\sim 35^\circ$ and $\sim 60^\circ$ maxima. The first value happens when one O_{yl} approaches an O-hexagon of the clay surface, sinking in slightly; otherwise, the second angle occurs. Greathouse et al.¹⁵ found tilt angles of 45° in their Monte Carlo study. We think their result is about the average of our two values if they also obtained a bimodal distribution. Since polarized-EXAFS experiments reveal a preferred tilt angle in between 0° and 90° ,⁵³ our result is within the experimental range.

During the simulation one or two uranyl first-shell water molecules form hydrogen bonds with clay surface oxygen atoms belonging to a Si tetrahedron. The average number of these HI–clay hydrogen bonds is 1.4 per uranyl and most likely have an $\text{O}_{\text{clay}}\text{—O}_1$ distance of 2.37 \AA . Parts a and b of Figure 4 show

examples of singly and doubly H-bonded surface complexes and examples of the two predominant tilt angles, $\sim 35^\circ$ and $\sim 60^\circ$, respectively.

Figure 5 shows the U atoms probability density in the xy plane when they are attached to one of the clay layers on either

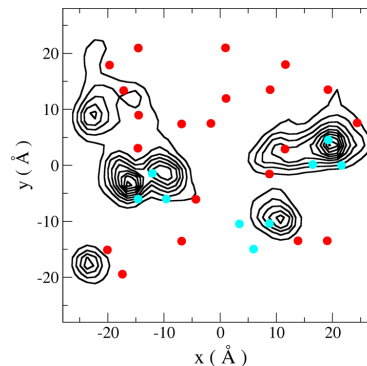


Figure 5. Probability density map of the xy coordinates of the U atoms when they are bound to one of the clay layers on either side. Mg atoms are represented as circles: blue if they belong to an interaction site and red otherwise.

side. The map of the other layer can be found in the SI (Figure S2). Most of the density lies close to groups of substitutions forming triangles. We have identified this feature as an *interaction site* of the surface, where the uranyl cations interact strongly and are retained, preventing their free diffusion. Figure 4c depicts one of these sites. An interaction site is composed of three Mg octahedra separated by only one Al octahedron. This can happen if three substituted octahedra share a central Al octahedron or if they are located at every other vertex of a hexagonal arrangement of octahedra. Both possibilities have equivalent effects on the dynamics. By chance, the random substitution of Mg by Al when constructing our system made three interaction sites in each clay layer. Figure 6 is another piece of evidence of the strength of these interaction sites. The radial distribution function (RDF) U–Mg (site), i.e., for Mg

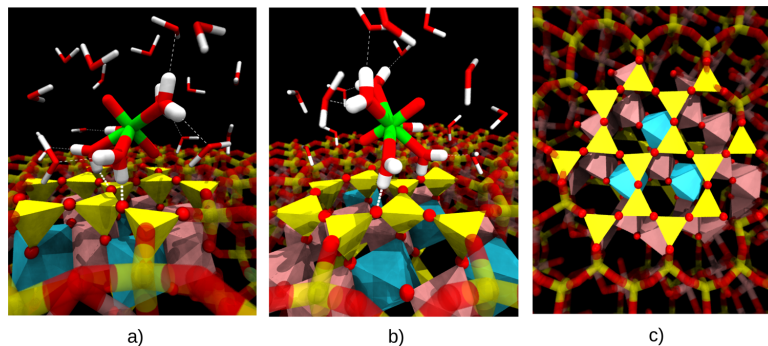


Figure 4. (a) Outer-sphere HI–clay complex with a tilt angle of $\sim 35^\circ$ forming two H-bonds with the surface. (b) Outer-sphere HI–clay complex with a tilt angle of $\sim 60^\circ$ forming one H-bond with the surface. (c) Picture of an interaction site of the clay surface. An interaction site has three Mg octahedra separated by only one Al octahedron. Al octahedra (pink), Mg octahedra (blue), Si tetrahedra (yellow), O atoms (red), uranium atoms (green), and H atoms (white) are displayed. Most of the clay surface is faded and clay H atoms are omitted for clarity.

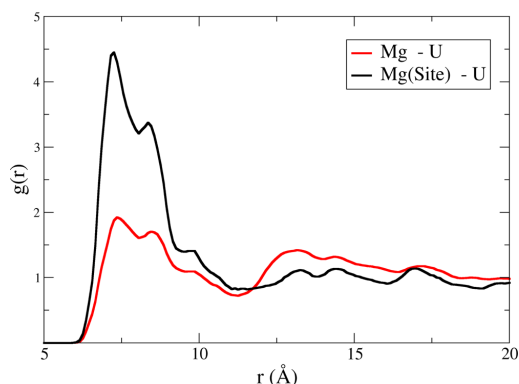


Figure 6. Mg–U (red) and Mg_{interaction site}–U (black) RDFs.

atoms belonging to an interaction site, is about twice as intense as the total U–Mg RDF.

Figure 5 has smaller probability density in regions between sites. We infer from this fact a hopping (or jumping) mechanism for uranyl mobility in the clay interlayer. This mechanism involves cation oscillation around an interaction site until it detaches and rapidly moves to another site, restarting the cycle. More evidence of this mechanism is the fact that the uranyls lie on average close to a site about 70% of the time. Zaidan et al. also suggested a jump–diffusion mechanism for uranyls from their MD trajectory.¹⁴

The electrostatic potential map of one of the four surfaces is shown in Figure 7. The non-Coulomb contribution is not

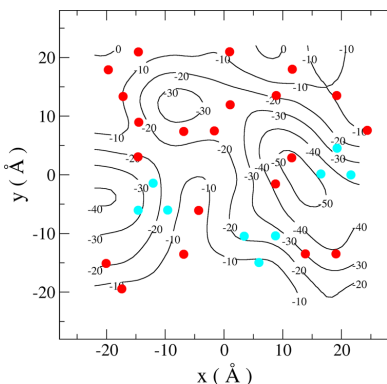


Figure 7. Contour lines of the electrostatic potential ($\text{kcal mol}^{-1} \text{e}^{-1}$) in the xy plane with z equal to -10 \AA . The U z -density profile has a maximum at this z value. The maximum corresponds to uranyl being bound to the surface. Mg atoms are represented as circles: blue if they belong to an interaction site and red otherwise.

provided, since it is fairly flat. This map is calculated on a plane at the same height as the uranyl maximum of the z -density profile. The maps of the other surfaces can be found in the SI (Figure S3). The electrostatic minima differ from the interaction site positions; therefore, to understand the observed behavior, other contributions must be invoked, such as the solvent competition to hydrate either the surface or the cations,

cation competition for the interaction sites, and the maximization of interaction distances.

Hydration Structure. The hydrated uranyl ion excludes cations within a radius of $\sim 7.5 \text{ \AA}$, roughly up to its second hydration shell. This forces Na^+ ions to squeeze together with an average $\text{Na}^+–\text{Na}^+$ distance of $\sim 4.4 \text{ \AA}$, roughly up to its second hydration shell maximum. The sum of these volumes is $\sim 60\%$ of the total interlayer volume if we consider the uranyl exclusion volume to be semispherical due to its attachment to the surface. The RDF of the cations contained in the interlayer with other cations is included in the SI (Figure S4).

The hydration structure of $[\text{UO}_2(\text{H}_2\text{O})_5]^{2+}$ in the montmorillonite resembles its hydration in solution (Figure 8). The average of $\text{U}–\text{O}_{\text{yl}}$ and $\text{U}–\text{O}_{\text{i}}$ distances are 1.75 and 2.45 \AA , respectively, just like solution.²⁴ Therefore, the first shell remains unchanged going from solution to the mineral system, as experimentally observed.⁴ The second shell peak of the RDF in solution and in the clay differ in the intensities and coordination numbers, but not in the position. The presence of the clay creates a region around the aqua ion in which water molecules are excluded but whose volume is accounted for in the RDF normalization. This reduces the intensity of the RDF.

Since $[\text{UO}_2(\text{H}_2\text{O})_5]^{2+}$ is an anisotropic ion, we will make use of the multisite cavity solute definition to compute the coordination number.⁵⁴ The strategy locates spheres on solute-exposed atoms with radii equal to the first minimum of the RDF of the atom and O_w . The coordination number is the average number of water molecules inside the volume generated by the set of interlocking spheres. The multisite solute coordination number for the pentahydrate is 16.6 ± 0.1 , with a standard deviation between the different uranyls of 0.14. The coordination is significantly lower than its solution value of 22. As described earlier, one or two clay surface oxygen atoms replace two equatorial water molecules, acting as second-shell H-bond acceptors. Since one of the O_{yl} atoms in the most likely orientations of the uranyl axis is close to the surface, water molecules are excluded from their solution solvation caps. These two facts result in a five water molecule loss.

The $\text{Na}–\text{O}_w$ RDFs in the clay and in solution are compared in the SI (Figure S5). Just like uranyl, the hydration structure of Na^+ in the mineral phase resembles its solution hydration, except for a two water molecule dehydration of the second shell. The number of water molecules belonging to first or second shells of the 56 interlayer cations corresponds to 82% of the total interlayer water molecules. Since the clay layers are also charged and demand hydration, the competition within the clay for the water molecules is high, this explaining the second-shell partial dehydration.

Uranyl Diffusion Modeling. Figure 9a shows the mean square displacement of each individual $[\text{UO}_2(\text{H}_2\text{O})_5]^{2+}$ and their average for the system containing eight uranyl cations. Figure 9b shows the same for the alternative system with only 2 uranyl cations. The 8HI MSDs support our hypothesis that uranyl diffusion in the interlayer occurs through a hopping mechanism. First of all, only two cations show an approximately linear profile corresponding to diffusion (the green and light blue lines). The rest span different degrees of oscillatory motion characterized by flat or oscillating MSDs. These hydrated ions are located at interaction sites oscillating around them and on rare occasions diffuse to other sites. This is why the cations have MSDs with flat oscillatory intervals combined with short linear intervals. The average MSD for the 8HI simulation has evident diffusive character mixed with oscillatory

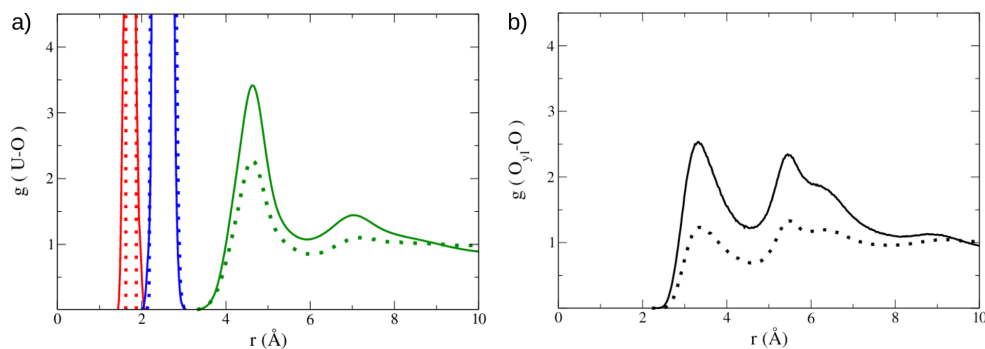


Figure 8. (a) U–O and (b) O–O_{yI} RDFs of $[\text{UO}_2(\text{H}_2\text{O})_5]^{2+}$ in the clay simulation (solid lines) and in aqueous solution²⁴ (dotted lines): U–O_{yI} (red), U–O_I (blue), U–O_W (green), and O_{yI}–O_W (black).

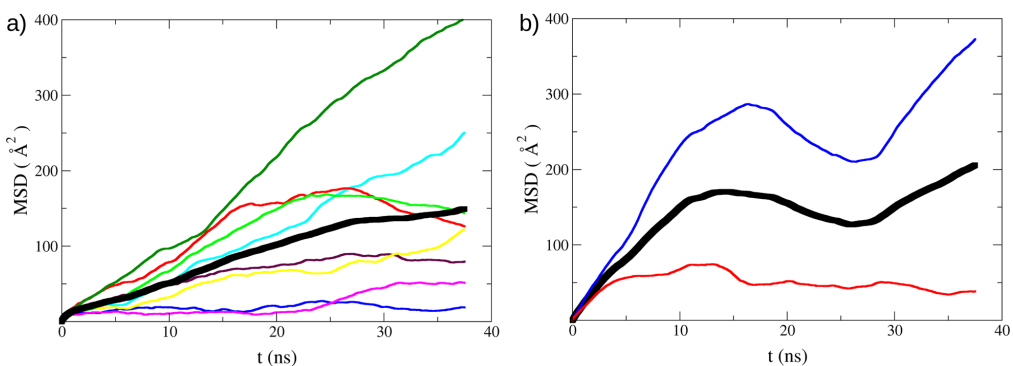


Figure 9. Mean square displacements of $[\text{UO}_2(\text{H}_2\text{O})_5]^{2+}$ in the clay systems with 8HI (a) and 2HI (b). Each colored line represents an individual HI. The average MSD in the interlayer is represented by the black thick line.

motion, hence the change of slope observed at ~ 27 ns. In any case, diffusion is strongly hindered overall if we consider the low values of the mean square displacements relative to the hydrated ion size (~ 7.5 Å diameter).

Figure 9b corresponds to a simulation containing a single HI per interlayer showing the lack of free diffusion, with oscillation being dominant. Parts a and b of Figure 9 are so different because in order for some of the cations to diffuse the interaction sites have to be at least partially occupied. This prevents free uranyl ions from attaching to them, facilitating uranyl diffusion. The surface coverage is an important factor in this system, since it is determined by uranyl concentration in the interlayer solution. The observed result at low uranyl concentration (2HI) indicates the complex diffusional description of the more concentrated sample (8HI), where the average mobility is the result of two different regimes.

The diffusion experiment of uranyl in montmorillonite that most resembles our simulation was done by Muurien⁵⁵ Bentonite MX-80 rock, the main component of which is Na-montmorillonite, is the absorbent material. The U-containing solutions used were artificial groundwaters at a low pH with a significant concentration of supporting electrolytes. This could lead to speciation or ionic strength effects not present in our simulation. However, this experimental work is chosen for comparison, since it is the only one at low pH preventing $[\text{UO}_2(\text{H}_2\text{O})_5]^{2+}$ hydrolysis and inner-sphere coordination.

The product ϵD^* depends on the clay dry bulk density, ρ_d . Thus, we have interpolated ϵD^* from the simulation of dry bulk density ($\rho_d = 1.4 \text{ g cm}^{-3}$), as done by Moore and Shackelford⁵ (details are given in the SI). Unfortunately, the level of partition of uranyl in the clay between the interlayers of montmorillonite microcrystals and the material macropores is unknown. Therefore, to use eq 4 we must assume that the interlayers contain most of the uranyl. In that case, the molar fractions of uranyl in the macropores and interlayers would be $\alpha_{\text{macropore}} \approx 0$ and $\alpha_{\text{interlayer}} \approx 1$. This is reasonable for compacted clays and has been done by Holmboe and Bourg.²⁶ We interpolated $\delta_{\text{int}}^{\text{exp}} \approx 0.61 \times 10^{-3}$ for $\rho_d = 1.4 \text{ g cm}^{-3}$.

In the simulation we obtain $D^{\text{MD}} = (0.009 \pm 0.004) \times 10^{-5} \text{ cm}^2 \text{ s}^{-1}$ for uranyl, splitting the simulation into two independent blocks and averaging over them. We obtain $\delta_{\text{int}} = 3.6 \times 10^{-3}$. Despite the complexity of the experimental system, our predicted constrictivity factor is 1 order of magnitude larger than the experimental value. This relative agreement seems to indicate that our model has captured part of the key features in this complex system. There are three main causes of discrepancy between our value and the experiment: the limitations of our clay model, the difference in interlayer composition, and the lack of statistics due to the long time scale of the jumps.

The great advantage of this theoretical estimation of diffusion parameters is the detailed microscopical knowledge obtained. MD predictions allow checking if the system model is consistent with experimental evidence and supplies knowledge unreachable from experiment. To the best of our knowledge, it is first time δ_{int} of uranyl in clays has been computed from MD simulations.

Apart from the attraction of uranyl to interaction sites, the crowding of Na^+ and $[\text{UO}_2(\text{H}_2\text{O})_5]^{2+}$ cations in the interlayer could be a factor reducing uranyl mobility. To study this, an analogous 8HI simulation was run, but without Na^+ , and the MSD profile seems to be unaffected by the presence of the Na. The mean square displacement can be found in the SI (Figure S6). Interestingly, $D_{\text{Na}}^{\text{MD}} = 0.4 \times 10^{-5} \text{ cm}^2 \text{ s}^{-1}$ in the 8HI simulation and $D_{\text{Na}}^{\text{MD}} = 0.7 \times 10^{-5} \text{ cm}^2 \text{ s}^{-1}$ if no uranyl is present. Therefore, uranyl strongly affects sodium diffusion, but not the contrary. This can be simply explained by the fact that, although their interaction is equal and opposite, the uranyl hydrated ion is an order of magnitude heavier and also that uranyl has a stronger interaction with the clay. Thus, $[\text{UO}_2(\text{H}_2\text{O})_5]^{2+}$ moves, pushing sodium out of its path, and Na^+ must divert the $[\text{UO}_2(\text{H}_2\text{O})_5]^{2+}$ signposts to move.

CONCLUSIONS

We have successfully developed the first ab initio interaction potential between montmorillonite clay and uranyl based on the hydrated ion model. The classical MD simulation of $[\text{UO}_2]^{2+}$ in clay shows that outer-sphere complexes appear in the simulation, as inferred from EXAFS data.⁴ The aqua ions adsorb strongly with the $[\text{UO}_2]^{2+}$ molecular axis at the preferred tilt angles of $\sim 35^\circ$ and $\sim 60^\circ$. The complex binds to the surface, forming on average 1.4 hydrogen bonds between first-shell water molecules and surface oxygen atoms. The second hydration shell of uranyl is dehydrated of five water molecules with respect to solution, due to the adsorption phenomena on the clay surface. The constrictivity factor of uranyl was computed from simulation. For this type of systems, to the best of our knowledge, it is the first time this has been done. The theoretical constrictivity factor overestimates by a factor of 6 the experimental value. This partial disagreement might be, in part, due to differences between the experimental conditions and those of the simulation. The clay has interaction sites formed by three close Mg octahedra. These sites are occupied by uranyl during most of the simulation time. Due to the interaction with the sites, $[\text{UO}_2(\text{H}_2\text{O})_5]^{2+}$ diffusion happens through a hopping mechanism. In order for some of the uranyl to have a proper diffusive motion, a partial surface site coverage must exist. Therefore, a concentration threshold must be reached in order for uranyl diffusion to occur. The interaction sites described in this work could become a new design parameter of montmorillonite-based liner materials for high-level radioactive waste facilities in order to maximize their retention capacity.

ASSOCIATED CONTENT

Supporting Information

The Supporting Information is available free of charge on the ACS Publications website at DOI: [10.1021/acs.jpcc.7b08479](https://doi.org/10.1021/acs.jpcc.7b08479).

Details of the interaction potential design, parameters, and fit quality; details of the interpolation of the constrictivity factor; the U-probability density of the other interlayer; additional electrostatic potential maps;

the cation–cation RDFs; comparison of the $\text{Na}-\text{O}_\text{W}$ RDFs for the clay and solution systems; and the MSD of uranyl in a sodium-less clay simulation ([PDF](#))

AUTHOR INFORMATION

Corresponding Author

*E-mail: sanchez@us.es. Phone: +34 955421005.

ORCID

Enrique Sánchez Marcos: [0000-0002-8367-9105](http://orcid.org/0000-0002-8367-9105)

Notes

The authors declare no competing financial interest.

ACKNOWLEDGMENTS

We thank Dr. Rafael R. Pappalardo for useful comments and computational support. This work was financially supported by Junta de Andalucía of Spain (Proyecto de Excelencia P11-FQM7607). S.P.-C. thanks the Spanish Ministry of Education, Culture and Sports for a Ph.D. grant (FPU14/02100).

REFERENCES

- (1) Miller, A. W.; Wang, Y. Radionuclide Interaction with Clays in Dilute and Heavily Compacted Systems: A Critical Review. *Environ. Sci. Technol.* **2012**, *46*, 1981–1994.
- (2) Moore, S. M.; Shackelford, C. D. Uranium Diffusion in Soils and Rocks. In *Tailings and Mine Waste 2011—Proceedings of the 15th International Conference on Tailings and Mine Waste*; Norman B. Keevil Institute of Mining Engineering, University of British Columbia, 2011; pp 549–561.
- (3) Gutowski, K. E.; Dixon, D. A. Predicting the Energy of the Water Exchange Reaction and Free Energy of Solvation for the Uranyl Ion in Aqueous Solution. *J. Phys. Chem. A* **2006**, *110*, 8840–8856.
- (4) Catalano, J. G.; Brown, G. E., Jr. Uranyl Adsorption onto Montmorillonite: Evaluation of Binding Sites and Carbonate Complexation. *Geochim. Cosmochim. Acta* **2005**, *69*, 2995–3005.
- (5) Morimoto, K.; Kato, M.; Uno, H.; Hamari, A.; Tamura, T.; Sugata, H.; Sunaoshi, T.; Kono, S. Preparation and Characterization of (Pu, U, Np, Am, Simulated FP) O_{2-x} . *J. Phys. Chem. Solids* **2005**, *66*, 634–638.
- (6) Greathouse, J. A.; Reifson, K.; Sposito, G. Molecular Dynamics Simulation of Water Mobility in Magnesium-smectite Hydrates. *J. Am. Chem. Soc.* **2000**, *122*, 11459–11464.
- (7) Zhang, N.; Liu, X.; Li, C.; Liu, C. Effect of Electrolyte Concentration on Uranium Species Adsorption: A Molecular Dynamics Study. *Inorg. Chem. Front.* **2015**, *2*, 67–74.
- (8) Greathouse, J. A.; Cygan, R. T. Molecular Dynamics Simulation of Uranyl (VI) Adsorption Equilibria onto an External Montmorillonite Surface. *Phys. Chem. Chem. Phys.* **2005**, *7*, 3580–3586.
- (9) Liu, X.-y.; Wang, L.-h.; Zheng, Z.; Kang, M.-l.; Li, C.; Liu, C.-l. Molecular Dynamics Simulation of the Diffusion of Uranium Species in Clay Pores. *J. Hazard. Mater.* **2013**, *244–245*, 21–28.
- (10) Marry, V.; Rotenberg, B.; Turq, P. Structure and Dynamics of Water at a Clay Surface from Molecular Dynamics Simulation. *Phys. Chem. Chem. Phys.* **2008**, *10*, 4802–4813.
- (11) Teich-McGoldrick, S. L.; Greathouse, J. A.; Cygan, R. T. Molecular Dynamics Simulations of Uranyl Adsorption and Structure on the Basal Surface of Muscovite. *Mol. Simul.* **2014**, *40*, 610–617.
- (12) Yang, W.; Zaoui, A. Behind Adhesion of Uranyl onto Montmorillonite Surface: A Molecular Dynamics Study. *J. Hazard. Mater.* **2013**, *261*, 224–234.
- (13) Greathouse, J. A.; Cygan, R. T. Water Structure and Aqueous Uranyl (VI) Adsorption Equilibria onto External Surfaces of Beidellite, Montmorillonite, and Pyrophyllite: Results from Molecular Simulations. *Environ. Sci. Technol.* **2006**, *40*, 3865–3871.
- (14) Zaidan, O. F.; Greathouse, J. A.; Pabalan, R. T. Monte Carlo and Molecular Dynamics Simulation of Uranyl Adsorption on Montmorillonite Clay. *Clays Clay Miner.* **2003**, *51*, 372–381.

- (15) Greathouse, J. A.; Stellalevinsohn, H. R.; Denecke, M. A.; Bauer, A.; Pabalan, R. T. Uranyl Surface Complexes in a Mixed-charge Montmorillonite: Monte Carlo Computer Simulation and Polarized XAFS Results. *Clays Clay Miner.* **2005**, *53*, 278–286.
- (16) Stone, A. *The Theory of Intermolecular Forces*, 2nd ed.; Oxford University Press: Oxford, 2013.
- (17) Guillaud, P.; Wipff, G. Hydration of Uranyl (UO_2^{2+}) Cation and Its Nitrate Ion and 18-crown-6 Adducts Studied by Molecular Dynamics Simulations. *J. Phys. Chem.* **1993**, *97*, 5685–5692.
- (18) Pappalardo, R. R.; Martinez, J. M.; Sánchez Marcos, E. Application of the Hydrated Ion Concept for Modeling Aqueous Solutions Containing Highly Charged Ions: A Monte Carlo Simulation of Cr^{3+} in Water Using an Ab Initio Intermolecular Potential. *J. Phys. Chem.* **1996**, *100*, 11748–11754.
- (19) Pappalardo, R. R.; Sánchez Marcos, E. Recovering the Concept of the Hydrated Ion for Modeling Ionic Solutions: A Monte Carlo Study of Zinc(2+) in Water. *J. Phys. Chem.* **1993**, *97*, 4500–4504.
- (20) Martinez, J. M.; Pappalardo, R. R.; Sánchez Marcos, E. First-principles Ion-water Interaction Potentials for Highly Charged Monatomic Cations. Computer Simulations of Al^{3+} , Mg^{2+} , and Be^{2+} in Water. *J. Am. Chem. Soc.* **1999**, *121*, 3175–3184.
- (21) Sánchez Marcos, E.; Pappalardo, R. R.; Barthelat, J. C.; Xavier Gadea, F. Theoretical Suggestion for the Aquazinc(2+) Formation. *J. Phys. Chem.* **1992**, *96*, 516–518.
- (22) Galbis, E.; Hernández-Cobos, J.; den Auwer, C.; Le Naour, C.; Guillaumont, D.; Simoni, E.; Pappalardo, R. R.; Sánchez Marcos, E. Solving the Hydration Structure of the Heaviest Actinide Aqua Ion Known: The Californium (III) Case. *Angew. Chem.* **2010**, *122*, 3899–3903.
- (23) Martínez, J. M.; Torrico, F.; Pappalardo, R. R.; Sánchez Marcos, E. Understanding the Hydration Structure of Square-Planar Aquaoions: The $[\text{Pd}(\text{H}_2\text{O})_4]^{2+}$ Case. *J. Phys. Chem. B* **2004**, *108*, 15851–15855.
- (24) Pérez-Conesa, S.; Torrico, F.; Martínez, J. M.; Pappalardo, R. R.; Sánchez Marcos, E. A Hydrated Ion Model of $[\text{UO}_2]^{2+}$ in Water: Structure, Dynamics, and Spectroscopy from Classical Molecular Dynamics. *J. Chem. Phys.* **2016**, *145*, 224502.
- (25) Bickmore, B. R.; Rosso, K. M.; Nagy, K. L.; Cygan, R. T.; Tadanier, C. J. Ab Initio Determination of Edge Surface Structures for Dioctahedral 2:1 Phyllosilicates: Implications for Acid-Base Reactivity. *Clays Clay Miner.* **2003**, *51*, 359–371.
- (26) Holmboe, M.; Bourg, I. C. Molecular Dynamics Simulations of Water and Sodium Diffusion in Smectite Interlayer Nanopores As a Function of Pore Size and Temperature. *J. Phys. Chem. C* **2014**, *118*, 1001–1013.
- (27) Holmboe, M.; Wold, S.; Jonsson, M. Porosity Investigation of Compacted Bentonite Using XRD Profile Modeling. *J. Contam. Hydrol.* **2012**, *128*, 19–32.
- (28) Cygan, R. T.; Liang, J.-J.; Kalinichev, A. G. Molecular Models of Hydroxide, Oxyhydroxide, and Clay Phases and the Development of a General Force Field. *J. Phys. Chem. B* **2004**, *108*, 1255–1266.
- (29) Jorgensen, W. L.; Chandrasekhar, J.; Madura, J. D.; Impey, R. W.; Klein, M. L. Comparison of Simple Potential Functions for Simulating Liquid Water. *J. Chem. Phys.* **1983**, *79*, 926–935.
- (30) Jensen, K. P.; Jorgensen, W. L. Halide, Ammonium, and Alkali Metal Ion Parameters for Modeling Aqueous Solutions. *J. Chem. Theory Comput.* **2006**, *2*, 1499–1509.
- (31) Helm, L.; Merbach, A. E. Inorganic and Bioinorganic Solvent Exchange Mechanisms. *Chem. Rev.* **2005**, *105*, 1923–1960.
- (32) Neese, F. The Orca Program System. *Wiley Interdiscip. Rev. Comput. Mol. Sci.* **2012**, *2*, 73–78.
- (33) Cao, X.; Dolg, M. Segmented Contraction Scheme for Small-core Actinide Pseudopotential Basis Sets. *J. Mol. Struct.: THEOCHEM* **2004**, *673*, 203–209.
- (34) Weigend, F.; Ahlrichs, R. Balanced Basis Sets of Split Valence, Triple Zeta Valence and Quadruple Zeta Valence Quality for H to Rn: Design and Assessment of Accuracy. *Phys. Chem. Chem. Phys.* **2005**, *7*, 3297–3305.
- (35) Dunning, T. H., Jr. Gaussian Basis Sets for Use in Correlated Molecular Calculations. I. The Atoms Boron through Neon and Hydrogen. *J. Chem. Phys.* **1989**, *90*, 1007–1023.
- (36) Woon, D. E.; Dunning, T. H., Jr. Gaussian Basis Sets for Use in Correlated Molecular Calculations. IV. Calculation of Static Electrical Response Properties. *J. Chem. Phys.* **1994**, *100*, 2975–2988.
- (37) Woon, D. E.; Dunning, T. H., Jr. Gaussian Basis Sets for Use in Correlated Molecular Calculations. III. The Atoms Aluminum through Argon. *J. Chem. Phys.* **1993**, *98*, 1358–1371.
- (38) Kendall, R. A.; Dunning, T. H., Jr.; Harrison, R. J. Electron Affinities of the First-row Atoms Revisited. Systematic Basis Sets and Wave Functions. *J. Chem. Phys.* **1992**, *96*, 6796–6806.
- (39) Wilson, A. K.; van Mourik, T.; Dunning, T. H., Jr. Gaussian Basis Sets for Use in Correlated Molecular Calculations. VI. Sextuple Zeta Correlation Consistent Basis Sets for Boron through Neon. *J. Mol. Struct.: THEOCHEM* **1996**, *388*, 339–349.
- (40) Dunlap, B. I.; Connolly, J. W. D.; Sabin, J. R. On Some Approximations in Applications of X_α Theory. *J. Chem. Phys.* **1979**, *71*, 3396–3402.
- (41) Van Alsenoy, C. Ab Initio Calculations on Large Molecules: The Multiplicative Integral Approximation. *J. Comput. Chem.* **1988**, *9*, 620–626.
- (42) Kendall, R. A.; Frücht, H. A. The Impact of the Resolution of the Identity Approximate Integral Method on Modern Ab Initio Algorithm Development. *Theor. Chem. Acc.* **1997**, *97*, 158–163.
- (43) Eichhorn, K.; Treutler, O.; Öhm, H.; Häser, M.; Ahlrichs, R. Auxiliary Basis Sets to Approximate Coulomb Potentials. *Chem. Phys. Lett.* **1995**, *240*, 283–290.
- (44) Eichhorn, K.; Weigend, F.; Treutler, O.; Ahlrichs, R. Auxiliary Basis Sets for Main Row Atoms and Transition Metals and Their Use to Approximate Coulomb Potentials. *Theor. Chem. Acc.* **1997**, *97*, 119–124.
- (45) Neese, F.; Wennmohs, F.; Hansen, A.; Becker, U. Efficient, Approximate and Parallel Hartree-Fock and Hybrid DFT Calculations. A “Chain-of-Spheres” Algorithm for the Hartree-Fock Exchange. *Chem. Phys.* **2009**, *356*, 98–109.
- (46) Tunega, D.; Haberhauer, G.; Gerzabek, M. H.; Lischka, H. Theoretical Study of Adsorption Sites on the (001) Surfaces of 1:1 Clay Minerals. *Langmuir* **2002**, *18*, 139–147.
- (47) Tunega, D.; Bencic, L.; Haberhauer, G.; Gerzabek, M. H.; Lischka, H. Ab Initio Molecular Dynamics Study of Adsorption Sites on the (001) Surfaces of 1:1 Dioctahedral Clay Minerals. *J. Phys. Chem. B* **2002**, *106*, 11515–11525.
- (48) Todorov, I. T.; Smith, W.; Trachenko, K.; Dove, M. T. DL_POLY_3: New Dimensions in Molecular Dynamics Simulations Via Massive Parallelism. *J. Mater. Chem.* **2006**, *16*, 1911–1918.
- (49) Frenkel, D.; Smit, B. *Understanding Molecular Simulation. From Algorithms to Applications*, 2nd ed.; Academic Press: San Diego, CA, 2002.
- (50) Bourg, I. C.; Sposito, G. Connecting the Molecular Scale to the Continuum Scale for Diffusion Processes in Smectite-rich Porous Media. *Environ. Sci. Technol.* **2010**, *44*, 2085–2091.
- (51) Dykhuizen, R. C.; Casey, W. H. An Analysis of Solute Diffusion in Rocks. *Geochim. Cosmochim. Acta* **1989**, *53*, 2797–2805.
- (52) Grathwohl, P. *Diffusion in Natural Porous Media: Contaminant Transport, Sorption/Desorption and Dissolution Kinetics*; Springer Science & Business Media: New York, 1997.
- (53) Denecke, M. A.; Bauer, A.; Kim, J. I.; Moll, H. Polarization Dependent XANES of Uranium (VI) Sorbed onto Smectite. *Miner. Interact. Close Equilib.* **1999**, *35*–37.
- (54) Melchior, A.; Martinez, J. M.; Pappalardo, R. R.; Sánchez Marcos, E. Hydration of Cisplatin Studied by an Effective Ab Initio Pair Potential Including Solute-Solvent Polarization. *J. Chem. Theory Comput.* **2013**, *9*, 4562–4573.
- (55) Muurinen, A. Diffusion of Uranium in Compacted Sodium Bentonite. *Eng. Geol.* **1990**, *28*, 359–367.
- (56) Bourg, I. C.; Sposito, G.; Bourg, A. Tracer Diffusion in Compacted, Water-Saturated Bentonite. *Clays Clay Miner.* **2006**, *54*, 363–374.

SUPPORTING INFORMATION

Hydration and Diffusion Mechanism of Uranyl in Montmorillonite Clay: Molecular Dynamics Using an *Ab Initio* Potential.

Sergio Pérez-Conesa, José M. Martínez and Enrique Sánchez Marcos

*Departamento de Química Física, Universidad de Sevilla,
41012 Sevilla, Spain. e-mail:sanchez@us.es*



[UO₂ · (H₂O)₅]²⁺-Montmorillonite interaction potential, the Hydrated Ion-Clay interaction detailed information

All system interactions can be obtained from literature except for the interaction of the hydrated ion with the clay; denoted as Hydrated Ion Clay interaction, HIC. The development of this force field is crucial to reach the goals of this study.

To introduce the HIM in a solid material the basic ideas of the model have to be preserved: the hydrated ion is the reference species and the interaction between the atoms of the hydrated ion and a surface are fitted simultaneously. The surface of the clay presents different possible interaction centers. We considered two of them: a “hexagonal center” and an “oxygen center”.

To model the surface we carved small molecular clusters from the two surface interaction centers. QM calculations of clay clusters interacting with uranyl have been reported in the literature (*Langmuir* 2002, 18, 139–147 and *J. Phys. Chem. B* 2002, 106, 11515–11525). Our model stands on the reasonable assumption the non-electrostatic component of the interaction is fairly local and can be approximated by a surface cluster, since the known models provide the electrostatics. We only used unsubstituted ones since their difference from substituted cluster is mainly electrostatic. To deal with a reasonable cluster size (~100 atoms), they contained part of the octahedral AlO₆ sheets and part of one of the tetrahedral SiO₄ sheets. The cluster was carved of the crystal structure and the relative atomic positions were unchanged. Some oxygen atoms were saturated with H atoms.

To obtain a set of QM structures to be fitted, unrelaxed scans were performed with the aquaion in its gas phase minimum geometry. Examples of these scans are depicted in Figure 2 of the main text. For the hexagonal center cluster, the aquaion approaches vertically on the center of the hexagonal cluster with three different actinyl axis tilts: perpendicular, parallel and 45°. An additional scan was performed on the same cluster with the HI forming a hydrogen bond with a clay oxygen. For the interaction of the O-center cluster with the pentahydrate two scans were performed, both with 45° tilt angles. In one of them the ion approaches to the central clay oxygen and in the other on a lateral clay oxygen.

The hydrated ion-clay interaction energy is defined as:

$$E_{\text{int}}^i = E_{[\text{UO}_2 \cdot (\text{H}_2\text{O})_5]^{2+} - \text{clay}}^i - E_{[\text{UO}_2 \cdot (\text{H}_2\text{O})_5]^{2+}} - E_{\text{clay}} \quad (1)$$

E_{int}^i splits into a purely electrostatic interaction term and a non-coulomb term. The charges of the atom types used were those of their respective force fields except for the ones of the saturation hydrogens which were adjusted to neutralize the cluster.

The non-coulomb term contains mostly van der Waals interactions but also implicitly aquaion-clay polarization and other many-body effects. This interaction is fitted to the difference between the QM interaction energy and the classical electrostatic term. We fitted only the non-coulomb interactions between U, O_{yl} and O_I (first-shell water molecule oxygen) atom types of the hydrated ion with the O and O_H (hydroxyl oxygen) atom types of the clay, to which we shall refer collectively as O_{clay}. It was necessary to include additionally a O_{yl}-Si term. To fit the interactions r^{-n} polynomials were used. The full HIC functional form is presented below:

$$\begin{aligned}
E_{\text{int}} &= E_{\text{Coul.}}^i + E_{\text{non-Coul.}}^i \\
&= \sum_i^{\text{aquaion}} \sum_j^{\text{clay}} \frac{q_i q_j}{r_{ij}} + \sum_i^{\text{U, O}_{\text{yl}}, \text{O}_1} \sum_j^{\text{O}_{\text{clay}}} \frac{C_4^{ij}}{r_{ij}^4} + \frac{C_6^{ij}}{r_{ij}^6} + \frac{C_8^{ij}}{r_{ij}^8} + \frac{C_{12}^{ij}}{r_{ij}^{12}} \\
&\quad + \sum_i^{\text{O}_{\text{yl}}} \sum_j^{\text{Si}} \frac{C_4^{ij}}{r_{ij}^4} + \frac{C_6^{ij}}{r_{ij}^6} + \frac{C_8^{ij}}{r_{ij}^8} + \frac{C_{12}^{ij}}{r_{ij}^{12}}
\end{aligned} \tag{2}$$

The HIC interaction potential developed is the first *ab initio* force field for clay uranyl interactions. The non-coulomb interaction potential parameters fitted to ~ 250 QM single points are given in Table.

Table S1: Coefficients from the fitting of the HIC interaction potential and RMSE. Any oxygen atomtype of the clay is considered O_{Clay}

Coefficients	$\text{kcal mol}^{-1} \text{\AA}^{-n}$	Coefficients	$\text{kcal mol}^{-1} \text{\AA}^{-n}$
$C_4^{\text{UO}_{\text{Clay}}}$	0.57660E+04	$C_4^{\text{O}_{\text{I}}\text{O}_{\text{Clay}}}$	-0.77970E+03
$C_6^{\text{UO}_{\text{Clay}}}$	-0.99426E+05	$C_6^{\text{O}_{\text{I}}\text{O}_{\text{Clay}}}$	0.69205E+04
$C_8^{\text{UO}_{\text{Clay}}}$	0.20131E+06	$C_8^{\text{O}_{\text{I}}\text{O}_{\text{Clay}}}$	-0.43570E+04
$C_{12}^{\text{UO}_{\text{Clay}}}$	0.26171E+08	$C_{12}^{\text{O}_{\text{I}}\text{O}_{\text{Clay}}}$	-0.13897E+04
$C_4^{\text{O}_{\text{yl}}\text{O}_{\text{Clay}}}$	-0.14412E+04	$C_4^{\text{O}_{\text{yl}}\text{Si}}$	0.34305E+04
$C_6^{\text{O}_{\text{yl}}\text{O}_{\text{Clay}}}$	0.90564E+04	$C_6^{\text{O}_{\text{yl}}\text{Si}}$	-0.39344E+05
$C_8^{\text{O}_{\text{yl}}\text{O}_{\text{Clay}}}$	0.18621E+03	$C_8^{\text{O}_{\text{yl}}\text{Si}}$	0.21823E+06
$C_{12}^{\text{O}_{\text{yl}}\text{O}_{\text{Clay}}}$	-0.66662E+05	$C_{12}^{\text{O}_{\text{yl}}\text{Si}}$	-0.22146E+07
RMSE _{total}		5 kcal mol ⁻¹	

The HIC potential reproduces correctly the training set data: root mean square error, $RMSE = 5 \text{ kcal mol}^{-1}$. Though the RMSE seems high, relative to the interaction energies that can be as high as $-100 \text{ kcal mol}^{-1}$ it is satisfactory. Figure S1 is the correlation diagram for the QM interaction and the interaction potential energies. The ability of the potential to reproduce interaction energies outside of the fitted set was tested using structures extracted from the molecular dynamics simulation and computing their QM energy.

Interpolation of the experimental $\delta_{\text{interlayer}}$

To obtain the $\delta_{\text{interlayer}}$ of a clay with the dry bulk density ρ_d of our clay (1.4 g cm^{-3}) we must know the components of the following equation:

$$\frac{\epsilon D^*}{D_0} = \frac{\alpha_{\text{macropore}} + \alpha_{\text{int}} \delta_{\text{int}}}{G_i} \quad (3)$$

We assume that $\alpha_{\text{macropore}} \approx 0$ and $\alpha_{\text{macropore}} \approx 1$. G_i is not a function of ρ_d and for water saturated Na-Montmorillonite is 4.0 ± 1.6 (Bourg, I. C.; Sposito, G.; Bourg, A. Clays and Clay Minerals 2006, 54, 363–374). D_0 is equal to $4.9 \cdot 10^{-5} \text{ cm}^2 \text{ s}^{-1}$ (Muurinen, A. Engineering Geology 1990, 28, 359 – 367). In the work of Shackelford and Moore (Moore, S. M.; Shackelford, C. D. Uranium diffusion in soils and rocks. 2011) ϵD^* of the experiments of Muurinen (Muurinen, A. Engineering Geology 1990, 28, 359 – 367) is interpolated as function of ρ_d :

$$D_e = \epsilon D^* = 2.62 \cdot 10^{-10} \exp(-5.83\rho_d) \quad (4)$$

Therefore, $\epsilon D^* = 7.5 \cdot 10^{-14} \text{ cm}^2 \text{ s}^{-1}$ and then $\delta_{\text{int}} = 0.61 \cdot 10^{-3}$

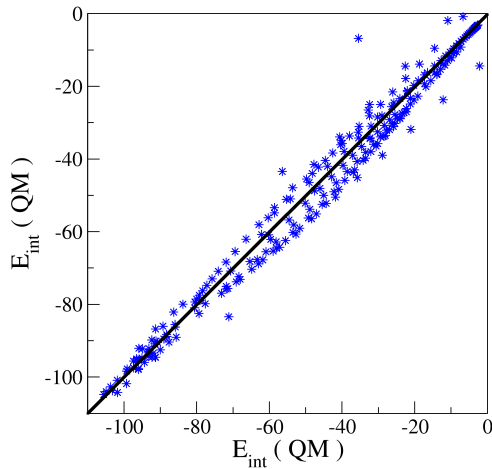


Figure S1: Quantum mechanical (QM) and classical (CM) interaction energies for all structures used to fit the hydrated ion-clay (HIC) potential.

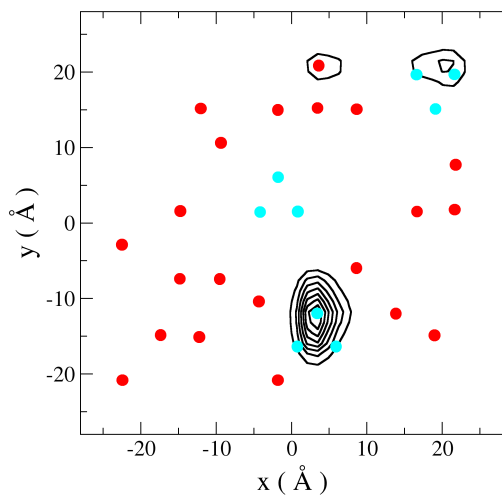


Figure S2: Probability density map of the xy coordinates of the U atoms when they are bound to one of the clay layers on either side. Mg atoms are represented as circles: blue if they belong to a site and red otherwise.

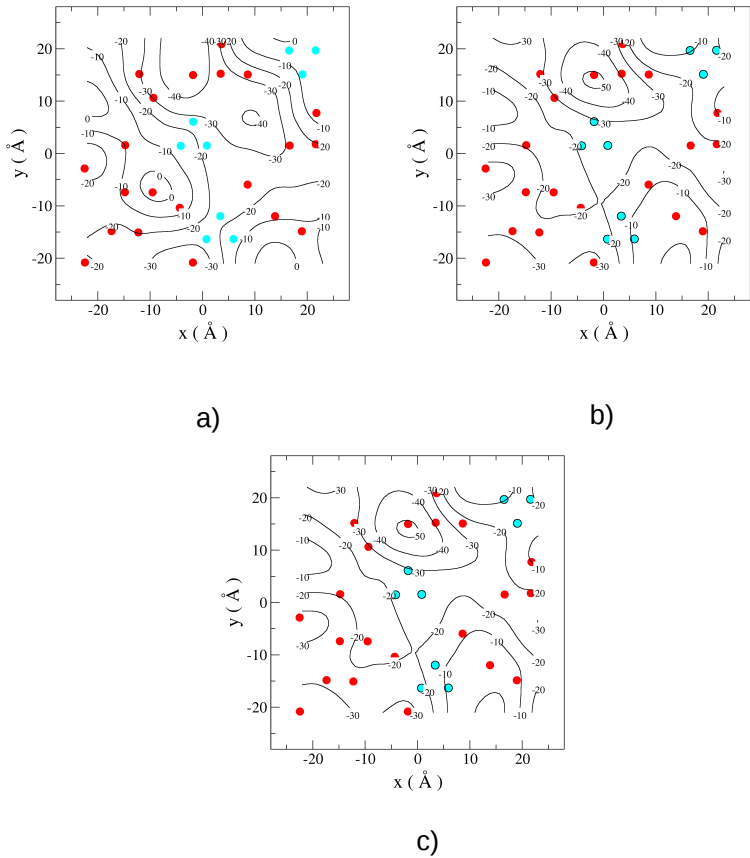


Figure S3: Contour lines of the electrostatic potential in the xy plane with z equal to -4 \AA (a), 10 \AA (b), 15 \AA (c). At these z values the U z-density profile has maxima. Therefore, these z values correspond to uranyl being bound to the surface. The units are $\text{kcal mol}^{-1} \text{ e}^{-1}$. Mg atoms are represented as circles: blue if they belong to a site and red otherwise.

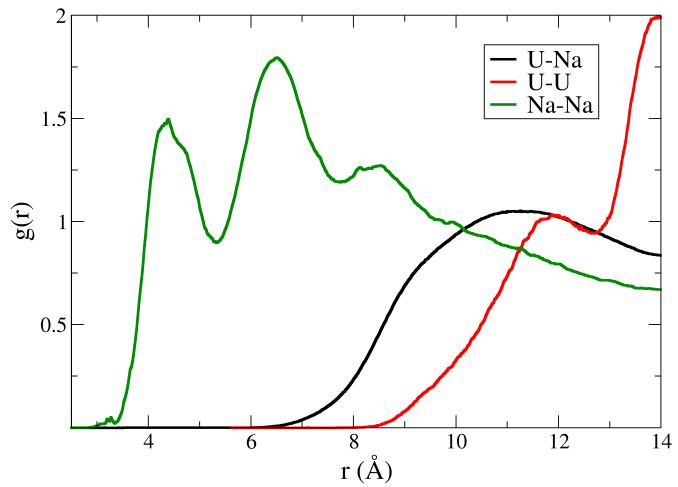


Figure S4: Cation-cation RDFs obtained from the 8 uranyl ion simulation. a) U-Na (black), b) U-U (green), c) Na-Na (red).

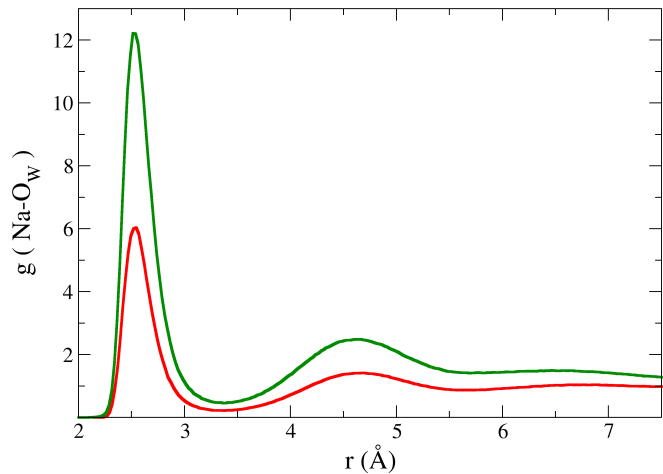


Figure S5: Na-O_W RDFs obtained from the 8 uranyl ion simulation (green) and solution (red).

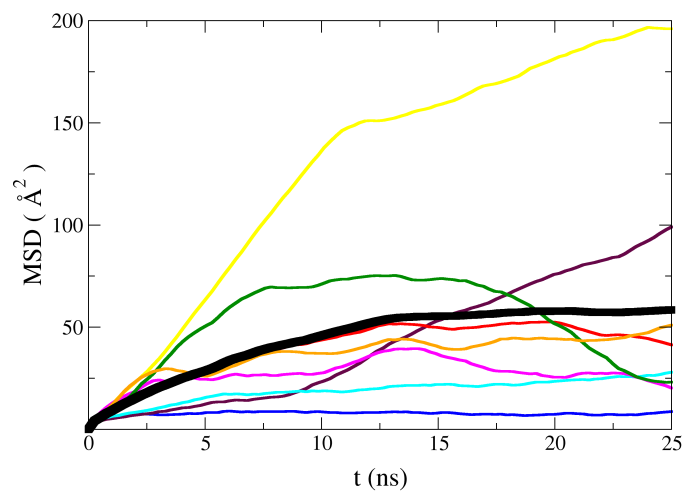


Figure S6: Mean square displacements of $[\text{UO}_2 \cdot (\text{H}_2\text{O})_5]^{2+}$ in the clay simulations for the systems with 8HI but without any Na^+ in the interlayer. Each colored line represents an individual HI. The average of the individuals in the interlayer are represented by the black thick line.

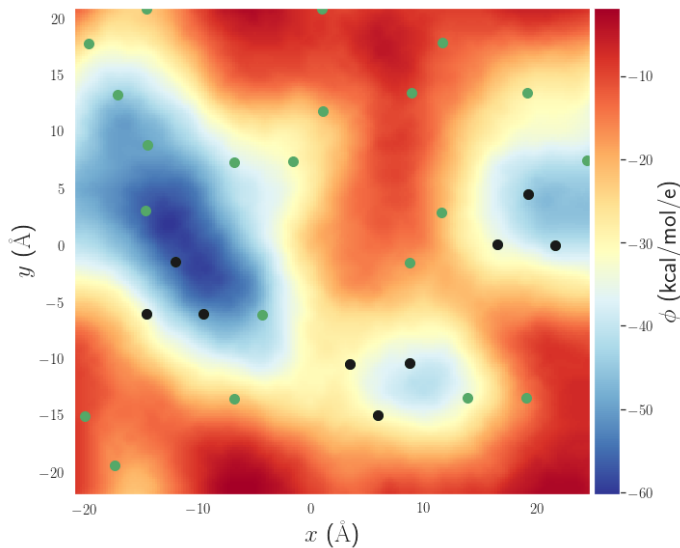


Figure 8.1 Corrected electrostatic potential (ϕ) surface at $z = -10\text{\AA}$ in $\text{kcal mol}^{-1}\text{e}^{-1}$ as it should have appeared in the article. The published figure had the sign of both axis changed. Mg are represented as green circles or black circles if they are part of a site.

8.2. Erratum

When preparing the material for the thesis manuscript, I realized that the electrostatic potential energy surface published in the article of this chapter (Figure 7) was wrong. The correct figure would have had changed signs of both the x and y axis. Figure 8.1 contains the correct information.

We find that the electrostatic potential is minimum in the regions close to the sites. On the contrary to our speculation in the article, the strong interaction with the sites is electrostatic. The strength of the interaction is very high which explains the low diffusion of the cations. Additionally, the strength of the interaction varies in each site due to the different substitution pattern around them. The electrostatic potential is screened by the water molecules and the rest of the cations. The strength of this screening is different if there is

one HI per interlayer or four. The different screening in either system explains the difference in cation diffusivity.

In the section “Uranyl Diffusion Modeling”, the translational self-diffusion coefficient published was mistranscribed. The actual value is $D^{\text{MD}} = 0.004 \pm 0.002 \cdot 10^{-5} \text{ cm}^2 \text{ s}^{-1}$. Fortunately, the parameter that was analyzed, the constrictivity factor was correct.

A local fingerprint for hydrophobicity and hydrophilicity: from methane to peptides

9.1. *J. Chem. Phys.* 2019, **150**, 204103–204108



A local fingerprint for hydrophobicity and hydrophilicity: From methane to peptides

Cite as: J. Chem. Phys. 150, 204103 (2019); doi: 10.1063/1.5088418

Submitted: 10 January 2019 • Accepted: 29 April 2019 •

Published Online: 22 May 2019



S. Pérez-Conesa,¹ Pablo M. Piaggi,^{2,3} and Michele Parrinello^{3,4,a}

AFFILIATIONS

¹ Department of Physical Chemistry, University of Seville, 41012 Seville, Spain

² Theory and Simulation of Materials (THEOS), École Polytechnique Fédérale de Lausanne (EPFL), CH-1015 Lausanne, Switzerland

³ Facoltà di Informatica, Istituto di Scienze Computazionali, and National Center for Computational Design and Discovery of Novel Materials (MARVEL), Università della Svizzera Italiana (USI), Via Giuseppe Buffi 13, CH-6900 Lugano, Switzerland

⁴ Department of Chemistry and Applied Biosciences, ETH Zurich, c/o USI Campus, Via Giuseppe Buffi 13, CH-6900 Lugano, Switzerland

^a Electronic mail: parrinello@phys.chem.ethz.ch

ABSTRACT

An important characteristic that determines the behavior of a solute in water is whether it is hydrophobic or hydrophilic. The traditional classification is based on chemical experience and heuristics. However, this does not reveal how the local environment modulates this important property. We present a local fingerprint for hydrophobicity and hydrophilicity inspired by the two body contribution to the entropy. This fingerprint is an inexpensive, quantitative, and physically meaningful way of studying hydrophilicity and hydrophobicity that only requires as input the water-solute radial distribution functions. We apply our fingerprint to octanol, benzene, and 20 proteinogenic amino acids. Our measure of hydrophilicity is coherent with chemical experience, and moreover, it also shows how the character of an atom can change as its environment is changed. Finally, we use the fingerprint as a collective variable in a funnel metadynamics simulation of a host-guest system. The fingerprint serves as a desolvation collective variable that enhances transitions between the bound and unbound states.

Published under license by AIP Publishing. <https://doi.org/10.1063/1.5088418>

I. INTRODUCTION

“Like dissolves like” is one of the earliest chemical rules a scientist learns in relation to solvation. It implies that solutes that are chemically similar to water have a favorable interaction with water and are hydrophilic. On the other hand, solutes that are not like water will tend to repel water and be hydrophobic.^{1,2} Typically, one assigns to each atom its own hydrophobicity or hydrophilicity based on chemical experience and heuristics. Despite the importance of these intuitive classifications, none of them is quantitative nor takes into account thermodynamics or solvent structure. Processes like protein folding, the assembly of molecules, or crystallization depend crucially on their interaction with water. Thus, it would be of great help to have a measure of the hydrophobicity and hydrophilicity of the atoms in a solute molecule and understand how these parameters change as the environment changes. There is a vast and at times

controversial literature on the concept of hydrophilicity, and we do not want to enter into this arena, nor do we want to replace what is already available in the literature.

For instance, in the context of protein science, many hydrophobicity scales for amino acids have been proposed based on empirical or computational data without any definitive consensus.³ Scales that focus on the hydrophobicity of selected heavy atoms have also been proposed. Some of them are based on local compressibility or density fluctuations of the hydration layers of proteins and surfaces.^{4,5}

Here, we propose to use a concept related to the density fluctuations, namely, the radial distribution function (RDF). Thus, we define a local fingerprint that is a function of the RDF between solute atoms and water oxygen atoms. This fingerprint has been inspired by our previous work on using approximated expressions for the entropy in order to distinguish between solidlike and liquidlike

environments.^{6,7} We emphasize that the goal of this work is not to calculate the entropy and that we ignore angular correlations that play an important role in a complex liquid such as water.^{8–20} With respect to other hydrophobicity measures, our fingerprint has the advantage of being easy to compute and defined for each atom, and in principle, it can also be experimentally measured. One can thus assess the hydrophobicity of each individual atom and the modifications that result from changes in its environment. We apply this fingerprint to water and methane as representatives of optimal hydrophilicity and hydrophobicity and to more complex systems such as octanol, benzene, and 20 proteinogenic amino acids.

The local fingerprint does not only provide an inexpensive and quantitative assessment of hydrophobicity, but it is also a suitable collective variable (CV) to describe solvation in enhanced sampling simulations. In many cases, solvation and desolvation represent a kinetic bottleneck in spite of not being the main processes under study. This is the case in protein folding, ligand binding, and crystallization. We illustrate the usefulness of the fingerprint in enhanced sampling simulations by using it in a funnel metadynamics simulation of a host-guest system. The fingerprint enhances the transition between the bound and unbound states through a dynamical description of solvation.

II. FINGERPRINT FOR HYDROPHOBICITY AND HYDROPHILICITY

Theory provides an expansion of the entropy of a liquid as a sum of many-body correlation functions.^{21–23} Inspired by this theoretical framework, we propose the following term of the expansion as a local fingerprint for hydrophobicity and hydrophilicity of atom *i*:

$$S_i^c = -2\pi\rho_{w,loc} \int_0^\infty \{ g_{iw}(r) \ln[g_{iw}(r)] - g_{iw}(r) + 1 \} r^2 dr, \quad (1)$$

where $\rho_{w,loc}$ is the local number density of water and $g_{iw}(r)$ is the radial distribution function of atom *i* of the solute and water oxygen atoms. The reader should bear in mind that this is not an expression for the excess entropy of the system but rather one of its contributions. Calculating the entropy requires including higher order terms and angular correlations^{8–12} at a much higher computational cost. This defeats our purpose of having an inexpensive, semiquantitative fingerprint useful also in enhanced sampling simulations. Furthermore, Eq. (1) can be seen in a different light if it is interpreted as a Bregman divergence between $g_{iw}(r)$ and the perfect gas RDF, i.e., $g(r) = 1 \forall r$.²⁴ From this point of view, it represents a distance between these two functions. Equation (1) is also connected to the Kirkwood-Buff²⁵ integrals since both are integrals involving the radial distribution function.

It is instructive to calculate the fingerprint value in the simple case of a spherical cavity of radius *R* embedded in an ideal solvent. In this particular case, $g_{iw}(r)$ in Eq. (1) is

$$g_{iw}(r) = \begin{cases} 0, & \text{if } r \leq R, \\ 1, & \text{if } r > R. \end{cases} \quad (2)$$

If we introduce this step function in Eq. (1), the following formula for the fingerprint of a cavity of volume $V = \frac{4}{3}\pi R^3$ is obtained:

$$S_i^{cav} = -\frac{\rho k_B V}{2}. \quad (3)$$

This expression is the leading term of the solvation entropy in the information theory model of hydrophobic interactions^{1,26,27} if one assumes that the solvent behaves ideally.

III. COMPUTATIONAL METHODS

All the systems used in this work for unbiased simulations were solutions of a single solute molecule with 1000 SPC/E²⁸ water molecules at water density 0.997 g cm⁻³. The solutes studied were an SPC/E water molecule, methane, n-octanol, benzene, and 20 proteinogenic amino acids. The amino acids were simulated in their standard physiological protonation state and with N-methylated and C-acetylated termini. The OPLS²⁹ force field was used for methane and octanol. AMBER03³⁰ was used for the amino acids and benzene. The partial charges of benzene were calculated at the B3LYP/cc-PVTZ level using the ESP method,³¹ and the polarizable continuum model³² was used to mimic the aqueous environment. Water molecules were kept rigid using the SETTLE algorithm.³³ For the rest of the solutes, the bonds involving hydrogen were constrained with the P-LINKS algorithm.³⁴ Lennard-Jones cross-term parameters were assigned using $\epsilon_{ij} = (\epsilon_i \epsilon_j)^{(1/2)}$ and $\sigma_{ij} = \frac{\sigma_i + \sigma_j}{2}$, except in the case of AMBER03 where $\sigma_{ij} = (\sigma_i \sigma_j)^{(1/2)}$ was used.

The host-guest system studied by metadynamics simulation was obtained from the SAMPL5³⁵ blind contest. The host-guest system studied has code name OAMe/OA-G2, and the structure and topology files used were those provided for the contest. The force fields used were GAFF³⁶ and SPC/E.²⁸

All molecular dynamics (MD) simulations were run with GROMACSv5.1.1³⁷ in the NVT ensemble using the stochastic velocity rescaling thermostat³⁸ at 298 K and a relaxation time $\tau = 0.1$ ps. The equations of motion were integrated using the leapfrog algorithm with a 2 fs time step for a total time of 10 ns. The simulation time for the metadynamics simulation was 300 ns although a shorter simulation would have sufficed to achieve convergence. Periodic boundary conditions were used, and long-range electrostatic interactions were calculated with the PME method.^{39,40} Short range van der Waals interactions were truncated at 10 Å.

The calculations of the fingerprint were done using a development version of PLUMED 2.⁴¹ The RDF is calculated using a kernel density estimation of the radial distribution function,^{6,7} which for a Gaussian kernel is

$$g_{iw}(r) = \frac{1}{4\pi\rho_{w,loc} r^2} \sum_{j \neq w} \frac{1}{\sqrt{2\pi\sigma^2}} e^{-(r-r_j)^2/(2\sigma^2)}, \quad (4)$$

where r_j is the distance between the fingerprinted atom, *i*, and the *j*th water molecule where *j* runs over the set of water molecules. σ is the Gaussian kernel bandwidth. Kernel density estimation ensures that $g_{iw}(r)$ is continuous and differentiable with respect to atomic positions for its use as a collective variable in enhanced sampling simulations. In addition, this decreases the noise when the statistics are poor. Nevertheless, a conventional RDF would give identical results. The value of σ was 0.05 Å producing RDFs that are smooth but yet preserve all the relevant features. The fingerprint was integrated

using the trapezoid rule. The upper integration limit was chosen to be $r_{max} = 10 \text{ \AA}$. Equation (4) corresponds to the single configuration $g_{iw}(r)$. To reduce noise, $g_{iw}(r)$ is averaged for its use in Eq. (1).

The local number density of water $\rho_{w,loc}$ is generally different from the bulk water density ρ_w . This is a consequence of the excluded volume of the solute. For big solutes such as the amino acids considered below, the deviation of $\rho_{w,loc}$ from ρ_w can be very significant. For this reason, we have used the local density both in Eqs. (1) and (4). This choice ensures that the RDFs are all equivalently normalized regardless of the excluded volume of the solute.

Well tempered metadynamics (WTMetaD) simulations^{42,43} were run on the host-guest system in its funnel variant.⁴⁴ Funnel metadynamics adds a constant bias potential on the guest such that it remains in a funnel-shaped region with the conical part placed in the cavity of the host and the thin cylindrical region outside host. In this way, the guest diffuses in a region of space where it can easily access the host and not diffuse through all space. The funnel has a length of 23 Å with the cone apex at 15 Å and a cone angle of 45°. The funnel restrain was quadratic with a force constant of 40 kJ Å⁻². The entropy loss due to this restrain is corrected analytically^{44,45} *a posteriori* using Eq. (1) of the supplementary material.

WTMetaD was performed using two CVs: the inverse of the square root of host-guest contact map and a CV based on the fingerprint S_s that we shall refer to as S_{CV} . Using the inverse of the square root of the contact map ensures that both states are sampled in a balanced fashion. This compensates for the fact that a bound and unbound state have ranges of contact-map values that are very uneven. The chosen contacts are specified in PLUMED's input shown in the supplementary material. S_{CV} is defined as the sum of S_s of several atoms of both the host and the guest. Only some solute atoms are included for the calculation of S_{CV} in order to reduce their computational cost. The atoms used can found in Fig. S6 of the supplementary material. An additional simulation without biasing S_{CV} was performed as a reference.

The WTMetaD simulation was carried out using the same molecular dynamics parameters as the unbiased simulations. The Gaussians were deposited every 1 ps with an initial height of 5 kJ mol⁻¹. The Gaussian σ s were 0.005 and 0.05 k_B for the contact map CV and the fingerprint CV. A bias factor of 24 was used. The free energy surfaces were reweighted by the method of Tiwary and Parrinello.⁴⁶ The statistical uncertainties are presented as the standard error of the mean calculated using block averages. Further details of the simulation can be found in the supplementary material.

IV. RESULTS AND DISCUSSION

A. Simple solutes

Water and methane are paradigmatic cases of hydrophilic and hydrophobic solutes. Thus, their fingerprint values can be used as references. Water has an S_s of -1.57 ± 0.01 and methane of -2.78 ± 0.01 . Figure 1 clarifies the physics behind these numbers. The top graph shows the radial distribution functions of the solutes and the bottom graph the integrand $I_i(r)$ of the fingerprint

$$I_i(r) = -2\pi\rho_W \{g_{iw}(r) \ln[g_{iw}(r)] - g_{iw}(r) + 1\} r^2. \quad (5)$$

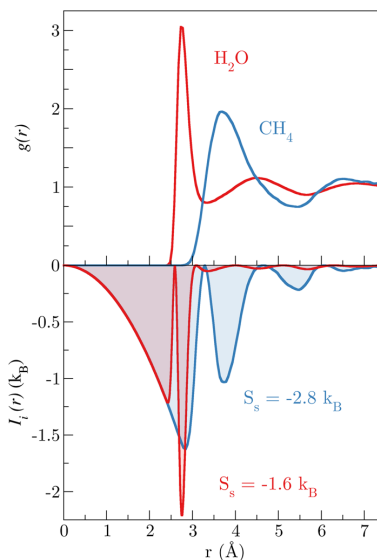


FIG. 1. Top: C-O radial distribution function for the aqueous methane simulation (blue) and O-O radial distribution function for a pure water simulation (red). Bottom: for the same pairs, the integrand, $I_i(r)$, of the fingerprint is plotted.

The figure shows how S_s varies with the radial structure of the solvent around the solute. In essence, S_s becomes more negative the larger the deviation of the RDF from one. The more the solvent is structured around the solute, the smaller S_s . Because of the r^2 factor, the structuring at larger distances is especially effective in decreasing S_s . At short distances, for r less than a distance r_c of the order of the molecular radius, $g_{iw}(r) \approx 0$ and this small r region gives a contribution proportional to r_c^3 . This contribution to S_s corresponds to the cavity formation entropy. Methane has a lower S_s than water for two reasons. First, it generates a larger cavity. Second, although its first hydration shell peak is less structured, it is wider; it is located at distances larger than the first hydration shell of water and contains 4 times more water molecules.

We shall use the S_s values for water and methane as representative of extreme hydrophilicity and hydrophobicity. It is therefore convenient to rescale the values of S_s introducing an index h that is +1 for water and -1 for methane. Thus, in this scale, the sign of h determines whether the atom is hydrophobic or hydrophilic.

We now turn to discuss the properties of octanol chosen for its amphiphilic character. Figure 2 shows octanol, water, and methane with their heavy atoms colored according to their h values. The index clearly distinguishes between hydrophobic and hydrophilic atoms. The trend in h values is in accordance with what could have been expected. The index can also deal with intermediate cases as the carbon atom attached to the alcohol group. This atom should be labeled as less hydrophobic than aliphatic carbons due to its partial positive

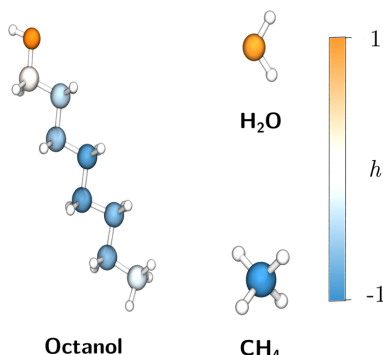


FIG. 2. Octanol, water, and methane molecules with their heavy atoms colored according to the h index. The scale ranges from hydrophobic (blue), to intermediate (white), and to hydrophilic (orange).

charge generated by the electronegativity difference with the oxygen it is bonded to. Nevertheless, since the influence of a hydrophilic atom on the fingerprint of others is limited, the fingerprint is local with respect to the atoms of the molecule. The terminal CH_3 has a lower h than the CH_2 carbons. This can be ascribed to the fact that the solvation shells of neighboring CH_2 groups in the aliphatic chain overlap. This shifts the RDF first solvation peak to higher distances thus increasing h . Since CH_3 has only one neighbor, this effect is less pronounced. Figure S3 of the [supplementary material](#) illustrates this by analyzing the RDFs of primary, secondary, and tertiary carbon atoms and methane. Figure S4 of the [supplementary material](#) includes the numeric values of the fingerprint of the atoms in octanol.

An interesting case is that of ions, in which their classification into hydrophilic or hydrophobic could be misleading. The fingerprint S_s for Na^+ is -3.9 k_B which would mistakenly classify it as more hydrophobic than methane. This is mostly due to the intensity of the first shell peak of the $\text{Na}^+–\text{H}_2\text{O}$ RDF which decreases strongly the value of S_s because of the strong interaction with the ion (Fig. S2 of the [supplementary material](#)). In the classical electrochemistry or coordination chemistry notion of the hydrated ion,⁴⁷ we consider the ion and its first hydration shell as the solute. In this context, we can consider the sodium cation as a buried atom and the first hydration shell atoms as the solvent exposed atoms in which to measure the fingerprint. This concept has been useful in the development of metal ion force fields.^{48,49} The first-shell water molecules have an S_s of -0.9 k_B which is more hydrophilic than bulk water. Therefore, if we use the hydrated ion as the solute, we can conclude the Na^+ hydrated ion is hydrophilic as expected.

B. Amino acids

The fingerprint for the heavy atoms of the 20 proteinogenic amino acids was computed, offering the possibility of testing our fingerprint on a wide range of chemical groups. This is a first step

for future use in the study of hydrophobic and hydrophilic interactions in proteins. Figure 3 shows the different amino acid molecules with the heavy atoms in the side chains colored according to their h value. The backbone atoms are shown only for glycine, but a similar picture is obtained for the other amino acids. As in the case of octanol, h assigns a hydrophobic value to aliphatic carbons and a hydrophilic value to polar N and O atoms of hydrophilic residues. All the heavy atoms of the backbone have h values adequate to the hydrophilicity or hydrophobicity that chemical intuition suggests. A list of h values can be found in Fig. S5 of the [supplementary material](#).

While most of the h values reflect the expected behavior, some apparently surprising values can be seen. For instance, the aromatic C are placed in the middle of the h scale, and thus, they are classified as neither properly hydrophilic nor hydrophobic. In reality, this result is in line with the known solvation behavior of benzene which is much more soluble than its aliphatic counterpart cyclohexane. The reasons for this effect have been discussed in the literature.^{50–53} As seen from the point of view of our fingerprint, this results from the fact that the other atoms in the ring exclude some of the solvation water leading to a reduction in the RDF peak height. In order to confirm that this behavior is not an artifact of our force field, we have calculated S_s using the benzene RDF kindly provided to us by Choudary and Chandra obtained using *ab initio* MD.⁵⁴ The *ab initio* value, $S_s = -1.9 \text{ k}_\text{B}$, is very close to that of the AMBER force field. Here, we did not scale the S_s values since we do not have the *ab initio* reference point for methane.

Another h value that deserves some discussion is that of the sulfur atoms with $h \sim 0$. This can be linked to the fact that the electronegativity of sulfur is intermediate between carbon and oxygen and to the ability of sulfur to accept weak H bonds.^{55,56}

Since we relate h to the water solvation structure and the water structure around each atom and the conformation of the solute can fluctuate as a function of time, we also looked at the distribution of this index. We consider the h value obtained from RDF averaged over a 400 ps moving window to allow the fingerprint to vary and study its distribution. The data obtained from all the amino acid simulations were put in a histogram in which we considered separately aliphatic C, aromatic C, S, and O, and N of the side chains. The histograms are shown in Fig. 4.

In the histogram, the hydrophobic aliphatic C are clearly separated from the hydrophilic O and N of the side chains, proving the usefulness of the fingerprint. As discussed previously, the distribution of the aromatic C and S are centered around $h \sim 0$. The distribution of the hydrophilic O and N of the side chains (shown in red in Fig. 4) presents two peaks and a shoulder. The peak at $h \sim 0.8$ corresponds to all the hydrophilic O and N of charged amino acids with the exception of arginine, while the other peak at $h \sim 1.4$ corresponds to hydrophilic O and N of neutral amino acids and arginine. Charged residues have a lower h than neutral ones because they induce more structure in water. Arginine is an exception to this rule due to its higher charge delocalization and therefore leads to a less well-defined solvation structure. The shoulder at $0 < h < 0.6$ in the histogram of O and N of the side chains corresponds to glutamate since carboxylate oxygen atoms have a very negative effective charge with respect to the rest of hydrophilic atoms. The histogram of hydrophobic aliphatic C has two peaks. The peak at $h \sim -0.4$

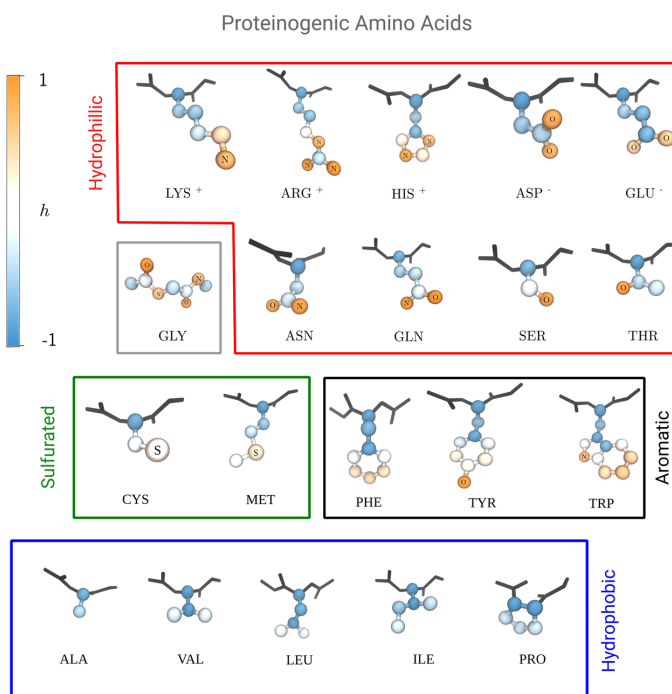


FIG. 3. Structures of the proteinogenic amino acids with their heavy atoms colored according to the h index. The scale ranges from hydrophobic (blue) to intermediate (white) and to hydrophilic (orange). Unlabeled atoms are carbon. Hydrogen atoms are omitted. Since all backbone atoms have similar h index, only side chain atoms are considered. Backbone atoms are visible for glycine (gray box). The boxes organize the amino acids by families: hydrophilic (red), glycine (gray), sulfur-containing (green), aromatic (black), and hydrophobic (blue).

corresponds to CH_3 carbon atoms, while the broad peak at $h \sim -1.75$ corresponds to CH_2 and CH carbon atoms. This behavior has been discussed earlier in Sec. IV A for octanol. The histogram for aromatic C shows three peaks. The two peaks around $h \sim 0.25$ correspond to the more solvent exposed aromatic C, while the remaining peak centered at $h \sim -1.25$ corresponds to C closer to the $\text{C}\beta$.

It is also interesting to test whether our fingerprint correlates with the notion of hydrophilicity given by the free energy of solvation. In Fig. S1 of the supplementary material, we study the correlation between the maximum h value of the amino acids side chain with the experimental free energy of solvation.³⁷ The correlation is satisfactory with correlation coefficient (R^2) 0.57.

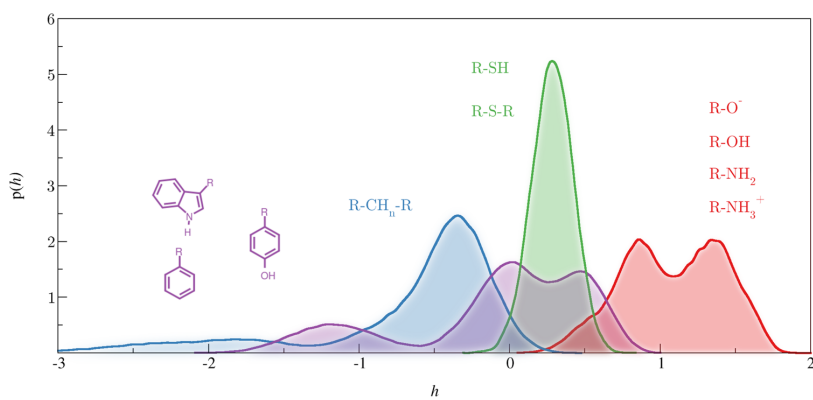


FIG. 4. Probability densities of the hydrophobicity fingerprint, h , of different groups of atoms in their respective simulations. The lines are the distributions of h for C atoms of hydrophobic amino acids (blue), N and O atoms of hydrophilic amino acids (red), aromatic C atoms (purple), and S atoms (green).

C. Enhanced sampling simulations

In Subsections IV A and IV B, we used the fingerprint to describe the hydrophobicity and hydrophilicity of different solutes. In this section, we will show that the fingerprint can also be used as a collective variable to describe solvation in enhanced sampling simulations. Figure 5(b) shows the system chosen for the funnel WTMetaD simulations. It is a host-guest system consisting of a barrel-shaped host molecule and a ligand guest molecule that can fit in the cavity.

As in many ligand-protein systems, desolvation is a key collective variable and a kinetic barrier to the binding if unbiased. If only the contact map is biased, the guest has to wait close to the entrance of the host until it desolvates and binding can happen (Fig. S8 of the [supplementary material](#)). As a consequence, the simulation lacks diffusion in CV space and the simulation's convergence is compromised. This has been observed for this system in previous metadynamics simulations by Bhakat and Söderhjelm.⁵⁸ Their solution was to add a static bias potential that desolvates the interior of the host during the metadynamics and then correct the free energy of binding with a desolvation free energy term obtained from a separate free energy perturbation simulation.

Here, we bias two CVs with WTMetaD: the inverse of the square root of host-guest contact map and a CV based on the fingerprint S_s that we shall refer to as S_{CV} . This results in convergence

of the simulation and free diffusion of the system from bound to unbound (Fig. S8). S_{CV} acts as desolvation CV that allows the host and guest to desolvate during the binding process. From the simulation, we calculate the free energy surface (FES) as a function of the vertical distance between the centers of the guest and the bottom atoms of the host, z , and S_{CV} . The FES is plotted in Fig. 5(a). In state (1), the guest is unbound and fully solvated. Along the diagonal path from (2) to (3), the guest is about 6 Å away from its bound position. The guest and host desolvate at the same time the guest enters the host. We can interpret this as the guest forcing water molecules out of the host-guest adduct as it is drawn by intermolecular forces into the opening of the barrel. Finally, from (3) to (4), there is a desolvation of the host and guest at nearly constant z . This is a situation in which the guest is at the host's doormat but requires a fluctuation of the solvent in order for there to be room in the host to enter. Our interpretation of the S_{CV} as a desolvation CV is supported by the mirroring of the presented FES and an equivalent FES using the number of water molecules in the barrel instead of S_{CV} . This FES is shown in Fig. S7 of the [supplementary material](#).

Finally, the free energy of binding of the host to the guest is $-28.1 \pm 0.8 \text{ kJ mol}^{-1}$. This results from a projection of the FES onto z and the entropy correction of the funnel. This result is close to the experimental value $-21.6 \text{ kJ mol}^{-1}$ ¹⁵⁹ and statistically identical to the value obtained by Bhakat and Söderhjelm⁵⁸ using a different simulation protocol.

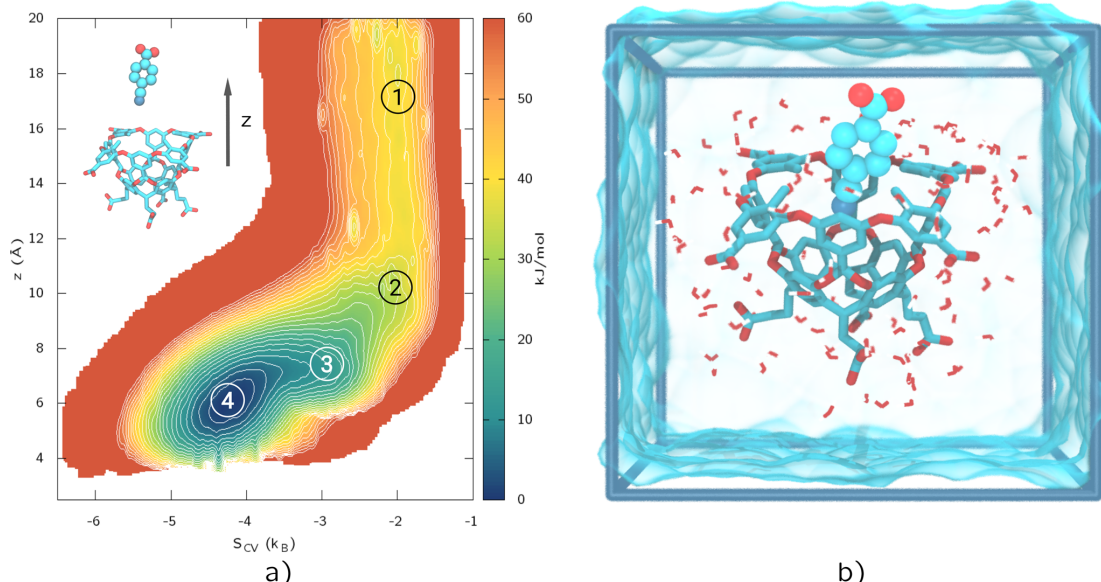


FIG. 5. (a) Reweighted free energy surface of the host-guest system as a function of the vertical distance between the centers of the guest and the bottom atoms of the host, z , and the fingerprint collective variable. (b) Schematic (not to scale) representation of the host-guest system (OAMe-OAG2 in the SAMPL5³⁵ contest). The solvation is represented by the surface and some of the water molecules are explicitly depicted.

V. CONCLUSIONS

We have developed a local fingerprint for hydrophobicity and hydrophilicity. The fingerprint is inspired by the two body solute water contributions to the entropy, which is a function of the RDF. In this context, whether an atom is hydrophobic or hydrophilic is a consequence of the structure of water around it. This feature allows us to understand how the character of a solute is modulated by its environment. We have also introduced an index of hydrophilicity h that uses methane and water as representatives of hydrophobic and hydrophilic behavior. We show the usefulness of the fingerprint in enhanced sampling simulations by studying a host-guest system in which the fingerprint serves as a desolvation CV and allows for fast transition between the bound and unbound states. We expect that the fingerprint could also provide insight into more complex phenomena where hydrophobicity plays an important role, such as protein folding.

SUPPLEMENTARY MATERIAL

See [supplementary material](#) for a PDF file containing additional information including extra radial distribution functions, fingerprint integrands, numeric values of the local fingerprint, free energy surfaces, and metadynamics details not displayed in the text.

ACKNOWLEDGMENTS

The authors thank Ashu Choudhary and Amalendu Chandra for kindly providing us with their *ab initio* benzene RDF. The authors also thank Enrique Sánchez Marcos, Riccardo Capelli, and Tarak Karmakar for helpful discussions. S.P.-C. also acknowledges the Spanish Ministry of Education, Culture and Sports for the Ph.D. Grant (No. FPU14/02100). P.M.P. and M.P. acknowledge support from the NCCR MARVEL funded by the Swiss National Science Foundation and from European Union Grant No. ERC-2014-AdG-670227/VARMET. The computational time for this work was provided by the Swiss National Supercomputing Center (CSCS) under Project ID p503.

REFERENCES

- ¹D. Chandler, *Nature* **437**, 640 (2005).
- ²K. Lum, D. Chandler, and J. D. Weeks, *J. Phys. Chem. B* **103**, 4570 (1999).
- ³S. Simm, J. Einloft, O. Mirus, and E. Schleiff, *Biol. Res.* **49**, 31 (2016).
- ⁴P. J. Rossky, *Faraday Discuss.* **146**, 13 (2010); e-print [arXiv:1009.4658](https://arxiv.org/abs/1009.4658).
- ⁵E. Xi, V. Venkateshwaran, L. Li, N. Rego, A. J. Patel, and S. Garde, *Proc. Natl. Acad. Sci. U. S. A.* **114**, 13345 (2017).
- ⁶P. M. Piaggi, O. Valsson, and M. Parrinello, *Phys. Rev. Lett.* **119**, 015701 (2017).
- ⁷P. M. Piaggi and M. Parrinello, *J. Chem. Phys.* **147**, 114112 (2017).
- ⁸T. Lazaridis and M. E. Paulaitis, *J. Phys. Chem.* **96**, 3847 (1992).
- ⁹T. Lazaridis and M. E. Paulaitis, *J. Phys. Chem.* **98**, 635 (1994).
- ¹⁰T. Lazaridis, *J. Phys. Chem. B* **104**, 4964 (2000).
- ¹¹M. Kinoshita, N. Matubayasi, Y. Harano, and M. Nakahara, *J. Chem. Phys.* **124**, 024512 (2006).
- ¹²M. Liu, Q. A. Besford, T. Mulvaney, and A. Gray-Weale, *J. Chem. Phys.* **142**, 114117 (2015).
- ¹³R. M. Lynden-Bell and J. C. Rasaiah, *J. Chem. Phys.* **107**, 1981 (1997).
- ¹⁴D. L. Bergman, A. P. Lyubartsev, and A. Laaksonen, *Phys. Rev. E* **60**, 4482 (1999).
- ¹⁵T. Lazaridis, *J. Phys. Chem. B* **102**, 3531 (1998).
- ¹⁶C. N. Nguyen, T. Kurtzman Young, and M. K. Gilson, *J. Chem. Phys.* **137**, 044101 (2012).
- ¹⁷Z. Li and T. Lazaridis, *Computer Drug Discovery and Design* (Springer, 2012), pp. 393–404.
- ¹⁸R. Abel, T. Young, R. Farid, B. J. Berne, and R. A. Friesner, *J. Am. Chem. Soc.* **130**, 2817 (2008).
- ¹⁹D. J. Huggins and M. C. Payne, *J. Phys. Chem. B* **117**, 8232 (2013).
- ²⁰C. N. Nguyen, A. Cruz, M. K. Gilson, and T. Kurtzman, *J. Chem. Theory Comput.* **10**, 2769 (2014).
- ²¹H. S. Green, *The Molecular Theory of Fluids* (North-Holland Publishing Company, Amsterdam, 1958).
- ²²R. E. Nettleton and M. S. Green, *J. Chem. Phys.* **29**, 1365 (1958).
- ²³A. Baranyai and D. J. Evans, *Phys. Rev. A* **40**, 3817 (1989).
- ²⁴P. M. Piaggi and M. Parrinello, *Proc. Natl. Acad. Sci. U. S. A.* **115**, 10251 (2018).
- ²⁵J. G. Kirkwood and F. P. Buff, *J. Chem. Phys.* **19**, 774 (1951).
- ²⁶S. Garde, G. Hummer, A. E. Garcia, M. E. Paulaitis, and L. R. Pratt, *Phys. Rev. Lett.* **77**, 4966 (1996).
- ²⁷G. Hummer, S. Garde, A. E. Garcia, A. Pohorille, and L. R. Pratt, *Proc. Natl. Acad. Sci. U. S. A.* **93**, 8951 (1996).
- ²⁸H. J. C. Berendsen, J. R. Grigera, and T. P. Straatsma, *J. Phys. Chem.* **91**, 6269 (1987).
- ²⁹G. A. Kaminski, R. A. Friesner, J. Tirado-Rives, and W. L. Jorgensen, *J. Phys. Chem. B* **105**, 6474 (2001).
- ³⁰Y. Duan, C. Wu, S. S. Chowdhury, M. C. Lee, G. Xiong, W. Zhang, R. Yang, P. Cieplak, R. Luo, T. Lee, J. Caldwell, J. Wang, and P. Kollman, *J. Comput. Chem.* **24**, 1999 (2003).
- ³¹B. H. Besler, K. M. Merz, and P. A. Kollman, *J. Comput. Chem.* **11**, 431 (1990).
- ³²J. Tomasi, B. Mennucci, and R. Cammi, *Chem. Rev.* **105**, 2999 (2005).
- ³³S. Miyamoto and P. A. Kollman, *J. Comput. Chem.* **13**, 952 (1992).
- ³⁴B. Hess, *J. Chem. Theory Comput.* **4**, 116 (2008).
- ³⁵J. Yin, N. M. Henriksen, D. R. Slochower, M. R. Shirts, M. W. Chiu, D. L. Mobley, and M. K. Gilson, *J. Comput.-Aided Mol. Des.* **31**, 1 (2017).
- ³⁶J. Wang, R. M. Wolf, J. W. Caldwell, P. A. Kollman, and D. A. Case, *J. Comput. Chem.* **25**, 1157 (2004); e-print [arXiv:0204](https://arxiv.org/abs/0204).
- ³⁷M. J. Abraham, T. Murtola, R. Schulz, S. Pälli, J. C. Smith, B. Hess, and E. Lindahl, *SoftwareX* **1**-**2**, 19 (2015); e-print [arXiv:1503.05249v1](https://arxiv.org/abs/1503.05249v1).
- ³⁸G. Bussi, D. Donadio, and M. Parrinello, *J. Chem. Phys.* **126**, 014101 (2007); e-print [arXiv:0803.4060v1](https://arxiv.org/abs/0803.4060v1).
- ³⁹T. Darden, D. York, and L. Pedersen, *J. Chem. Phys.* **98**, 10089 (1993); e-print [arXiv:9807099](https://arxiv.org/abs/9807099) [cond-mat].
- ⁴⁰U. Essmann, L. Perera, M. L. Berkowitz, T. Darden, H. Lee, and L. G. Pedersen, *J. Chem. Phys.* **103**, 8577 (1995).
- ⁴¹G. A. Tribello, M. Bonomi, D. Branduardi, C. Camilloni, and G. Bussi, *Comput. Phys. Commun.* **185**, 604 (2014).
- ⁴²A. Barducci, G. Bussi, and M. Parrinello, *Phys. Rev. Lett.* **100**, 020603 (2008).
- ⁴³J. F. Dama, M. Parrinello, and G. A. Voth, *Phys. Rev. Lett.* **112**, 240602 (2014).
- ⁴⁴V. Limongelli, M. Bonomi, and M. Parrinello, *Proc. Natl. Acad. Sci. U. S. A.* **110**, 6358 (2013); e-print [arXiv:1408.1149](https://arxiv.org/abs/1408.1149).
- ⁴⁵T. W. Allen, O. S. Andersen, and B. Roux, *Proc. Natl. Acad. Sci. U. S. A.* **101**, 117 (2004).
- ⁴⁶P. Tiwary and M. Parrinello, *J. Phys. Chem. B* **119**, 736 (2015).
- ⁴⁷D. T. Richens, *The Chemistry of Aqua Ions* (J. Wiley, West Sussex, England, 1997).
- ⁴⁸J. M. Martínez, R. R. Pappalardo, and E. Sánchez Marcos, *J. Am. Chem. Soc.* **121**, 3175 (1999).
- ⁴⁹E. Galbis, J. Hernández-Cobos, C. den Auwer, C. Le Naour, D. Guillaumont, E. Simoni, R. R. Pappalardo, and E. Sánchez Marcos, *Angew. Chem.* **122**, 3899 (2010).
- ⁵⁰C. McAuliffe, *J. Phys. Chem.* **70**, 1267 (1966).
- ⁵¹S. Cabani, P. Gianni, V. Mollica, and L. Lepori, *J. Solution Chem.* **10**, 563 (1981).
- ⁵²D. Ben-Amotz, *Annu. Rev. Phys. Chem.* **67**, 617 (2016).
- ⁵³R. C. Harris and B. M. Pettitt, *J. Phys.: Condens. Matter* **28**, 083003 (2016).

- ⁵⁴A. Choudhary and A. Chandra, *Phys. Chem. Chem. Phys.* **18**, 6132 (2016).
- ⁵⁵H. S. Biswal, P. R. Shirhatti, and S. Wategaonkar, *J. Phys. Chem. A* **114**, 6944 (2010).
- ⁵⁶V. Rao Mundlapati, S. Ghosh, A. Bhattacherjee, P. Tiwari, and H. S. Biswal, *J. Phys. Chem. Lett.* **6**, 1385 (2015).
- ⁵⁷R. Wolfenden, L. Andersson, P. Cullis, and C. Southgate, *Biochemistry* **20**, 849 (1981).
- ⁵⁸S. Bhakat and P. Söderhjelm, *J. Comput.-Aided Mol. Des.* **31**, 119 (2017).
- ⁵⁹M. R. Sullivan, P. Sokkalingam, T. Nguyen, J. P. Donahue, and B. C. Gibb, *J. Comput.-Aided Mol. Des.* **31**, 21 (2017).

Supporting information for: A local fingerprint for hydrophobicity and hydrophilicity: from methane to peptides

S. Pérez-Conesa,[†] Pablo M. Piaggi,[‡] and Michele Parrinello^{*,§}

[†]*Department of Physical Chemistry, University of Seville, 41012 Seville, Seville, Spain*

[‡]*Theory and Simulation of Materials (THEOS), École Polytechnique Fédérale de Lausanne (EPFL), CH-1015 Lausanne, Switzerland*

^{*}*Facoltà di Informatica, Istituto di Scienze Computazionali, and National Center for Computational Design and Discovery of Novel Materials (MARVEL), Università della Svizzera italiana (USI), Via Giuseppe Buffi 13, CH-6900, Lugano, Switzerland*

[§]*Department of Chemistry and Applied Biosciences, ETH Zurich, c/o USI Campus, Via Giuseppe Buffi 13, CH-6900, Lugano, Switzerland*

E-mail: parrinello@phys.chem.ethz.ch



1 Fingerprint Additional Figures

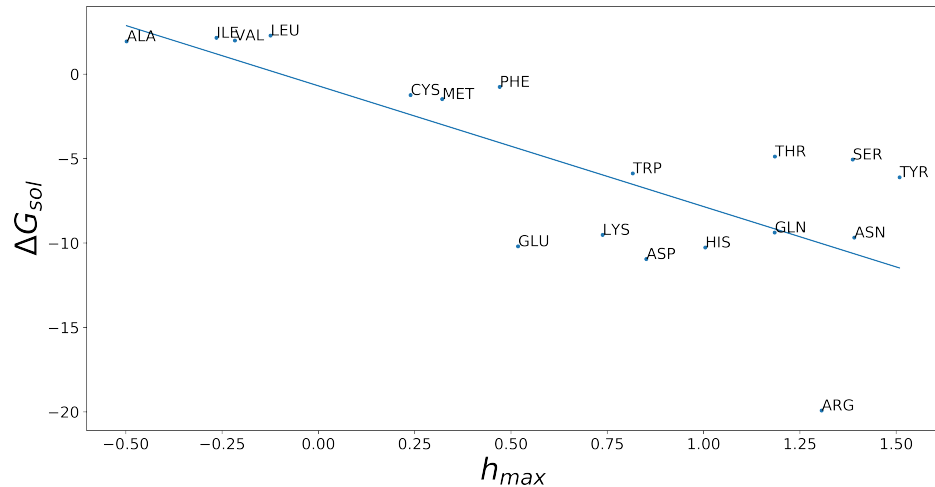


Figure S1: Correlation between the experimental free energy of solvation^{S1} of the proteinogenic amino acids and their sidechain's maximum fingerprint value h_{max} . The correlation coefficient obtained (R^2) is 0.57. To put this value in context, Schauperl et al. obtain a value of 0.64 with a sophisticated calculation of the free energy of solvation based on solvent correlation functions.^{S2}

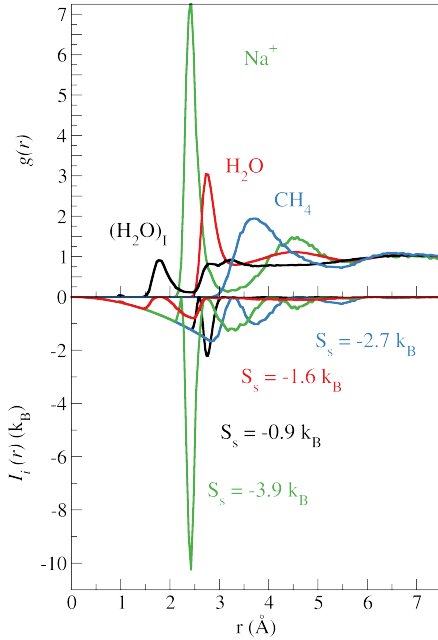


Figure S2: Top: RDFs of C-O for the aqueous methane simulation (blue), of O-O of a pure water simulation (red), of Na^+ -O of a $\text{Na}^+(\text{aq})$ solution simulation and of $\text{O}_1\text{-O}$ where O_1 stands for first-shell water molecule oxygen atom of $\text{Na}^+(\text{aq})$. Bottom: for the same pairs, the integrand, $I_i(r)$, of the fingerprint is plotted.

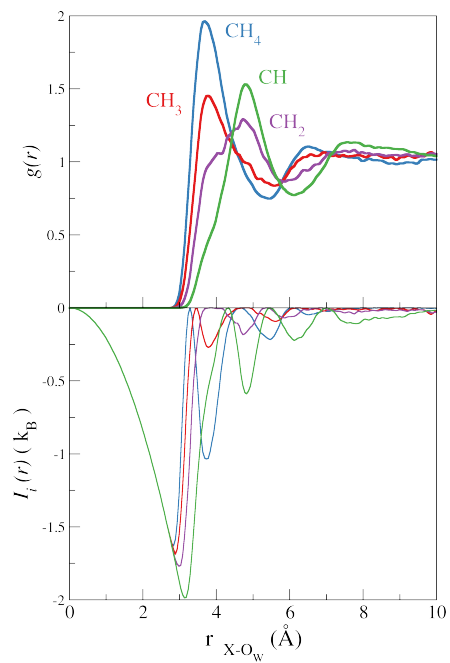


Figure S3: Top: C-O RDFs of carbons with different number of substituents: CH_4 (blue), CH_3 (red) and CH_2 (purple) of octanol and CH (green) of leucine. Bottom: integrand $I_i(r)$ of the pair entropy fingerprint for the corresponding RDFs.

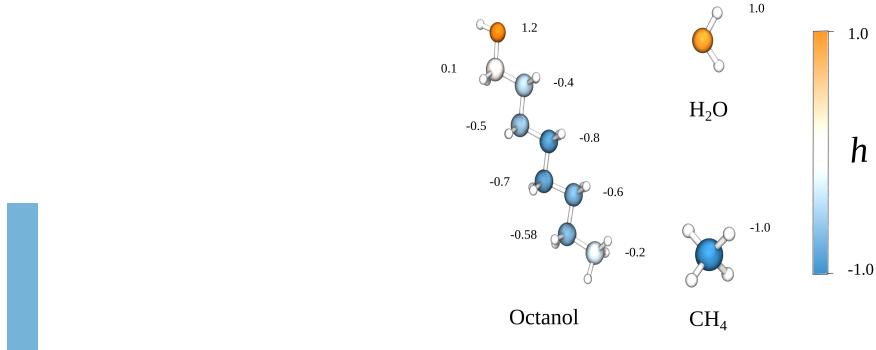


Figure S4: Octanol, water and methane with their heavy atoms colored and labeled according to the hydrophobicity index h . The scale ranges from hydrophobic (blue), to intermediate (white), to hydrophilic (orange).

S4

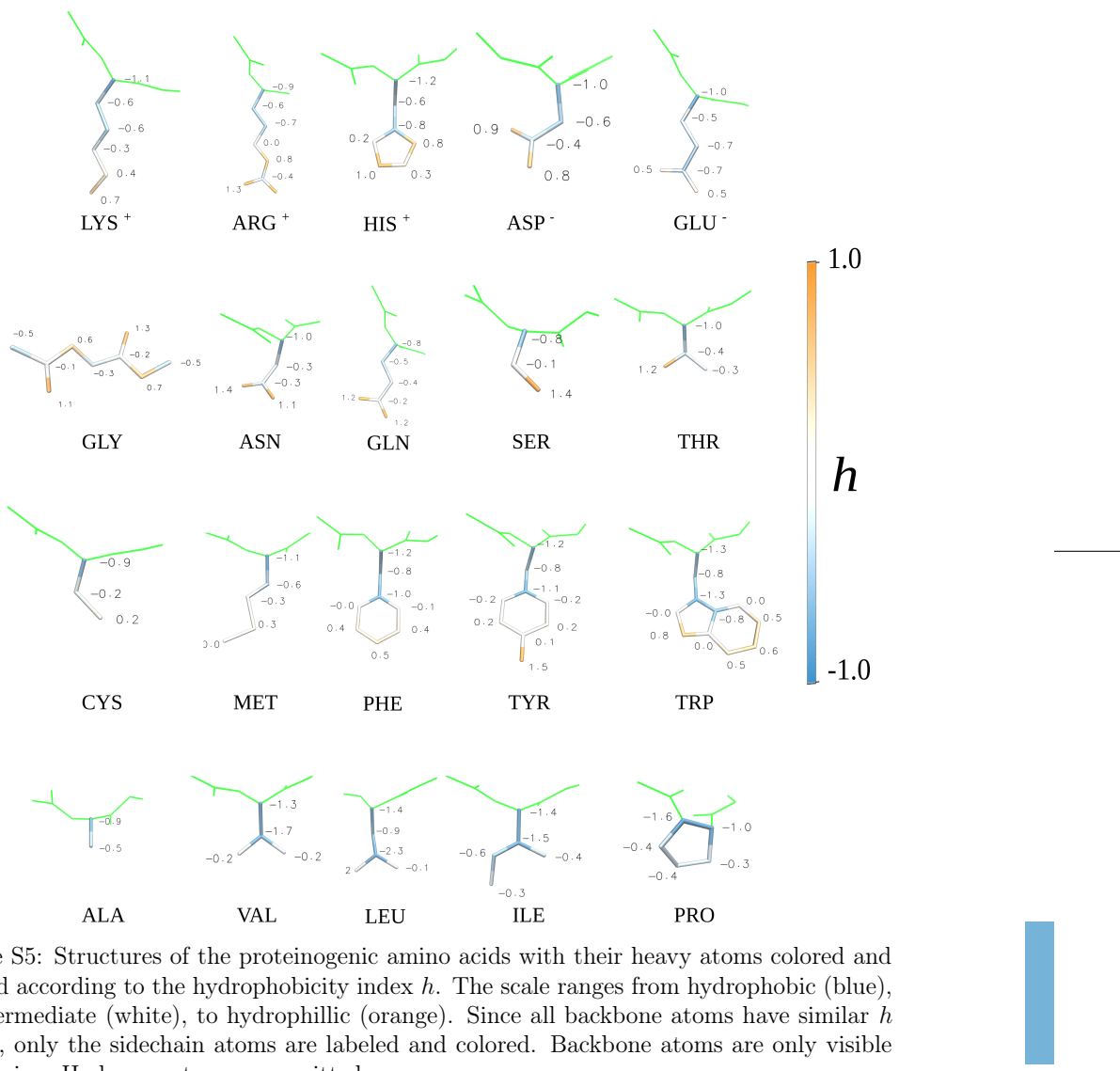


Figure S5: Structures of the proteinogenic amino acids with their heavy atoms colored and labeled according to the hydrophobicity index h . The scale ranges from hydrophobic (blue), to intermediate (white), to hydrophilic (orange). Since all backbone atoms have similar h values, only the sidechain atoms are labeled and colored. Backbone atoms are only visible for glycine. Hydrogen atoms are omitted.

2 Plumed Input Files.

2.1 Metadynamics plumed.dat

```
# vim:ft=plumed
#Water oxygens
ow: GROUP NDX_FILE=index.ndx NDX_GROUP=OW
#MOL is the guest/ligand. Group of atoms of the ligand without H
MOL_noh: GROUP NDX_FILE=index.ndx NDX_GROUP=MOL_noh
#OCB is the barrel shaped host
OCB: GROUP NDX_FILE=index.ndx NDX_GROUP=OCB
#Low RMSF atoms of the host for alignment
low_rmsf: GROUP NDX_FILE=index.ndx NDX_GROUP=low_rmsf
ener: ENERGY
WHOLEMOLECULES ENTITY0=OCB
#conf_template3.pdb is a reference structure for the alignment of the guest
FIT_TO_TEMPLATE STRIDE=1 REFERENCE=conf_template3.pdb TYPE=OPTIMAL
lig: COM ATOMS=MOL_noh # you need the COM of your ligand/molecule
pock: CENTER ATOMS=low_rmsf # you need the COM of your ligand/molecule
DISTANCE ATOMS=pock,lig LABEL=d1 COMPONENTS
CONTACTMAP ...
LABEL=cm
#Contacts between the lower part of the guest and the lower part of the host (so the ligand does not enter upside-down)
ATOMS1=204,14 SWITCH1=RATIONAL R_0=0.4 NN=6 MM=12
ATOMS2=204,5 SWITCH2=RATIONAL R_0=0.4 NN=6 MM=12
ATOMS3=204,28 SWITCH3=RATIONAL R_0=0.4 NN=6 MM=12
ATOMS4=204,30 SWITCH4=RATIONAL R_0=0.4 NN=6 MM=12
ATOMS5=199,57 SWITCH5=RATIONAL R_0=0.5 NN=6 MM=12
ATOMS6=199,75 SWITCH6=RATIONAL R_0=0.5 NN=6 MM=12
ATOMS7=199,63 SWITCH7=RATIONAL R_0=0.5 NN=6 MM=12
ATOMS8=199,69 SWITCH8=RATIONAL R_0=0.5 NN=6 MM=12
#Contact between the center of the ligand and the center of the host, the long R_
#makes the switch function very slowly decaying so it is not flat even at high R.
#It acts as if we were biasing the distance rather than a coordination.
ATOMS9=lig,pock SWITCH9=RATIONAL R_0=1.2 NN=6 MM=8
SUM
... CONTACTMAP
#The function of the contact map is used such that both states are sampled equally, because if
#the ranges of the values of the contact map for both states is very uneven. The term
#0.0000001 is to avoid numerical instabilities.
fof_cm: MATHEVAL ARG=cm FUNC=(x+0.0000001)^(-0.5) PERIODIC=NO
PAIRENTROPIES ...
LABEL=s2_all
#Only the bottom part of the guest is used because the top part of the guest remains solvated in both states.
SPECIESA=129,130,131,132,9,21,34,40,3,13,35,37,200,198,197,201,204
SPECIESB=ow
MAXR=1.0
SIGMA=0.05
NHIST=35
LOCAL_DENSITY
MASS=1.0
MEAN
# This is only necessary to allow calculation of the CV derivatives.
# If the fingerprint is not used as a CV a step function is used.
```

```

SWITCH=RATIONAL R_0=1.0
... PAIRENTROPIES
radius: MATHEVAL ARG=d1.x,d1.y VAR=x,y FUNC=sqrt(x*x+y*y) PERIODIC=NO
# The bottom of the funnel is at -0.3nm.
#1.->Position of ZCC
#45°-> alpha
#1.2 ->Position of the tip of the cone (in unbound region) ZCC+R_cyl*tan(alpha)
#0.2 ->Cylinder radius R_cyl
#Outside the funnel positive value of funnel coordinate
#When z<ZCC
#Inside bound region, conical section.
#The radial distance to the wall of the cone is:
# -tan(alpha)*(ZCC+R_cyl*tan(alpha)-z)+r
#This is the first term in the expression of the equation given to PLUMED.
#When z>ZCC
#Unbound region, cylindrical part of the cone.
#The funnel coordinate becomes the radial distance (positive or negative) to the funnel side. r-R_cyl
#This is the second term in the expression of the equation given to PLUMED.
funnel: MATHEVAL ARG=radius,d1.z VAR=r,z FUNC=(r+1.0*(-1.2+z))*step(-z+1.)+(r-0.2)*step(z-1.) PERIODIC=NO
#Bias on the funnel wall when the funnel coordinate is positive (the ligand is out of the cone or cylinder)
UPPER_WALLS AT=0 ARG=funnel KAPPA=4000.0 LABEL=funnelwall
# Wall on distance to prevent the going through the host.
LOWER_WALLS AT=-0.3 ARG=d1.z KAPPA=4000.0 EXP=-2 LABEL=lower_wall
# Wall on distance to prevent the ligand exit from top of funnel.
UPPER_WALLS AT=1.8 ARG=d1.z KAPPA=4000.0 EXP=-2 LABEL=upper_wall
METAD ...
LABEL=metad
ARG=fof_cm,s2_all.mean
SIGMA=0.005,0.05
HEIGHT=5.0
BIASFACTOR=24
TEMP=298
PACE=500
GRID_MIN=0.4,-8.0
GRID_MAX=1.8,0.0
REWEIGHTING_NGRID=1400,800
... METAD
PRINT STRIDE=500 ARG=* FILE=COLVAR

```

2.2 Metadynamics Reweighting.dat

```

# vim:ft=plumed
s2_all: READ FILE=../COLVAR IGNORE_TIME VALUES=s2_all.mean IGNORE_FORCES
z: READ FILE=../COLVAR IGNORE_TIME VALUES=d1.z IGNORE_FORCES
funnelwall: READ FILE=../COLVAR IGNORE_TIME VALUES=funnelwall.bias IGNORE_FORCES
upper_wall: READ FILE=../COLVAR IGNORE_TIME VALUES=upper_wall.bias IGNORE_FORCES
lower_wall: READ FILE=../COLVAR IGNORE_TIME VALUES=lower_wall.bias IGNORE_FORCES
metad: READ FILE=../COLVAR IGNORE_TIME VALUES=metad.rbias IGNORE_FORCES
reweight: REWEIGHT_BIAS TEMP=298.0 ARG=metad.rbias,funnelwall.bias,upper_wall.bias,lower_wall.bias
HISTOGRAM ...
BANDWIDTH=0.025
LOGWEIGHTS=reweight
GRID_MIN=0.0,-8.0
GRID_MAX=2.0,0.0

```

```

GRID_BIN=500,500
ARG=z,z,s2_all.mean
NORMALIZATION=true
LABEL=hh3
UPDATE_FROM=50000
... HISTOGRAM
fes3: CONVERT_TO_FES GRID=hh3 TEMP=298.
DUMPGRID GRID=fes3 FILE=fes1d_z.dat FMT=

```

2.3 Correction to the Free Energy

The free energy of binding of the guest to the host, ΔF^b , can be calculated approximately by adding a term to the free energy of binding obtained from the simulation to correct for the entropy loss due to the funnel:^{S3,S4}

$$\Delta F^b = \Delta F_{\text{MetaD}}^b - k_B T \ln(\pi R_{\text{cyl}}^2 C^0) \quad (1)$$

$\Delta F_{\text{MetaD}}^b$ is the free energy difference of binding of the WTMetaD simulation, k_B is the Boltzmann constant, T the temperature, R_{cyl} the radius of the unbound section of the funnel and C^0 the standard concentration.



2.4 Extra Metadynamics Figures.

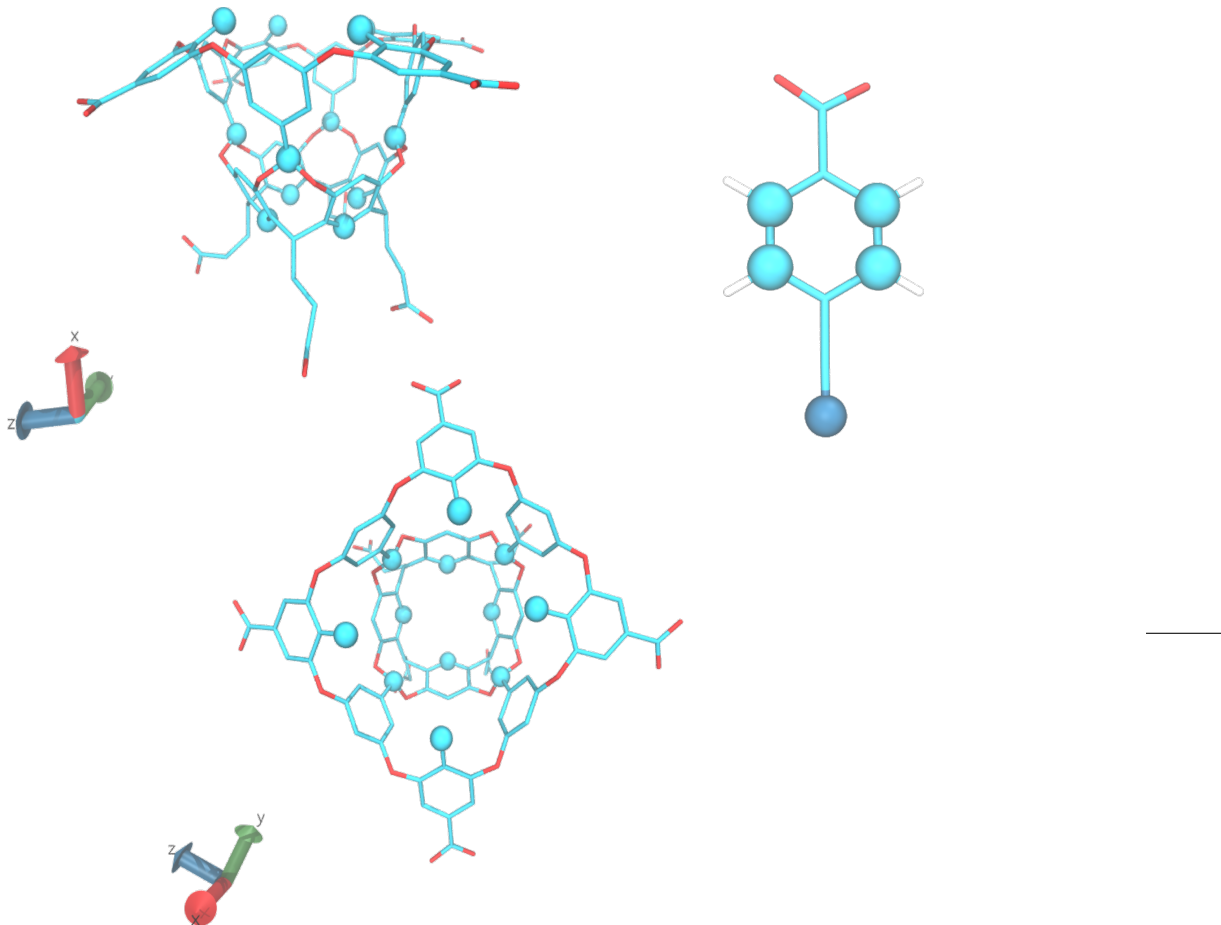


Figure S6: Host and guest molecules used in the WTMetaD simulations. The atoms represented as spheres were included in the calculation of the pair entropy fingerprint S_{CV} . Only some of the atoms were included to reduce the cost of the on-the-fly calculation of the CV.

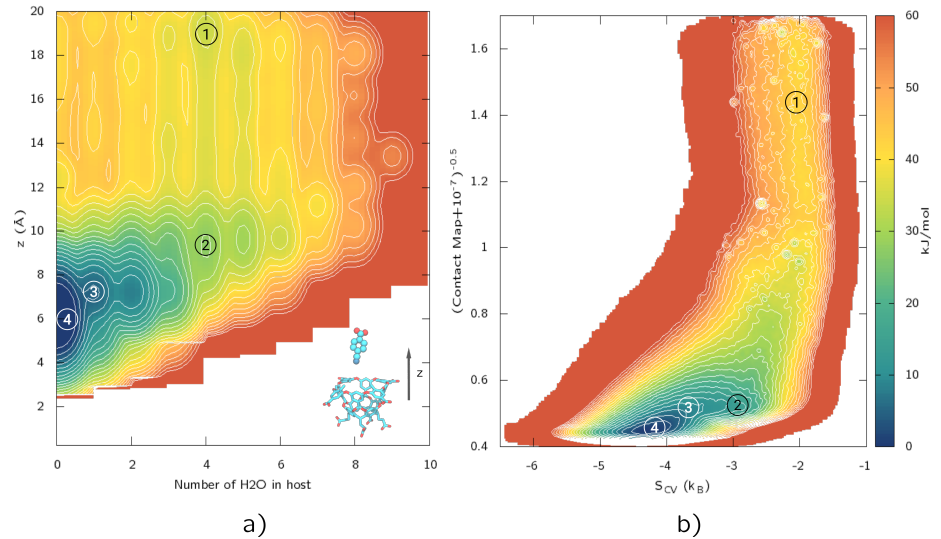


Figure S7: a) Reweighted free energy surface of the host-guest system as a function of the vertical distance between the centers of the guest and the bottom atoms of the host, z , and the number of water molecules in the host. b) Reweighted free energy surface of the host-guest system as a function of the inverse square root of the contact map and the fingerprint collective variable. The function of the contact map is used such that both states are sampled equally, because the ranges of the values of the contact map for both states is very uneven. The term 10^{-7} is to avoid numerical instabilities. The numbers correspond to the positions of the other free energy surface described in the text.

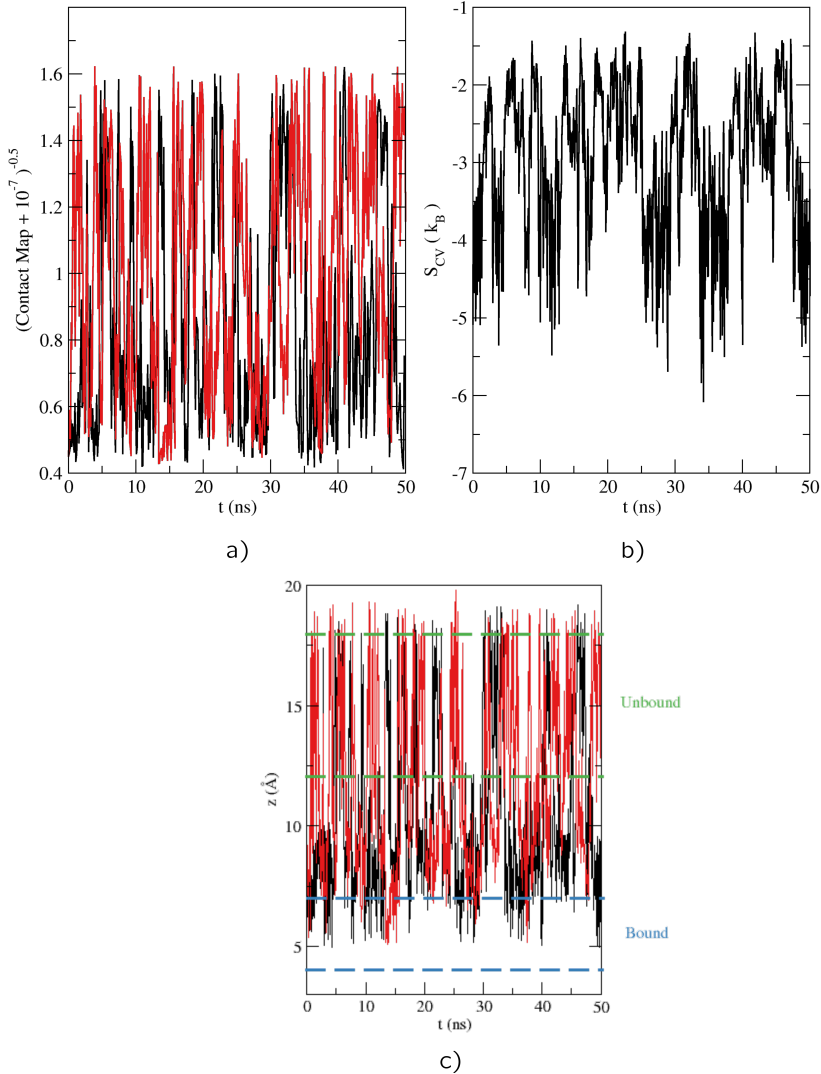


Figure S8: Time evolution of collective variables in a WTMetaD simulation biasing the inverse square root of the contact map (red) and another one that additionally includes the pair entropy fingerprint S_{CV} (black). a) Inverse square root of the contact map, b) pair entropy fingerprint S_{CV} , c) vertical distance between the centers of the guest and the bottom atoms of the host, z . Transitions from bound to unbound are nearly doubled by the presence of the second CV.

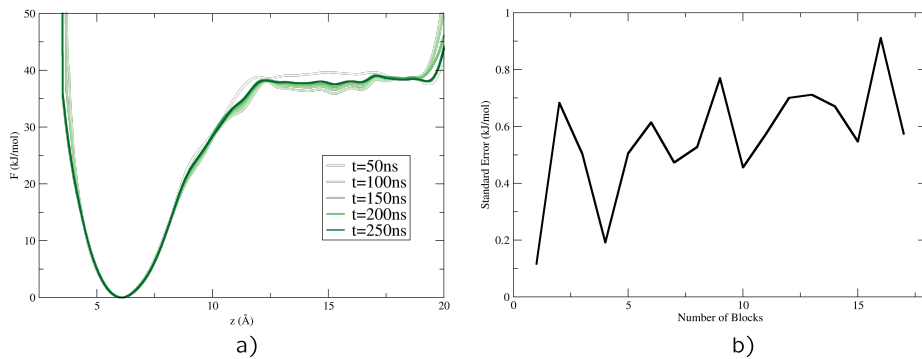


Figure S9: a) Convergence of the reweighted free energy surface as function of simulation time. b) Standard error of the mean between blocks in which the simulation is split as a function of number of blocks.

References

- (S1) Wolfenden, R.; Andersson, L.; Cullis, P. M.; Southgate, C. C. *Biochemistry* **1981**, *20*, 849–855.

- (S2) Schauperl, M.; Podewitz, M.; Waldner, B. J.; Liedl, K. R. *J. Chem. Theory Comput.* **2016**, *12*, 4600–4610.
- (S3) Limongelli, V.; Bonomi, M.; Parrinello, M. *Proc. Natl. Acad. Sci.* **2013**, *110*, 6358–6363.
- (S4) Allen, T. W.; Andersen, O. S.; Roux, B. *Proc. Natl. Acad. Sci.* **2004**, *101*, 117–122.



Table 9.1 Hydrophobicity/hydrophilicity fingerprint values of actinyl atoms obtained from the simulations of Chapter 5.

	h	h^{HI}	$h_{0-90^\circ}^{\text{HI}}$
An	-7.9	-5.2	-
O _{yl}	-1.9	0.4	-2.1
O _{W1}	0.8	1.5	0.5
H ₂ O	1.0	1.0	-
CH ₄	-1.0	-1.0	-

9.2. Hydrophobicity hydrophilicity fingerprint of actinyls.

Given the amphiphilic nature of the solvation of actinyls, the simulations carried out in Chapters 4 and 5 are perfect candidates to study the fingerprint behavior in complex cationic systems. We present the fingerprints of the heavy atoms of uranyl as representative of the rest of actinyls since due to their similarity in solvation the fingerprint values must be very similar even for [NpO₂]⁺. The reference values of S_s were calculated from a pure TIP4P-water simulation and a methane TIP4P-water simulation. Three versions of the fingerprint were examined:

- h : uses the RDF between the atom of interest and all water molecules.
- h^{HI} : uses the RDF between the fingerprinted atom and all bulk water molecules excluding the first-shell.
- $h_{0-90^\circ}^{\text{HI}}$: uses the 0-90° angle-solved RDF between the fingerprinted atom and all bulk water molecules. The 0-90° cone is calculated in the same fashion as in the angle-resolved RDFs of the O_{yl} atom in Chapter 4.

The last two definitions connect with the HIM philosophy by considering first-shell water molecules part of the solute and not of the solvent. The fingerprint values are collected in Table 9.1.

The first shell water molecules (O_{W1}) are correctly labeled as hydrophilic by the fingerprint in all versions. In contrast, the O_{yl} atoms are labeled as hydrophilic by h^{HI} and hydrophobic by h . h^{HI} is conceptually a better fingerprint

since first-shell water molecules do not solvate the O_{yl} atom. Unfortunately, it also misclassifies the O_{yl} atom as hydrophilic.

As we have seen in Chapter 4, the solvation of the uranyl atoms is very anisotropic and standard RDF can lead to wrong conclusions i. e. the O_{yl} RDF includes solvent molecules that are in the bridge solvation region and are not solvating the O_{yl} atom. For this reason we decided to use as the fingerprint input the 0-90° angle-solved RDF. In this way, the solvent molecules included in the RDF are the ones that solvate the atom. $h_{0-90^\circ}^{\text{HI}}$ classifies correctly the O_{yl} and O_{W1} atoms but it considers O_{W1} to be less hydrophilic than bulk water molecules.

The fingerprint classifies the actinoid cation as hydrophobic which is clearly an artifact. In Section 9.1 this effect was also described for Na⁺. The order imposed on the solvent structure by the doubly charged cation is very high and thus obtaining h values much lower than methane.

In conclusion, the fingerprint appears to be unfit to classify the central atoms of cations with charge higher or equal to one. For the rest of the heavy atoms of the hydrated ion mixed results are obtained.

The fingerprint is too coarse for complex solutes like actinyls. A future improved fingerprint could probably make use of orientational pair entropy in addition to some technique to consider the anisotropicity of the solute in complex environments.

Results and Discussion

In this section we will review the main results of the thesis. Their significance and relation to other works in the literature will be discussed.

10.1. Force Field Development

10.1.1. Actinyl Force Fields In Solution

The largest body of force fields designed concerned the actinyl cations. In particular $[AnO_2 \cdot (H_2O)_5]^{2+}$ for An=U, Np, Pu, Am and $[NpO_2 \cdot (H_2O)_5]^+$. This work was rooted in a chapter of the thesis of F. Torrico, a former PhD student of the group.¹

These are the first hydrated ion models for actinyls and the first to have a molecular cation rather than a monoatomic cation. Using an interaction potential which contains the *ab initio* information of the system is very convenient in actinoid systems. Unlike other compounds, the lack of experimental data complicates parametrizing actinoid compounds empirically.²

The actinyl force fields were developed using as reference structure the pentahydrate cation, $[AnO_2 \cdot (H_2O)_5]^{2+/+}$. The interaction potential was split into four components:

$$E = E_{IMC} + E_{IW1} + E_{HIW} + E_{W-W} \quad (10.1)$$

The first three components are shown in Figure 10.1. The first interaction

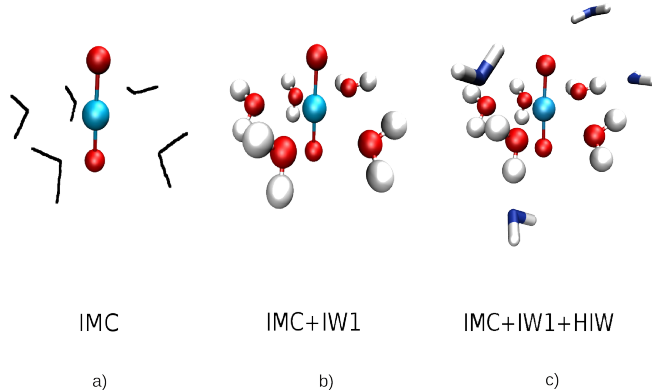


Figure 10.1 Schematic representation of the components of the HIM force field of actinyl ions. The ball and stick representation shows the atoms involved in each of the terms. In a) the first shell is not fully drawn since it does not participate in the IMC but they are added to calculate the interaction energies for the IMC following the HIM.

potential is the Intra-Molecular Cation (IMC). This interaction potential controls the motion within the molecular cation, $[AnO_2]^{2+/+}$. It has the following mathematical expression:

$$E_{IMC} = \sum_i^{\text{sites}} \left(\frac{C_4^{\text{AnO}_{\text{yl}}}}{r_{\text{AnO}_{\text{yl},i}}^4} + \frac{C_6^{\text{AnO}_{\text{yl}}}}{r_{\text{AnO}_{\text{yl},i}}^6} + \frac{C_8^{\text{AnO}_{\text{yl}}}}{r_{\text{AnO}_{\text{yl},i}}^8} + \frac{C_{12}^{\text{AnO}_{\text{yl}}}}{r_{\text{AnO}_{\text{yl},i}}^{12}} \right) + \sum_i^{\text{sites}} \frac{q_{\text{An}} q_{\text{O}_{\text{yl},i}}}{r_{\text{AnO}_{\text{yl},i}}} \quad (10.2)$$

The second term (Equation 10.3) is the ion-first shell water interaction (IW1). In our model we have assumed that the first-shell water molecules to be rigid and have the geometry of the gas phase optimization of the hydrated ion. The IW1 term makes the aqua ion flexible. It has the following mathematical expression:

$$E_{IW1} = \sum_i^{\text{sites}} \frac{C_4^{\text{iO}_1}}{r_{\text{iO}_1}^4} + \frac{C_6^{\text{iO}_1}}{r_{\text{iO}_1}^6} + \frac{C_8^{\text{iO}_1}}{r_{\text{iO}_1}^8} + \frac{C_{12}^{\text{iO}_1}}{r_{\text{iO}_1}^{12}} + \sum_i^{\text{sites}} \sum_j^{\text{1st shell water}} \frac{q_i q_j}{r_{ij}} \quad (10.3)$$

The final term (Equation 10.4) is the hydrated ion-bulk water interaction potential (HIW). This term parametrizes the interaction of the hydrated ion with

any of the bulk water molecules (second shell and further). It has the following mathematical expression:

$$E_{\text{HIW}} = \sum_i^{\text{HI sites}} \sum_j^{\text{water sites}} \left(\frac{C_4^{ij}}{r_{ij}^4} + \frac{C_6^{ij}}{r_{ij}^6} + \frac{C_8^{ij}}{r_{ij}^8} + \frac{C_{12}^{ij}}{r_{ij}^{12}} + \frac{q_i q_j}{r_{ij}} \right) \quad (10.4)$$

The employed bulk water model was TIP4P.³

The partial charges appearing in Equations 10.2-10.4 were assigned with the Merzt-Kollmann method.^{4,5} These charges were calculated in the gas phase QM minimum energy structures and using a wavefunction polarized by bulk solvent represented by a Polarizable Continuum Model (PCM).^{6,7} In the case of $[\text{NpO}_2 \cdot (\text{H}_2\text{O})_5]^+$ only the actinyl unit was given partial charges. Due to the low charge transfer and polarization of this monocation, the first-shell geometries and charges were taken to be equal to those of the TIP4P water model. The coefficients of the force fields were parametrized with a series of QM scans. E_{IMC} and E_{IW1} were parametrized with deformations following the main normal modes of the pentahydrate: symmetric and asymmetric An-O_{yl} tension, O_{yl}-An-O_{yl} bending and lengthening of a An-O_{W1} distance. E_{HIW} was parametrized with scans of a second-shell water molecule moving around the hydrated ion at different distances and orientations. The root mean square errors of the fits were about 1-3 kcal mol⁻¹. All the interaction potentials were calculated specifically for every cation except for the HIW potential which was proven to be very similar across the cations studied. The level of theory for the quantum chemistry calculations was B3LYP with Stuttgart semi-relativistic pseudopotentials and their recommended basis sets on actinoids and aug-PVDZ on light atoms.⁸⁻¹¹ In all electronic structure calculations the first shell of water molecules was included. This was done so that even the IMC truly models the molecular cation in the aqueous medium.

It is important to use a high level of theory in order to shed light on the complicated XAS spectroscopy of actinyls. For this reason a NEVPT2¹²⁻¹⁴-level force field was developed for $[\text{NpO}_2 \cdot (\text{H}_2\text{O})_5]^+$. In this way we treated explicitly the multi-reference nature of the cation instead of using the mean field strategy of DFT. The active space chosen for the CASSCF consisted of the atomic-like f -orbitals of the actinoid and four π/π^* and two σ/σ^* molecular orbitals formed by O_{yl} p -orbitals and actinoid bond-participating f -orbitals. This resulted in a CASSCF(n,10) space where n is six plus the number of actinoid unpaired electrons. A state average between the doubly degenerate

ground state solutions was performed. All calculations were run using the RI and RIJK approximations.^{15–19} to reduce the scaling with basis set size. The chosen basis sets were ma-def2-TZVP for O, def2-SVP for H, and SD(60,MWB)//DEF-TZVP for actinoids.^{11,20,21}

Going from the DFT level of theory to the NEVPT2 level of theory does not change significantly any of the properties of the actinyls in solution. The only exception is bondlengths which are increased a few hundredths of an angstrom for the An-O_{yl} distances and decreased a few hundredths of an angstrom for the An-O_{W1} distances. The sensitivity of EXAFS spectrum is so high that such small changes in structure generate significant changes in the spectrum. This explains the interest in the use a very high level of theory potential energy surface.

Although these systems have been studied in the literature with *ab initio* MD²² or with QM/MM,²³ they were highly limited by the simulation times, system size and quantum mechanical level. This last aspect is particularly important given the size of the second-shell. *Ab initio* force fields provide a cost-effective solution to have near-QM forces spending classical MD CPU hours. Of course, the price to be paid is in human hours of force field development.

Despite there are many force fields for uranyl,^{24–29} the first actinyl force field beyond uranyl was developed by Maggin's group.^{28,30} They realized the importance of many body effects such as polarization of the first shell and their QM calculations were done including four water molecules in the first-shell. We went one step further and implemented the full HIM philosophy to the force field: differentiation of first-shell and bulk water molecules, by partial charge transfer and full hydration shell in the QM calculations. Our force fields are the first force fields to explicitly parametrize bulk water-HI interactions through the HIW potential, making them particularly suitable to describe the second shell region. In addition, other force fields observe residence times of the first shell shorter than experiment^{30–33}. We observe none, which is what is expected given the simulation time.

The complexity of our potential development and the number of parameters fitted makes our set of force fields highly versatile to derive actinyls under different environments due to their first-principles nature. Moreover, we were able to increase even further the accuracy to develop a NEVPT2-level force field for the neptunyl monocation. A proof of its high accuracy is its ability to reasonably reproduce experimental data of a wide variety of types: structure,

dynamics, spectroscopy and thermodynamics.

Unfortunately, the interaction potential functional form prevents the use of combination rules. Therefore, they are essentially limited to the hydrated ion in pure water. This is the “one system, one force field” problem of the HIM. Fortunately, in the case of actinyls the transferability of the HIW potential, the potential requiring the most QM calculations, avoids having to parametrize it for each actinyl. In this way, only the IW1 and IMC potential must be parametrized for each particular actinyl.

10.1.2. Auxiliary Am³⁺ force field

The force field of $[Am \cdot (H_2O)_8]^{3+}$ was generated as an auxiliary tool for a greater goal. It was developed *ad hoc* to reproduce the experimental EXAFS spectrum of Am³⁺. This was done in order to have a better insight in the experimental EXAFS spectrum of an Am³⁺/AmO₂²⁺ mixture since only the EXAFS of a pure Am³⁺ aqueous solution has been recorded. The QM level of theory used was MP2 using a Stuttgart semirelativistic pseudopotential³⁴ with the recommended basis set on Am and cc-PVTZ^{10,35–37} on light atoms. The pseudopotential used includes in the core the f-orbitals since they are internal (unlike in actinyls) and do not participate in bonding. In this way the complex can be modeled using closed-shell techniques. The structure was minimized using S₈ symmetry. RESP³⁸ partial charges were used for the interaction potential. These charges were calculated in the minimized geometry using a wavefunction calculated with the PCM method.^{6,7} Harmonic bond and harmonic angular terms were added to keep the structure of the hydrate with equilibrium bondlengths and angles taken from the optimized structure. The force constants were fitted to reproduce the experimental EXAFS spectrum of Am³⁺ using the structures generated by the MD simulation. Lennard-Jones parameters of TIP4P were added to the first-shell water molecules to interact with the TIP4P bulk water molecules.

10.1.3. Hydrated Ion-Clay Interaction Potential

For the simulations of uranyl in montmorillonite clay interlayers the HI clay interaction (HIC) did not exist in the literature. A new strategy had to be developed since this was the first time the interaction of a HI with a surface was being studied. In the literature^{39–46} the Wipff-Guilbaud model of uranyl

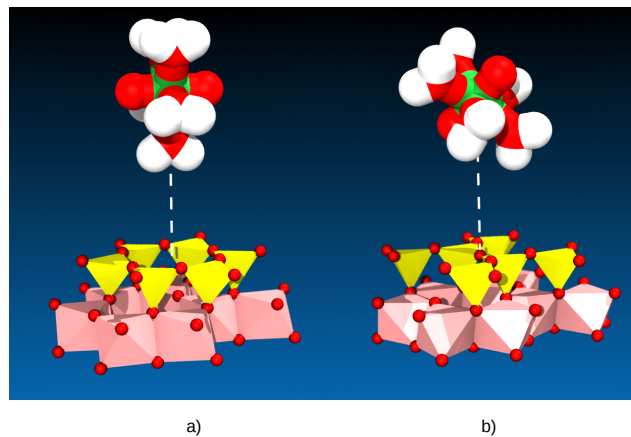


Figure 10.2 Some of the clay cluster-hydrated ion scans used to parametrize the HIC potential. a) Hexagonal center scan with a uranyl axis tilt angle of 90° with respect to the surface normal. b) O-center cluster with a tilt angle of 45° . The color coding is as follows: Al octahedra (pink), Si tetrahedra (yellow), O atoms (red), uranium atoms (green), and H atoms (white)

with combination rules was used, and therefore, to the best of our knowledge, this force field is the first *ab initio* force field for actinyl-clay systems.

The force field was parametrized from the interaction energies of QM scans of $[\text{UO}_2 \cdot (\text{H}_2\text{O})_5]^{2+}$ approaching a cluster of atoms carved from the clay surface (Figure 10.2). The level of theory for the QM calculations was MP2 with RI^{15–19} and RIJCOSX⁴⁷ scaling reduction techniques due to the large size of the systems. U, Al and Si were described by Stuttgart semirelativistic pseudopotentials and their recommended basis sets;^{48,49} O and H were described by the aug-cc-PVDZ basis sets.^{10,35–37,50} The interaction potential function had the following mathematical definition:

$$\begin{aligned}
 E_{\text{HIC}} &= E_{\text{Coul.}} + E_{\text{non-Coul.}} \\
 &= \sum_i^{\text{aqua ion clay}} \sum_j \frac{q_i q_j}{r_{ij}} + \sum_i^{\text{U, O}_{\text{yl}}, \text{O}_1} \sum_j^{\text{O}_{\text{clay}}} \frac{C_4^{ij}}{r_{ij}^4} + \frac{C_6^{ij}}{r_{ij}^6} + \frac{C_8^{ij}}{r_{ij}^8} + \frac{C_{12}^{ij}}{r_{ij}^{12}} \\
 &\quad + \sum_i^{\text{O}_{\text{yl}}} \sum_j^{\text{Si}} \frac{C_4^{ij}}{r_{ij}^4} + \frac{C_6^{ij}}{r_{ij}^6} + \frac{C_8^{ij}}{r_{ij}^8} + \frac{C_{12}^{ij}}{r_{ij}^{12}}
 \end{aligned} \tag{10.5}$$

The root mean square error of the fit was $\sim 5 \text{ kcal mol}^{-1}$, a reasonable value considering that the interaction energies can be as low as $-100 \text{ kcal mol}^{-1}$. Structures obtained from the MD trajectories were used as a test set of data to check if the HIC potential reproduced the quantum interaction energies in structures outside of the training data set.

A good indicator of the quality of the force field is that it reproduces the experimental finding that the first-shell is identical in the clay as in aqueous solution.⁵¹ Thisoutersphere complex formation was not imposed on the model. Therefore it was observed because the force field made this phenomenon to be favored over a partial dehydration into the tetrahydrate. In addition, the tilt-angle of the uranyl axis was compatible with the experimental evidence that showed it to be neither perpendicular nor parallel to the clay surface.⁵²

10.2. Physico-chemical properties of actinyls in solution

MD simulations were run on the actinyl hydrated ions in aqueous solution with the newly developed HIM *ab initio* force fields. In general, the properties calculated related closely to their experimental values. In addition the properties are of a wide variety: structure, dynamics, spectroscopy and thermodynamics. This good correlation with experiment and the fact that the force field is *ab initio* gives us confidence when computing properties that cannot be compared to experiment.

The theoretical ΔH_{hyd} of the doubly-charged actinyls was fairly close to the value given by Marcus⁵³ for uranyl although further away from the value of Gibson.⁵⁴ In the case of $[\text{NpO}_2]^+$, the ΔH_{hyd} value matched the experimental value of Gibson.⁵⁴ The translational self-diffusion coefficients of actinyls overestimated their experimental values. We found this to be caused by the overestimated diffusivity of water by the TIP4P bulk water model since the normalization of the coefficients by those of water gave a close agreement between theory and experiment.

Our estimation of normal mode frequencies with respect to infrared and Raman spectra was satisfactory (maximum relative error of 15%) considering that the B3LYP potential energy surface limits the model accuracy. If the NEVPT2 force field developed for $[\text{NpO}_2]^+$ is used in simulation, the frequencies of the symmetric and asymmetric stretchings is even closer to experiment

than if the DFT force field is used. This follows the idea that *ab initio* force fields can be improved by improving the QM data set.

Despite the specificity of E_{IW1} and E_{IMC} , all hexavalent actinyls, $[AnO_2 \cdot (H_2O)_5]^{2+}$, presented very similar physico-chemical properties: solvation structure, diffusion coefficients, hydration enthalpies (ΔH_{hyd}), and second-shell mean residence times. The only exceptions were their vibrational and XAS spectra. Interestingly, even lowering the charge in the $[NpO_2]^{2+/+}$ pair barely affected most hydration properties. The only exceptions were a small lengthening of the distances, a decrease of ΔH_{hyd} and shortening of the second shell mean residence times. Therefore, knowledge of a single actinyl in these regards can be generalized to the whole family. This is an interesting conclusion for experimentalists who can choose to work with the least radiotoxic of them, uranyl, when dealing with the properties that we find equivalent.

An interesting outcome of the actinyl studies was understanding their hydration. Since the cation is a linear molecule, the asymmetry of the solvation required different analysis tools than for conventional cations. Integrating the RDF of the second shell gave second-shell coordination numbers of 30, much higher than the other values in the literature, ~20. The reason for such number is that the RDF assumes spherical symmetry and spherically averages the distribution. When facing with non-spherical problems, non-spherical techniques must be employed. Using the multisite cavity coordination number⁵⁵ second-shell coordination numbers of 22-23 are obtained. The method gives similar results if used on other actinyl models. Angularly-resolved RDFs were also used to investigate the solvation structure.

No hydrogen bonding was found between water molecules and the O_{yl} atoms. This agrees with *ab initio* MD simulations^{22,23,56} and classical simulations using *ab initio* force fields.^{27,28,57} We hypothesize that this apical hydrogen bond could be an artifact of empirical force fields²⁴⁻²⁶ and static QM calculations.⁵⁸ We describe actinyls as anisotropic amphiphilic solutes which have a conventional solvation sphere capped at the poles by hydrophobic regions.

Two clear solvation regions are observed. The equatorial region has the typical first-second shell interactions of cations: the first-shell water molecules form two hydrogen bonds with the second-shell ones, i. e. a hydrophilic solvation structure. Axially there is a hydrophobic solvation: the water molecules form water-water structures around the O_{yl} atoms without interacting directionally with it. The final picture is that actinyls are amphiphilic anisotropically solvated solutes that have conventional cation solvation capped

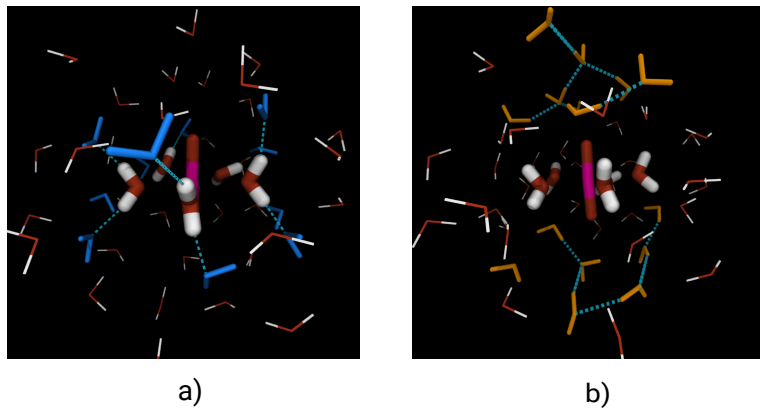


Figure 10.3 MD snapshots of $[NpO_2 \cdot (H_2O)_5]^{2+}$ in water. a) Equatorial water molecules solvating the first-shell hydrophilically (blue). b) Axial water molecules hydrophobically solvating the O_{yl} atom (orange).

at the poles by hydrophobic regions (Figure 10.3). This solvation is very unusual since a very small and highly charged cation holds two distinct solvation regions.

The most important achievement of this part of the thesis is the proposal of a general picture of the solvation of actinyls. Our view concurs with other works in the literature.^{22,23,27,28,56,57} Nevertheless, our picture stands on the extension of a robust methodology due to:

1. The ability of the hydrated ion model to capture complicated many-body effects.
2. Our explicit parametrization of the bulk-HI interaction which separates our modeling from the rest of *ab initio* force fields. Additionally, this interaction is universal among actinyls.
3. The use of a classical potential allowed reaching larger system sizes and timescales than in *ab initio* MD.

10.3. Modelling of actinyl EXAFS spectra

The theoretical EXAFS spectra of the actinyls was calculated from the MD trajectories using the B3LYP level force fields. Here we shall not refer to americium since its particular case will be explained in the next section. The simulated

EXAFS spectrum of uranyl gave a reasonable agreement with the experimental one. Nevertheless, the rest of actinyls showed a qualitative agreement but far from that of uranyl or of other cations modeled using the group's methodologies. Since uranyl is the only closed shell actinyl of the set, we wondered if the potential energy surface used to build the force field was biased by the mean-field treatment done by unrestricted DFT in the open-shell systems. The NEVPT2 calculations of the actinyls had the effect of lengthening the An-O_{yl} distance and as a result a shortening of the An-O_{W1} distance. Although the changes are in the order of hundredths of an angstrom, these may cause a certain impact on the EXAFS spectra which are quite sensitive to structure.

We calculated the theoretical EXAFS of [NpO₂]⁺ using the NEVPT2-level *ab initio* force field. There was a significant improvement in the correspondence of the spectra with experiment with respect to the correspondence obtained using the DFT-level force field. The increase of the level of theory produced overall an improvement in the correspondence with experiment of the spectra. Nevertheless, the shoulder at low k appears to be the most complex to predict since in this region of the spectrum both An-O_{yl} and An-O_{W1} have significant weight.

10.4. Modelling of americyl XAS spectra

Our modeling of americyl XAS spectra was an example of how theory and experiment can breed deep insights when combined. This part of the project started when trying to compare our theoretical americyl spectrum to experiment. We found that the only available experimental EXAFS spectrum were of a mixture of Am(VI)/Am(III), published in 2016.⁵⁹ The experimentalists were unable to disentangle the mixture spectrum into the spectra of the two species. In addition, their modeling of the EXAFS equation gave some unusual structural parameters. They obtained a Debye-Waller factor for the Am-O_{yl} distance which was higher than for Am-O_{W1}. This is unusual since covalent bonds as the oxo-bond (Am=O) are generally stiffer than coordinative bonds (Am-O_{W1}) and thus have lower thermal dispersion. With this information in mind we decided to tackle the problem with some of our newly developed actinyl force fields.

MD simulations of aqueous [AmO₂·(H₂O)₅]²⁺ and [Am·(H₂O)₈]³⁺ were run using the newly developed force fields; *ab initio* for Am(VI) and empirical

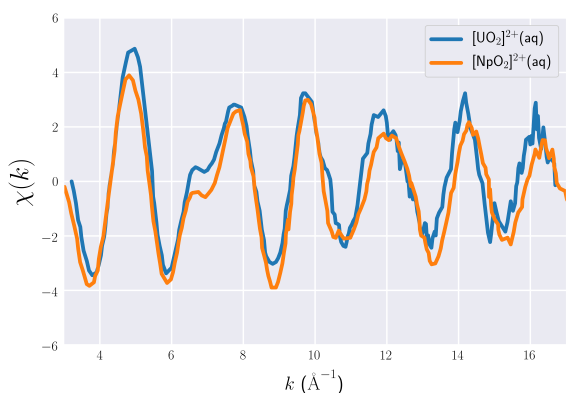


Figure 10.4 L_3 -edge k^2 -weighted EXAFS spectrum of Am experimental (dashed) and simulated (solid). Top: Am^{3+} aqueous solution experimental⁶⁰ and simulated spectra. Middle: pure $[AmO_2]^{2+}$ simulated spectrum (red) and of the ionic mixture.⁵⁹ Bottom: Experimental spectrum of the ionic mixture⁵⁹ and simulated spectrum of $[AmO_2]^{2+}$ and Am^{3+} weighted with 70/30 (pink) and 55/45 (blue) ratios.

for Am(III). The theoretical EXAFS and XANES spectra for both compounds were calculated. The Am(III) spectra matched the experiment as expected since the potential was built *ad hoc* to do so. We generated the weighted sum of the XAS spectra of both pure theoretical spectra to produce the theoretical spectrum of the mixture. The weights were given according to the relative abundance of the species reported by the experimentalists. The agreement of the theoretical spectrum of the mixture and experiment was really good. The experimentalists determined that the initial Am(VI)/Am(III) ratio of the species, 70/30, was likely to have changed due to radiation damage or the redox instability Am(VI). Varying the weights of the simulated spectra of Am(VI)/Am(III) we found a 55/45 ratio to give the best match between the experimental and theoretical spectra (Figure 10.4).

In this work we simulated XAS spectra (EXAFS and XANES) of a mixture of species which is consistent with the experiment. This is a very stimulating result given the complexity of EXAFS modeling in general, specially on actinyls (see Chapter 7) and in a mixture of species. The results provide confidence in the developed methodology.

This synergic theoretical-experimental findings gave strong evidence that our simulation of $[AmO_2 \cdot (H_2O)_5]^{2+}$ was fairly accurate. This allowed us to

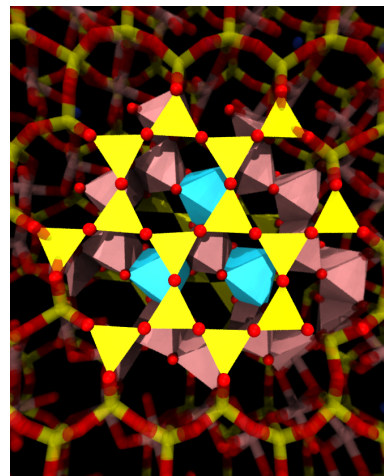


Figure 10.5 Interaction site for uranyl at the montmorillonite clay surface: three Mg octahedra separated from each other by a single central Al octahedron. Al octahedra (pink), Mg octahedra (blue), Si tetrahedra (yellow), O atoms (red), uranium atoms (green), and H atoms (white)

predict the distances, Debye-Waller factors and XAS spectra of pure americyl aqueous solution, which has never been obtained experimentally. In addition, our parameters recover the usual trend that the stronger bond should have the lowest Debye-Waller factor.

10.5. Diffusion of uranyl in montmorillonite clay

MD simulations were run on hydrated montmorillonite clay introducing uranyl cations in the interlayer in exchange for the Na^+ cations. We studied the diffusion and dynamics of the uranyl cations inside the interlayers. Two simulations were run. One contained a single uranyl cation per interlayer and the other one four ions per interlayer. We have studied only uranyl but given the similarities between the actinyls, the information is likely to be extended to the rest of them. This is particularly important since the most hazardous actinoids of spent nuclear fuel are neptunium, plutonium and americium.

The diffusion of the uranyl cations within the clays was greatly hindered with respect to solution. The diffusion occurs on the clay surface with very few transitions of the cations from one surface to the middle of the interlayer or the other surface. This work is the first to calculate from MD the constrictivity

factor, δ_{int} , which measures the uranyl diffusivity in the interlayer with respect to solution. Our estimation of δ_{int} was close to one order of magnitude higher than experiment⁶¹ encouraging the idea that on broad strokes we capture the physics of the system. The disagreement between theory and experiment should be put in context with the difficulties of modeling a very homogeneous system like real clays in complex electrolytes. The main causes of discrepancy could be the relatively short-time of the simulation, the inaccuracies in force field development, the differences between our idealized system and the real clays, and the fact that the δ_{int} is a fitted parameter in Fick-equation modeling and other effects could contribute.

The key finding of the work was the identification of strong interaction sites for uranyl. We observed that uranyls tightly bound to the surface in regions were three substitutions occurred forming a triangle of Mg-octahedra around an Al-octahedron (See Figure 10.5). The electrostatic potential maps of the surface showed that the strong interaction is driven by electrostatics. The identification of the sites allowed us to propose a hopping diffusion mechanism. In this mechanism the uranyl cations oscillate around the interaction sites until they are able to escape and diffuse away until reaching another site, then the motion becomes oscillatory again.

The other interesting result of the simulations was that increasing the concentration of uranyl cations in the clay increased their diffusion. We found the explanation for this phenomenon in the strong interaction sites. If there are more uranyl cations in the interlayer there will be more occupied sites on average and thus a diffusing cation will have larger displacements before falling into a site. In addition, the repulsion between cations can promote one cation “pushing” others out of their sites also increasing diffusion.

The microscopical information obtained from our studies gives a complementary view to uranyl diffusion in clays to what is typically studied with macroscopic Fick-equation modeling.

10.6. Development of a local hydrophobicity/hydrophilicity fingerprint for enhanced sampling simulation

A local fingerprint for hydrophobicity and hydrophilicity was developed inspired by the expansion of entropy in terms of increasing correlation terms

(Equation 3.8). The fingerprint for solute heavy atom, i , in aqueous solution is:

$$S_s^i = -2\pi\rho_{w,loc} \int_0^\infty \{ g_{iw}(r) \ln [g_{iw}(r)] - g_{iw}(r) + 1 \} r^2 dr \quad (10.6)$$

Where $\rho_{w,loc}$ is the local water density around the solute atom and $g_{iw}(r)$ is the radial distribution function (RDF) of atom i with water molecules, w. S_s^i is then rescaled into h_i , which is defined to be 1 for water and -1 for methane to give perspective to the fingerprint numerical values. The reader must be cautioned that the fingerprint is not a measurement of hydration entropy, since it is only one term of the expansion of the translational entropy of the system. Our goal is to find a fingerprint that measures in simple fashion hydrophobicity or hydrophilicity locally.

The fingerprint was able to correctly classify as hydrophilic or hydrophobic the atoms of the 20 proteinogenic amino acids which have a large variety of chemical groups and environments. Figure 10.6 shows the amino acids with their heavy atoms colored according to their h values. It is striking that some of the aromatic atoms are colored as slightly hydrophilic. Interestingly this can be explained because experimentally the properties of aromatic compounds are not as hydrophobic as aliphatic carbons.^{62–65}

The fingerprint is very simple in formulation and calculation. It just takes as input the RDF which is routinely obtained in simulation. It is a local fingerprint that measures atomic hydrophobicity/hydrophilicity in contrast with most scales in the literature which focus on the whole residue.⁶⁶ The maximum fingerprint value of the amino acid was found to correlate with its hydration free energy. The correlation is not very strong but is very similar to the one obtained by Schauperl et al.⁶⁷ In their work they used a much more complex and computationally demanding technique that unlike our fingerprint is dedicated fully to thermodynamical property calculation. Therefore, our fingerprint gives a measurement of the hydrophobicity or hydrophilicity which is simple, local, inexpensive and useful to classify the atoms of molecular solutes.

The instantaneous value of the fingerprint can be calculated on-the-fly in MD simulation. The fingerprint can become a CV in enhanced sampling simulations using a differentiable continuous version of the RDF. The fingerprint serves as a desolvation CV. In order to prove the usefulness of the fingerprint as a CV, we ran WTMetaD simulations. The model system chosen was a host-guest system in aqueous solution. Host-guest systems are model systems for protein-ligand complexes. The host is a barrel-shaped molecule that can

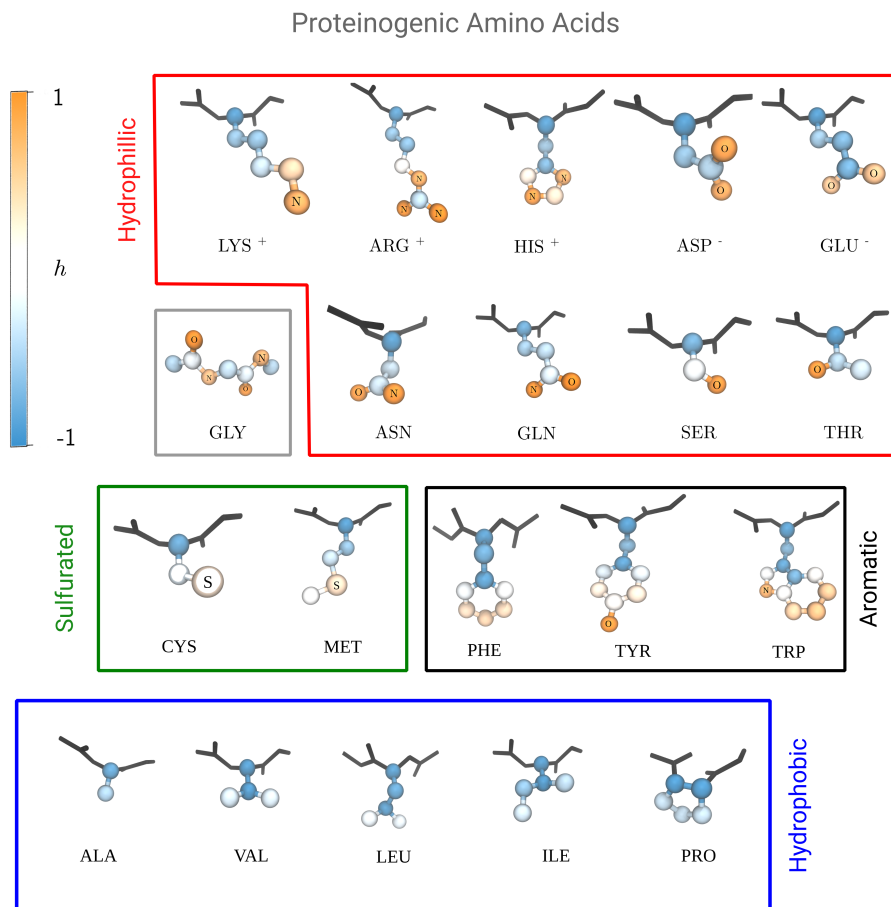


Figure 10.6 Structure of the 20 proteinogenic amino acids with their heavy atoms colored by their hydrophobicity/hydrophilicity fingerprint values. The color scale varies from hydrophilic (orange), to intermediate (white), to hydrophobic (blue). Hydrogen atoms are omitted. Unlabeled atoms are carbon atoms. The backbone is only shown for glycine since its fingerprint value is very similar in all cases.

host a smaller molecule, the guest. In this system in particular the literature showed that desolvation of the host was a crucial slow mode of the binding.⁶⁸ Therefore, in addition to a binding CV (a contact map) a desolvation CV (the fingerprint CV) had to be used in order to converge the simulations.

Using the fingerprint as a desolvation CV allowed the convergence of the WTMetaD simulations. This was done in a single simulation whereas in the literature it required an additional free energy perturbation calculation.⁶⁸ The analysis of the free energy surface of the host-guest binding showed that the removal of the two last water molecules within the barrel is a kinetic barrier in the process.

The fingerprint serves as an alternative to other solvation CVs like the coordination number of water molecules which just counts the number of water molecules around a solute atom. Our CV is more detailed since apart from measuring the amount of solvation around the molecule it also accounts for the structure of this solvation.

10.6.1. Application to actinyl hydration

The fingerprint of the actinyl pentahydrate atoms was calculated. The fingerprint has mixed results in classifying the atoms of the actinyl pentahydrates and appears to be too coarse for such systems. The fingerprint mistakenly classifies the actinoid atom as hydrophobic. This had also been observed in Na^+ . It also mislabels the O_{yl} atom as hydrophilic. We attribute this fact to the use of the total RDF which captures the water molecules of the bridge-solvation region that do not directly solvate the O_{yl} atom. Using an angle-solved RDF in the fingerprint correctly classifies both oxygen atom types but unfortunately considers the O_{W1} atom less hydrophilic than bulk water.

A future improved fingerprint should probably make use of orientational pair entropy in addition to some technique to consider the anisotropicity of the solute in complex environments.

10.7. Bibliography

- 
1. Torrico Perdomo, F. M. Estudio Cuántico-Estadístico de la Hidratación de Cationes Pesados. Ph.D. thesis, Universidad de Sevilla, Spain, 2005.
 2. Marcus, Y. *Ions in Solution and their Solvation*; John Wiley & Sons: Hoboken, NJ, 2016.

3. Jorgensen, W. L.; Chandrasekhar, J.; Madura, J. D.; Impey, R. W.; Klein, M. L. *J. Chem. Phys.* **1983**, *79*, 926–935.
4. Singh, U. C.; Kollman, P. A. *J. Comput. Chem.* **1984**, *5*, 129–145.
5. Besler, B. H.; Merz, K. M.; Kollman, P. A. *J. Comput. Chem.* **1990**, *11*, 431–439.
6. Miertuš, S.; Scrocco, E.; Tomasi, J. *Chem. Phys.* **1981**, *55*, 117–129.
7. Cancès, E.; Mennucci, B.; Tomasi, J. *J. Chem. Phys.* **1997**, *107*, 3032–3041.
8. Becke, A. D. *J. Chem. Phys.* **1993**, *98*, 5648–5652.
9. Stephens, P. J.; Devlin, F. J.; Chabalowski, C. F.; Frisch, M. J. *J. Phys. Chem.* **1994**, *98*, 11623–11627.
10. Woon, D. E.; Dunning Jr., T. H. *J. Chem. Phys.* **1993**, *98*, 1358–1371.
11. Küchle, W.; Dolg, M.; Stoll, H.; Preuss, J. *J. Chem. Phys.* **1994**, *100*, 7535–7542.
12. Angeli, C.; Cimiraglia, R.; Evangelisti, S.; Leininger, T.; Malrieu, J.-P. *J. Chem. Phys.* **2001**, *114*, 10252–10264.
13. Angeli, C.; Cimiraglia, R.; Malrieu, J.-P. *Chem. Phys. Lett.* **2001**, *350*, 297–305.
14. Angeli, C.; Cimiraglia, R.; Malrieu, J.-P. *J. Chem. Phys.* **2002**, *117*, 9138–9153.
15. Dunlap, B. I.; Connolly, J. W. D.; Sabin, J. R. *J. Chem. Phys.* **1979**, *71*, 3396–3402.
16. Van Alsenoy, C. *J. Comp. Chem.* **1988**, *9*, 620–626.
17. Kendall, R. A.; Früchtl, H. A. *Theor. Chem. Acc.* **1997**, *97*, 158–163.
18. Eichkorn, K.; Treutler, O.; Öhm, H.; Häser, M.; Ahlrichs, R. *Chem. Phys. Lett.* **1995**, *240*, 283–290.
19. Eichkorn, K.; Weigend, F.; Treutler, O.; Ahlrichs, R. *Theor. Chem. Acc.* **1997**, *97*, 119–124.
20. Weigend, F.; Ahlrichs, R. *Phys. Chem. Chem. Phys.* **2005**, *7*, 3297–3305.
21. Rappoport, D.; Furche, F. *J. Chem. Phys.* **2010**, *133*, 134105–134115.
22. Bühl, M.; Kabrede, H.; Diss, R.; Wipff, G. *J. Am. Chem. Soc.* **2006**, *128*, 6357–6368.
23. Frick, R. J.; Hofer, T. S.; Pribil, A. B.; Randolph, B. R.; Rode, B. M. *J. Phys. Chem.*

- A* **2009**, *113*, 12496–12503.
24. Guilbaud, P.; Wipff, G. *J. Mol. Struc. THEOCHEM* **1996**, *366*, 55–63.
 25. Guilbaud, P.; Wipff, G. *J. Phys. Chem.* **1993**, *97*, 5685–5692.
 26. Kerisit, S.; Liu, C. *J. Phys. Chem. A* **2013**, *117*, 6421–6432.
 27. Hagberg, D.; Karlström, G.; Roos, B. O.; Gagliardi, L. *J. Am. Chem. Soc.* **2005**, *127*, 14250–14256.
 28. Pomogaev, V.; Tiwari, S. P.; Rai, N.; Goff, G. S.; Runde, W.; Schneider, W. F.; Maginn, E. *J. Phys. Chem. Chem. Phys.* **2013**, *15*, 15954–15963.
 29. Duvail, M.; Dumas, T.; Paquet, A.; Coste, A.; Berthon, L.; Guilbaud, P. *Phys. Chem. Chem. Phys.* **2019**, *21*, 7894–7906.
 30. Tiwari, S. P.; Rai, N.; Maginn, E. *J. Phys. Chem. Chem. Phys.* **2014**, *16*, 8060–8069.
 31. Helm, L.; Merbach, A. E. *Chem. Rev.* **2005**, *105*, 1923–1960.
 32. Richens, D. T. *The Chemistry of Aqua Ions*; J. Wiley: West Sussex, England, 1997.

 33. Panasci, A. F. Ligand exchange kinetics of environmentally relevant metals. Ph.D. thesis, University of California, Davis, 2014.
 34. Moritz, A.; Cao, X.; Dolg, M. *Theor. Chem. Acc.* **2007**, *117*, 473–481.
 35. Dunning Jr., T. H. *J. Chem. Phys.* **1989**, *90*, 1007–1023.
 36. Kendall, R. A.; Harrison, R. J.; Dunning Jr., T. H.; Harrison, R. J. *J. Chem. Phys.* **1992**, *96*, 6796–6806.
 37. Woon, D. E.; Dunning Jr., T. H. *J. Chem. Phys.* **1994**, *100*, 2975–2988.
 38. Bayly, C. I.; Cieplak, P.; Cornell, W.; Kollman, P. A. *J. Phys. Chem.* **1993**, *97*, 10269–10280.
 39. Greathouse, J. A.; Cygan, R. T. *Phys. Chem. Chem. Phys.* **2005**, *7*, 3580–3586.
 40. Greathouse, J. A.; Cygan, R. T. *Environ. Sci. Technol.* **2006**, *40*, 3865–3871.
 41. Yang, W.; Zaoui, A. *J. Hazard. Mater.* **2013**, *261*, 224–234.
 42. Liu, X.-y.; Wang, L.-h.; Zheng, Z.; Kang, M.-l.; Li, C.; Liu, C.-l. *J. Hazard. Mater.* **2013**, *244*, 21–28.
 43. Teich-McGoldrick, S. L.; Greathouse, J. A.; Cygan, R. T. *Mol. Simul.* **2014**, *40*, 610–617.

44. Zhang, N.; Liu, X.; Li, C.; Liu, C. *Inorg. Chem. Front.* **2015**, *2*, 67–74.
45. Zaidan, O. F.; Greathouse, J. A.; Pabalan, R. T. *Clays Clay Miner.* **2003**, *51*, 372–381.
46. Greathouse, J. A.; Stellalevinsohn, H. R.; Denecke, M. A.; Bauer, A.; Pabalan, R. T. *Clays Clay Miner.* **2005**, *53*, 278–286.
47. Neese, F.; Wennmohs, F.; Hansen, A.; Becker, U. *Chem. Phys.* **2009**, *356*, 98–109.
48. Cao, X.; Dolg, M. *J. Mol. Struct. THEOCHEM* **2004**, *673*, 203–209.
49. Weigend, F.; Ahlrichs, R. *Phys. Chem. Chem. Phys.* **2005**, *7*, 3297–3305.
50. Wilson, A. K.; van Mourik, T.; Dunning Jr., T. H. *J. Mol. Struct. THEOCHEM* **1996**, *388*, 339–349.
51. Catalano, J. G.; Brown Jr, G. E. *Geochim. Cosmochim. Acta* **2005**, *69*, 2995–3005.
52. Denecke, M. A.; Bauer, A.; Kim, J. I.; Moll, H. *Miner. Interact. Close to Equilib.* **1999**, 35–37.
53. Marcus, Y.; Loewenschuss, A. *J. Chem. Soc. Faraday Trans.* **1986**, *82*, 2873–2886.
54. Gibson, J. K.; Haire, R. G.; Santos, M.; Marçalo, J.; de Matos, A. *J. Phys. Chem. A* **2005**, *109*, 2768–2781.
55. Melchior, A.; Martínez, J. M.; Pappalardo, R. R.; Sánchez Marcos, E. *J. Chem. Theor. Comput.* **2013**, *9*, 4562–4573.
56. Nichols, P.; Bylaska, E. J.; Schenter, G. K.; de Jong, W. *J. Chem. Phys.* **2008**, *128*, 124507–124514.
57. Rai, N.; Tiwari, S. P.; Maginn, E. J. *J. Phys. Chem. B* **2012**, *116*, 10885–10897.
58. Siboulet, B.; Marsden, C. J.; Vitorge, P. *Chem. Phys.* **2006**, *326*, 289–296.
59. Riddle, C.; Czerwinski, K.; Kim, E.; Paviet, P.; Weck, P.; Poineau, F.; Conradson, S. *J. Radioanal. Nucl.* **2016**, *309*, 1087–1095.
60. Stumpf, S.; Stumpf, T.; Dardenne, K.; Hennig, C.; Foerstendorf, H.; Klenze, R.; Fanghänel, T. *Environ. Sci. Technol.* **2006**, *40*, 3522–3528.
61. Moore, S. M.; Shackelford, C. D. Uranium diffusion in soils and rocks. Tailings Mine Waste Conf. Vancouver, BC, 2011; pp 549–561.
62. McAuliffe, C. *J. Phys. Chem.* **1966**, *70*, 1267–1275.

63. Cabani, S.; Gianni, P.; Mollica, V.; Lepori, L. *J. Solution Chem.* **1981**, *10*, 563–595.
 64. Ben-Amotz, D. *Annu. Rev. Phys. Chem.* **2016**, *67*, 617–638.
 65. Harris, R. C.; Pettitt, B. M. *J. Phys. Condens. Matter* **2016**, *28*, 083003–083026.
 66. Simm, S.; Einloft, J.; Mirus, O.; Schleiff, E. *Biol. Res.* **2016**, *49*, 31–49.
 67. Schauperl, M.; Podewitz, M.; Waldner, B. J.; Liedl, K. R. *J. Chem. Theory Comput.* **2016**, *12*, 4600–4610.
 68. Bhakat, S.; Söderhjelm, P. *J. Comput. Aided. Mol. Des.* **2017**, *31*, 119–132.
-
- 

Conclusions

In this thesis we have presented a set of *ab initio* HIM force fields for $[AnO_2 \cdot (H_2O)_5]^{2+}$ for An=U, Np, Pu, Am in water as well as an additional one for the interaction of uranyl with montmorillonite clay. These interaction potentials offer an alternative to current ones in particular since they parametrize the HI-bulk water interactions. They have proven to reproduce satisfactorily many experimental properties of the systems: XAS spectra, hydration enthalpies, diffusion coefficients...

The developed potentials allowed the detailed study of the solvation of the actinyls. Their solvation was found to be amphiphilic and anisotropic which is remarkable considering the small size of the ion and its charge. From the MD simulations we calculated the XAS spectra of the actinyls and compared them to experiment. This allowed us to assess the quality of their structural model and to interpret the keys of their complex spectra. In particular, we interpreted the experimental XAS spectra of an $Am^{3+}/[AmO_2]^{2+}$ mixture reproducing the theoretical EXAFS spectrum of a mixture. With the experimental validation of our simulation we were able to predict the structural parameters and the EXAFS and XANES spectra of a pure $[AmO_2 \cdot (H_2O)_5]^{2+}$ solution, a solution that has never been obtained. This will be a striking experimental challenge for actinoid solution chemistry in the near future.

The uranyl montmorillonite clay simulations allowed us to study the diffusion of the HI in the interlayers. We identified the existence of strong interaction sites for uranyl. These sites force the uranyl to diffuse following a hopping

mechanism. Because of this, uranyl diffusion increases with uranyl concentration due to cation-cation interactions and a larger coverage of surface sites.

Another methodological achievement of this thesis has been the development of a simple local fingerprint for hydrophobicity and hydrophilicity. The fingerprint was able to classify correctly the atoms of amino acids in water which have varied functional groups and chemical environments. The fingerprint has also been proven to be a useful solvation/desolvation CV in enhanced sampling simulations. When applied to characterize the different hydration regions around actinyls, fingerprint values do not seem to provide such a clear view as in the amino acid case. This opens the door to refinement of the index when dealing with metal cations and ions in general.

In conclusion, this thesis provides a different perspective to the study of aqueous actinyls and actinyls in clay interlayers. This different perspective is based on the usage of newly developed methodologies that enable a cost effective and fairly accurate view of these important systems.

